3D non-linear modelling of soil-structure interaction of masonry towers in dynamic conditions. = Modellazione tridimensionale non-lineare dell'interazione terreno-struttura di

Abstract

Masonry towers are widespread in many European countries and in Italy as well, representing one of the most prominent parts of our cultural and historical legacy. Recently, the seismic performance assessment of these structures has become a central topic in structural engineering because of their high seismic vulnerability. This is mainly due to their peculiar structural configuration and poor mechanical properties which generally characterizes the masonry texture. Hence, a huge effort has already been made to assess the seismic response of these historical monuments from a structural point of view, generally neglecting the soil compliance effect in favour of a perfectly fixed-base condition. However, a fixed-base scheme is not always suitable to represent the actual in-situ conditions as the foundation deposits can be characterized by soft soils sequences that should not allow to use this approximation. Indeed, the occurrence of a tower resting on deformable deposits is not so remote and in addition it is often associated to relevant seismic hazard levels of the area. Nevertheless, a soil-structure interaction analysis is just occasionally considered because of the huge complexity of the problem, which is highly interdisciplinary and involves seismic, structural and geotechnical engineering expertise. In this context, this thesis has focused on investigating the soil-structure interaction influence on the seismic performance of masonry towers. The mechanical response of the masonry material has been described through an advanced constitutive model which accounts for a plastic-damage behaviour. The research framework has mainly covered three aspects of the problem. First of all, the role of the soil deposit conditions has been studied through the investigation of the soil stratigraphic heterogeneity influence. Secondly, the impact of the soil dynamic behaviour has been examined following two different modelling approaches, i.e a linear visco-elastic and an equivalent-linear visco-elastic strategy. Finally, the relationship between the soil-structure interaction effects and the tower structural slenderness has been analysed. The numerical simulations have been carried out through non-linear time-history analyses adopting a 3D model of the problem. The results of the study suggest that the soil-structure interaction phenomena can clearly affect the seismic performance of ancient masonry towers, modifying the modal properties, the seismic demand and the possible collapse modes affecting the structure if compared to the fixed-base scheme.

Aldo Fabio D'Oria
DICATECh
2022

D. R. R. S.

Doctor of Philosophy in Risk and Environmental, Territorial and Building Development

Coordinator: Prof. Michele Mossa

XXXV CYCLE
ICAR/07 - ICAR/09

DICATECh
Department of Civil, Environmental, Land, Building Engineering and Chemistry

Aldo Fabio D'Oria

3D non-linear modelling of soil-structure interaction of masonry towers in dynamic conditions

Prof. Gaetano Elia
Prof. Giuseppina Uva
DICATECh Politecnico di Bari, Italy

Dr. Annamaria di Lernia
DICATECh Politecnico di Bari, Italy

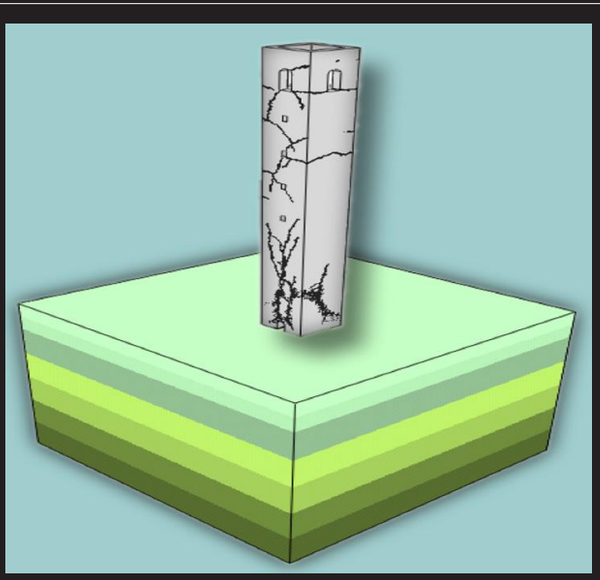

POLITECNICO DI BARI

12

2022

3D non-linear modelling of soil-structure interaction of masonry towers in dynamic conditions

D.R.R.S

Doctor of Philosopy in Risk and Environmental, Territorial and Building Development

Coordinator: Prof. Michele Mossa

XXXV CYCLE
ICAR/07 - ICAR/09

DICATECh
Department of Civil, Environmental, Land, Building Engineering and Chemistry

POLITECNICO DI BARI

12
2022

3D non-linear modelling of soil-structure interaction of masonry towers in dynamic conditions

Prof. Gaetano Elia
Prof. Giuseppina Uva
DICATECh Politecnico di Bari, Italy

Dr. Annamaria di Lernia
DICATECh Politecnico di Bari, Italy

Aldo Fabio D'Oria

D.R.R.S

POLITECNICO DI BARI

12

2022

Dottorato di Ricerca in Rischio e Sviluppo Ambientale, Territoriale ed Edilizio

Coordinatore: Prof. Michele Mossa

XXXV CICLO
ICAR/07 - ICAR/09

DICATECh
Dipartimento di Ingegneria Civile, Ambientale, del Territorio, Edile e di Chimica

Modellazione tridimensionale non-lineare dell'interazione terreno-struttura di torri in muratura in condizioni dinamiche

Prof. Gaetano Elia
Prof. Giuseppina Uva
DICATECh Politecnico di Bari, Italia

Dr. Annamaria di Lernia
DICATECh Politecnico di Bari, Italia

Aldo Fabio D'Oria

EXTENDED ABSTRACT *(eng)*

Masonry towers are widespread in many European countries and in Italy as well, representing one of the most prominent parts of our cultural and historical legacy. Recently the seismic performance assessment of these structures has become a central topic in structural engineering because of their high seismic vulnerability. This is mainly due to their peculiar structural configuration and poor mechanical properties which generally characterizes the masonry texture. Hence, a huge effort has already been made to assess the seismic response of these historical monuments from a structural point of view, generally neglecting the soil compliance effect in favour of a perfectly fixed-base condition. However, a fixed-base scheme is not always suitable to represent the actual in-situ soil conditions as the foundation deposits can be characterized by soft soils sequences that should not allow to use this approximation. Indeed, the occurrence of a tower resting on deformable deposits is not so remote and in addition it is often associated to relevant seismic hazard levels of the area. Nevertheless, a soil-structure interaction analysis is just occasionally considered because of the huge complexity of the problem, which is highly interdisciplinary and involves seismic, structural and geotechnical engineering expertise. In this context, this thesis has focused on investigating the soil-structure interaction influence on the seismic performance of masonry towers. The mechanical response of the masonry material has been described through the use of an advanced constitutive model which accounts for a plastic-damage behaviour and is able to catch the main features that characterize the dynamic response of a masonry structure. The research framework has mainly covered three aspects of the problem. First of all, the role of the soil de-

posit conditions has been studied throughout the investigation of the soil stratigraphic heterogeneity influence. Secondly, the impact of the soil dynamic behaviour has been examined following two different modelling approaches, i.e a linear visco-elastic and an equivalent-linear visco-elastic strategy. Finally, the relationship between the soil-structure interaction effects and the tower structural slenderness has been analysed. The numerical simulations have been carried out adopting a three-dimensional model of the problem and performing non-linear time-history analyses. The results of the study suggest that the soil-structure interaction phenomena can clearly affect the seismic performance of ancient masonry towers, modifying the modal properties, the seismic demand and the possible collapse modes affecting the structure if compared to the fixed-base scheme.

key words

Dynamic soil-structure interaction; masonry towers; seismic vulnerability; finite element modelling; nonlinear response

EXTENDED ABSTRACT *(ita)*

Le torri in muratura sono diffuse in molti paesi europei ed in particolare in Italia, rappresentando una porzione rilevante del nostro patrimonio storico-culturale. Recentemente gli studi di vulnerabilità sismica effettuati su queste strutture sono diventati un argomento centrale nell'ambito dell'ingegneria strutturale. Ciò è dovuto principalmente alla loro peculiare configurazione strutturale e alle proprietà meccaniche scadenti che generalmente ne caratterizzano la tessitura muraria. Per questi motivi è stato già profuso un grande sforzo atto a valutare la risposta sismica di antiche torri murarie da un punto di vista prettamente strutturale, trascurando però l'influenza della deformabilità del deposito fondale ed approssimando ad un incastro perfetto la condizione di vincolo imposta alla base del modello. Tuttavia, uno schema a base fissa non sempre rappresenta in maniera realistica le effettive condizioni riscontrabili in-situ, dal momento che i depositi fondali possono essere caratterizzati da sequenze stratigrafiche di terreni soffici che non consentono tale approssimazione. Peraltro, la possibilità di imbattersi in una torre edificata su depositi più o meno deformabili non è così remota ed inoltre è spesso associata a rilevanti livelli di pericolosità sismica della zona. Ciononostante, l'analisi di interazione terreno-struttura è solo occasionalmente effettuata a causa della grande complessità del problema che è altamente interdisciplinare e coinvolge competenze di ingegneria sismica, strutturale e geotecnica. In questo contesto, il lavoro di tesi si è quindi focalizzato sugli effetti che i fenomeni di interazione terreno-struttura determinano sulla risposta sismica di torri in muratura. Il comportamento meccanico della muratura è stato descritto mediante l'utilizzo di un modello costitutivo avanzato che prevede plasticità e danno ed è in grado di cogliere le caratteristiche

salienti della risposta dinamica di una struttura muraria. La ricerca ha riguardato principalmente tre aspetti del problema di interazione. In primo luogo, è stato analizzato l'effetto indotto dalle diverse condizioni di sito definendo diversi profili stratigrafici caratterizzati da un differente grado di eterogeneità. In secondo luogo, l'influenza determinata dalla modellazione del comportamento dinamico del terreno è stata esaminata utilizzando due diversi approcci: una modellazione visco-elastica lineare ed una visco-elastica equivalente. Infine, è stata analizzata la relazione che intercorre tra gli effetti di interazione terreno-struttura e la snellezza strutturale delle torri. Le simulazioni numeriche sono state condotte adottando una modellazione tri-dimensionale del problema ed effettuando analisi di tipo time-history non-lineare. I risultati dello studio suggeriscono che i fenomeni di interazione dinamica terreno-struttura possono sicuramente influenzare la risposta sismica delle torri in muratura, modificandone le proprietà modali, la domanda sismica ed i possibili meccanismi di collasso rispetto ad una schematizzazione a base fissa.

key words

Interazione dinamica terreno-struttura; torri in muratura; vulnerabilità sismica; modellazione agli elementi finiti; comportamento non-lineare.

INDEX

LIST OF THE FIGURES

LIST OF THE TABLES

CHAPTER 1: INTRODUCTION

Masonry towers are very widespread in many European countries and represent one of the most prominent parts of our cultural and historical legacy. Just focusing on the Italian country, masonry towers are the actual symbol of some of the most popular Italian cities, like Pisa and Bologna. Indeed, the "Pisa Tower" or "Torre degli Asinelli" and "Torre della Garisenda" (Fig. 1.1a,b) receive every year thousands of people coming from all over the world.

Fig. 1. 1 – a) The Pisa Tower and b) the Bologna Towers: Torre degli Asinelli and Torre della Garisenda.

The most emblematic town represented by its towers is San Gimignano, located between Siena and Florence in Italy, that it is also known as “the city of a hundred towers”, even if in the Middle Ages counted 72 and now only 14 of them still remain (Fig. 1.2).

Fig. 1. 2 – San Gimignano towers (Italy).

These are only some of the most striking examples, but masonry towers are almost present in every Italian city centre, as stand-alone clock or bell towers or incorporated in churches or medieval castles. Their geometric characteristics change a lot from case to case, while the material used for the construction usually depends on the raw material availability in the specific area.

Tab. 1.1 reports a summary of the major Italian towers, provided by de Silva et al. (2015a). The towers are collected according to some of their main features (height (H), base width (B), slenderness (H/B), material), together with the subsoil and seismic hazard conditions. The towers are divided into three different slenderness classes: squat ($H/B<3$), slender ($3<H/B<6$) and very slender ($H/B>6$). Indeed, the heights are very variable and cover a wide range, from 8 m (Cala d’Arena, Saline, Capo Falcone Towers) to even more than 100 m (Torazzo Bell Tower); the base widths are less variable and usually measure around 10 m. The masonry units are made of different types of bricks or stones depending on the site location.

	Tower	Location	H (m)	B (m)	H/B	Date	Material	Subsoil	PGA (g)
Squat (H/B<3)	Cala d'Arena	Stintino	8	12	0.67	1611	schist stone	calcarenites	<0.025
	Casamatta di Salignano	Costrignano del Capo	15	20	1	1550	limestone	marly limestones	0.068
	Spinelli	Napoli	11	14	0.77	1500	tuff	alluvial sand	0.168
	Saline	Stintino	8	10	0.80	1570	schist stone	marine sand	<0.025
	Capo Falcone	Capo Falcone	8	10	0.84	1577	schist stone	calcarenites	<0.025
	Brava	Napoli	13	14	0.90	1500	tuff	alluvial sand	0.168
	Pelosa	Golfo dell'Asinara	9	10	0.90	1525	schist stone	marine sand	<0.025
	Poseidonia fortress	Paestum	14	9	1.48	600 a.C.	limestone	travertino	0.100
	South-west	Alife	15	10	1.50	1060	limestone	limestone conglomerate	0.223
	Dovecote	Minerbio	15	10	1.50	1536	brickwork	alternations of sand-silt-clay	0.166
	Dungeon	Rocca San Felice	15	10	1.50	~1100	limestone	limestone	0.268
	Dungeon	Montella	16	~10	1.61	1200	limestone	limestone	0.188
	Viscontea	Monza	~20	~10	2.00	1325	brickwork	gravelly silt	0.054
	Elefante	Cagliari	35	~14	2.50	1307	limestone	limestone	<0.025
	San Pancrazio	Cagliari	37	~14	2.50	1305	limestone	limestone	<0.025
	Annunziata bell tower	Sulmona	65	7	2.50	1565		clay	0.256
	Castellare	Galliera	22	9	2.54	~1200	brickwork	alternations of sand-silt-clay	0.166
	Conserva	Galliera	18	7	2.57	1500	brickwork	alternations of sand-silt-clay	0.166
	Matilde di Canossa	Tarquinia	29	10	2.90	~1400	limestone	calcarenites	<0.025
	S. M.Assunta bell tower	S.Agata de'Goti	~30	~10	3.00	~1400	tuff	tuff	0.161
	S. Domenico bell tower	Taormina	~30	~10	3.00	~1400	limestone	limestone	0.215
Slender (3<H/B<6)	Corneto	Tarquinia	~30	~8	3.75	~1100	limestone	calcarenites	0.078
	Bell tower	Pisa	58	16	3.77	1173	marble	clay	0.118
	Mariano II	Oristano	29	8	3.87	1290	sandstone brickwork	alluvial gravel and sand	<0.025
	S.Apollinare b. tower*	Ravenna	38	10	3.98	1000	brickwork	clay and silt	0.162
	Watchtower	Finale d'Emilia	40	~10	4.00	1213	brickwork	sandy clay	0.149
	Watchtower	Novi di Modena	40	~10	4.00	1600	brickwork	clay	0.137
	Bell tower**	Mirandola	48	~11	4.36	1400	brickwork	sand-clay	0.140
	S. Maria bell tower***	Ravenna	21	5	4.57	1000	brickwork	clay and silt	0.162
	Milizie	Roma	50	10	5.00	1200	brickwork	fluvial gravels and sands	0.107
	S. Lucia bell tower****	Serra S. Quirico	32	~6	5.33	1600	limestone	sand	0.174
	Grossa*****	San Gimignano	60	~10	5.40	~1300	limestone	calcarenites	0.141
	Giungi	Lucca	44	~8	5.53	~1300	brickwork	alluvial deposits	0.130
	Civic tower	Ravenna	38	7	5.76	1200	brickwork	clay	0.162
	Cathedral bell tower	Trani	59	~10	5.90	1230	limestone	marine sand	0.146
Very slender (H/B>6)	Salvucci sud	San Gimignano	43	7	6.12	1200	limestone	calcarenites	0.141
	Garisenda***	Bologna	48	7	6.49	1100	brickwork	silty clay-clayey silt	0.166
	Watchtower	Pavia	40	6	6.67	~1100	brickwork	alluvial gravel and sand	0.069
	Tower	Pavia	~40	6	6.67	~1100	brickwork	alluvial gravel and sand	0.069
	Carmine b. tower+	Napoli	68	10	6.80	1400	tuff	alluvial sand	0.168
	Frari bell tower++	Venezia	65	10	6.84	1361	brickwork	clayey silt-fine sand	0.071
	S. Luca b. tower+++	Valenzano	46	6	7.36	1774	limestone	sand on limestone	0.070
	Salvucci nord	San Gimignano	41	6	7.51	1200	limestone	calcarenites	0.141
	Ghirlandina b. tower++++	Modena	87	11	8.06	~1100	brickwork	silty clay	0.163
	Bell tower Torrazzo	Cremona	112	13	8.62	1200	brickwork	sand-clay	0.081
	Tower	Pavia	~55	6	9.17	~1100	brickwork	alluvial gravel and sand	0.069
	Asinelli***	Bologna	97	8	11.9	1110	brickwork	silty clay-clayey silt	0.166

Tab. 1. 1 – Summary of the of the main Italian tower collected according to their slenderness ratio, as reported in de Silva et al. (2015a).

The subsoil nature can be as well very heterogeneous and characterised by stiff deposits, as calcarenite and limestone, but also by soft soils like clay or alluvial sand lithological sequences.

Finally, the peak ground acceleration (PGA) at the rigid outcropping rock, corresponding to a return period of 475 years, is also reported. It appears that most of these towers fall in areas potentially subjected to earthquakes with PGA higher than 0.10 g and, hence, are exposed to relevant seismic hazard.

Moreover, most of the times the static stress state induced by gravitational loads is often already close to the limit resistance of the masonry material. In addition, soil deformability might also cause problems related to rotation at the base or due to uncontrolled settlements during the construction and following stages that can lead to leaning instability of the structure (Burland & Viggiani 1994; Lancellotta 2013).

For all these reasons, ancient masonry towers present a high seismic vulnerability and exposure that, if combined also with the hazardous location, make these type of structure extremely sensitive to seismic risk, as demonstrated by recent earthquakes that have hit Central Italy (Figs. 1.3-1.4).

Fig. 1. 3 – Collapse of the Finale Email Clock Tower (Italy) after the May 2012 Emilia Romagna earthquake sequence.

Fig. 1. 4 – Collapse of the Sant'Agostino Bell Tower of Amatrice (Italy) after the 2016-2017 Central Italy earthquake sequence.

Thus, it is not surprising that the seismic performance assessment of masonry towers has recently become a central topic in structural engineering. A huge effort has already been done to study the problem from a structural point of view, investigating, for example, the influence given by their geometrical features together with the presence of irregularities, such as inclination or relevant openings, the masonry mechanical behaviour role, the in-situ constraints related to the connection with other building complexes or also the role of the vertical seismic component.

Nevertheless, the effect of the soil compliance is still just occasionally considered in favour of a perfectly fixed-base condition, despite it is well known that soil deformability can cause significant deviations from a fixed-base dynamic behaviour.

In this context, this thesis is aimed at investigating the effects of soil-structure interaction phenomena on the seismic performance of masonry towers, analysing the structural response both in the elastic and non-linear fields.

The whole study is performed exploiting the finite element (FE) code Abaqus (2014), a commercial software used in various civil engineering problems among which structural and geotechnical applications.

The thesis is organized as follows:

1) At first, a literature review is conducted; an overview on the dynamic soil-structure interaction is presented and then the main outcomes of masonry towers seismic vulnerability assessments are shown, separating the fixed-base studies from the ones that consider soil deformability.
2) A brief introduction about the masonry mechanical behaviour is discussed, highlighting the main features of this material. Afterwards, the constitutive model herein adopted to simulate the masonry behaviour, i.e. the Concrete Damaged Plasticity (CDP) model (Lee & Fenves 1998; Lubliner et al. 1989), is described. The CDP model is a constitutive model available in the Abaqus material library and already used in numerous masonry applications.
3) Then, the selected case study taken from the literature is described and the dynamic fully coupled soil-tower analyses are discussed, starting from a preliminary validation of the dynamic boundary conditions adopted for the soil medium, moving to the analyses carried out adopting linear elastic relationships and finally describing the simulations accounting for the soil and structural non-linear response.
4) In the end, a parametric study conducted considering different tower slenderness is presented, highlighting the mutual relationship between the structure and the soil.

CHAPTER 2: STATE OF THE ART

2.1 Introduction

The thesis deals with the dynamic soil-structure interaction of masonry towers, an interdisciplinary problem involving seismic, structural and geotechnical engineering expertise. Hence, the present chapter starts with an overview of the problem, highlighting the main aspects that characterise the mutual interaction between a generic structure and the surrounding soil. Then, the core of the chapter is dedicated to the literature review related to the seismic vulnerability assessment of ancient masonry towers.

2.2 Dynamic soil-structure interaction

During an earthquake, the soil deformations induced by the propagation of seismic waves cause the motion of the foundation and consequently of the structure, where inertial forces arise. The distribution of these forces, in turn, produce a translational and rotational motion of the foundation itself, which differs from that of the soil deposit under free-field conditions. The foundation motion induces further deformations in the soil, generating other waves propagating from the foundation towards the soil bedrock, resulting in an energy dispersion at the soil-foundation interface. In response to the motion of the soil beneath the foundation, the structure undergoes further dynamic displacements, which once again generate inertial forces, and so on.

This phenomenon, that represents the result of the mutual interaction between the structure itself, the supporting foundation and the surrounding soil, is commonly

known as dynamic soil-structure interaction (SSI) (Jennings & Bielak 1973; Veletsos & Meek 1974; Veletsos & Nair 1975; Wolf 1985; Gazetas & Mylonakis 1998; Kim & Stewart 2003).

Two mechanisms rule the physics of the phenomenon:

a) the inertial interaction, linked to the generation of inertia forces due to the oscillations of the structure, which gives rise to not negligible changes in the characteristics of the stresses transferred to the base; consequently, the foundation motion is deviated from that of the ground in free-field conditions;
b) the kinematic interaction, due to the presence of the foundation, typically much stiffer than the surrounding soil; this causes the alteration of the foundation motion from that of the ground in free-field conditions because of two different aspects: i) the so called "base slab averaging" that is the result of spatial variation in the free-field ground motion over the foundation footprint due to the wave inclination and incoherency during the propagation process (Veletsos & Prasad, 1988) and ii) the type of foundation and its depth.

From an energetic point of view, the energy introduced in the system by the seismic event firstly affects the soil deposit and then reaches the foundation level, where part of the energy is reflected or refracted. At the same time, a portion of the energy is transmitted to the structure in elevation, generating its oscillation and possibly activating its structural damping. When the seismic waves reach the building roof, they are completely reflected and a new propagation starts downward. As the seismic waves come to the soil-foundation interface, they are partly reflected, continuing to get trapped in the structure, and partly refracted, returning in the soil deposit. Here, part of the vibration energy is dissipated by radiation and hysteretic damping depending on the deformation level induced by the earthquake.

If the structure is founded on a rigid subsoil (for example calcarenite or limestone), the base structural displacements are inhibited; in this case, the system is characterised by a fixed-base scheme. When the subsoil is deformable, the base of the structure can undergo both translation and rotation, resulting in the so called flexible-base scheme.

It is obvious that if the same signal is applied to a fixed-base or a flexible-base structure, the structural response will be affected only by the structural damping in the first case, while in the second case the response is controlled also by the radiation damping and soil hysteretic damping, whose effects do not always mitigate the seismic response (Mylonakis & Gazetas 2000). As a result, an accurate representation of the dynamic SSI phenomena can play a crucial role in the seismic response of the structure.

2.2.1 Methods for the dynamic soil-structure interaction analysis

The dynamic SSI is a very complex topic that requires a careful representation of the structural and soil response, in order to adequately catch the overall behaviour of the system. Generally, two different approaches are used to face the problem:

a) the direct method that consists in a fully coupled analysis of the whole soil-structure system;
b) the substructure method, consisting in decoupling the problem to separately analyse the full system into its three constitutive parts (soil, foundation and structure in elevation).

The most rigorous approach is the direct method, which enables to study the problem in a single calculation, considering at the same time the kinematic and inertial phenomena. This procedure usually needs the support of a numerical calculation code (for example based on the finite element or discrete element method), capable of directly evaluating the response of the system by solving the equations of motion underlying the problem:

$$[M]\{\ddot{u}\}+\left[K^*\right]\{u\}=-[M]\left\{\ddot{u}_g\right\} \tag{2.1}$$

where $[M]$ and $\left[K^*\right]$ represent the matrices of the masses and complex stiffnesses of the whole soil-structure system, while $\left\{\ddot{u}_g\right\}$ is the vector of the accelerations applied to the base of the geometric model (Fig. 2.1).

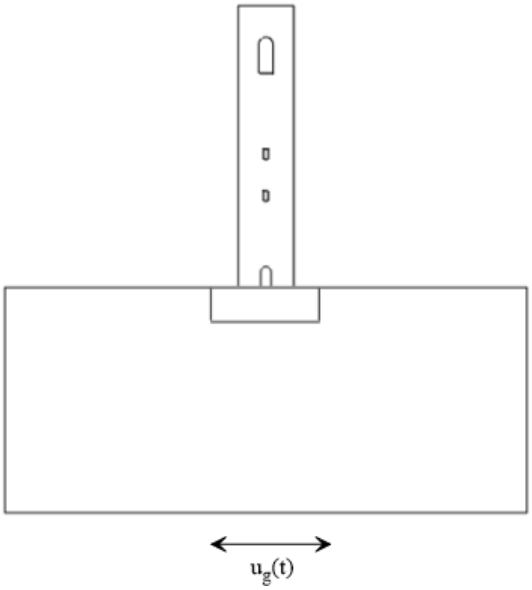

Fig. 2. 1 – Sketch of the direct approach.

In this approach an adequate soil portion close to the structure is modelled until the artificial boundaries, since it is impossible to represent an infinite space (soil) with finite elements with a limited dimension. Hence, particular emphasis must be spent to the choice of the dimensions of the calculation grid and to the dynamic boundary conditions of the soil domain, in order to avoid any wave reflection in the region of interest, which would represent a potential source of error in the analysis. One of the possible solutions to overcome this issue might be to place viscous dampers on the outer contours of the model to adsorb the incoming wave energy.

The direct approach enables to study very complex problems with a high degree of accuracy, considering for example three-dimensional geometries, possible interaction with adjacent structures, non-linear soil behaviour adopting more or less advanced constitutive hypotheses depending on the needs or the variability of the physical-mechanical properties of the soil at different depths (Casciati & Borja 2004; Torabi & Rayhani 2014; Amorosi et al. 2017; di Lernia et al. 2019).

The major drawbacks of the method consist in the huge computational effort still required to perform the analysis and in the great amount of variables that can influence the model response, which imply a strong user expertise.

For these reasons, a common strategy adopted is to downgrade and simplify the problem at its constitutive parts by using the substructure method. In this case, soil, foundation and structure are separately analysed and the kinematic and inertial interaction effects are investigated one by one and subsequently combined to provide the full system response. Therefore, the problem is solved by superimposing the effects, implicitly assuming the linearity of the behaviour of both soil and structure.

A complete flowchart of the process is illustrated in Fig. 2.2 (Mylonakis et al. 2006)

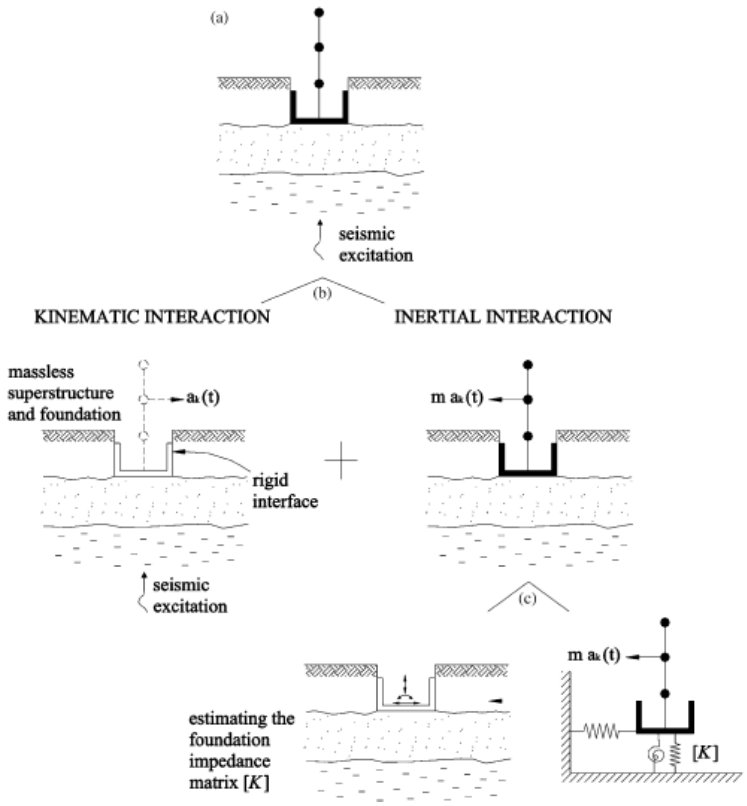

Fig. 2. 2 – Substructure approach flowchart (Mylonakis et al. 2006).

Three different phases can be recognized:

a) Evaluation of the seismic foundation motion usually known as foundation input motion (FIM) ($a_k(t)$ in Fig. 2.2b), i.e. the motion of the foundation, setting the foundation mass to its actual value and the one of the superstructure equal to zero (in contrast with the direct approach depicted in Fig. 2.2a). The FIM motion is generally less intense than the one recorded under free-field conditions and it is dependent on the stiffness and geometry of the foundation, since it is strictly related to the kinematic interaction.
b) Determination of the dynamic impedance functions, which are directly associated with each degree of freedom of the foundation. They describe the interaction relationship between the foundation and the soil by considering the geometry and stiffness of the foundation, the stratigraphy of the soil deposit and the mechanical properties of the soil itself.
c) Dynamic analysis of the structure in elevation standing on a flexible support that simulates the SSI by means of springs and dashpots considering the FIM determined in the previous phase (Fig. 2.2c).

Numerous authors have proposed analytical solutions for the separate evaluation of the effects of both kinematic interaction (Elsabee & Morray 1977; Day 1978; Kim & Stewart 2003) and inertial interaction (Veletsos & Verbic 1973; Veletsos & Meek 1974; Wolf 1985; Mylonakis et al. 2006, Maravas et al. 2014). Anyway, despite the fact that the substructure method allows a quick evaluation of the SSI effects, it has some limitations related to the hypotheses on which it is based. It is directly linked to the superposition principle which relies on the elastic theory, thus allowing to adopt only linear elastic relationships; furthermore, it is not suitable. for three-dimensional problems applications.

The present work focuses on the seismic assessment of ancient masonry towers interacting with deformable soil deposits. The dynamic SSI effects on the towers have been investigated through the direct method performed adopting three-dimensional coupled analyses and simulating the nonlinear response of both masonry material and soil deposit with appropriate constitutive models.

2.2.2 Effects of the inertial interaction

2.2.2.1 Inertial effects on SDOF structure

The dynamic response of a single degree of freedom (SDOF) structure resting on an elastic and homogeneous half-space, excited by three types of signals (harmonic, impulsive and seismic), has been firstly studied by Veletsos & Meek (1974). In their formulations, Veletsos & Meek (1974) assumed that the foundation is infinitely rigid and weightless.

The response of the soil-foundation-structure system is found to be influenced by the geometric characteristics of the foundation and the structure and by the physical-mechanical properties of the soil. They also defined non-dimensional parameters through which it is possible to evaluate the effects of the inertial interaction:

- the relative soil-structure stiffness ratio defined as:

$$\sigma = \frac{V_S}{f_0 h} \tag{2.2}$$

- the slenderness ratio defined as:

$$\bar{h} = \frac{h}{r} \tag{2.3}$$

- the relative structure to soil mass ratio defined as:

$$\gamma_m = \frac{m}{\pi \rho r^2 h} \tag{2.4}$$

where V_S is the shear wave velocity of the soil deposit, f_0 is the frequency of the superstructure under a fixed-base condition (FB), h is the distance from the base of the centroid of the structure, r is the equivalent radius of the foundation, m is the mass of the superstructure and ρ is the soil density.

For most of the conventional structures, the relative soil-structure stiffness ratio σ is greater than 2, while the mass ratio γ_m ranges in the interval 0.1-0.2 (di Lernia 2014).

The inertial interaction effects mainly imply a reduction in the oscillation frequency of the soil-structure system compared to that of the FB structure and a variation of the damping factor that modifies the structural response in terms of peak amplitude.
The motion amplitude of the structure is influenced by two opposite mechanisms related to the soil deformability. Indeed, its increase produces a build-up in the dissipative capacity of the whole system if compared to the FB one because of the radial damping action; on the other hand, the consequent greater rotation of the foundation determines an increase in the acceleration of the structure and hence an increase in the forces of inertia associated with it.
Therefore, for squat structures, in which the rotational component of the motion is very small, an increase in the effective damping and a consequent reduction in the amplitude of the motion will be observed; conversely, for slender structures, dominated by the rotational vibration mode, the geometric damping rate will be small enough to induce an increase of the motion of the system (Veletsos & Meek 1974).
Furthermore, the response of the system is strongly influenced by the relationship between the predominant frequency of the signal and the frequency of the system. In fact, when these are close to each other, the response of the structure may undergo to resonance phenomena.
The dynamic response of a generic structure resting on a deformable deposit can be studied with reference to an equivalent oscillator, resting on a rigid support, characterised by the modified dynamic properties, i.e. the oscillation frequency f_e and the damping ratio ξ_e:

$$\frac{f_e}{f_0} = \frac{1}{\sqrt{1+\frac{k}{k_x}+\frac{kh^2}{k_\vartheta}}} \tag{2.5}$$

$$\xi_e = \left|\left(\frac{f_e}{f_0}\right)^3\left[\xi_0 + \frac{(2-\nu)\pi^4\gamma_m}{2\sigma^3}\left(\frac{\beta_x}{\alpha_x(\alpha_x+ia_0\beta_x)}\frac{r^2}{h^2}+\frac{\beta_\vartheta}{\alpha_\vartheta(\alpha_\vartheta+ia_0\beta_\vartheta)}\right)\right]\right| \tag{2.6}$$

where k is the stiffness of the FB structure, $k_x = \alpha_x K_x$ and $k_\vartheta = \alpha_\vartheta K_\vartheta$ are the dynamic stiffnesses of the foundation-soil system in the two horizontal directions. The

dynamic impedance coefficients α_j can be evaluated with an iterative procedure on the equivalent frequency f_e, according to the formulation proposed by Veletsos & Verbic (1973).

In the expression (2.6), the first part represents the damping of the FB structure, proportional to the cube of the ratio f_e/f_0, which denotes that the effective damping of the equivalent system is not just a sum of the two dissipative contributions (structural and radial), but it also depends on the reduction of the natural frequency f_e. For structures with a slenderness ratio greater than 2, the contribution of the imaginary part can be neglected. Therefore, the damping of the equivalent system can be evaluated as follows:

$$\xi_e = \left| \left(\frac{f_e}{f_0} \right)^3 \left[\xi_0 + \frac{(2-\nu)\pi^4 \gamma_m}{2\sigma^3} \left(\frac{\beta_x}{\alpha_x^2} \frac{r^2}{h^2} + \frac{\beta_\vartheta}{\alpha_\vartheta^2} \right) \right] \right| \tag{2.7}$$

Basically, the problem of the inertial interaction consists in solving the equation of motion of a simple oscillator on a FB condition, characterized by the oscillation frequency f_e and damping factor ξ_e, subjected to the horizontal motion $\ddot{u}_{FIM}(t)$:

$$m\ddot{u}(t) + c_e\dot{u}(t) + k_e u(t) = -m\ddot{u}_{FIM}(t) \tag{2.8}$$

which turns into:

$$\ddot{u}(t) + 2\xi_e\omega_e\dot{u}(t) + \omega_e^2 u(t) = -\ddot{u}_{FIM}(t) \tag{2.9}$$

where:

$$\omega_e = 2\pi f_e = \sqrt{\frac{k_e}{m}} \tag{2.10}$$

and

$$\xi_e = \frac{c_e\omega_e}{2k_e} \tag{2.11}$$

The f_e/f_0 and the ξ_e variation as a function of the stiffness ratio σ is shown in Fig. 2.3 for three values of the slenderness ratio $\bar{h}$ and assuming the mass ratio γ_m equal to 0.16 (di Lernia 2014). The frequency ratio f_e/f_0 decreases as the parame-

ter σ reduces, while the equivalent damping increases for structures with low slenderness ratio. This can easily be traced back to what was previously said: for squat structures, in which the translational mode is predominant, a greater dissipation of energy by radiation is observed, resulting in an increased overall damping; on the other hand, for slender structures a lower geometrical dissipation is involved, leading to a less damped response even if compared to the damping of the FB structure.

The FB condition occurs for high values of σ, any time that the structure rests on very stiff subsoil ($V_S \to \infty$) or when the structure is really flexible ($f_0 = 1/T_0 \to 0$). Indeed, for $\sigma \geq 20$ the soil-structure behaviour of the system becomes close to that of the FB structure ($f_e/f_0 \approx 1$ and $\xi_e \approx \xi_0$).

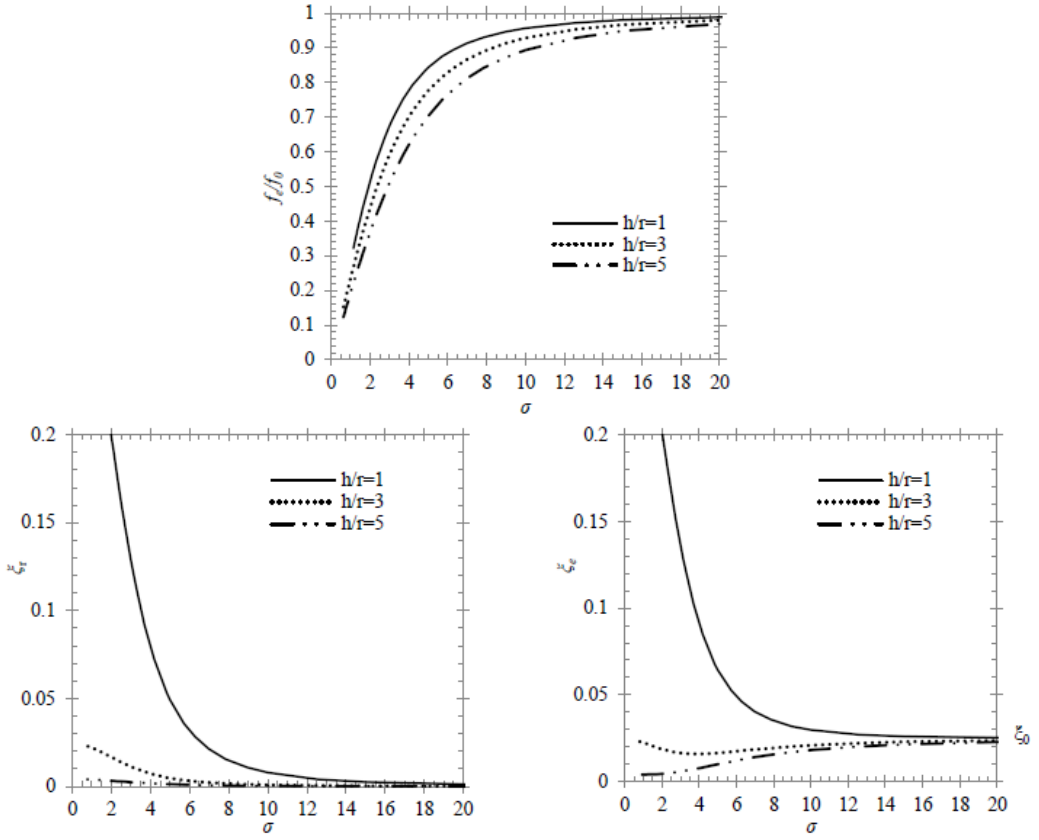

Fig. 2. 3 – Variation of the frequency ratio f_e/f_0, the radiation damping ξ_r and the equivalent damping ξ_e as a function of the relative soil-structure stiffness σ for SDOF structure with rigid circular foundation on an elastic half-space, according to the solution of Veletsos & Meek (1974) (ν =0.33, ξ_0 =2%, γ_m =0.16), as reported in di Lernia (2014).

Veletsos & Nair (1975) included the soil damping in the analytical formulation for the determination of the dynamic characteristics of the equivalent simple oscillator, through the dynamic impedance coefficients proposed by Veletsos & Verbic (1973). The contribution provided by the soil damping ξ appears to be almost negligible for squat structures, while it plays an important role in reducing the response of slender structures, as depicted in Fig. 2.4 showing the variation of ξ in the case of elastic half-space and visco-elastic half-space (di Lernia 2014); in addition, the more the

structure is rigid with respect to the subsoil deposit, the greater the SSI effects are significant.

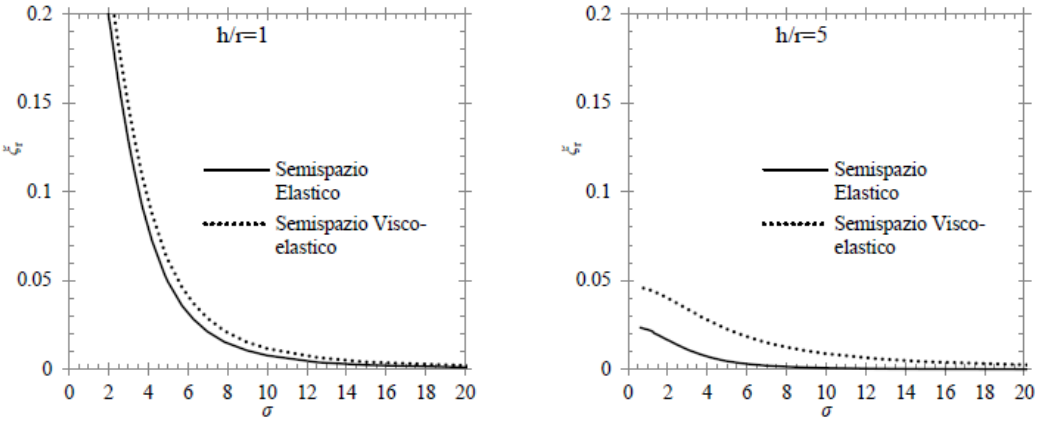

Fig. 2. 4 Radiation damping ξ_r variation as a function of the relative soil-structure stiffness σ for SDOF structure with rigid circular foundation on elastic and visco-elastic half-space (soil hysteresis behaviour according to Veletsos & Verbic (1973)) for two slenderness ratio h/r according to the solution of Veletsos & Nair (1975) (ν =0.33, γ_m =0.16), as reported in di Lernia (2014).

2.2.2.2 Inertial effects on masonry towers

Based on the results of parametric analyses carried out on representative cases of Italian monumental towers, de Silva et al. (2014a) generated diagrams that allow for a preliminary evaluation of the period and damping variation of the flexible base tower compared to the FB one. The analyses were carried out for three masonry towers having height equal to 68, 29 and 9 m, which result in a squat, slender and very slender case, respectively; moreover, four different homogenous soil deposits were considered having shear waves velocity V_S constant with depth and equal to 100, 200, 400 and 800 m/s.

The diagrams obtained are reported in Fig. 2.5 in terms of the ratio between the period of the SSI system and that of the FB system, T_e / T_0, and damping factor ξ_e.

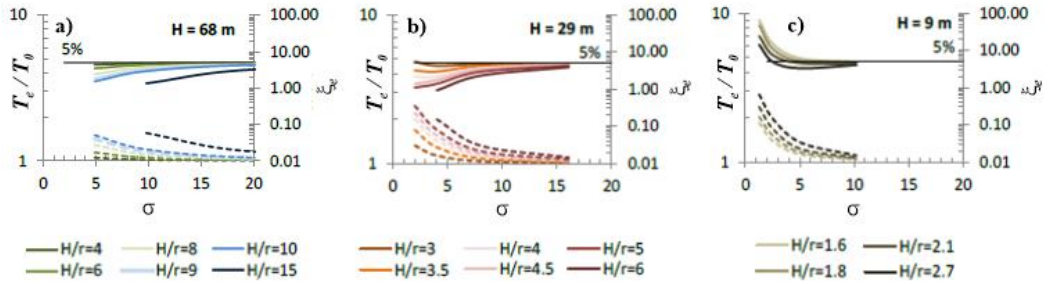

Fig. 2. 5 – Results of the parametric analyses as function of the relative soil-structure stiffness σ, expressed in terms of T_e / T_0 ratio (dashed lines) and equivalent damping factor ξ_e (solid lines) for a) very slender (68 m), b) slender (29 m) and c) squat tower (9 m) (modified from de Silva et al. 2014a).

For the three considered structural heights, the period of the deformable base system T_e always increases with respect to T_0 (dashed lines in Fig. 2.5); moreover, the interaction in the first two cases, i.e. 68 m and 29 m, reduces the overall damping ξ_e with respect to the FB value, while it increases significantly for the smallest tower. The effects are more significant the smaller the foundation radius is, if compared to the height, and tend to decrease as σ increases, which is indicative of the increase in soil stiffness.

Fig. 2.6 shows the trends for T_e and damping ξ_e as a function of the shear wave velocity V_S. It emerges that the towers are affected by SSI phenomena for different shear wave velocity thresholds: the very slender tower (Fig. 2.6a) moves away from the FB condition only for rather deformable soils (V_S <400m/s), the slender tower (Fig. 2.6b) for rather stiff soils (V_S <600m/s) and the squat tower (Fig. 2.6c) even for rigid soils ($V_S \approx$800m/s). These values represent common values of stiffness close to the top surface of shallow foundation soil deposits, proving that SSI can influence a wide range of real masonry towers.

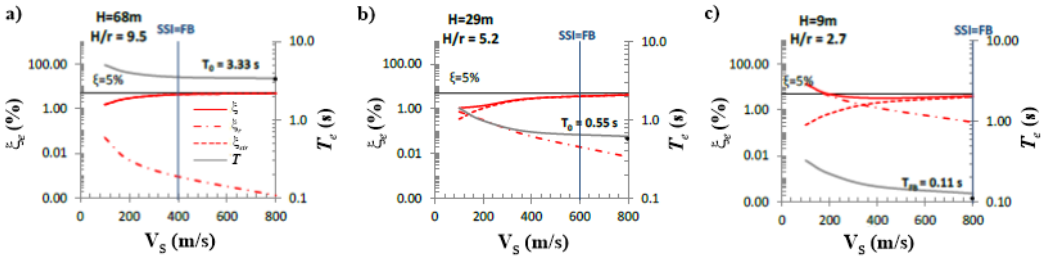

Fig. 2. 6 – Equivalent period T_e and damping factor ξ_e of the deformable base structure as a function of the shear wave velocity V_S for a) very slender (68 m), b) slender (29 m) and c) squat tower (9 m) (modified from de Silva et al. 2014a).

In de Silva et al. (2014b), similar parametric analyses considering the fixed-base and small (G_0) and large ($G_{\deg}$) deformations mobilized in the soil, show that the value of the slenderness ratio h/r where the damping trend changes is equal to 1.6 (h =9m), representing the critical value for which the structure goes from slender to squat (Fig. 2.7).

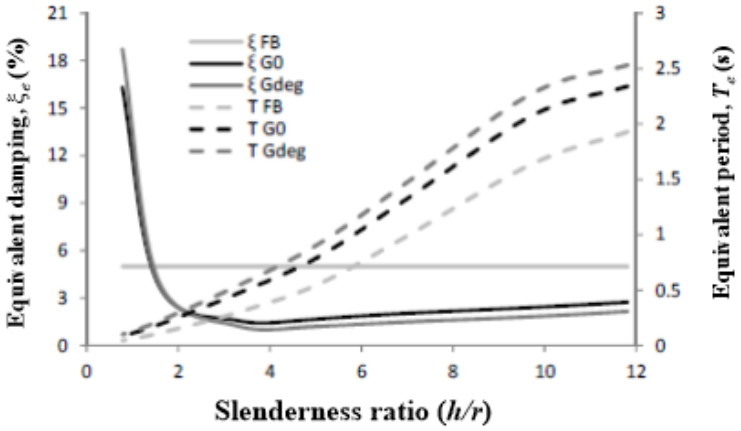

Fig. 2. 7 – Equivalent period T_e (solid line) and damping factor ξ_e (dashed line) variation as a function of the slenderness of the tower as reported in de Silva et al. (2014b).

Sica et al. (2013) investigated the effect induced by different modelling of springs, simulating the compliance of the soil deposit, on the SSI system period as the stiffness of the deposit varies (Fig. 2.8).

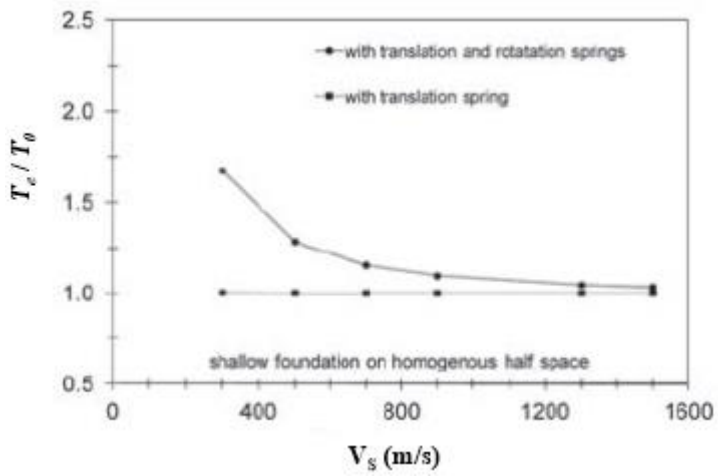

Fig. 2. 8 - Variation of the T_e / T_0 as a function of V_S considering different springs implementation as reported in Sica et al. (2013).

Indeed, the translational spring seems to have a negligible effect on the equivalent period of the structure even for low shear wave velocity (V_S =300m/s) due to the high deformability of the structure itself. On the contrary, a significant effect is observed when the rotational springs are considered, with an increase in the period between 5% and about 70% depending on V_S.

2.3 The seismic response of masonry towers

In this section an overview of the studies available in the literature on the seismic response of ancient masonry towers is provided. After highlighting some of the main factors that control the seismic behaviour of the towers, the section presents two distinguished parts. In the first one, the works carried out considering the classical fixed-base scheme are shown; the case studies that accounts for soil compliance are discussed in the second part.

2.3.1 Factors controlling the seismic behaviour of masonry towers

Italy is world-wide known for its cultural heritage and historical monuments. Consequently, the topic of their preservation and conservation is of paramount importance and is even more relevant considering the intrinsic vulnerability of these historic sites, often coupled to severe seismic hazard conditions.

In this context, Italy is one of the few countries that is provided with its own guidelines for the vulnerability analysis and seismic risk mitigation of the historic built heritage, i.e. the DPCM released on the 9th of February 2011 (DPCM 2011). The document contains also a section titled "Towers, bell towers and other structures with predominant vertical extension" (Section 5.4.4 of the document), which immediately gives some important indications about the main features characterising the dynamic response of this type of structures.

Indeed, it is stated that the seismic behaviour of masonry towers is dependent on some specific factors:

- the slenderness of the structure;
- the degree of connection of the walls;
- the possible presence of lower adjacent structures, capable of providing a horizontal constraint and limiting the effective structural tower slenderness;
- the presence at the top of slender architectural elements (spiers, merlons, etc.) or bell cells;
- any other geometrical irregularities given by inclination, relevant openings or vaults which generate additional thrusts;
- the presence of pre-existing damage, due for example to vibrations induced by bells or problems at the foundation level.

Slenderness can vary in a wide range: in fact, there are very squat towers like Renaissance defence bastions or very slender clock and bell towers.

The wall connection is a key requirement to ensure that the tower behaves like a monolithic body with a stiffness associated to the entire wall section, often formed by multi-leaf walls and internal heterogeneous infill, and not just to distinct walls.

Very frequent is the case of towers placed in contact with other structures of lower height, like the bell towers incorporated or placed next to churches or defence towers incorporated into the walls of medieval castles. The presence of horizontal restraints at different heights can deeply change the behaviour of the tower, limiting its effective slenderness and creating localized stiffen areas that can produce possible stress concentration.

Another critical element is represented by the belfry area in bell towers. It is usually characterised by large openings that produce slender and lightly loaded pillars subjected to shear failure and to out of plane collapse, due to the modest vertical load associated only with their own weight.

Finally, it should be remembered that the masonry material characteristics and aging frequently constitute another major player for the capacity of the structure to withstand earthquake motions, due to the low resistance which is often close to the induced gravitational stress state.

All these aspects contribute to outline some of the key points controlling the seismic response of a masonry tower, as highlighted in the following sections.

2.3.2 The seismic response of masonry towers: fixed-base conditions

In the previous section, it was pointed out that there are several aspects taking part to the global dynamic behaviour of a tower, which could manifest a peculiar response depending on the specific analysed case, also resulting in different collapse mechanisms.

It is known that the probability of occurrence of one mechanism rather than another is basically dependent on the specific geometrical and mechanical properties of the investigated case study. In agreement with the experience gained with the failures observed in the post-earthquake surveys or from advanced numerical simulations, according to Sarhosis et al. (2018) a preliminary assumption can be made based on the most probable one. Among all the possible mechanisms, five types have been selected by the authors (Fig. 2.9):

1. rocking with vertical splitting into two parts

2. monolithic rocking
3. Heyman's diagonal cracking and rocking (Heyman 1992)
4. a combination of Heyman's mechanism with vertical splitting
5. base shear sliding.

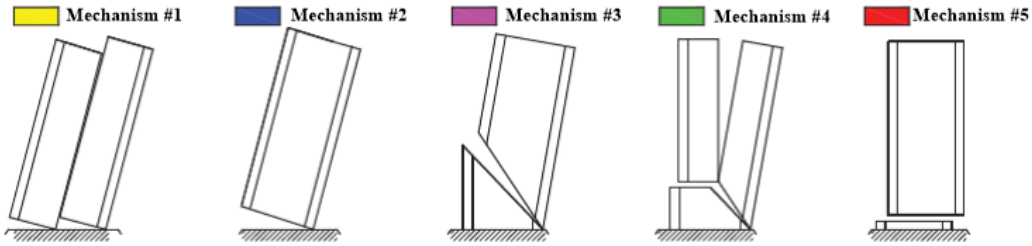

Fig. 2. 9 – Different mechanisms considered by Sarhosis et al (2018): Mechanism #1 - rocking with vertical splitting; Mechanism #2 - monolithic rocking; Mechanism #3 - Heyman's diagonal cracking and rocking; Mechanism #4 - mixed Heyman's mechanism with vertical splitting; Mechanism #5 - base shear sliding (modified from Sarhosis et al. 2018).

A huge number of kinematic-simplified limit analyses on idealized tower were carried using a Monte Carlo approach and considering three different mechanical properties for masonry (Fig. 2.10):

a) Case 1 is characterized by a fairly good cohesion, an almost vanishing tensile strength, which well approximates the no tension material hypothesis done both by the Italian Guidelines D.P.C.M. (2011) and by Heyman (1992), and a reasonable friction angle, very close to that assumed by the Italian Code NTC2008.
b) Case 2 presents both low cohesion and tensile strength, with small friction angle which favours a sliding failure mechanism, at least for low slenderness.
c) Case 3 is finally characterized by very good cohesion, small but non-zero tensile strength and reasonable friction angle.

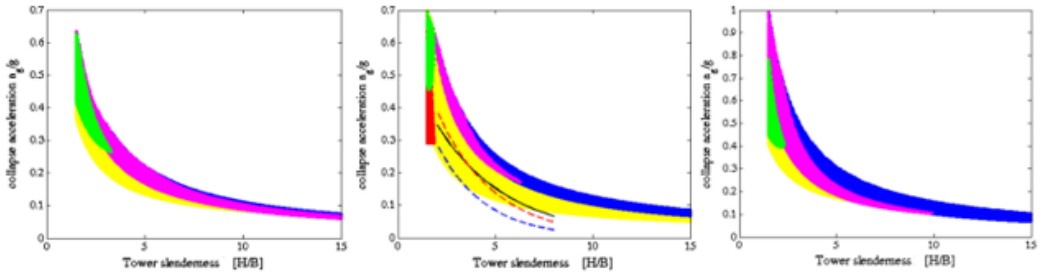

Fig. 2. 10 – Collapse acceleration a_g/g variation with the tower slenderness H/B obtained through Monte Carlo simulations (5 mln points) - a) Case 1 b) Case 2 c) Case 3 (modified from Sarhosis et al. 2018); the colours correspond to the 5 different mechanisms as reported in Fig. 2.9.

As can be observed in Fig. 2.10, the Monte Carlo results cumulate on well-defined areas of influence with different colours (each one refers to the colour of the mechanism defined by the legend in Fig. 2.9), clearly indicating that different failure mechanisms are active for different ranges of slenderness.

A first general interesting remark can be done about the blue colour rocking failure mechanism (#2) that is active only for large values of slenderness for each analysed scenario.

Looking at Case 1, the failure mechanisms with highest occurrence are “Heyman-type” collapses (#3), vertical splitting into two portions (#1) or a combination of them (#4). Such outcome appears fully in agreement with post-earthquake surveys (Fig. 2.11).

Fig. 2. 11 – a) Vertical splitting collapse for the “Clock Tower” located in Finale Emilia; b) “Heyman type” mechanism for the “San Felice sul Panaro Tower” located near Modena.

Mechanism#4 constitutes the smooth passage between vertical splitting and inclined rocking, in the case of smaller slenderness, probably because of the pure shear failure of the upper left portion of the tower. Monolithic rocking at the base is possible (blue failure mechanism), but not probable and occurs only for very slender towers. For Case 2 all failure mechanisms are possible, with a strong reduction of the area where the inclined rocking (#3) is active, in favour of monolithic rocking (#2). Also, vertical splitting is possible with higher probability and associated to collapse accelerations lower than those obtained with Mechanism #2. The relatively small friction angle allows, in this case, a sliding failure (red mechanism #5) which obviously occurs for towers exhibiting small slenderness. Case 3 is intermediate and, indeed, four of the five possible mechanisms are active. Mechanism #2 increases its probability of occurrence, as shown by the extension of the blue scattered area.

At least qualitatively, this last case seems the closest to the Italian code predictions as will be later discussed, with a larger range of slenderness where rocking failure is possible.

Despite these charts provide a versatile and effective way to evaluate collapse acceleration, this simplified approach may lead to unreliable prediction of the failure mode when geometric irregularities and vaults play an important role in the tower conformation (Milani 2019).

Indeed, the inclination, section area dimension, the presence of openings and any kind of geometrical and material irregularities generate modifications in the seismic response of masonry structures. Valente & Milani (2018) investigated this topic through a comprehensive study on eight real Italian towers by means of non-linear dynamic analyses (NLDA), establishing some general trends of the seismic behaviour of the towers as a function of their main typological features.

A preliminary eigenfrequency analysis highlighted some important considerations:

- the largest participating mass ratios in the two orthogonal directions always correspond to the first two flexural modes, while the third mode is predominantly torsional except for towers which present large openings at the top;
- the values of the first two periods are very similar for the majority of the towers due to the nearly square cross section, except for towers affected by irregular cross section or large openings at the bottom;
- the third mode period is much smaller than the first two modes.

Moreover, looking at the typical code response spectra, some other comments can be made:

- for towers with low slenderness, the periods of the first two modes fall within the constant branch of the response spectrum, providing the maximum value of the spectral acceleration;
- for slender and tall towers, the local higher modes with significant participating mass ratio (in particular, bell towers show local modes involving mainly the upper part where large openings are present) correspond to the maximum value of the spectral acceleration.

The results of the performed NLDA are reported in Fig. 2.12 and Fig. 2.13 as a function of the inclination and opening area percentage, respectively.

Looking at Fig. 2.12, it is evident that a marked inclination value (about 3°) is the most important parameter influencing the seismic performance of high towers (Tower VI and Tower III are about 50m high), since they exhibit the maximum normalized top displacement along both the x and y horizontal directions. On the other hand, its effect seems to be less important when the height and the slenderness of the tower significantly decreases, as in the case of Tower I, which is only 21m high with a slenderness ratio smaller than 3 and a large thickness of the walls at the base. The importance of the inclination factor is also confirmed by the comparative study by Ferrante et al. (2019), carried out on an inclined ideal vertical model.

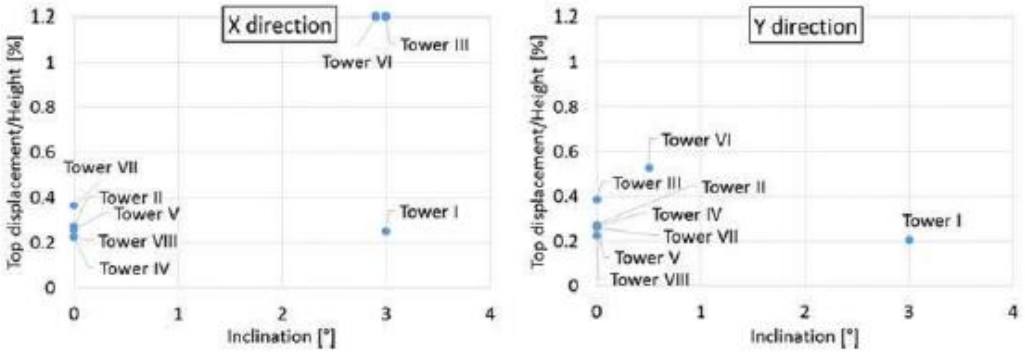

Fig. 2. 12– a) Values of the maximum normalized top displacement (top displacement/height) obtained by the non-linear dynamic analyses (PGA=0.1g) as a function of the inclination of the towers, as reported in Valente & Milani (2018).

The presence of openings, instead, increases the normalized top displacements and decreases the normalized base shear (Fig. 2.13), even if a clear trend may not be deduced from the diagrams, especially for the base shear. Nevertheless, the presence of openings plays a crucial role at the local level, representing a region where damage generally concentrates (base and upper part).

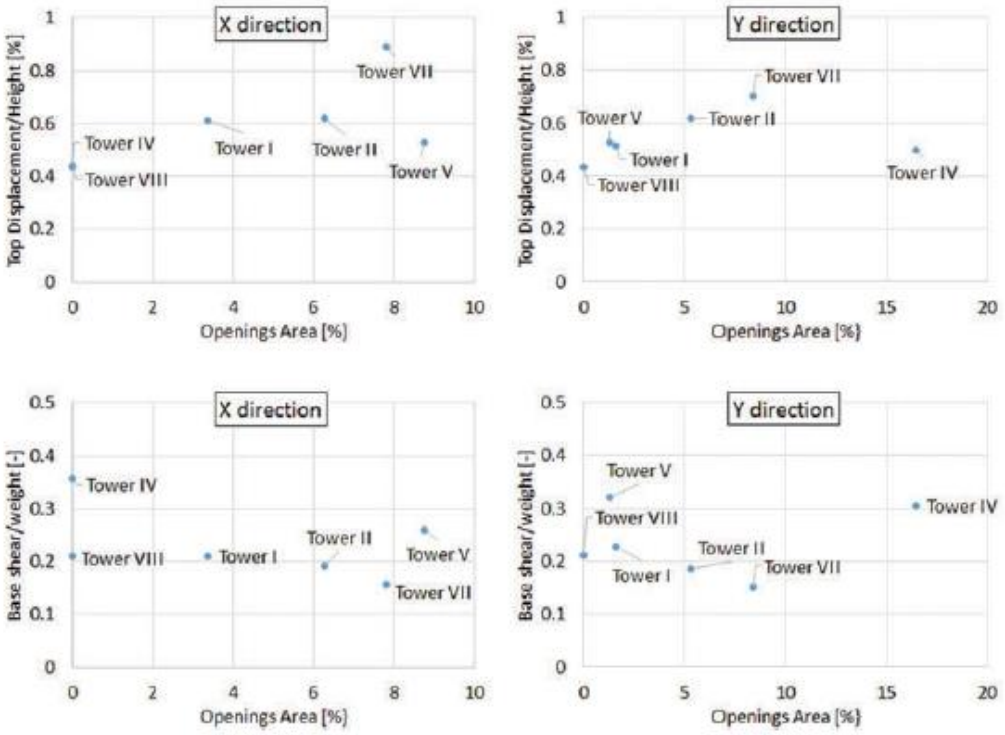

Fig. 2. 13– a) Values of the maximum normalized top displacement (top displacement/height) and of the normalized base shear (base shear/weight) derived from the non-linear dynamic analyses (PGA=0.2g) as a function of the openings area of the towers, as reported in Valente & Milani (2018).

In addition to the horizontal components of the ground motion, the seismic performance of masonry slender tall towers is very sensitive to the vertical component of the ground motion. Studies conducted by Casolo (1998, 2001) investigated significant ground motion parameters for the evaluation of the seismic performance of slender masonry towers. It was found that a strong vertical ground motion component can induce a marked increase in the response of the model. This effect depended markedly on the characteristics of the ground motions in combination with the tower height.

The effect of the vertical acceleration component has been also investigated for other type of slender masonry structures, such as chimneys and minarets. Breccolotti & Materazzi (2016) stated that the collapse of masonry chimneys during earthquakes

can be generally ascribed to the loss of equilibrium produced by the overturning moments, not sufficiently balanced by the stabilizing vertical load provided by the chimney's self-weight, significantly reduced by the effect of the vertical ground motion. Similar results have been described for masonry minarets, as shown by Bayraktar et al. (2018) using linear and non-linear analysis. In their work, the authors pointed out that the vertical component has a significant effect on the structural vertical displacement pattern rather than on the horizontal one, which clearly increase in magnitude in the case of non-linear behaviour (Figs. 2.14-2.15).

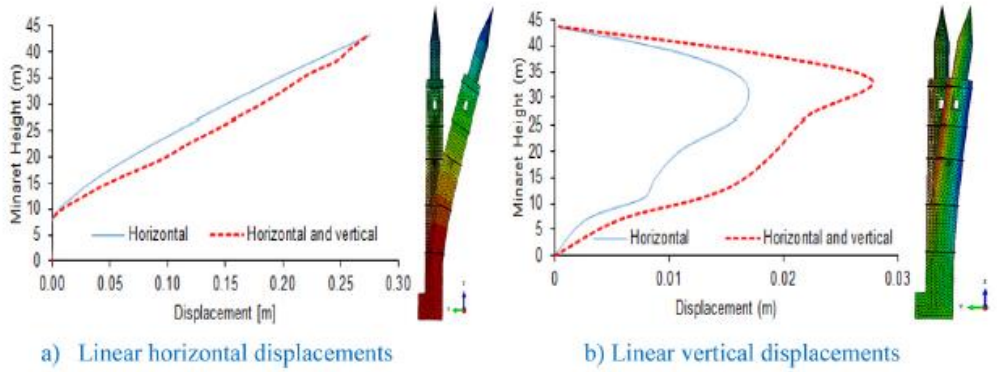

Fig. 2. 14 – Variations of linear horizontal and vertical displacements along the minaret height, as reported in Bayraktar et al. (2018).

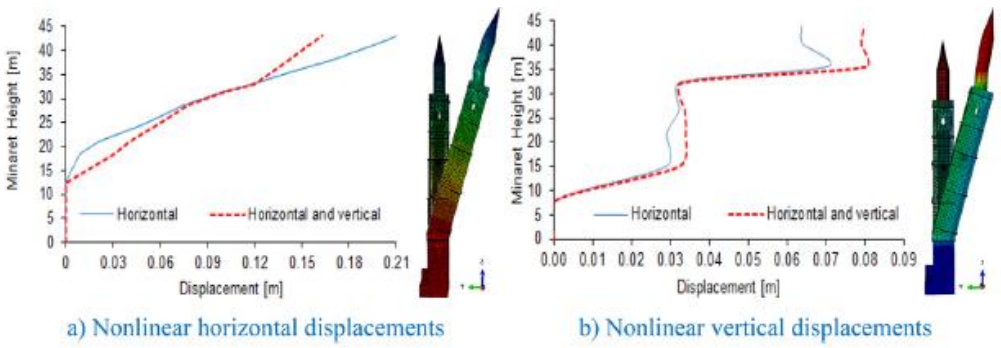

Fig. 2. 15 – Variations of non-linear horizontal and vertical displacements along the minaret height, as reported in Bayraktar et al. (2018).

As previously stated, another relevant aspect is played by the restraint action due to adjacent buildings. This eventuality has been studied by Bartoli et al. (2006, 2013), evaluating the seismic reliability of the "Torre Grossa" located in San Gimignano (Italy). The assessment was performed throughout a dynamic characterization of an elastic FE model, where the in situ dynamic tests allowed to estimate the restraint degree offered by the neighbour building. In D'Ambrisi et al. (2012), the structural identification allowed the evaluation of the masonry Young modulus and the constraint effect given by the adjacent constructions to a historical masonry tower, while, in Pieraccini et al. (2014), the numerical model of the Mangia's tower in Siena (Italy) was equipped by linear springs at the lower level to reproduce the effects of the neighbouring buildings.

If the aforementioned works refer to dynamic identification in the elastic field, which is a strong limitation when studying the behaviour of masonry structures, in Bartoli et al. (2016, 2019) several FE pushover analyses were performed to evaluate the tower seismic performance comparing isolated and confined models, also considering different degrees of constraint. The results showed strong differences between isolated and confined schemes. The pushover curves in Fig. 2.16 depict a remarkable change in the displacement capacity and in the peak strength offered by the structure. The isolated tower (IT0) is characterized by a more ductile behaviour at the cost of a more limited ultimate resistance. Inversely, the confinement influence is really evident and shows a stiffening effect that leads to more consistent lateral strengths at the cost of a loss in ductility capacity as the restraint level increases (passing from CT1 to CT2 model).

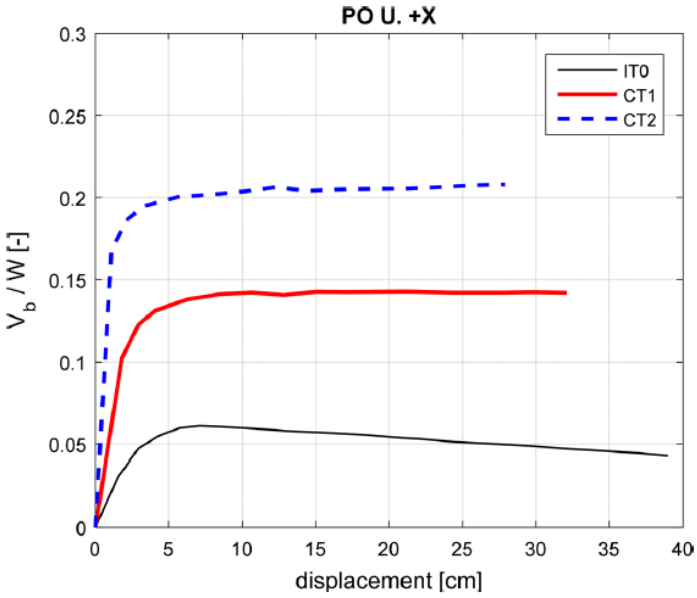

Fig. 2. 16 – Comparison between capacity curves in X direction for the isolated (IT0), confined (CT1) and more confined (CT2) models, as reported in Bartoli et al. (2016).

Other interesting insights can be deduced form the damage pattern reported in Fig. 2.17, highlighting different distribution contours for the analysed scenarios. With respect to the corresponding isolated tower case (Fig. 2.17a), the confined models (Fig. 2.17b,c) show that the damage is mainly concentrated along the perimeter of the tower, at the top of the fornices, with a damage distribution that is predominantly horizontal and more intense ($D \approx 1$) in those elements in contact with the elastic blocks modelling the interaction with the surrounding buildings, especially when the highest restraint level is considered (CT2).

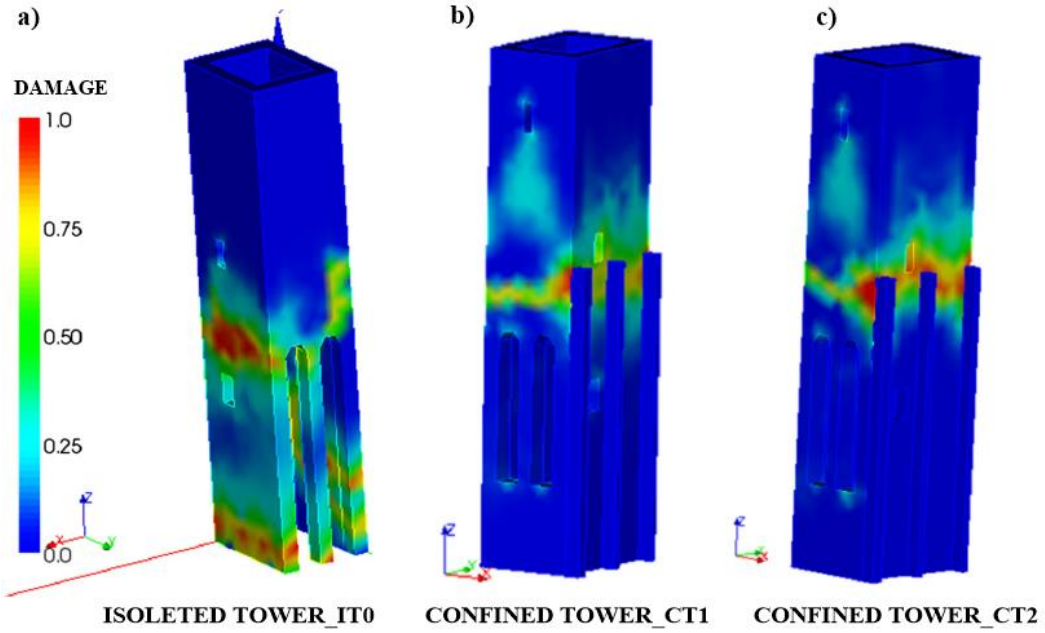

Fig. 2. 17 – Comparison between the damage patterns derived for a) the isolated (IT0), b) the confined (CT1) and c) the more confined (CT2) towers (modified from Bartoli et al. 2016).

Similar findings are given by Castellazzi et al. (2018), where the tower of the "San Felice sul Panaro" fortress is analysed by means of both pushover and NLDA. It is demonstrated that the actual crack pattern of the structure, hit by the devastating seismic sequence occurred in May 2012 in the Northern part of the Emilia region (the so-called ''Emilia earthquake''), is generally more in agreement with the numerical output suggested by the non-isolated structure rather than the free-standing one.

Another crucial aspect is that even the type of numerical analysis can lead to different failure modes predictions. In this context, discrete element methods (DEM) have recently shown a good prediction capability (Clementi et al. 2020; Poiani et al. 2018) in reproducing the local damage pattern in comparison with finite element methods (FEM), generally showing a more widespread trend along the structure body.

Furthermore, pushover analysis usually provides a flexural collapse mode (Acito et al., 2014) and often a too conservative seismic vulnerability (Minghini et al., 2014) with respect to NLDA. The main causes at the base of such different behaviour are two-

fold: firstly, an accelerogram is applied during the NLDA model and, secondly, the unloading phase is not active in a pushover static simulation (Milani, 2019).
According to Shehu (2021), the most accurate approach for mimicking seismic loads in a pushover analysis is by gradually imposing incremental accelerations, thus eliminating fixed patterns of loads, which constrain the damage distributions; moreover, if a force-based approach is implemented, the role of the material is less relevant when compared with other features of the structure.
However, as discussed, it has been shown that masonry tower seismic assessment usually requires a deep degree of knowledge of the structure, that most of the time is possible only if an extensive (and expensive) survey campaign is executed. Moreover, the adoption of non-linear modelling needs a huge computational effort and a strong expertise that is not always easy to be sustained in professional practice.
To overcome this drawback, a simplified approach, consisting in a qualitative analysis performed through simplified mechanical models, is proposed by the Italian Guidelines (IG) for built heritage (DPCM 2011), known as LV1. This is a method conceived for a territorial scale level assessment and it is aimed at providing a comparative ranking risk of homogeneous typology of buildings, eventually postponing more advanced analyses to subsequent in-depth investigations. The whole procedure is based on a limited number of geometrical and mechanical parameters (or qualitative visual tests) and, in the case of a masonry tower, enables to schematize the structure as a cantilever beam subjected to a system of static horizontal forces.
According to the IG, the collapse can occur according to a combined compressive and bending stress mode (rocking-flexural mode), indiscriminately associated with all the towers regardless of their slenderness, typology of walls and construction technique. This is a very burdensome assumption, since it has been previously highlighted that masonry towers reveal completely different collapse modes depending on many aspects. As a reference, the charts proposed by Sharhosis et al. (2018) reported in Fig. 2.10 show that only the Case 3 seems to be the closest to the Italian code predictions, with a larger range of slenderness ratio where rocking failure is possible.

Anyway, the value of the method lies in its relatively simple application, providing a preliminary vulnerability assessment and not an absolute risk assessment or seismic safety evaluation.

Paying attention to these issues, the method divides the structure in *n* sectors by horizontal cuts. Each sector has uniform geometric, inertial and material properties. At the base section of each sector, the acting bending moment (seismic demand) and the resisting one (seismic capacity) are evaluated. The comparison of these two values allows to estimate the seismic safety of the structure. According to the Italian Code, the resisting bending moment M_{ui} in the i-th section is given by:

$$M_{ui} = \frac{\sigma_{0i} A_i}{2}\left(b_i - \frac{\sigma_{0i} A_i}{0.85 a_i f_d}\right) \tag{2.12}$$

where σ_{0i} is the average compressive stress due to the gravity loads, f_d is the design compressive strength of the masonry, A_i, b_i and a_i, are the area of the cross section and the dimensions of the parallel and perpendicular sides of the section (without openings) with respect to the analysed seismic direction.

The acting bending moment is simply evaluated by assuming a linear distribution of horizontal loads along the height of the tower. The force F_i to be applied at the centre of mass of the i-th sector is given by:

$$F_i = \frac{W_i z_i}{\sum_{k=1}^{n} W_i z_i} 0.85 S_d(T_1) \frac{W}{g} \tag{2.13}$$

where W_i denotes the weight of the sector, z_i is the height of its centre of mass with respect to the foundations and $S_d(T_1)$ is the ordinate of the design response spectrum, function of the main period T_1 of the tower in the considered load direction. This value is calculated dividing the ordinate of the elastic response spectrum by the behaviour factor q; the IG suggests a value equal to 3.6 in the case of regular structures in elevation or reduced to 2.8 in presence of sharp changes in stiffness along the height or of adjacent structures. The symbol W represents the whole structural weight, while g denotes the gravity acceleration.

Once the value of the seismic force in each sector has been calculated, it is possible to evaluate the seismic resultant acting at the base section of the i-th sector:

$$F_{hi} = \frac{\sum_{j=i}^{n} W_j z_j}{\sum_{k=1}^{n} W_k z_k} 0.85 S_d\left(T_1\right) \frac{W}{g} \tag{2.14}$$

The acting bending moment M_{si} is then:

$$M_{si} = F_{hi}\left(z_{hi} - z_i^*\right) \tag{2.15}$$

with:

$$z_{hi} = \frac{\sum_{j=i}^{n} W_j z_i^2}{\sum_{k=1}^{n} W_k z_k} \tag{2.16}$$

where z_{hi} is the height of application of F_{hi} and z_i^* is the height of the i-th section with respect to the base of the tower.

Moreover, the IG introduce two synthetic indexes that quantify the safety level of the structure. The first is the seismic safety index $I_{s,SLV}$, i.e. the ratio between the return period T_{SLV} of the earthquake which gets the tower to reach the ultimate limit state and the expected return period $T_{R,SLV}$ =475 years of the design earthquake of the site:

$$I_{s,SLV} = \frac{T_{SLV}}{T_{R,SLV}} \tag{2.17}$$

The second index is the acceleration factor $f_{a,SLV}$. It is calculated as the ratio between the peak ground acceleration of the earthquake which gets the tower to the ultimate limit state a_{SLV} and the peak ground acceleration of the design earthquake $a_{g,SLV}$, both referred to a rigid soil of type A:

$$f_{a,SLV} = \frac{a_{SLV}}{a_{g,SLV}} \tag{2.18}$$

Several literature studies have consequently tried to investigate the effectiveness of this approach, carrying out advanced non-linear analysis aiming to determine the collapse critical acceleration and comparing the results obtained with the guidelines (Casolo et al., 2013a; Acito et al. 2014; Valente & Milani 2016; Bartoli et al. 2017, 2019). From all these studies it can be stated that generally the IG simplified approach provides reasonable synthetic predictions of the tower vulnerability.

For example, a graph reporting the predicted collapse accelerations derived with IG and pushover analyses (NLSP), in a study carried out on 8 Italian towers having different geometric features, is shown in Fig. 2.18 (Valente & Milani, 2016).

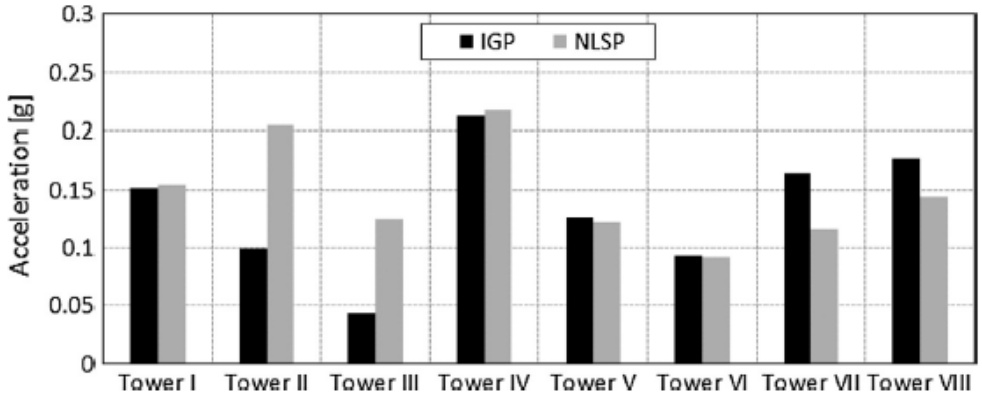

Fig. 2. 18 – Values of the collapse acceleration found by Italian Guidelines procedure (IGP) and non-linear static procedure (NLSP) for the different analysed towers, as reported in Valente & Milani (2016).

The accelerations obtained through pushover analyses are reasonably in agreement with those obtained by the simplified sectional approach, with a slight conservative tendency of the simplified approach.

However, in general, the simplified approach is unable to give precise information on the active failure mechanisms and the areas undergoing severe damages due to its intrinsic limitations. Therefore, it seems that more advanced sophisticated analyses are necessary to correctly understand the seismic structural behaviour of the towers.

So far, the analysed case studies have highlighted the main aspects characterising the masonry towers seismic vulnerability under a fixed-base scheme. The following section will present some insights derived from the available works that have modelled the presence of a soil deposit, highlighting the soil-structure interaction effects on the dynamic response of the towers.

2.3.3 The seismic response of masonry towers: soil compliance conditions

In the previous section it has been discussed how the dynamic behaviour of masonry towers is the result of several aspects characterising the structure, such as its geometrical features, the material mechanical response and many others. Among these aspects, a relevant role can be played by the lithological sequence of the subsoil foundation on which the tower is founded, that can significantly change the overall tower response subjected to earthquakes, due to the occurrence of SSI phenomena with respect to a FB scheme (Section 2.2).

Indeed, also the IG for built heritage (DPCM 2011) point out that a critical amplification phenomenon can affect the upper part of the tower due to the mutual interaction occurring between the seismic signal, soil deposit, foundation and structure in elevation; this can lead to the severe damages observed after post-earthquake surveys, especially in the belfry area.

For example, a soil amplification effect has been recognized for the “Sant’Agostino Bell Tower” located in Amatrice (Italy), hit by the long seismic shock sequence dated 2016-2017 (Gazzini et al. 2018), and for the “Mirandola Bell Tower” located in Mirandola (Italy) (Fioravante et al. 2013) as reported in Fig. 2.19 and Fig. 2.20, respectively.

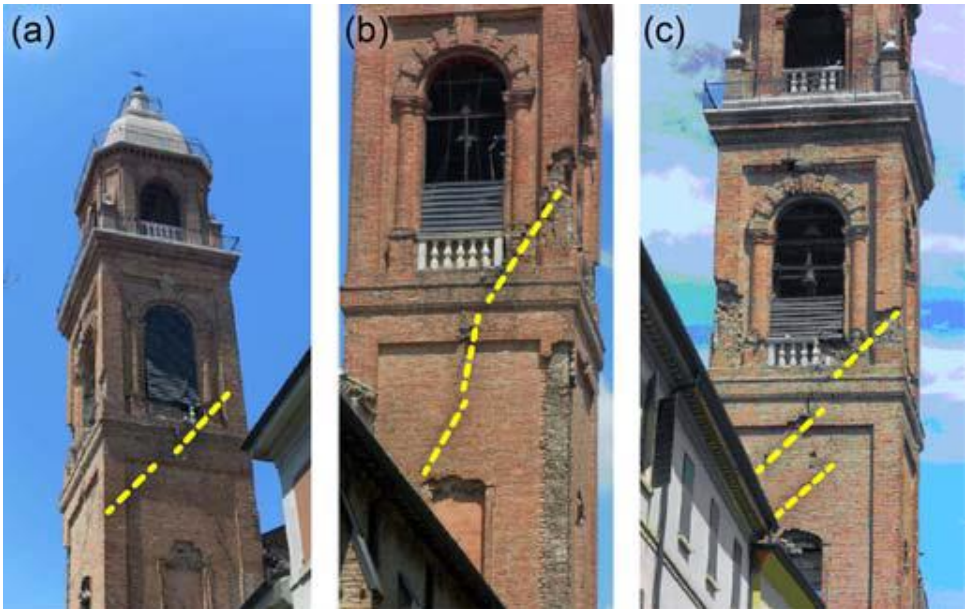

Fig. 2. 19 – Damage of bell tower of the Mirandola cathedral (a) east view, (b) west view and (c) south view, as reported in Fioravante et al. (2013).

Fig. 2. 20 – Collapse of the Sant'Agostino Bell Tower in Amatrice due to soil amplification effects.

Despite these evidences, the soil compliance is still just occasionally considered even if the occurrence of a tower standing on a deformable soil is not so remote (de Silva et al. 2015a).

The reason why SSI is generally still neglected probably stands in the huge complexity of the model that such analysis requires. Nevertheless, the soil deformability can significantly modify the dynamic behaviour of a building (Section 2.2). Even if in some cases the SSI might be neglected, like for the "Torre Grossa Tower" in San Gimignano (Madiai et al. 2017), the dynamic identification has demonstrated that the hypothesis of a compliant base is often necessary in order to reproduce the tower vibration modes and measured frequencies, such as for the "Ghirlandina Tower" in Modena (Cosentini et al. 2015), the "Pisa Tower" (Fiorentino et al. 2017), the "Carmine Bell Tower" in Napoli (de Silva et al. 2018), the "Giotto Bell Tower" in Florence (Lacanna et al. 2019) and the "Santa Sofia Bell Tower" in Benevento (De Angelis et al. 2022). As a matter of fact, the comparison between FB and SSI schemes has evidenced that the best match with the experimental data is caught by the latter ones, which are able to reproduce higher modes especially if full complete 3D models are adopted (De Angelis et al. 2022).

Besides these linear dynamic identification examples, few studies have performed a comprehensive research work on the dynamic behaviour of the SSI system. In the following sections, the main findings derived from these available case studies are presented, with a special focus on the case of the "Carmine Bell Tower".

2.3.3.1 The Carmine Bell Tower case study

The "Carmine Bell Tower" located in Napoli (Fig. 2.21) represents one of the few well-documented case studies where the SSI effects on a masonry tower have been investigated.

Fig. 2. 21 – View of the Carmine monumental complex located in Naples.

The tower is a highly slender structure built on deformable soils and, therefore, potentially subjected to amplification and resonance phenomena, as it has been witnessed by the almost total collapse of the original structure caused by a strong earthquake. Indeed, the current 17th century body of the bell tower stands on a previous 14th century structure, severely damaged by a violent earthquake occurred in 1456 with its epicentre in Sannio. A schematic view of the actual structure together with the soil stratigraphy profile is illustrated in Fig. 2.22.

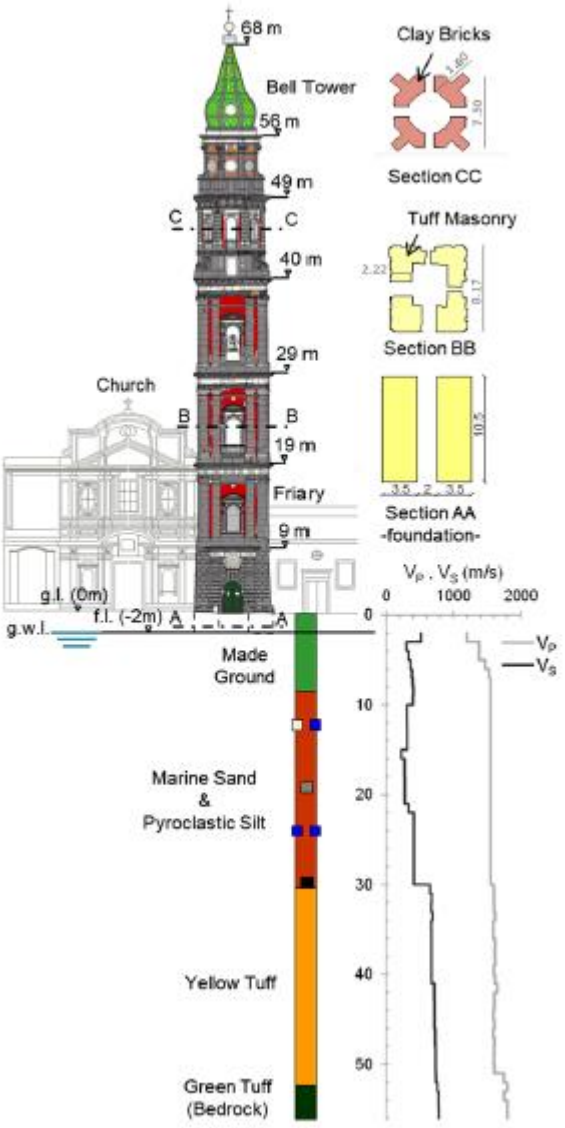

Fig. 2. 22 – Front view and cross sections of the Carmine monumental complex with the layered soil lithological sequence and V_P, V_S profiles below the bell tower (modified from de Silva et al. 2018a).

From the basement up to 40 m, the cross section of the current structure is square and the walls are made of externally dressed yellow-tuff stone masonry, while the oc-

tagonal cell and the dome are made of clay bricks. A brickwork octagonal cell raises from 40 to 56 m, covered on the top by a pyramidal spire.

The footings resulted as an embedment and an enlargement of the E-W main walls, deepening 2 m below the ground level and widening out about 0.3 m in the centre and 0.5 m in the corners.

The lithological sequence, derived from a borehole executed very close to the external access to the bell tower, is characterised by man-made ground down to 10 m, followed by alternation of Marine Sand and Pyroclastic Silt down to 31 m, overlying Yellow and Green Tuff. The water table was intercepted at a depth of 2 m, exactly at the foundation level of the tower.

A Down-Hole test was also performed in the borehole to measure the compression (V_P) and shear (V_S) wave velocity down to 56 m. The V_P profile increases slightly with the depth, keeping around the value of 1500 m/s, typical of saturated soils. The V_S profile increases with the depth in the man-made ground from 300 to 400 m/s, reducing to 300 m/s in the upper layer of Marine Sand. A significant seismic impedance contrast was detected in the Tuff formation, where the values of V_S gradually increase from 650 m/s measured on the roof of the Yellow Tuff to 785 m/s relevant to the Green Tuff. More details on the field and laboratory tests are reported in de Silva et al. (2015a).

The research focused on different aspects of the soil interaction with the structure, starting from a seismic ground response analysis (SRA) (de Silva et al. 2014b) performed with an equivalent visco-elastic approach, adopting seven different input signals following the Italian Code NTC2008 indications. The results, reported in Fig. 2.23, revealed that the average of the seven acceleration spectra on the surface derived with the SRA procedure significantly exceeds the guidelines of the Italian Code. In particular, in the range of periods of ordinary structures, spectral accelerations would be underestimated up to about the 25%, while the deviation reduces as the deformability of the structure increases. Moreover, the natural period of the structure predicted by NTC2008 significantly underestimates the experimental one obtained from modal operational analysis test (OMA) (Ceroni et al. 2009); the mismatch clearly

decreases considering the Rainieri & Fabbrocino (2012) expression specifically calibrated on masonry towers located in the South of Italy.

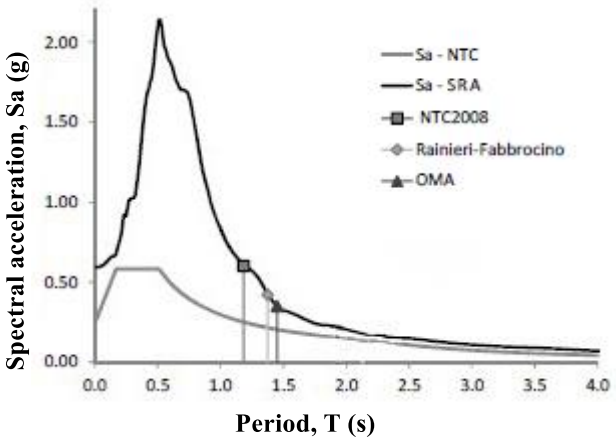

Fig. 2. 23 – Comparison between the NTC2008 acceleration spectrum (class C) and the average spectrum resulting from the SRA analysis (modified from de Silva et al. 2014b).

In addition, a series of full SSI numerical analyses of the tower were carried out, in order to investigate the structural behaviour dependency from the soil deformability. In de Silva et al. (2015b), the non-linear soil influence, described by an equivalent visco-elastic approach, was studied using an input motion whose amplitude was progressively scaled, respectively resulting in a weak, medium and strong intensity ground motion. The results were inspected along three verticals (Fig. 2.24) located under the foundation level and far enough from the structure to be representative of the free-field condition.

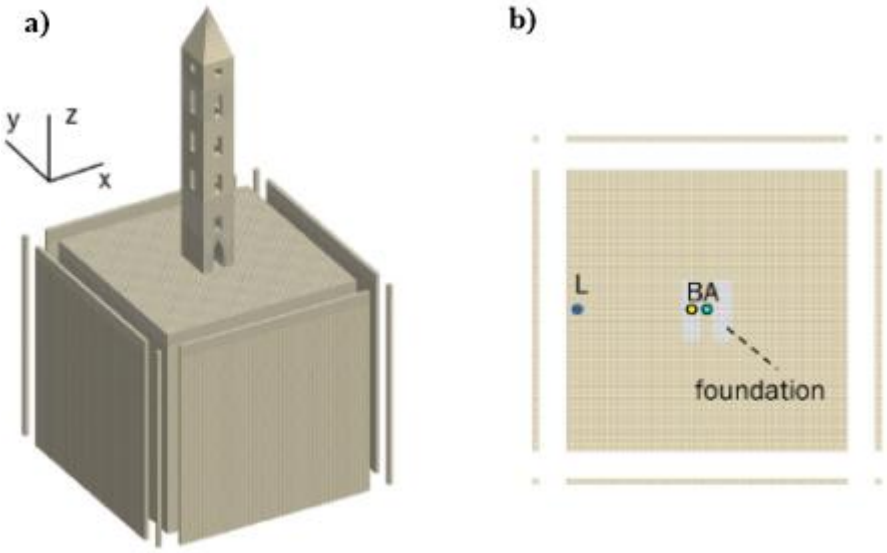

Fig. 2. 24 - a) Sketch of the three-dimensional SSI model and b) location of the inspected verticals (modified from de Silva et al. 2018a).

In Fig. 2.25 the maximum shear strains and acceleration profiles are depicted for the three verticals and for three intensity levels.

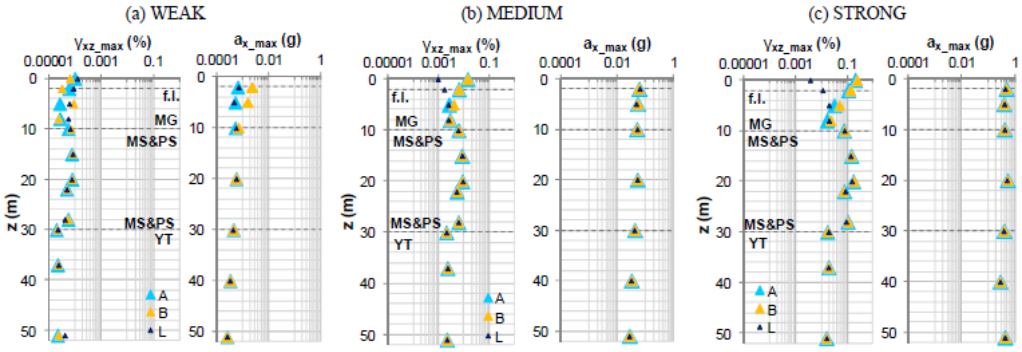

Fig. 2. 25 – Maximum shear strains and acceleration profiles along the soil deposit depth for a) weak, b) medium and c) strong seismic input motion intensity for the three verticals shown in Fig. 2.24b, as reported in de Silva et al. (2015b).

As expected, the weak input does not induce any non-linear soil behaviour in the whole soil volume. When the intensity level rises, the non-linear soil response is acti-

vated along the deposit depth. Under the tower, at the verticals A and B, a significant increase in $\gamma_{xz,\max}$ occurs if compared with the free-field vertical L, an effect which is likely due to the interaction with the structure. This interaction extinguishes within a depth of 5 m below the foundation plane of the bell tower, which roughly coincides with the semi-width of the base.

Moreover, the amplification functions (Fig. 2.26) highlight the soil excursion in the non-linear phase, evident from the damping increase and reduction of the resonance frequencies; additionally, the presence of the structure does not change the soil frequencies, but affects the amplification peaks with the exception of the first one.

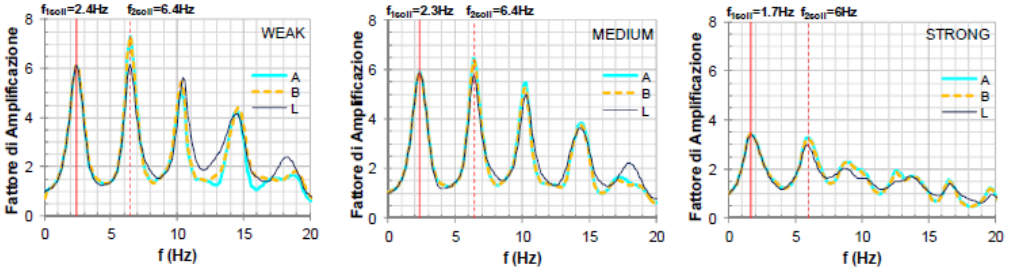

Fig. 2. 26 – Amplification functions derived for the weak, medium and strong seismic input motion intensity for the three verticals shown in Fig. 2.24b, as reported in de Silva et al. (2015b).

Further studies were conducted to investigate the restraining action exerted by the church and the friary. In de Silva et al. (2018a), the experimental frequencies are better simulated by the laterally restrained models. Furthermore, the restraining action seems not to affect the amplification amplitude of the first natural frequency, while some discrepancies are observed for the higher ones with respect to the free-standing condition (Fig. 2.27).

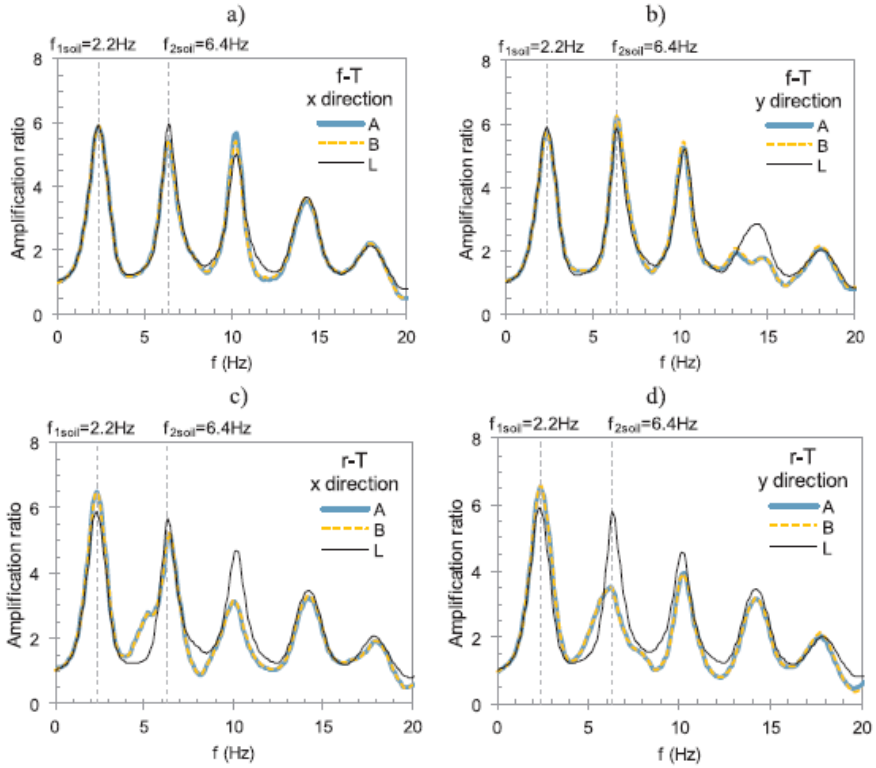

Fig. 2. 27 - Amplification functions relative to the laterally free, f-T (a, b) and the laterally restrained, r-T (c, d) models, along x (a, c) and y (b, d) directions, for the three verticals shown in Fig. 2.24b, as reported in de Silva et al. (2018a).

In addition, since the presence of the soil generally influences the behaviour at higher frequencies, it is thought that resonant phenomena can occur between the fundamental frequency of the soil and the higher modes of slender structures, which are mostly affected by soil compliance.

Moreover, the pushover analyses performed by de Silva et al. (2018b), accounting for the hysteretic behaviour for both structure and soil, have shown that the lateral restraint attenuates the effect of the SSI, since the first 19 m of the tower are practically incorporated in the church and hence fixed (Fig. 2.28).

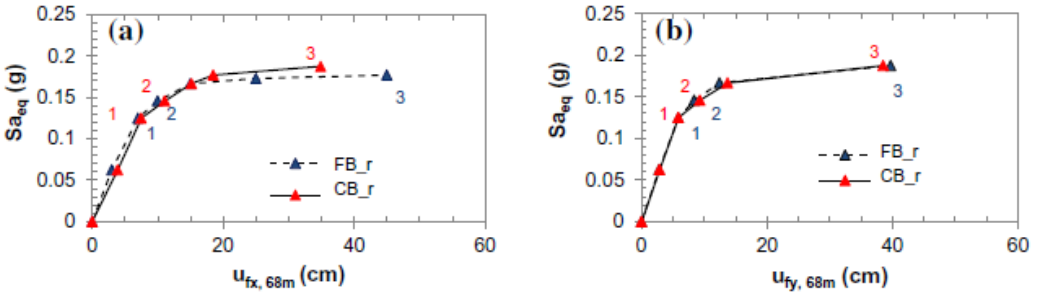

Fig. 2. 28 - Capacity curves derived in restraint conditions for the fixed-base (FB_r) versus compliant base models (CB_r) in x (a) and y (b) directions, as reported in de Silva et al. (2018b).

Conversely, in the laterally free models, the influence of the soil on the global deformability of the system is more pronounced when the tower is loaded along the direction that activates the highest stiffness for the structure (Fig. 2.29).

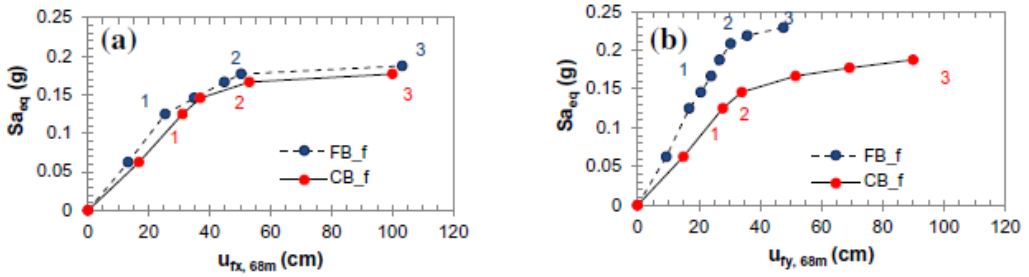

Fig. 2. 29 - Capacity curves derived in free standing conditions for the fixed-base (FB_f) versus compliant base models (CB_f) in x (a) and y (b) directions, as reported in de Silva et al. (2018b).

Finally, NLDA showed the plastic state distribution history induced by a seismic motion (Fig. 2.30) on the non-isolated model, considering the soil compliance. The collapse seems to involve the upper part the structure starting immediately above the restraint, not involving the beneath area, and resulting in an extended plastic hinge. Thus, the effect of the confinement on the collapse mode seems strong even when SSI is taken into account, also providing a reliable interpretation of the historical damages since, according to the chronicles, the original bell tower was completely destroyed by the historical event, except for the lowermost vaulted level.

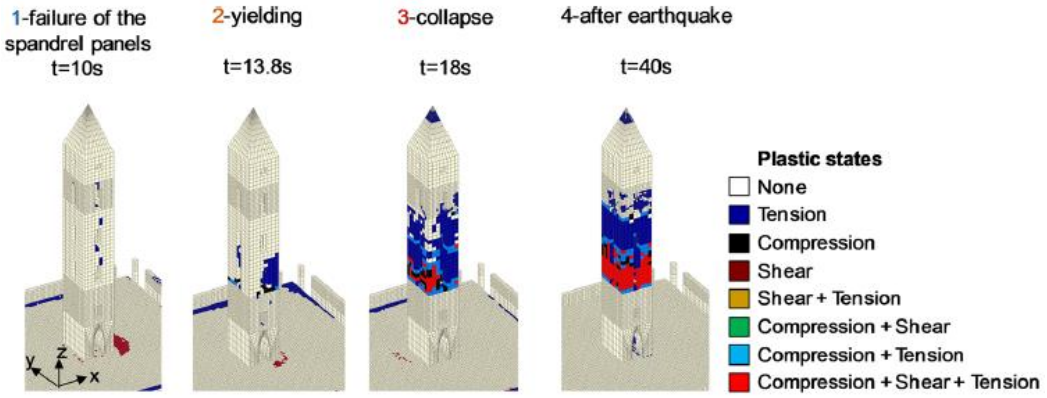

Fig. 2. 30 - Non-linear dynamic analysis results of the Tower under the Potenza input motion for the compliant base restrained model: evolutions with time of the plastic states, as reported in de Silva et al. (2018b).

2.3.3.2 Additional works dealing with masonry tower SSI

Apart from the aforementioned "Carmine Bell Tower" case study, there are very few other comprehensive works dealing with masonry tower SSI modelling.

Some of them refers to constructions located in the Middle East, for example typical religious structures such as minarets (Dogangun et al. 2007) or memorials, as in the case of the Gonbad-e Qabus tower in Iran, which is the world's tallest pure-brick tower, analysed by Mortezai & Motaghi (2016). The authors mainly focused on exploring the role played by the seismic input motion characteristics, performing time-history analyses adopting different accelerograms. The results suggested that the destructive effect of the input frequency content is greater than its magnitude and strong motion duration, and in particular the highest displacements and stresses were recorded for low frequency content motions.

Similar remarks are highlighted in Casolo & Uva (2013b) for an idealized masonry tower, where also the vertical component of the input acceleration was considered. Despite the vertical component may produce relevant effects on the structural response and on the final damaged configuration, it cannot be established a-priori if the effect is significantly worse for the structure and, above all, which structural part and

local mechanisms will be involved. The final situation will depend on the frequency content of the accelerograms and must be specifically examined case by case.
In Casolo et al. (2017) the damage pattern induced in the tower was also related to the modal shape change due to the soil deformability (Fig. 2.31). It was observed that the soil has little influence on the first modal shape (Fig. 2.31a), which is almost totally unchanged with respect to the cantilever condition, while the second mode is deeply modified changing the soil deformability (Fig. 2.31b).

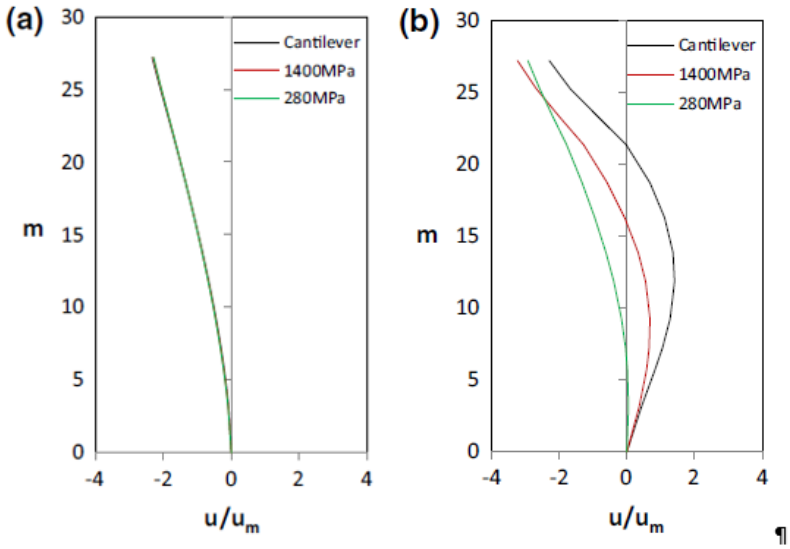

Fig. 2. 31 - Transverse displacement u depurated from rigid body motions and normalized by the average of the absolute value u_m for a) the 1st natural mode and for b) the 2nd natural mode (modified from Casolo et al. 2017).

This can have a direct impact on the damage pattern since the internal action distribution along the tower height might be significantly altered. Moreover, when the vertical component of the earthquake is considered, the soil compliance seems to mitigate the crack pattern development in the central part of the structure in comparison to the cantilever case (Fig. 2.32). This is justified by the authors pointing out that the presence of the structure causes a reduction of the high frequencies of the seismic signal

with respect to the free-field conditions, and this reduction is more marked as the soil is more deformable.

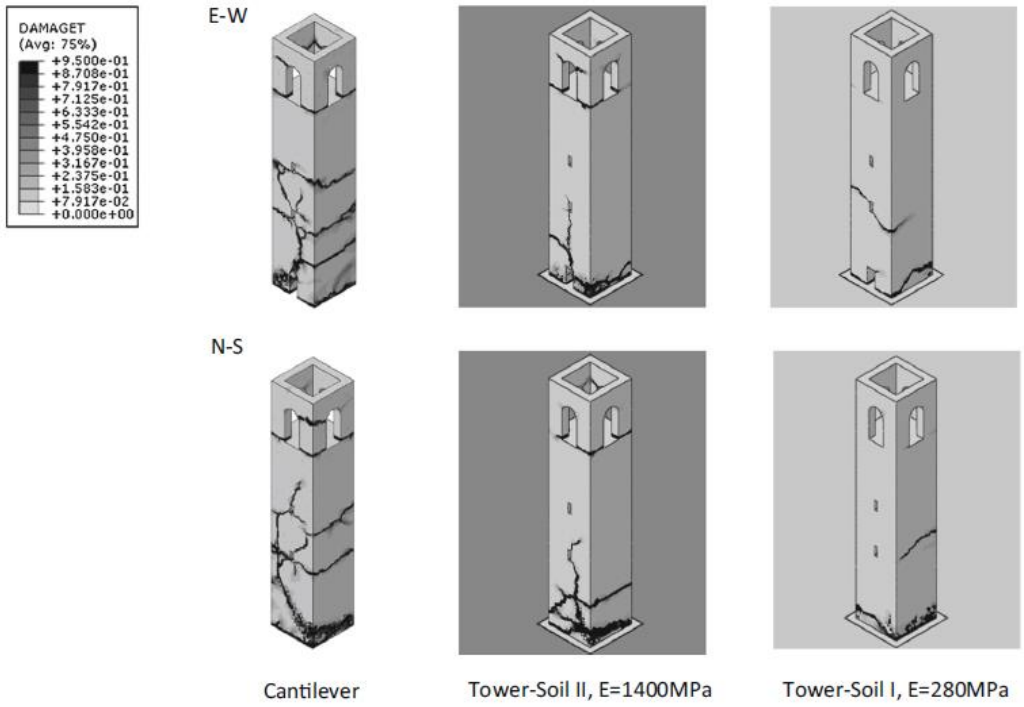

Fig. 2. 32 - Tensile damage patterns comparison among the cantilever condition and the complaint base cases considering the three special components of the Mirandola ground motion, as reported in Casolo et al. (2017).

Furthermore, de Silva (2022, 2020) evaluated the effects of soil-structure interaction on classes of idealized and real towers founded on different soil types. Through NLDA with increasing amplitude of the input motions, a probabilistic approach is defined to predict the mean annual rate of exceeding of different levels of the peak and residual bending displacement and foundation rotation demands. The result is the so-called 'demand hazard curve', which summarizes, in a probabilistic framework, the modification of the seismic hazard and fragility induced by soil compliance.

The study reveals that the soil compliance enhances the structural demand of slender towers but does not affect significantly very slender towers. Indeed, the structural

slenderness is beneficial on the seismic actions because the higher structural deformability increases the fundamental vibration period and leads to a reduction of the spectral ordinates. Conversely, tall monumental towers are more significantly affected by tilts induced by the foundation rocking motion and more prone to instability.

CHAPTER 3: MASONRY MECHANICAL MODELLING

3.1 Introduction to the masonry material

Masonry is one of the oldest building materials used since the dawn of civilization. It is the Near East that offers us the first examples of dry stone, circular and partially buried masonry settlements, dating back to 9000-8000 BC, found in the area of the Lake Hulen in Israel. The construction technique, then, evolved and the material begun to be used also for monuments and places of worship, which have come down to our days like the ancient Egyptian Pyramids (about 2800-2000 BC) (Fig. 3.1).

Fig. 3. 1 – Ancient Egyptian Pyramids.

However, it is with Romans that the technique of masonry constructions reaches the next level, since masonry was no longer used just for residential buildings but also for real civil works: in fact, until 1200 AD, there was a massive production of arches, columns, temples, churches, bridges and aqueducts (Fig. 3.2).

Fig. 3. 2 – Ancient Roman aqueduct Les Ferreres, Tarragona (Spain).

Anyway, in this context no real structural design was adopted and it was rather the empirical knowledge acquired over time that provided construction rules based on the different types of stone and on proportion criteria among the structural components, as described in the "De Architectura" by Vitruvio (25 BC).

In the Middle Ages and Gothic period (1200-1600 AD), the stone became worked to perfection and modelled inside the cathedrals in the form of elegant ribs and vaults, demonstrating a remarkable understanding of the action of the forces throughout the structure (Fig. 3.3).

Fig. 3. 3 – Milan Cathedral (Italy).

It was only since Renaissance that the theoretical explanation of the phenomena was also sought: Leonardo da Vinci, for example, was the first to affirm that the thrust followed a path that remained inside the arch. Well after Leonardo, in 1586 Simon Stevinus published the first statics book "De Beghinselen des Waterwichts" that will constitute the work at the base of the graphical statics that will spread in the XIX century.
Masonry, therefore, played the leading role in building materials until the late 1800, when the first industrial revolution and the availability of plentiful amount of steel used in the production of beams and columns started to replace it. Nevertheless, it is with the arrival of concrete, and the introduction of the rules for the structural design with this new material, that during the 1900 masonry was gradually abandoned.
Despite its long history, it is just in recent decades that the interest in masonry structures has significantly increased for the problems associated with the restoration and conservation of the enormous stock of existing buildings and structures spread all over the world. A particular incentive has also been given by the series of seismic events that hit the countries of the Mediterranean area, causing the collapse of numerous monuments and buildings and, at the same time, requiring safety assessment and structural consolidation interventions for the damaged ones.
However, catastrophic events are not the only cause of the ruin of masonry structures, but also the accumulation of damage over time due to various factors, such as traffic vibrations, wind, thermal loads and ground movements, can induce the degradation of the strength of the material.
Everything becomes even more complicated when studying historical constructions, full of uncertainties related to their evolution over time (modifications made to the structure), to the geometry and materials used within the structural elements, to the forces that act or have acted and to the consequent evolution of the damage (almost always present in ancient buildings), without mentioning the construction techniques varying not only from one period to another, but also from place to place.
Compared to other areas of research, such as either concrete or soil or rock mechanics, a real consolidated experience in the field of masonry has been lacking for long time, both in carrying out experimental tests and in the evaluation of the results, both

in the adopted structural analysis techniques. In fact, despite the simplicity of the material from the construction point of view (simple overlapping of units, with or without mortar), the full understanding of masonry mechanical behaviour is really challenging due to its highly non-linear response. Hence, in the next section a brief introduction to some of the main characteristics of masonry mechanical behaviour is presented.

3.1.1 The main characteristics of masonry material

Masonry is generally defined as a composite material, made of natural or artificial elements constituted by stones or bricks assembled in different ways and bonded together with mortar. One of its best properties is simplicity, that has been the main reason why masonry constructions are so diffuse all over the world and are still used in many countries. In Italy, both bricks and stones were used from very ancient times until today in different types of buildings, realized with an extreme diversification of construction technologies. Therefore, existing masonry buildings have not only different aesthetic qualities, but also different mechanical properties and durability characteristics.

Focusing on masonry structures made with stone blocks, they can be roughly classified into two groups:

- perfectly regular square stone masonry, that generally characterizes monumental buildings, made up of blocks of regular shape and size (Fig. 3.4a);
- irregular square shape stone masonry, that generally characterizes common residential buildings and is made up of blocks of more or less refined size and geometry and possibly with very chaotic textures (Fig. 3.4b,c).

If the mortar is not present, the walls are defined as dry stack masonry walls (Fig. 3.4d).

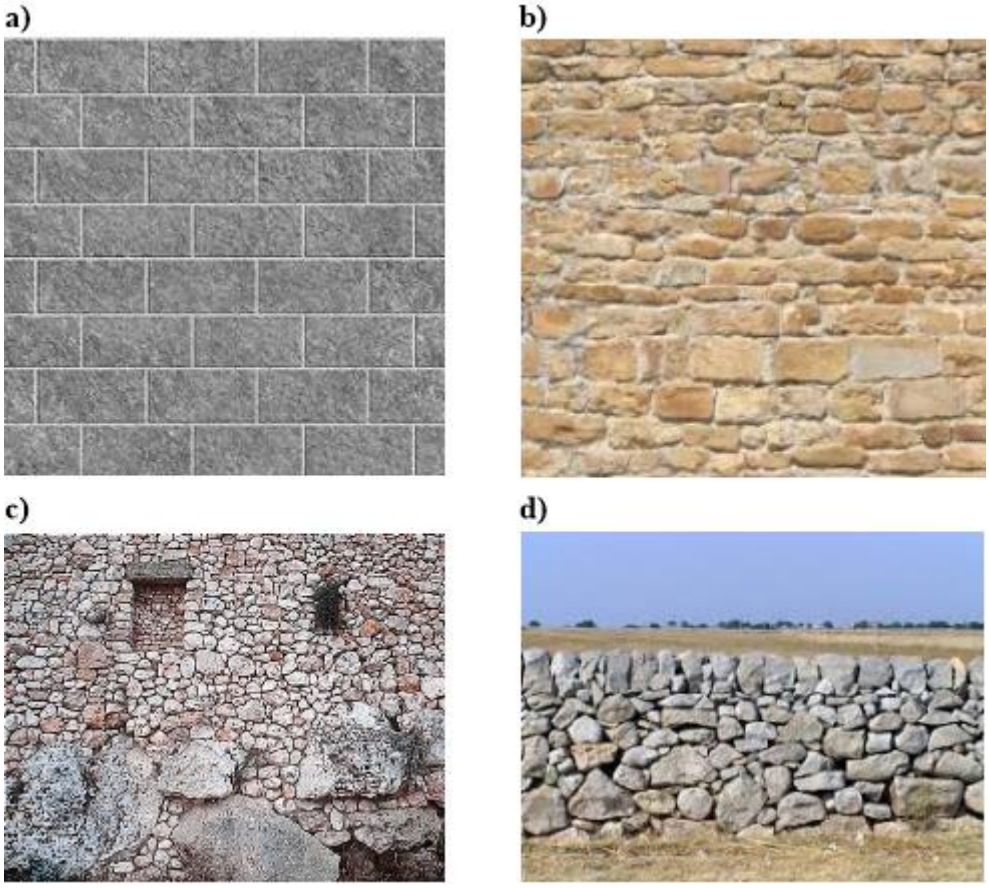

Fig. 3. 4 – Different stone masonry types: a) perfectly regular square units, b) irregular square units, c) rubble and d) dry stack masonry walls.

Hence, the walls can be built in various ways, depending on the degree of handmade refinement of the blocks. Moreover, the walls are often formed by a multi-leaf structure characterized by two outer stone layers that encase the internal loose material infill (Fig. 3.5). In this regard, it is very important that the connection between the double-leaf is guaranteed through some joints which enable to form a solid wall, whose faces work together.

Fig. 3. 5 – Multi-leaf masonry wall.

The mortar is the connecting element between the brick/stone blocks. The ingredients that make up mortar can be distinguished according to the age of construction: in the historic masonry, the mortar is generally characterized by a composition of sand, lime and water. Although it usually occupies only around 7% of the volume of the entire texture, its influence on the global behaviour of the structure goes beyond this simple percentage. In fact, in addition to the connection function, mortar also has the task of distributing the stresses between the blocks. Consequently, the accuracy of its layout is very important to allow a perfect adhesion between mortar and masonry unit, so that local stresses are avoided in order to prevent the breakdown of the unit itself.
In a masonry consisting of regular units, mortar is generally arranged according to two types of joints: continuous horizontals and discontinuous verticals. Both act as planes of weakness within the structure, thus giving to masonry material distinct directional properties. In particular, the horizontal joints represent potentially sliding planes; conversely, the staggered arrangement which characterizes the vertical direction gives rise to an interlocking effect among the units which enhance the overall material strength along this direction. For this reason, even if masonry is composed of two isotropic materials, as a whole it exhibits an orthotropic behaviour, i.e. a different mechanical response according to the two orthogonal directions given by the mortar joints (Fig. 3.6).

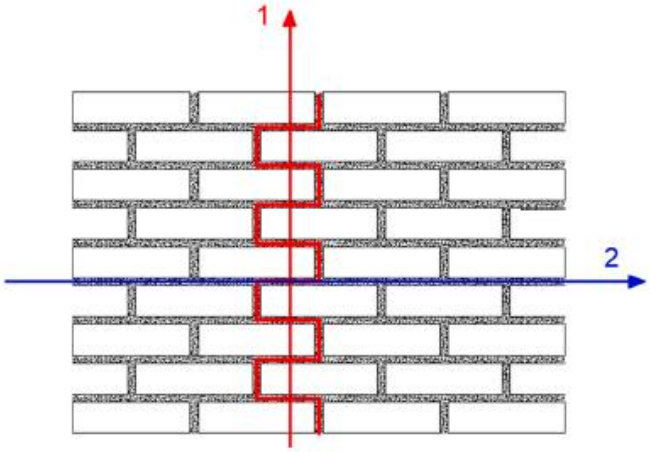

Fig. 3. 6 - Arrangement of the vertical (direction 1) and horizontal (direction 2) mortar joints in a regular texture masonry assembly (modified from Lasciarrea at al. 2019).

The determination of the global mechanical properties of masonry is one of the most studied aspects: this composite material, in fact, has no intermediate characteristics with respect to those of its components. As reported in Binda et al. (1994), the overall resistance of the whole brick-mortar assembly is lower than the dry brick alone, but greater than the resistance offered by a pure mortar prism specimen (Fig. 3.7).

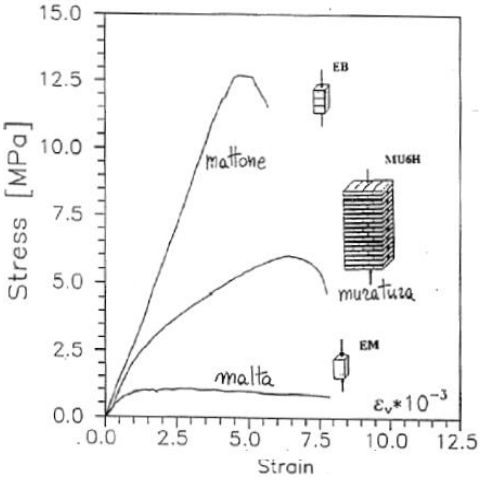

Fig. 3. 7 - Compressive stress-strain curve obtained from the bricks assembly (EB), the pure mortar prism specimen (EM) and the whole brick-mortar assembly (MU6H) according to Binda et al. (1994).

To explain this phenomenon, it is necessary to understand what kind of interactions occur between masonry units and mortar. Since the mortar and the units have a different deformability due to their different stiffness, a stress state is created inside the masonry which sees biaxial traction and uniaxial compression in the load direction for the unit and triaxial compression for the mortar joint (Fig. 3.8).

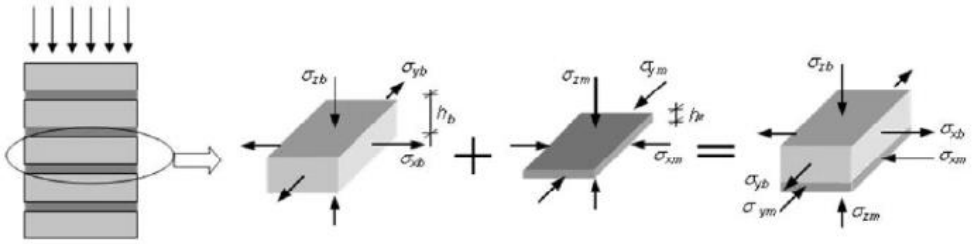

Fig. 3. 8 - Compressive stress state induced in the brick-mortar assembly (from Monti Di Sopra 2009).

For this reason, the global stress-deformation curve does not have intermediate characteristics with respect to those of its components, showing a fragile non-linear behaviour.

Moreover, masonry is characterized by a very low tensile strength (generally roughly evaluated around $1/10 \div 1/20$ of the compressive peak resistance), often completely neglected, which makes its mechanical response also asymmetric depending on the load type (Fig. 3.9).

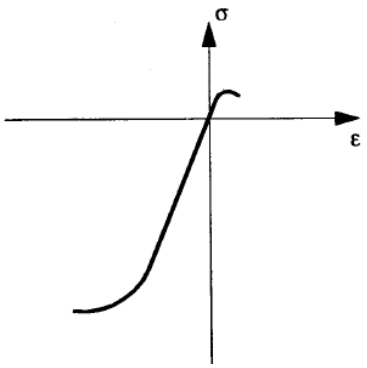

Fig. 3. 9 – Asymmetric mechanical response of masonry in compression and tension state (from Olivito 2003).

All these aspects contribute to determine the global response of the unit-mortar assembly and, hence, its different failure mechanisms. In particular, five failure modes can be recognized:

- Mode I: it is the tensile failure of mortar joints associated with the so-called first mode fracture energy (G_f^I), defined as the amount of energy needed to create a crack of unit area along the mortar-unit interface carrying out an uniaxial tensile test such as those performed by Van der Pluijm (1992) (Fig. 3.10). With this energetic approach it is possible to describe the masonry tensile softening behaviour. The results of Van der Pluijm tests showed that the G_f^I ranges between 0.005 and 0.02 Nmm/mm^2 for tensile strength values between 0.3 and 0.9 N/mm^2, depending on the different unit-mortar combinations.

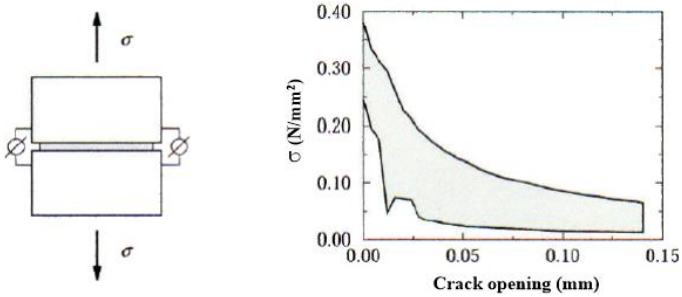

Fig. 3. 10 – Experimental test apparatus and stress-crack opening curve for Mode I mechanism (modified from Monti Di Sopra 2009).

- Mode II: it is the failure mode representative of the sliding along the horizontal mortar joints due to shear stress with limited normal precompression levels. Also in this case, the failure mode concerns only the joints as often occurs in masonry structures. It is possible to associate to this mechanism the second mode fracture energy (G_f^{II}), which can be obtained from the area beneath the experimental shear stress-displacement curve at different normal compression levels by carrying out a test such as those performed by Van der Pluijm

(1993) (Fig. 3.11). According to the results obtained by Van der Pluijm, the G_f^{II} values are between 0.01 and 0.25 Nmm/mm^2 with respect to an initial cohesion that oscillates between 0.1 and 1.8 N/mm^2, also in relation to the degree of confinement of the material.

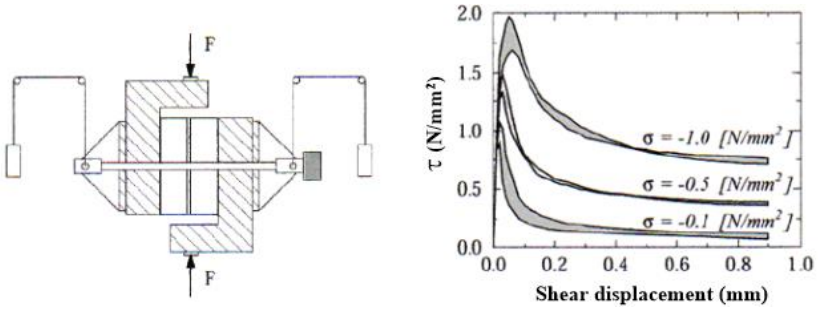

Fig. 3. 11– Experimental test apparatus and stress-displacement curve for Mode II mechanism (modified from Monti Di Sopra 2009).

- Mode III: blocks are broken by tension parallel to the direction of the horizontal mortar joints (Fig. 3.12). Two possible collapses can happen: i) cracks run in a zigzag shape between the vertical and horizontal joints or ii) a vertical crack crosses the unit in continuation with the vertical joints. In the first case the response of the specimen is controlled by the G_f^I of the vertical joints and by the G_f^{II} of the horizontal joints, while in the second case the response is controlled by the fracture energy of the units and vertical joints.

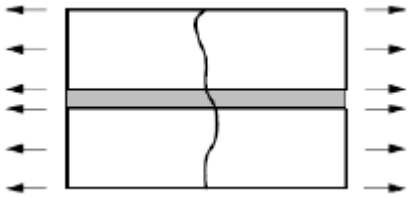

Fig. 3. 12 – Mode III mechanism (from Monti Di Sopra 2009).

- Mode IV: it consists in the failure of the blocks due to shear action when the normal compression acting on the horizontal mortar joints is able to prevent them from sliding, generating a high friction state in the joints. It is the alternative to mode II failure when the confinement pressure values are higher (Fig. 3.13).

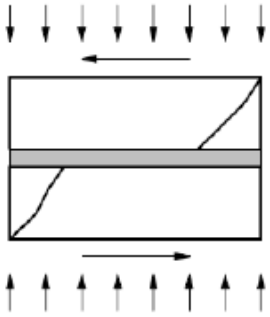

Fig. 3. 13 – Mode IV mechanism (from Monti Di Sopra 2009).

- Mode V: at very high normal compression, beyond the limit of the compressive strength, the blocks break due to splitting, characterized by a series of vertical cracks (Fig. 3.14). Also in this case, it is possible to describe the softening behaviour by means of the compression fracture energy (G_c), which is strongly dependent on the boundary conditions and on the size of the specimens. The G_c values are much higher than the tensile ones, in the order of 45 Nmm/mm^2.

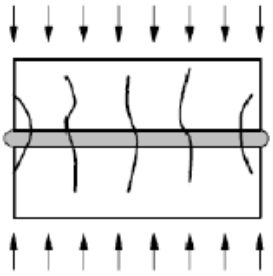

Fig. 3. 14 – Mode III mechanism (from Monti Di Sopra 2009).

It is worth noting that the two most considered mechanisms are modes I and II, since it is the non-linear response of the joints that generally characterizes the masonry overall behaviour. Therefore, it appears of paramount importance having a sufficient knowledge of the main mechanical properties coming from experimental tests. However, depending on the nature of the adopted material, the overall mechanical properties can have a rather wide range of values; thus, it is necessary to deeply know the behaviour of the components in order to evaluate the masonry structure response as a whole. Non-destructive, slightly-destructive or destructive tests can be performed for this purpose. However, the number of tests which can be carried out on an existing structure is often very limited, to minimize the disturbance on the building. Nevertheless, when destructive tests are not performed, which is typical in the engineering practice, the Italian Code NTC2018 provides values of the mechanical properties for different masonry typologies, as reported in Tab. 3.1. Even though they represent just a raw estimation, they can be still used for the structural verifications of a masonry structure.

Tipologia di muratura	f (N/mm²)	τ_0 (N/mm²)	f_{v0} (N/mm²)	E (N/mm²)	G (N/mm²)	w (kN/m³)
	min-max	min-max		min-max	min-max	
Muratura in pietrame disordinata (ciottoli, pietre erratiche e irregolari)	1,0-2,0	0,018-0,032	- -	690-1050	230-350	19
Muratura a conci sbozzati, con paramenti di spessore disomogeneo (*)	2,0	0,035-0,051	- -	1020-1440	340-480	20
Muratura in pietre a spacco con buona tessitura	2,6-3,8	0,056-0,074	- -	1500-1980	500-660	21
Muratura irregolare di pietra tenera (tufo, calcarenite, ecc.,)	1,4-2,2	0,028-0,042	- -	900-1260	300-420	13 ÷ 16(**)
Muratura a conci regolari di pietra tenera (tufo, calcarenite, ecc.,) (**)	2,0-3,2	0,04-0,08	0,10-0,19	1200-1620	400-500	
Muratura a blocchi lapidei squadrati	5,8-8,2	0,09-0,12	0,18-0,28	2400-3300	800-1100	22
Muratura in mattoni pieni e malta di calce (***)	2,6-4,3	0,05-0,13	0,13-0,27	1200-1800	400-600	18
Muratura in mattoni semipieni con malta cementizia (es.: doppio UNI foratura ≤40%)	5,0-8,0	0,08-0,17	0,20-0,36	3500-5600	875-1400	15

Tab. 3. 1 – Reference values of mechanical parameters (minimum and maximum) and mean self-weight for different unreinforced masonry typologies, referred to weak mortar (0.7-1.5 N/mm^2), uncoursed masonry, absent connections between wall leaves, texture following the "rule of the art" in case of regular elements; f_m = masonry mean compressive strength, τ_0 = masonry mean shear

strength; E = mean value of the elastic modulus; G = mean value of the shear modulus; w = mean self-weight of masonry (NTC 2018 – C8.5.3.1, Tab. C8.3.I).

In addition, the values reported in Tab. 3.1 should be corrected with the coefficients in Tab. 3.2, if the investigated masonry presents better characteristics or to evaluate the improvement due to strengthening interventions.

Tipologia di muratura	Stato di fatto			Interventi di consolidamento			
	Malta buona	Ricorsi o listature	Connessione trasversale	Iniezione di miscele leganti (*)	Intonaco armato (**)	Ristilatura armata con connessione dei paramenti (**)	Massimo coefficiente complessivo
Muratura in pietrame disordinata (ciottoli, pietre erratiche e irregolari)	1,5	1,3	1,5	2	2,5	1,6	3,5
Muratura a conci sbozzati, con paramenti di spessore disomogeneo	1,4	1,2	1,5	1,7	2,0	1,5	3,0
Muratura in pietre a spacco con buona tessitura	1,3	1,1	1,3	1,5	1,5	1,4	2,4
Muratura irregolare di pietra tenera (tufo, calcarenite, ecc.,)	1,5	1,2	1,3	1,4	1,7	1,1	2,0
Muratura a conci regolari di pietra tenera (tufo, calcarenite, ecc.,)	1,6	-	1,2	1,2	1,5	1,2	1,8
Muratura a blocchi lapidei squadrati	1,2	-	1,2	1,2	1,2	-	1,4
Muratura in mattoni pieni e malta di calce	(***)	-	1,3 (****)	1,2	1,5	1,2	1,8
Muratura in mattoni semipieni con malta cementizia (es,: doppio UNI foratura ≤40%)	1,2	-	-	-	1,3	-	1,3

Tab. 3. 2 – Maximum corrective coefficients to be applied to the mechanical parameters indicated in Tab. 3.1 in presence of: high-quality mortar, coursed masonry, transversal connections between wall leaves and strengthening interventions (NTC 2018 – C8.5.3.1, Tab. C8.3.II).

Finally, it is also worth reporting that the Eurocode 6 (Section 3.6.1.2) provides a general analytical equation to derive the compressive strength of the masonry as a function of the strength of bricks and mortar (Eq. 3.1):

$$f_k = K f_b^{\alpha} f_m^{\beta} \qquad \text{(Eq. 3.1)}$$

where f_k is the is the masonry compression strength (MPa), K is a coefficient which is function of the masonry texture, f_b is the compressive strength of the units (MPa), f_m is the compressive strength of the mortar (MPa), while α and β are two

tabulated coefficients depending on the units material and mortar composition and thickness.

3.1.2 Numerical modelling approaches for masonry material

From the mechanical point of view, masonry is a non-homogeneous, plastic and anisotropic material, characterized by a very low tensile strength. The structural analysis of masonry buildings is a rather complex problem and numerous strategies have been proposed in the scientific literature, depending on the degree of accuracy required for the analysis and eventually to the necessity of simplification.

A first important classification is related to the adopted modelling scale; indeed, the final goal of the structural analysis might change depending on whether the aim is to investigate the local mortar-unit interactions and the related failure mechanisms or to analyse the overall behaviour of an entire building. According to Lourenço et al. (1995), two different approaches can be adopted to face the problem, namely micro and macro-modelling.

In the micro-modelling approach, units and mortar are separately considered and are represented through continuous elements, with the addition of discontinuous unit-mortar interface elements to describe the interaction between the two materials (Fig. 3.15).

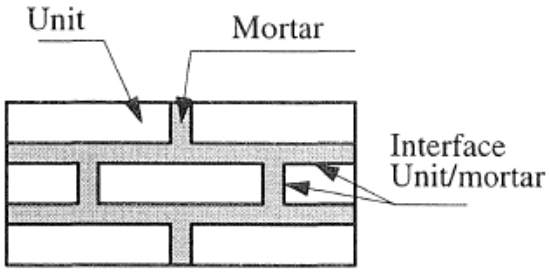

Fig. 3. 15 – Detailed micro-modelling approach (from Lourenço et al. 1995).

Thus, the Young modulus, the Poisson ratio and all the inelastic characteristics are distinctly evaluated for mortar and unit; the interface element represents a potential breaking/sliding plane to which is assigned a fictitious initial stiffness to avoid the in-

terpenetration of the elements. This procedure is conceived to describe the local behaviour of the material, allowing to catch the different abovementioned failure modes resulting from the interaction between units and mortar. Indeed, without detailed micro-modelling, it is not possible to distinctly identify a failure mode and understand what happens locally in a masonry structural element.

Unfortunately, the required computational effort is so high that the use of this modelling technique to analyse large portions of buildings is not easily attainable. For this reason, the simplified micro-modelling approach can be used to extend the analysis to elements of larger dimensions than a simple portion of masonry (Lourenço et al. 1995). In this strategy, the units are considered expanded in such a way not to vary the geometry of the problem and are mutually separated by discontinuous interface elements, whose behaviour is described in terms of relationships between stresses and displacements relative to the two opposite faces of the unit (Fig. 3.16). This is still a discrete modelling formulation, where units are not separated by mortar and interface elements as distinct entities, but they are concentrated in an "average" interface. Consequently, to maintain the geometry unchanged, the units are slightly larger than their actual size. Compared to the detailed approach, the simplified micro-modelling presents a slight but still evident loss of accuracy of the results in favour of lower computational effort.

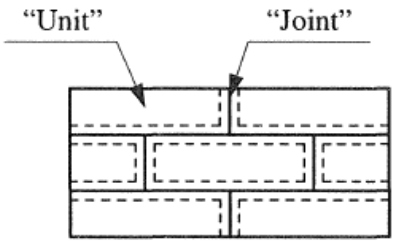

Fig. 3. 16 – Simplified micro-modelling approach (from Lourenço et al. 1995).

The last and more computational efficient strategy consists in the macro-modelling approach, in which the masonry is considered as a single continuous medium having characteristics of homogeneity and anisotropy and the individual components are no

longer distinguishable (Fig. 3.17). Since there is no distinction between mortar and units, the material is idealized as a homogeneous continuum, and the constitutive laws represent the relationship between average stresses and deformations. The resulting computational effort is notably reduced compared to the micro-modelling but, inevitably, the approach pays the price of being less detailed and affected by a higher degree of approximation. Anyway, even if synthetic, this approach represents the necessary compromise between precision and efficiency.

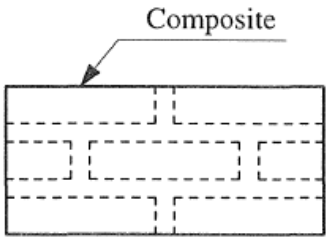

Fig. 3. 17 – Macro-modelling approach (from Lourenço et al. 1995).

A fundamental aspect in the macro-modelling procedure is the homogenization criterion adopted to obtain the final homogenised medium. The first step consists in identifying the so-called Representative Volume Element (RVE), that is the smallest part of the real medium that contains all the required information useful to reproduce the mechanical response of the material. Indeed, this operation exploits the periodic local structure of the masonry texture that, in principle, should enable to substitute the non-homogeneous material with the 'equivalent' homogeneous RVE (Fig. 3.18). The situation becomes more difficult when dealing with non-periodic and rubble masonry textures, as the RVE identification might not be an easy task, even if also in this case there are some available solutions (Gesualdo & Nunziante 2005).

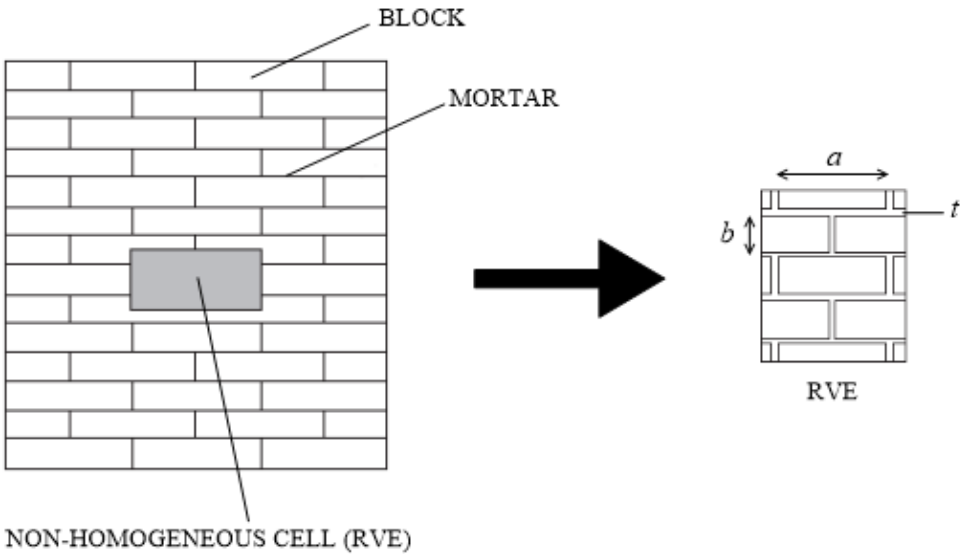

Fig. 3. 18 – Definition of the representative volume element (RVE).

Starting from Pande et al. (1989), several strategies have been proposed in the scientific literature to evaluate the equivalent medium mechanical properties, especially in the elastic range (Lourenço et al. 2007; de Felice et al. 2010; Taliercio 2014; Di Nino & Luongo 2019). Basically, the fundamental concept consists in modelling the behaviour of a masonry cell using suitable designed assemblies of in-series and in-parallel springs. Thereafter, an equivalent homogeneous and orthotropic material is defined so that it has the same stiffness of the original non-homogeneous assembly (Fig. 3.19). A further simplifying step might be passing to an equivalent isotropic medium in order to reduce the number of parameters required to perform the analysis (Di Nino & Luongo 2019).

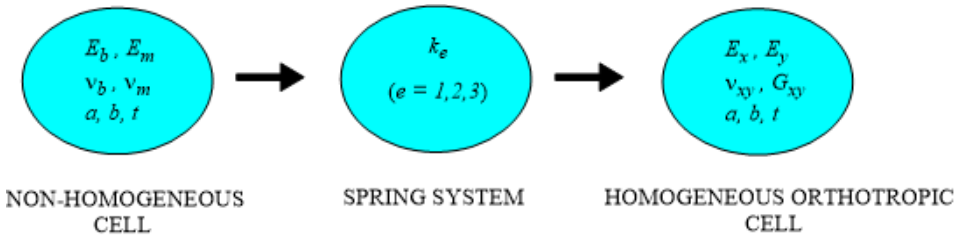

Fig. 3. 19 – Flowchart for the definition of the homogenization procedure.

3.2. The constitutive model for masonry: the Concrete Damage Plasticity model

3.2.1 Basic concepts of the plastic-damage theory

Several possibilities to model masonry material are available in the scientific literature which mainly differ in the description of the post-elastic branch. Indeed, the constitutive models can be subdivided into two main groups: plasticity models (Fig. 3.20a) and damage models (Fig. 3.20b).

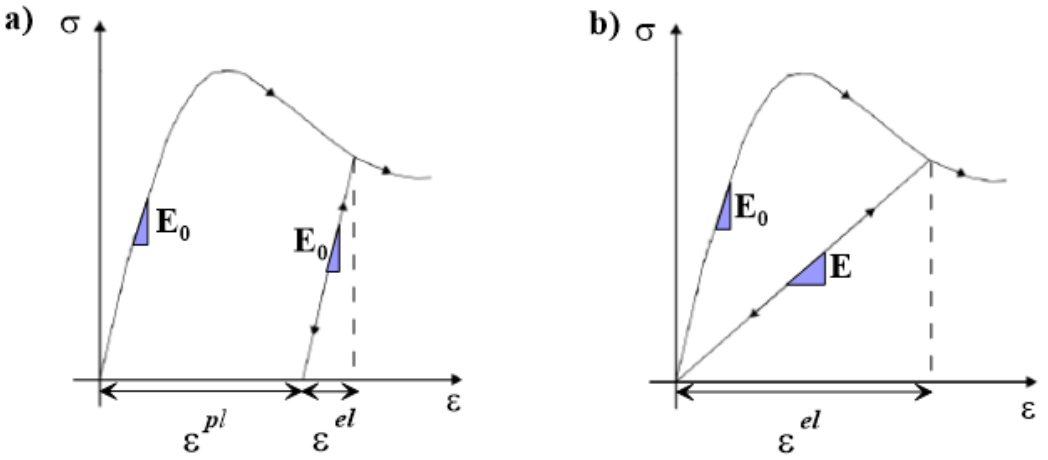

Fig. 3. 20 – a) Plasticity and b) damage models.

The plasticity theory assumes that the material has a strength limit beyond which permanent deformations are generated. The total deformation is thus composed of a reversible elastic contribution (ε^{el}) and an irreversible inelastic one (ε^{pl}), as shown in Fig. 3.20a.

In this case the elastic stiffness does not undergo modifications during the loading history and stays as the initial one (E_0); conversely, the plastic deformation process depends on the load path and not only on the value of the applied stress because of its dissipative nature, thus implying no one-to-one correspondence between stress and plastic deformation. Therefore, the relationship that link stresses and strains must

be written in incremental or differential form. Once the yield point is reached, i.e. the value for which plastic strains start to develop, the stress-strain relationship is usually modelled with a hardening, softening or perfectly plastic branch.

On the other hand, damage mechanics is a tool, like fracture mechanics, for studying the progressive degradation processes that develop in the materials due to mechanical, thermal or even chemical actions. Both fracture and damage mechanics aim to estimate the effect of damage processes (which consist in the formation, propagation and coalescence of micro-defects) on the macroscopic material response.

Fracture mechanics analyses the influence of the cracks propagation considered as discontinuities in the intact material, hence removing the hypothesis of continuity of the medium.

Starting from the hypothesis of continuity, damage mechanics, whose genesis is usually identified with the work by Kachanov (1958), studies the effect of the discontinuities of the microstructure on the selected RVE and, as a consequence, it is based on variables defined as averages on the considered volume.

Although the degradation processes are the consequence of what occurs at the microscopic scale, damage at a macroscopic level can manifest itself in various ways depending on the nature of the material and on the loading type; in particular, in brittle materials like masonry damage occurs in a locally restricted area of the medium.

A fundamental ingredient to define a damage model consists in selecting a continuous damage variable able to describe the degradation effect produced by the presence of micro-defects in the material. This variable represents a quantitative measure of the quantities that describe, at a macroscopic level, the degradation of the continuous medium.

Considering the RVE depicted in Fig. 3.21, the damage variable D at point M located on the plane with normal $\boldsymbol{n}$ is defined by the following expression:

$$D(M,\boldsymbol{n}) = \lim_{A \to 0} \frac{A_D}{A} \qquad \text{(Eq. 3.2)}$$

where A indicates the area with normal $\boldsymbol{n}$, while A_D is the area occupied by micro-defects in the section itself.

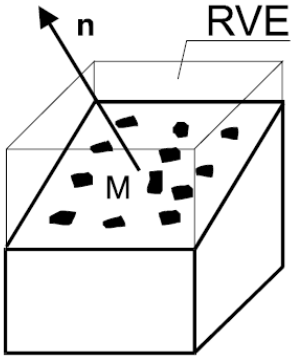

Fig. 3. 21 – Definition of the scalar damage variable in the RVE.

Assuming an isotropic distribution of the damage in the considered medium, there is no dependence of D from the normal $\boldsymbol{n}$. In this case, the continuous damage variable D is only a function of the material point and can be interpreted as the surface density of the micro-defects. The values that D can assume are subjected to physical limits and can vary in the range $0 \div 1$. In particular:

- $D = 0$ when the material is intact;
- $D = 1$ when the material is completely damaged.

Fig. 3.22 shows a uniaxial tensile test.

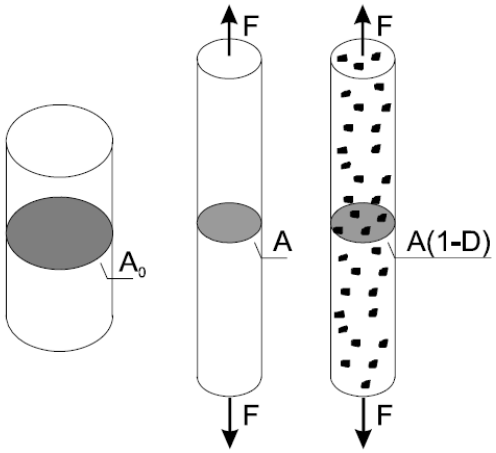

Fig. 3. 22 – Uniaxial tensile test.

The resistant section of the specimen is reduced as the stress increases both due to the transverse contraction and the longitudinal elongation of the specimen, both due to the genesis and growth of micro-defects in the material. Indicating with A_0 the area of the initial cross section before applying the load and with A the reduced area due to the transverse contraction of the specimen, the nominal stress σ_0 and the actual stress σ are respectively given by the following expressions:

$$\sigma_0 = \frac{F}{A_0} \qquad \text{(Eq. 3.3)}$$

$$\sigma = \frac{F}{A} \qquad \text{(Eq. 3.4)}$$

The effective stress $\bar{\sigma}$ is defined as the stress acting on the effectively resistant area and $\bar{A}$, defined as:

$$\bar{A} = A(1-D) \qquad \text{(Eq. 3.5)}$$

where D is the scalar damage variable previously introduced. The parameter $\bar{A}$ is equal to A when the material is intact (D=0) and can reduce to zero when the damage is completely widespread (D=1). Therefore, the effective stress $\bar{\sigma}$ defined on the basis of $\bar{A}$ is:

$$\bar{\sigma} = \frac{F}{\bar{A}} = \frac{F}{A(1-D)} = \frac{\sigma}{(1-D)} \qquad \text{(Eq. 3.6)}$$

The extension to the multiaxial case is immediate in the hypothesis of isotropy and the same area $\bar{A}$ reacts both in tension and compression. Thus, the effective stress tensor can be defined as:

$$\bar{\boldsymbol{\sigma}} = \frac{\boldsymbol{\sigma}}{(1-D)} \qquad \text{(Eq. 3.7)}$$

As a matter of fact, plasticity and damage mechanics are absolutely complementary. Indeed, the stiffness degradation is neglected by plastic theories, while permanent deformations are not considered within damage mechanics.

Hence, in this context a third class of models, known as plastic-damage models, are developed to combine the two theories in a single framework, able to take into ac-

count both the irreversible contributions due to plastic deformations and those related to the damage processes occurring in the material (Fig. 3.23).

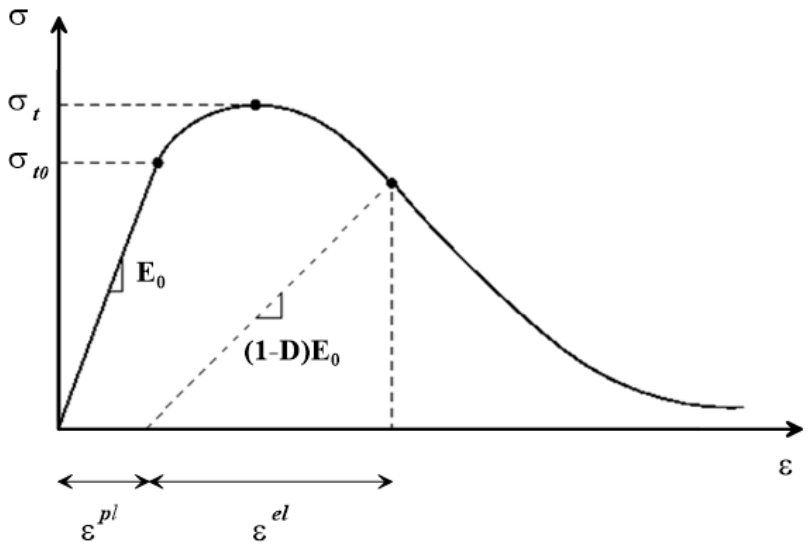

Fig. 3. 23 – Stress-strain curve for the plastic-damage model

Plastic-damage models are particularly suitable for cyclic dynamic analysis, where frequent alternative passages from compression to tension occur. In the next section, the selected plastic-damage model adopted in this work to reproduce the masonry mechanical behaviour is presented.

3.2.2 The Concrete Damage Plasticity model

The constitutive model adopted for describing the masonry behaviour in this thesis is the Concrete Damage Plasticity model (CDP) (Lubliner et al. 1989; Lee & Fenves 1998), available in the material model library of the computer code Abaqus (2014). It is part of the plastic-damage model class whose features have been discussed in the previous section.

Although CDP is originally conceived for isotropic fragile materials, such as concrete, the model has been adapted and successfully used in a wide number of masonry ap-

plications (Acito et al. 2014; Karimi et al. 2016; Tiberti et al. 2016; Castellazzi et al. 2018).

The model accounts for:

- Plastic-damage theory formulation;
- Isotropic behaviour;
- Asymmetrical material response, which allows to differently model tensile and compression behaviour;
- Stiffness recovery (unilateral effect) during cyclic/dynamic loading.

One of the main concerns about the use of the model could be related to the isotropic response, as it is well-known that masonry exhibits orthotropy. Nevertheless, it is rather difficult to evaluate the necessary anisotropic parameters in absence of ad-hoc experimental campaigns and, moreover, an orthotropic formulation would inevitably burden the computational algorithm. For these reasons, the use of isotropic models is usually accepted in the scientific community, as long as an adaptation of the mechanical properties to fit an average behaviour between vertical and horizontal compression is considered (Valente & Milani 2016).

The model accounts for scalar isotropic damage with distinct damage parameters in tension and in compression. Therefore, it is particularly suitable for masonry behaviour since this material exhibits asymmetry in terms of both damage and strength in tension and compression, especially in loading-unloading conditions such those occurring during seismic events. Consequently, a different behaviour in tension and compression can be introduced, as shown in Fig. 3.24.

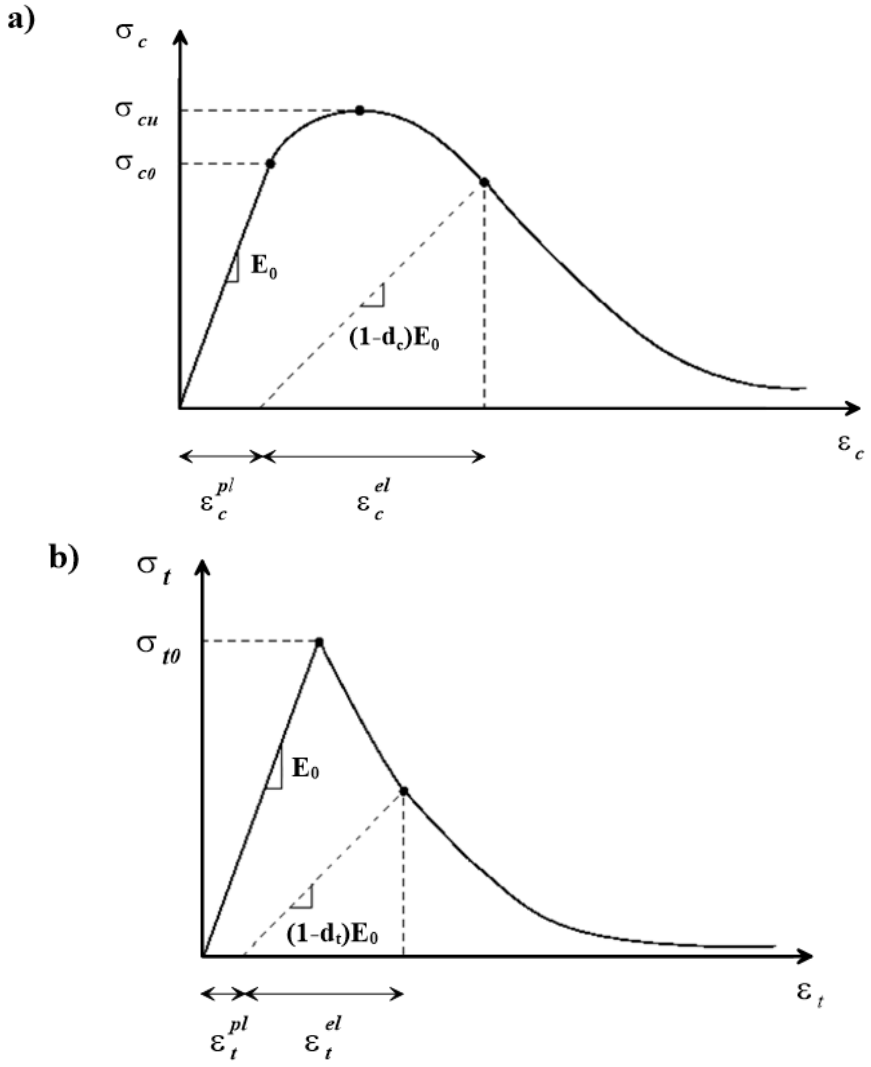

Fig. 3. 24 – CDP model response for monoaxial compression (a) and tension (b) loading.

The compression and tensile stresses σ_c and σ_t are derived through the following relationships:

$$\sigma_c = (1-d_c) E_0 \left(\varepsilon_c - \varepsilon_c^{pl}\right) \quad \text{(Eq. 3.8)}$$

$$\sigma_t = (1-d_t) E_0 \left(\varepsilon_t - \varepsilon_t^{pl}\right) \quad \text{(Eq. 3.9)}$$

where E_0 is the initial undamaged elastic modulus, d_c and d_t are the damage variables which are function of the deformation state, ε_c and ε_t are the total strains, ε_c^{pl} and ε_t^{pl} are the equivalent plastic strains; subindexes c and t refer to compression and tension, respectively.

For uniaxial cyclic loading-unloading conditions, the damage plasticity model assumes that the degradation of the elastic stiffness is given by:

$$E = (1-d)E_0 \qquad \text{(Eq. 3.10)}$$

where E is the reduced tangent stiffness and d is a scalar degradation variable, which is a function of the stress state and of the compression and tension damage variables (d_c and d_t, respectively):

$$(1-d) = (1-s_t d_c)(1-s_c d_t) \qquad \text{(Eq. 3.11)}$$

where s_c and s_t are dimensionless coefficients accounting for stress state and stiffness recovery effects, being given by:

$$s_c = 1 - w_c(1 - r^*(\sigma_{11})) \qquad \text{(Eq. 3.12)}$$

$$s_t = 1 - w_t r^*(\sigma_{11}) \qquad \text{(Eq. 3.13)}$$

In Equations (3.12) and (3.13), σ_{11} is the first principal uniaxial stress (positive for tension), r^* is a stress state parameter being $r^*(\sigma_{11}) = 1$ for tension and $r^*(\sigma_{11}) = 0$ for compression, and w_c and w_t are weighting factors ranging between 0 and 1. The factors w_c and w_t account for stiffness recovery effects. Usually, since the transition from the compressive state to the tensile one (but not the vice-versa) implies a quick reopening of the cracks that had already generated during the previous cycle (unilateral effect), w_c is set close or equal to 1, while w_t is set equal to 0.

Equations (3.12) and (3.13) show that s_c and s_t also range between 0 and 1. For a better understanding of the effect of s_c and s_t coefficients, Fig. 3.25 illustrates the uniaxial stress-strain loading-unloading curves. The initial elastic branch with slope E_0 reaches the descending branch at the peak point 1 and then cracking begins; later, unloading starts at point 2. At this point, there is no compression damage and

$d_c = 0$, $r^* = 1$, and $s_c = 1$; therefore, Equation (3.11) shows that $d = d_t$. Consequently, the linear unloading branch has slope $(1-d_t)E_0$. In the way to the stress reversing point 3, cracks begin to close. After point 3, $r^* = 0$, $s_c = 1 - w_c$, $s_t = 1$, $d_c = 0$, and Equation (3.11) shows that $d = (1-w_c)d_t$. Therefore, the slope of the ongoing compression segment of the branch depends on the parameter w_c.

In this regard, three options are plotted in Fig. 3.25:

- $w_c = 0$ (no crack is closed) with slope $(1-d_t)E_0$;
- $w_c = 0.5$ (half of the cracks are closed) with slope $(1-0.5d_t)E_0$;
- $w_c = 1$ (all cracks are closed) with slope E_0.

In the third option ($w_c = 1$) there is no compressive strength reduction. At point 4, an unloading branch starts; here, $r^* = 0$, $s_c = 1 - w_c$, $s_t = 1$ and Equation (3.11) shows that $(1-d) = (1-d_c)\left[1-(1-w_c)d_t\right] = (1-d_c)$. Point 5 corresponds again to a stress reversal; after it, assuming that $w_t = 0$, the slope of the ongoing branch is equal to $(1-d_t)(1-d_c)E_0$. Point 6 is the peak for the reduced tensile strength; after it, cracking reinitiates and a new descending branch is generated.

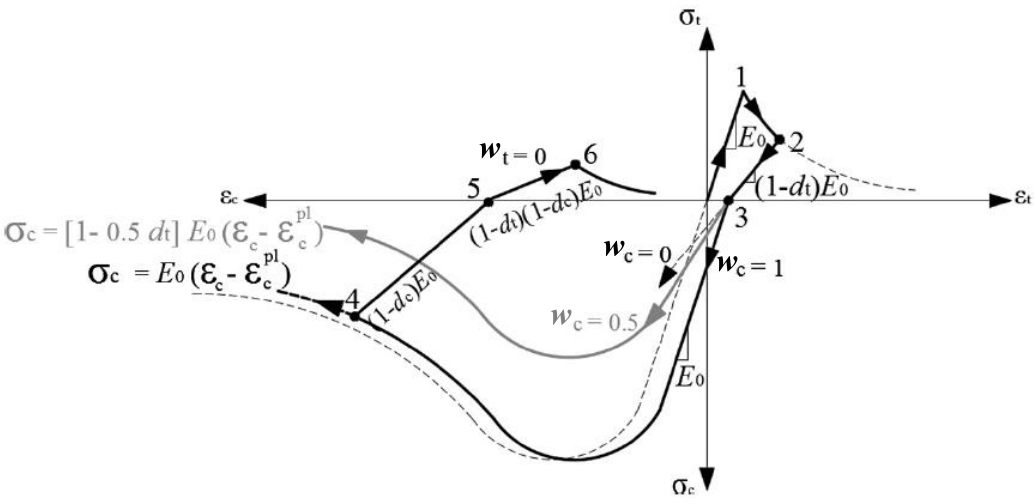

Fig. 3. 25 – CDP model uniaxial loading-unloading response (modified from Alfarah et al. 2017).

For multiaxial conditions, the stress-strain relationship is given by:

$$\boldsymbol{\sigma} = (1-d)\boldsymbol{D}_{\mathbf{0}}^{el} : (\boldsymbol{\varepsilon} - \boldsymbol{\varepsilon}^{pl}) \qquad \text{(Eq. 3.14)}$$

where $\boldsymbol{D}_{\mathbf{0}}^{el}$ is the elastic stiffness tensor and $\boldsymbol{\sigma}$ and $\boldsymbol{\varepsilon}$ are the stress and strain tensors, respectively. The scalar damage variable d keeps the same meaning as for uniaxial condition, although replacing the scalar factor r^* with a multiaxial one (Lee & Fenves 1998).

The yield condition is based on the function F proposed by Lubliner et al. (1989) with the subsequent modifications suggested by Lee & Fenves (1998) to account for different tension and compression strength evolution:

$$F = \frac{1}{1-\alpha}(q - 3\alpha p + \beta\langle\sigma_{\max}\rangle - \gamma - \langle\sigma_{\max}\rangle) - \overline{\sigma_c} = 0 \qquad \text{(Eq. 3.15)}$$

$$\alpha = \frac{(f_{b0}/f_{c0})-1}{2(f_{b0}/f_{c0})-1}; \qquad \beta = \frac{\overline{\sigma_c}}{\overline{\sigma_t}}(1-\alpha) - (1+\alpha); \qquad \gamma = \frac{3(1-K_C)}{2K_C - 1} \qquad \text{(Eq. 3.16)}$$

In Equations (3.15) and (3.16), $\langle\bullet\rangle$ is the Macaulay bracket, p is the hydrostatic pressure, q is the Von Mises-equivalent effective stress (where the effective stress is the stress divided by $(1-d)$), and f_{b0} and f_{c0} are the biaxial and uniaxial compressive yield strengths, respectively; since $f_{b0} \geq f_{c0}$, α ranges between 0 ($f_{b0} = f_{c0}$) and 0.5 ($f_{b0} \gg f_{c0}$).

The maximum principal effective stress is $\sigma_{\max}$, and $\overline{\sigma_c}$ and $\overline{\sigma_t}$ are the effective compressive and tensile cohesion stress, respectively. $\overline{\sigma_c}$ and $\overline{\sigma_t}$ are defined as $\overline{\sigma_c} = \sigma_c/(1-d_c)$ and $\overline{\sigma_t} = \sigma_t/(1-d_t)$; K_C is the ratio of second stress invariants on tensile and compressive meridians.

The shape of the yield surface in a plane stress state is reported in Fig. 3.26.

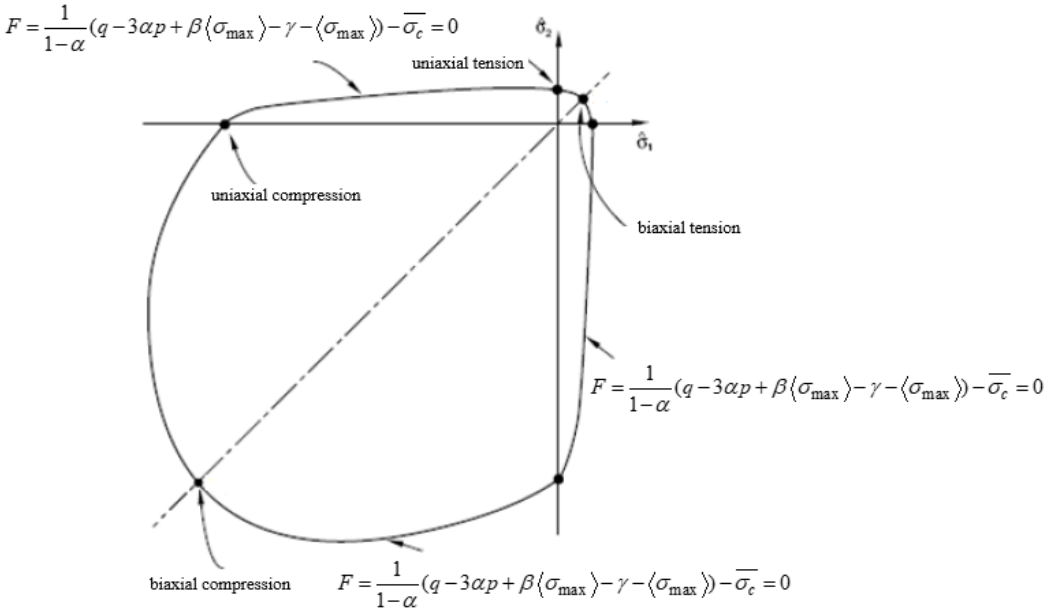

Fig. 3. 26 – CDP model yield surface in plane stress.

The plasticity model assumes a non-associated potential plastic flow rule:

$$\dot{\varepsilon}^{pl} = \dot{\lambda}\frac{\partial G(\overline{\sigma})}{\partial(\overline{\sigma})} \qquad \text{(Eq. 3.17)}$$

where $\dot{\varepsilon}^{pl}$ is the plastic strain rate vector and $\overline{\sigma}$ the stress vector.
The flow potential G is the Drucker-Prager hyperbolic function given by:

$$G = \sqrt{(\xi\sigma_{t0}\tan\psi)^2 + q^2} - p\tan\psi \qquad \text{(Eq. 3.18)}$$

where σ_{t0} is the uniaxial tensile stress at failure, ξ is the eccentricity of the plastic potential surface that defines the rate at which the function approaches the asymptote (the flow potential tends to a straight line as the eccentricity tends to zero), and ψ is the dilatancy angle measured in the $p-q$ deviatoric plane at high confining pressure. As previously discussed, K_C is the ratio between the magnitudes of deviatoric stress in uniaxial tension and compression; K_C ranges between 0.5 (Rankine yield surface)

and 1 (Von Mises). If one would refer to the Mohr-Coulomb yield surface function (Alfarah et al. 2017), K_C would be written as:

$$K_C = \frac{3-\sin\phi}{3+\sin\phi} \qquad \text{(Eq. 3.19)}$$

where ϕ is the friction angle of the material. It is suggested to use K_C equal to 2/3 for concrete. Nevertheless, in numerous masonry applications the value of K_C is usually kept the same as for concrete (Acito et al., 2014; Valente & Milani 2018; Milani 2019); this is also true for the value of the f_{b0}/f_{c0} ratio usually set equal to 1.16 and for the eccentricity ξ set equal to 0.1.

A sketch of the yield surface in the deviatoric plane for different K_C values is reported in Fig. 3.27.

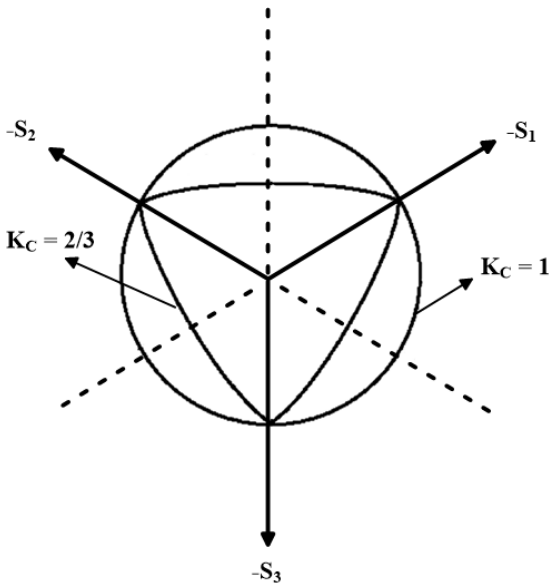

Fig. 3. 27 – CDP model yield surface in the deviatoric plane corresponding to different values of K_C.

The model is integrated using the backward Euler method, generally used for the plasticity models implemented in Abaqus. Moreover, the material models which exhibit softening behaviour and stiffness degradation often lead to severe convergence diffi-

culties. Some of these convergence issues can be overcome by using a visco-plastic regularization of the constitutive equations.

Hence, for the CDP model, Abaqus provides a Duvant-Lions regularization using visco-plasticity, which permits stresses to be outside of the yield surface. According to this strategy, the visco-plastic strain rate tensor, $\dot{\boldsymbol{\varepsilon}}_{\boldsymbol{v}}^{\boldsymbol{pl}}$, is defined as:

$$\dot{\boldsymbol{\varepsilon}}_{\boldsymbol{v}}^{\boldsymbol{pl}} = \frac{1}{\mu}(\boldsymbol{\varepsilon}^{\boldsymbol{pl}} - \boldsymbol{\varepsilon}_{\boldsymbol{v}}^{\boldsymbol{pl}}) \qquad \text{(Eq. 3.20)}$$

where μ is the viscosity parameter, representing the relaxation time of the visco-plastic system and $\boldsymbol{\varepsilon}^{\boldsymbol{pl}}$ is the plastic strain evaluated in the inviscid backbone model. Similarly, a viscous stiffness degradation variable, d_v, is defined for the visco-plastic system as:

$$\dot{d}_v = \frac{1}{\mu}(d - d_v) \qquad \text{(Eq. 3.21)}$$

where d is the degradation variable evaluated in the inviscid backbone model. The stress-strain relation of the visco-plastic model is given as:

$$\boldsymbol{\sigma} = (1 - d_v)\boldsymbol{D}_{\boldsymbol{0}}^{\boldsymbol{el}} : (\boldsymbol{\varepsilon} - \boldsymbol{\varepsilon}_{\boldsymbol{v}}^{\boldsymbol{pl}}) \qquad \text{(Eq. 3.22)}$$

The solution of the visco-plastic system relaxes to that of the inviscid case as $t/\mu \to \infty$, where t represents the time. Using the visco-plastic regularization with a small value for the viscosity parameter (small compared to the characteristic time increment) usually helps to improve the rate of convergence of the model in the softening regime, without compromising the accuracy of the results.

3.2.3 Shear mechanical response of the CDP model

The CDP model parameters refer to uniaxial compression and tensile laws that can be directly set into Abaqus. However, when dealing with seismic actions, it is well known that special attention should be paid to the performance of the model during shear. In this context, the following paragraph is intended to investigate the actual mechanical response of the constitutive model subjected to shear actions.

3.2.3.1 Numerical investigation of the CDP cyclic shear response on a single element specimen

The main purpose of the numerical investigation herein presented is to assess the cyclic shear response predicted by the CDP model. The simulations have been performed on a quadrilateral specimen of 1 m length, discretized with one 2D shell element with four nodes and reduced integration (CPS4R). A sketch of the model is displayed in Fig. 3.28 with the adopted load path. The specimen is perfectly fixed at the base, while on the upper surface the shear condition is applied through a prescribed displacement input in the X direction preventing any other movements.

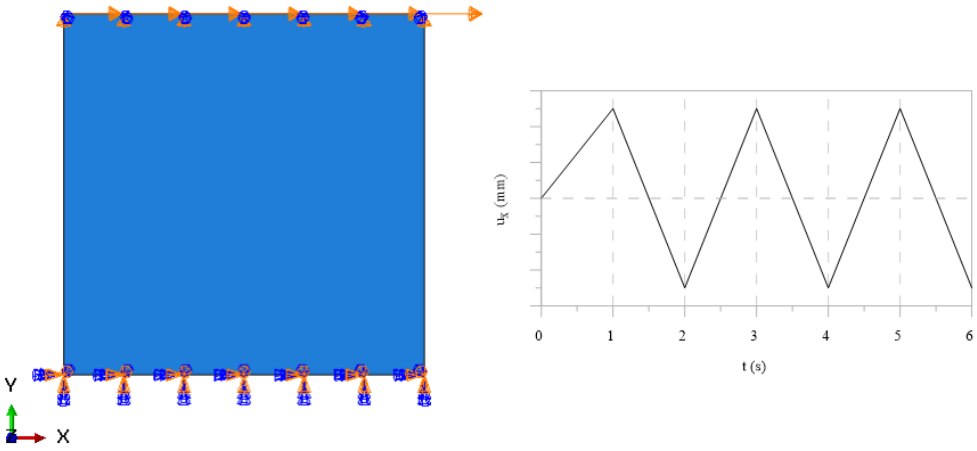

Fig. 3. 28 – Quadrilateral CPS4R element and load path adopted for the cyclic shear tests.

The stress-strain relationships and the damage laws adopted for the compressive and tensile behaviour of the CDP model refer to the study by Zizi et al. (2017) on the cyclic response of brick-cement mortar masonry walls (Figs. 3.29-3.30); the proposed calibration of the CDP parameters is also reported in Tab. 3.3.

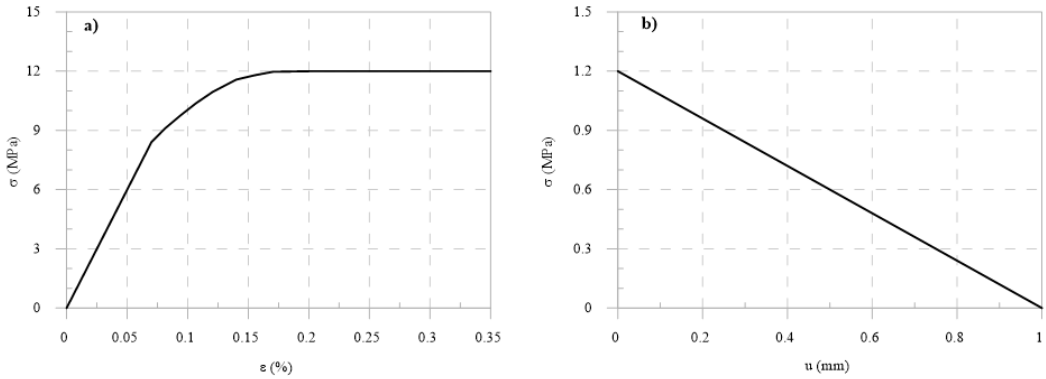

Fig. 3. 29 – Compressive (a) and tensile (b) uniaxial relationships adopted for the cyclic shear tests (Zizi at al. 2017).

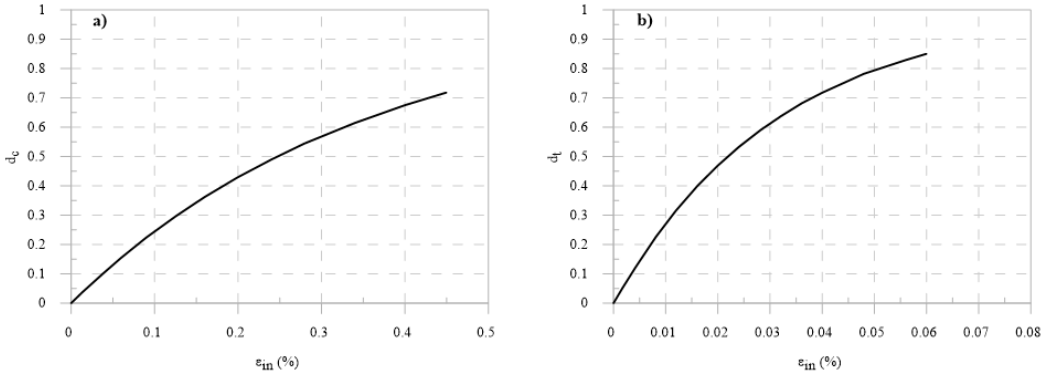

Fig. 3. 30 – Damage relationships adopted in compression (a) and tension (b) for the cyclic shear tests (Zizi at al. 2017).

ψ	w_c	ξ	K_C	f_{b0} / f_{c0}
(°)	(-)	(-)	(-)	(-)
35	0.27	0.1	1	1.16

Tab. 3. 3 – Model parameters adopted for the cyclic shear tests (Zizi et al. 2017).

The first set of analyses has focused on the CDP response at different levels of imposed deformation, adopting increasing displacement amplitudes: 0.1-0.5-1-2-3 mm. The results in terms of force-displacement curves are depicted in Fig. 3.31. For a target displacement equal to 0.1 mm (red curve), the response stays in the elastic range as the action is too weak to activate the non-linear capacities of the model. Converse-

ly, when higher displacement amplitudes are imposed the non-linear response of the model is mobilized. Indeed, starting from the 0.5 mm case (blue curve) the stiffness degradation and energy dissipation due to both plasticity and damage is observed in each simulation. It is also clear that, as the amplitudes keep rising up, these two aspects become increasingly relevant. Moreover, when the 2 and 3 mm target displacement are considered (yellow and magenta curves, respectively), a material strength reduction is also observed, leading to very low residual resistances.

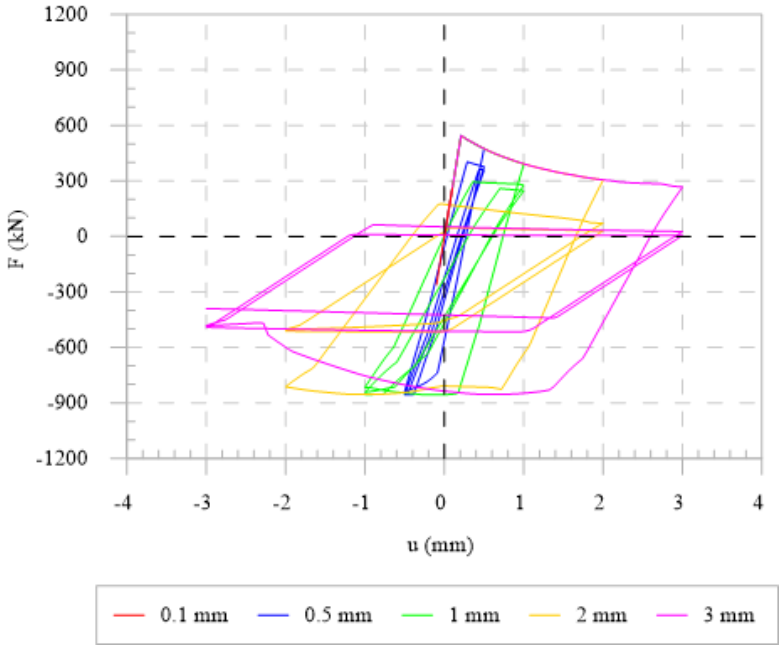

Fig. 3. 31 – Force-displacement curves derived for the different adopted amplitudes using the calibration proposed in Zizi et al. (2017).

Then, the numerical investigation has proceeded with a sensitive analysis concerning the model parameters, varying one by one the corresponding values reported in Tab. 3.3. The results are listed in Figs. 3.32-3.36 in terms of force-displacement curves obtained only for the target displacement equal to 1 mm.

In Fig. 3.32 the influence given by the dilatation angle is inspected in the range 0-50 (it is worth pointing out that it is not possible to set a null value for the dilation angle;

thus, it was approximated to $\psi = 0.01$). The loops suggest a remarkable dependency of the response predicted by the model from this parameter. Indeed, as the dilatancy angle increases, the curves show a progressive stiffer behaviour; meanwhile the material strengths exhibited at -1 mm tend to increase, attaining very significant values for $\psi = 35\text{-}50$ (yellow and magenta curves, respectively).

Hence, the dilation angle enhances the material shear strength, but careful attention should be paid when high values are used, as they can potentially lead to unreliable illimited residual resistance. This is also in agreement with the findings provided by Monti Di Sopra (2009).

A similar trend is observed for the stiffness recovery parameter w_c, as can be observed in Fig. 3.33. Also in this case, as the parameter values increase, the response becomes stiffer and the resistances start to increase because of the recovery effect, which reaches the full recovery for $w_c = 1$.

Conversely, the parametric analyses concerning the effects of the eccentricity ξ (Fig. 3.34), the K_C parameter (Fig. 3.35) and the f_{b0}/f_{c0} ratio (Fig. 3.36) do not highlight any sensitivity of the model from these parameters.

Therefore, the parameters that can significantly affect the cyclic shear response of the model are identified in the dilatancy angle and in the stiffness recovery parameter.

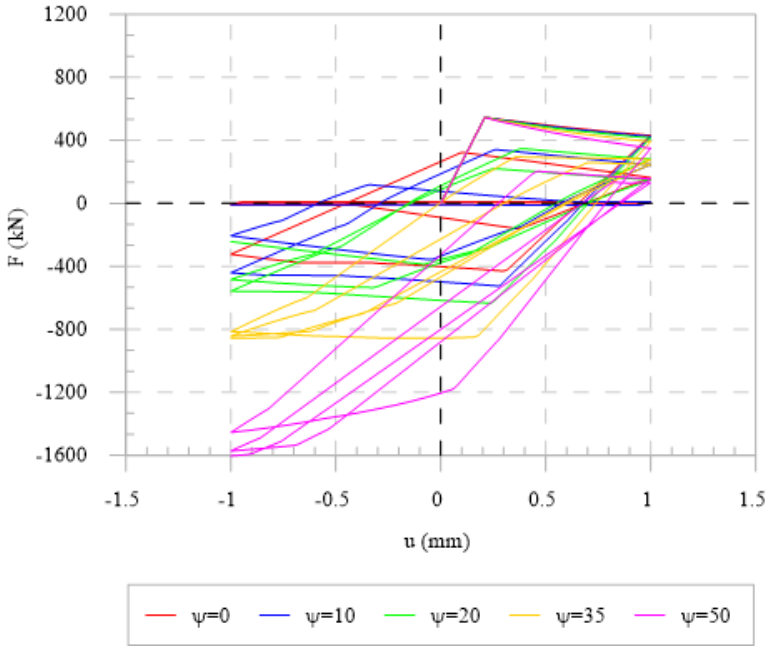

Fig. 3. 32 – Parametric analysis results: influence of ψ .

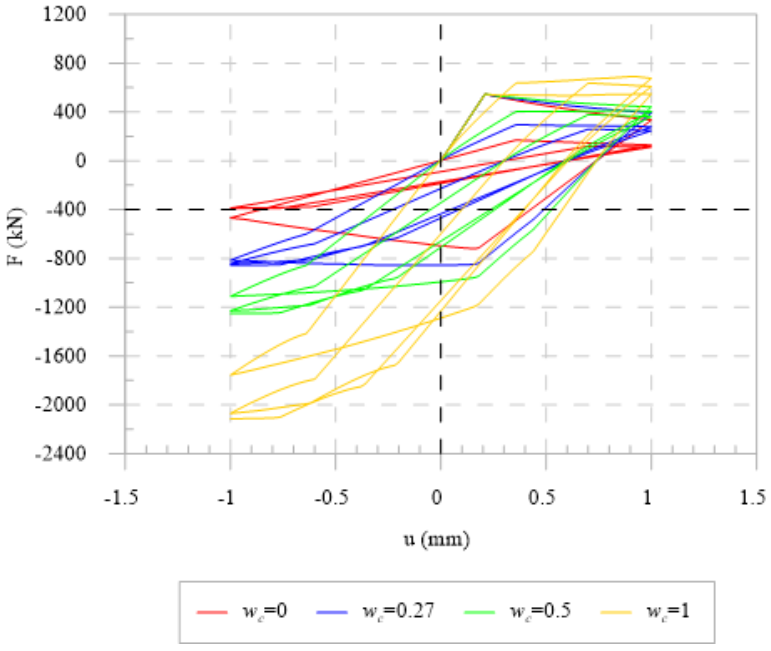

Fig. 3. 33 – Parametric analysis results: influence of w_c .

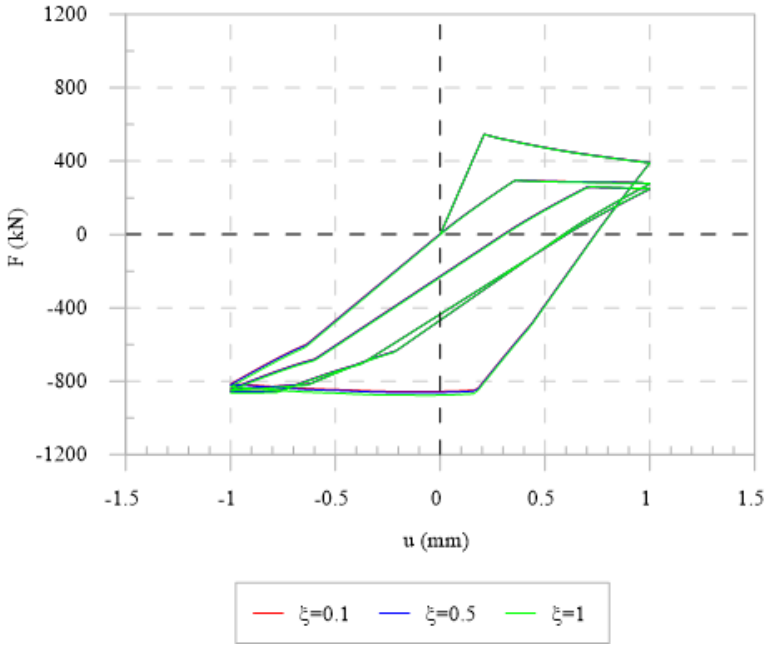

Fig. 3. 34 – Parametric analysis results: influence of ξ .

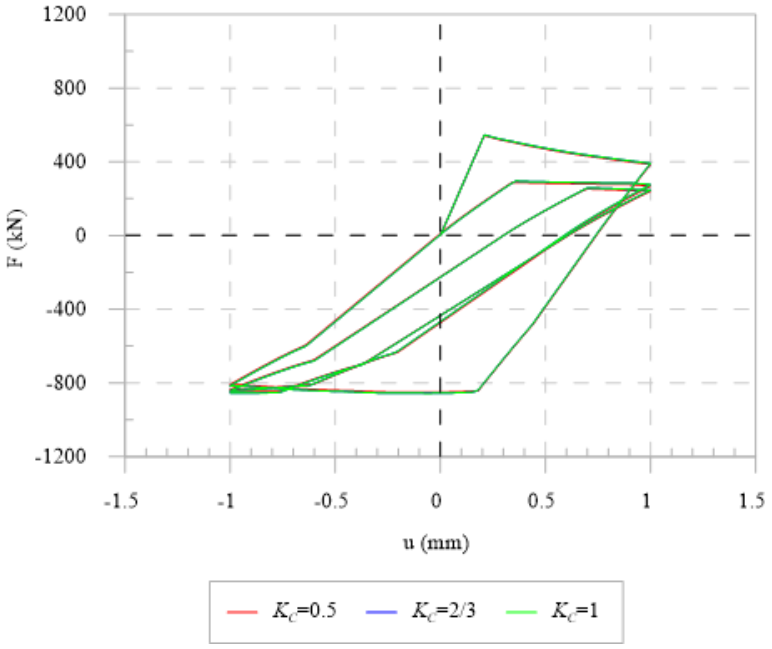

Fig. 3. 35 – Parametric analysis results: influence of K_C .

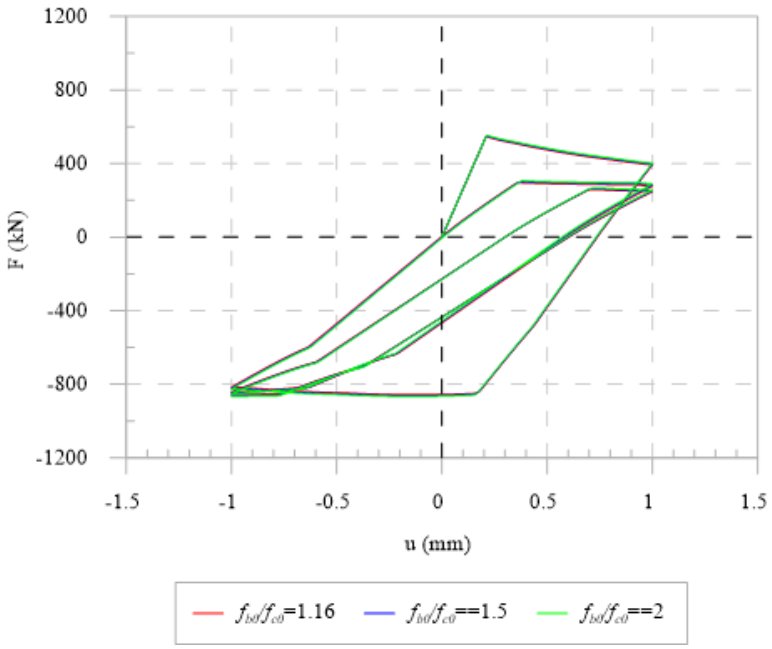

Fig. 3. 36 – Parametric analysis results: influence of f_{b0} / f_{c0}.

3.2.3.2 Shear response of masonry walls

In this section, the capabilities of the CDP model to predict the experimental response with reference to the lateral capacity of masonry walls is presented, taking into account both pushover and cyclic shear tests.

3.2.3.2.1 Pushover tests on masonry walls

The masonry walls herein analysed refer to two walls tested within the experimental campaign reported by Raijmakers & Vermeltfoort (1992). The panels are characterised by a width of 0.99 m, height of 1.00 m and thickness of 0.10 m, as depicted in Fig. 3.37. They are made of wire-cut solid clay bricks with dimensions 210×52×100 mm^3 and 10 mm thick mortar layers.

The first wall (MW1) does not present any irregularity, while the second one (MW2) is characterized by an opening of dimensions 400×235 mm^2, which is also not perfectly centred with respect to the vertical axis of symmetry. The tests were carried out by first applying a uniformly distributed vertical load equal to 300 kPa and then an in-

creasing horizontal displacement precluding any rotation and vertical displacement at the top of the walls up to the collapse.

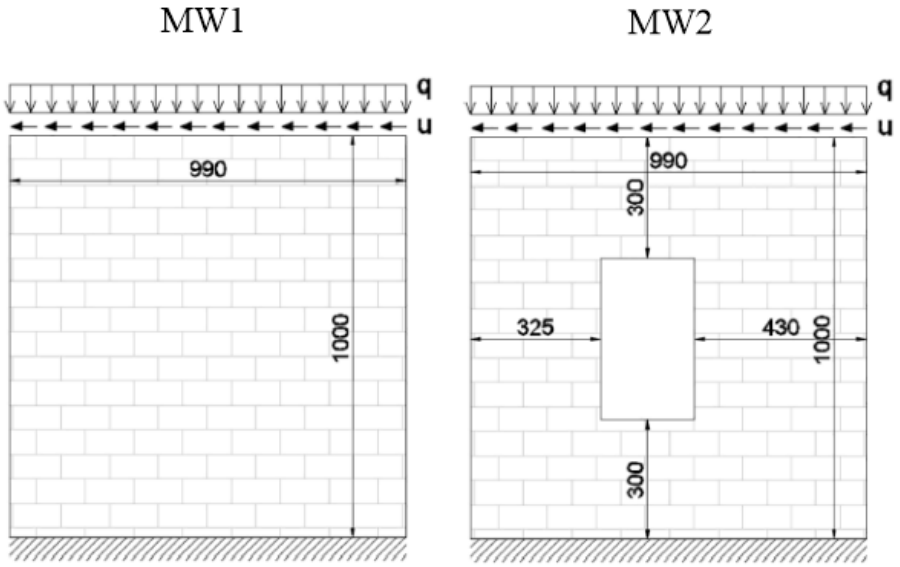

Fig. 3. 37 – Sketch of the MW1 and MW2 (modified from Lasciarrea et al. 2019).

The mechanical properties and most of the numerical parameters adopted for both walls have been derived from Annecchiarico et al. (2010), which already performed a numerical investigation on the MW1 wall, adopting the CDP model, according to an energetic approach for the description of the tensile material behaviour. In addition, the authors mainly focused on a sensitivity analysis on the tensile peak strength and on the mesh size used for the numerical simulations.

Herein, a macro-modelling approach is adopted with an elastic perfectly plastic behaviour in compression, reported in Fig. 3.38a, while a typical brittle material response with a linear softening is considered in tension after that the peak strength is reached, keeping about 10% of the residual resistance, as shown in Fig. 3.38b.

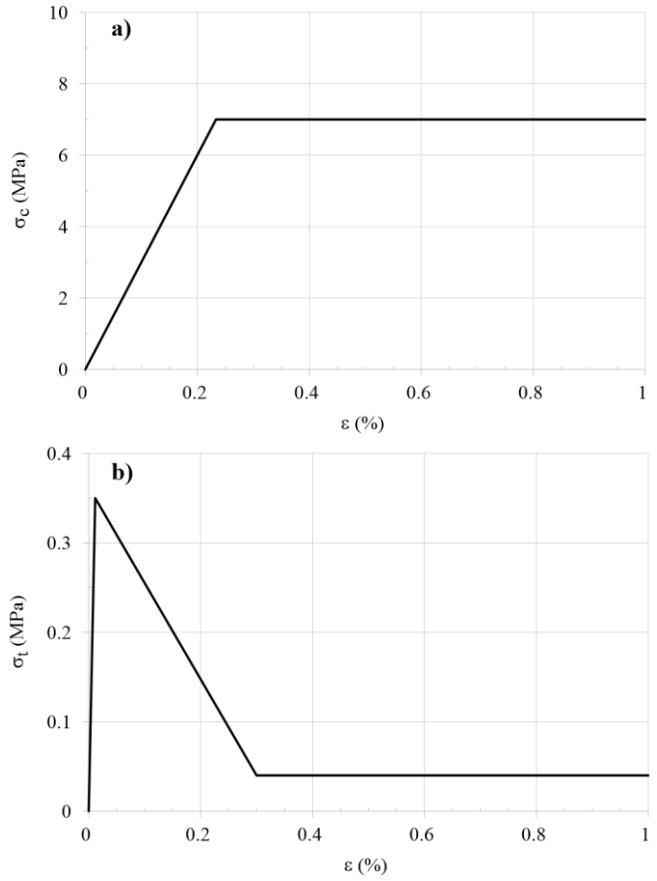

Fig. 3. 38 – Stress-strain relationships adopted for the two masonry walls in a) compression and b) tension.

The CDP parameters are summarized in Tab. 3.4.

ρ	E_0	ν	ψ	f_{b0} / f_{c0}	ε	K_C
(Kg/m^3)	(MPa)	(-)	(°)	(-)	(-)	(-)
1500	3000	0.15	20	1.16	0.1	2/3

Tab. 3. 4 – Model parameters adopted for the pushover analyses performed on MW1 and MW2.

The numerical analyses have been carried out using a 2D model generated using CPS3 linear triangular elements. The loading phases reproduce those implemented during the experimental test, consisting in a first phase in which the uniformly distrib-

uted prestress load is applied at the top of the wall and a second phase during which the shear condition is imposed. The prescribed target displacements are 5 mm and 20 mm, for MW1 and MW2 respectively.

Focusing on MW1, the main objective of this study is to investigate the influence played by the viscosity parameter μ on the lateral capacity of the wall. To this aim, a sensitivity analysis regarding this parameter has been carried out, keeping any other variable unchanged as reported in Tab. 3.4.

As shown in Fig. 3.39, the lateral capacity of the wall is assessed comparing the pushover curves obtained at the end of each simulation with the experimental ones (J4D and J5D specimens) and those of the numerical analyses by Annecchiarico et al. (2010) and Lourenço (1996). This latter one was obtained through a discrete model in which the joints were modelled as interface elements allowing for crack, slip or crushing, adopting a Mohr-Coulomb friction with tension cut-off and a cap for compressive failure.

Five values of μ have been assumed ranging from 0 to 2.5E-3. It is worth noting that the elastic response is not influenced by the viscosity value and, in all cases, the peak strength is caught quite well. If the viscosity is not considered ($\mu = 0$), the analysis fails in proximity of the peak resistance not allowing any post-peak softening branch. On the contrary, when the viscosity is taken into account, the analyses do not present significant convergence issues; additionally, as the viscosity values increase, the inclination of the softening branch becomes less marked.

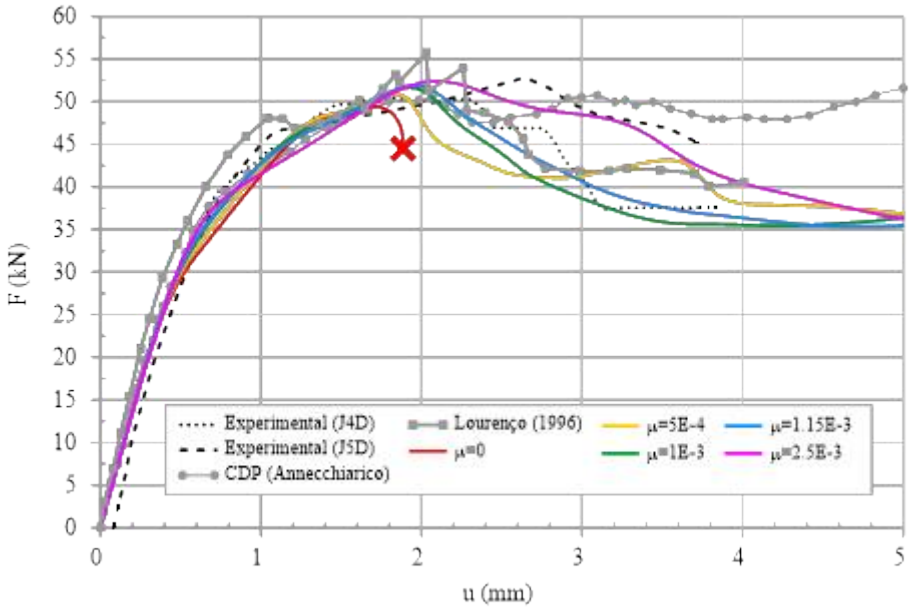

Fig. 3. 39 – Pushover analyses performed on MW1 with different values of viscosity parameter μ considering a fixed value of loading time t equal to 1 s.

All the presented simulations have been performed setting the loading time to $t = 1$ s. Since there is a direct relation between μ and t (Section 3.2.2), the next step has been to conduct a sensitivity analysis keeping μ fixed and equal to 1.15E-3 (blue curve in Fig. 3.39) and varying t in a range between 0.1-100 s.

The results are summarized in Fig. 3.40. They show that for small values of t, the analysis can face convergence issues and could potentially overestimate the peak resistance. Conversely, larger values of loading time seem to ensure a more stable solution; indeed, the 10 and 100 s analyses appear to be very close to each other, suggesting that the convergence of the numerical solution is attained.

All these findings about the relation between viscosity and loading time are in agreement with the studies carried out by Szczecina & Winnicki (2015, 2017) using CDP to model reinforced concrete structures.

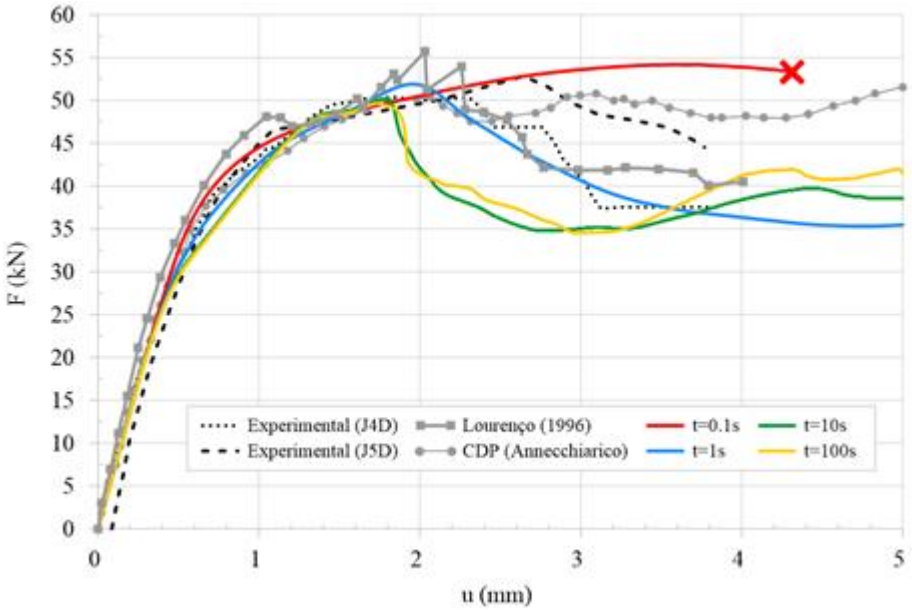

Fig. 3. 40 – Pushover analyses performed on MW1 with different values of loading time t considering a fixed value of viscosity parameter μ equal to 1.15E-3.

Finally, the crack patterns obtained from experimental tests on the panels (Fig. 3.41) are in fair agreement with the distribution of the plastic strain (Fig. 3.42) resulting from the numerical simulations performed assuming $t = 100$ s.

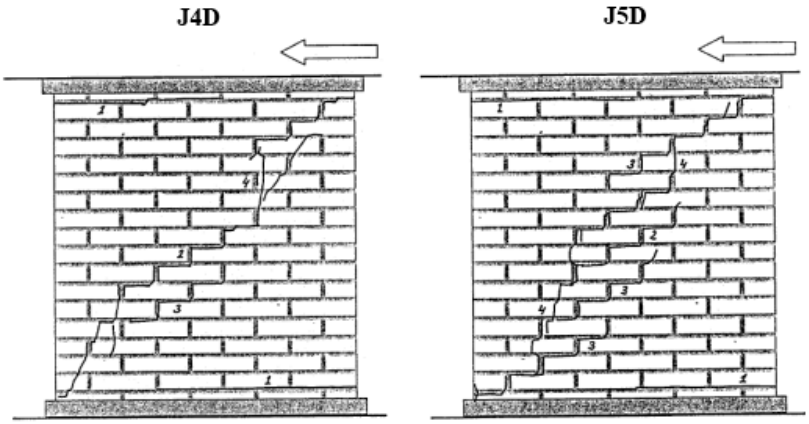

Fig. 3. 41 – Crack pattern recorded from the experimental test on two specimens of MW1, namely J4D and J5D.

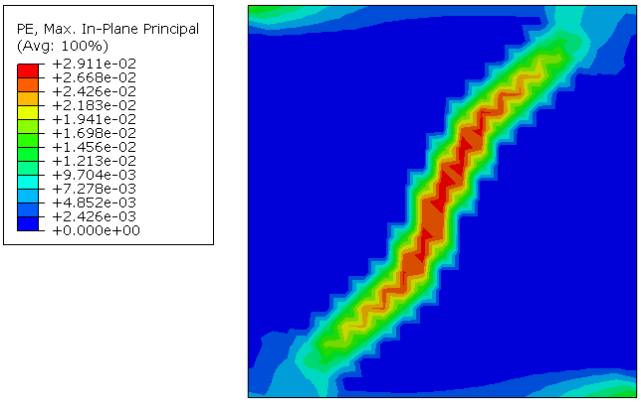

Fig. 3. 42 – Plastic strain (PE) contours recorded for the pushover analysis considering t =100 s.

The wall with an asymmetric opening, i.e. MW2 in Fig. 3.37, has been also analysed assigning the same material properties of the MW1 case. The wall presents an opening constituting an additional (geometric) non-linearity that causes further convergence issues in running the analysis. For this reason, the first step has consisted in assessing a proper value of the viscosity parameter to overcome this problem. The time t was kept equal to 20 s in each pushover test (the target displacement is 20 mm, thus 1 mm per second). The results are plotted in Fig. 3.43 together with the experimental data (J2G and J3G specimens) and the numerical curves provided by Lourenço (1996) and Lasciarrea et al. (2019). In Lasciarrea et al. (2019), the simulations were carried out through the so-called Jointed Masonry Model (JMM), an anisotropic elastic perfectly plastic constitutive model accounting for the directional properties of the medium by defining the orientation of three planes along which the Mohr-Coulomb yield criterion is applied.

Once again, if μ is neglected (red line Fig. 3.43), the analysis faces severe convergence problems, barely arriving at the peak structural strength. For viscosity equal to either 5E-4 or 1E-3 (respectively blue and green curve in Fig. 3.40), the simulations run successfully. However, the solutions look numerically disturbed and the residual strength is still quite underestimated in comparison with the experimental evidence. Adopting higher values of μ (but still rather small with respect to t) helps to mitigate these aspects, as shown by the yellow (μ =5E-3) and the magenta (μ =1E-2)

curves, which also fit better with the experimental data and the other numerical predictions.

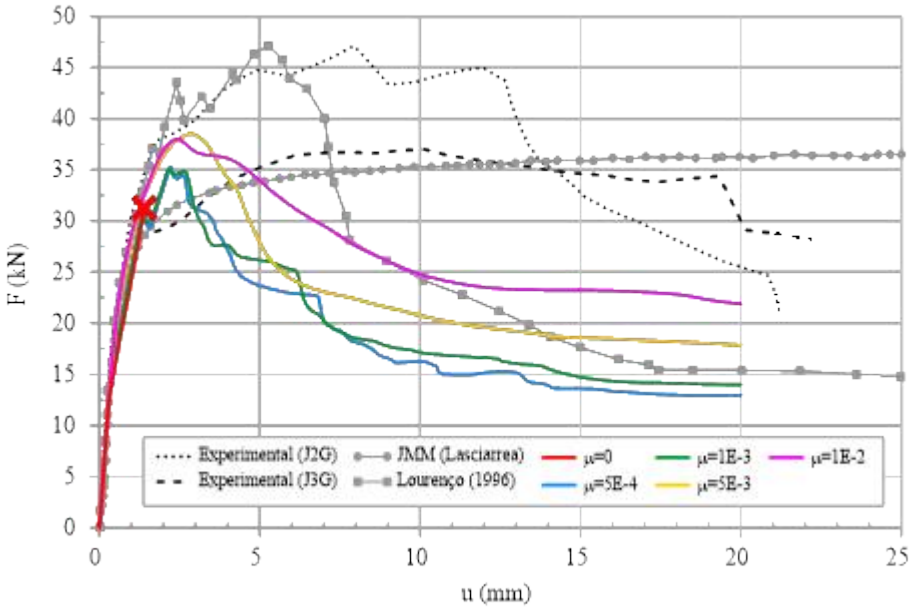

Fig. 3. 43 – Pushover analyses performed on MW2 with different values of viscosity parameter μ considering a fixed value of loading time t equal to 20 s.

The following step has been to assess the mesh sensitivity of the solution, considering three types of mesh refinement: coarse, fine and very fine. The size characteristics for each case are reported in Tab. 3.5, while the corresponding FE mesh discretization is shown in Fig. 3.44. These simulations have been executed adopting a viscosity value μ =1E-2.

MESH REFINEMENT	NUMBER OF ELEMENTS	NUMBER OF NODES
Coarse	314	190
Fine	1278	705
Very Fine	3646	1939

Tab. 3. 5 – Problem size characteristics for the coarse, fine and very fine mesh discretization.

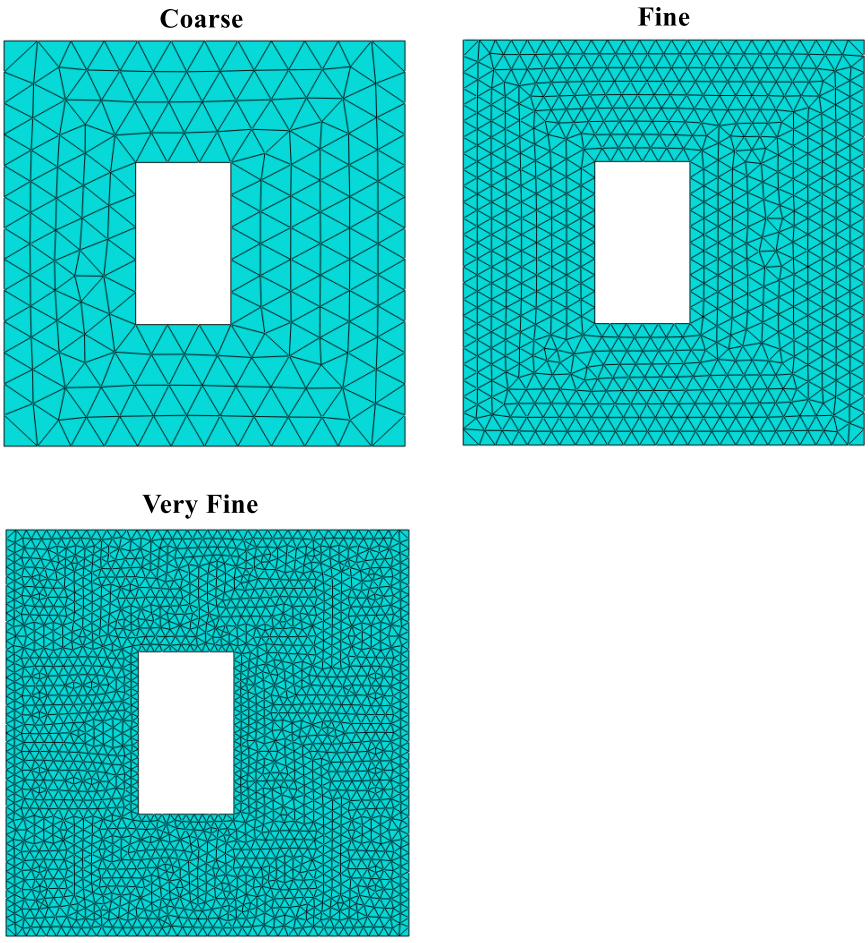

Fig. 3. 44 – Coarse, fine and very fine discretization adopted for the mesh sensitivity analysis on MW2.

The pushover curves are depicted in Fig. 3.45 and show that the model is affected by mesh-sensitivity issues. Indeed, the curves do not completely superimpose each other once the elastic phase is passed and, as a consequence, the post-peak response is different in each simulation. It is worth noting that the trends are anyway rather similar and the overall behaviour is well captured in comparison to the experimental tests and to other available numerical approaches results.

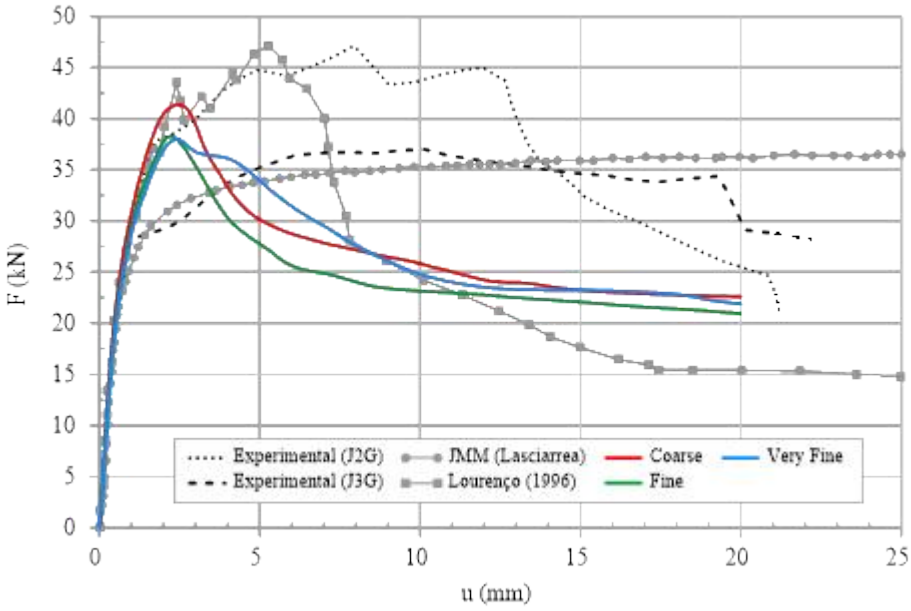

Fig. 3. 45 – Pushover curves obtained for the coarse, fine and very fine mesh discretization on MW2.

Moreover, in Fig. 3.46 and Fig. 3.47 the comparison between the crack patterns recorded during the experimental tests and the plastic strain contours obtained from the three meshes is presented. The experimental crack pattern mainly follows the mortar joints paths and is very similar for both specimen walls, characterized by a diagonal crack connecting the upper right corner to the bottom left one, involving the area close to the opening. Other horizontal cracks can be recognized in the upper part of the left edge of the J2G panel and in lower part of the right edge of both panels.

Looking at the numerical prediction, it is worth noting that even the coarse mesh model is able to give reliable indications about the failure mechanism of the masonry wall; surely, the accuracy increases with the mesh refinement. Indeed, the very fine mesh reproduces quite accurately all the main features of the experimental crack pattern.

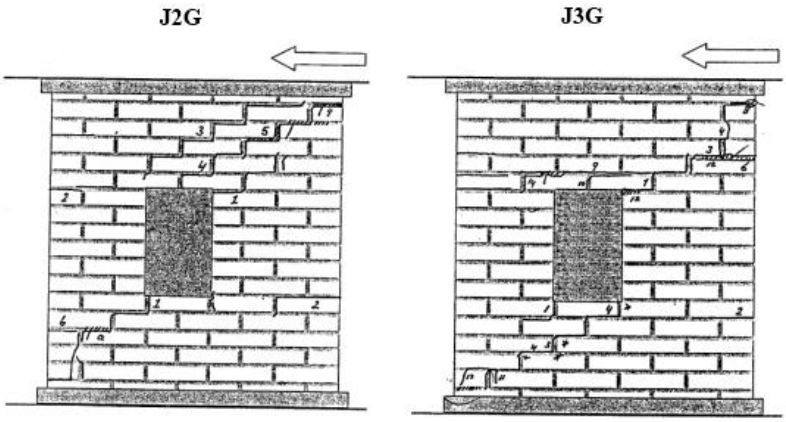

Fig. 3. 46 – Crack pattern recorded from the experimental test on two specimens of MW2, namely J2G and J3G.

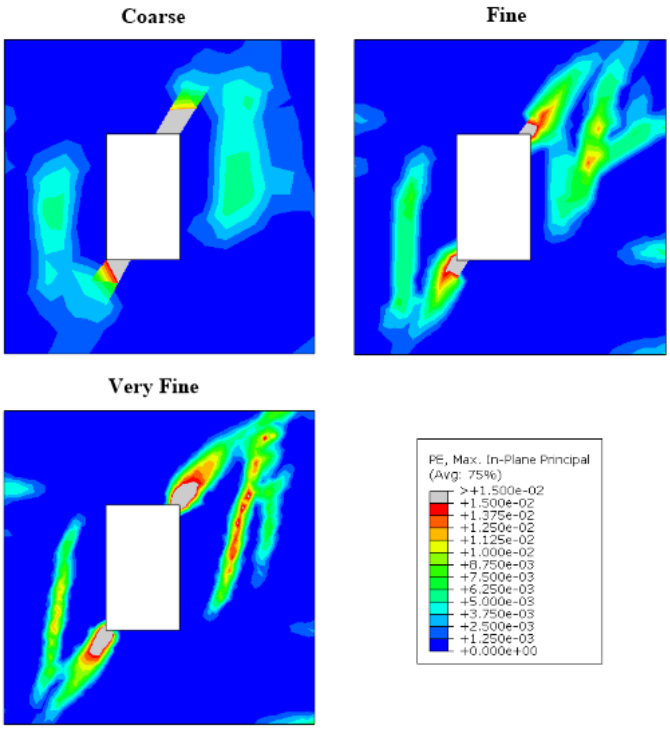

Fig. 3. 47 – Plastic strain (PE) contours recorded for the pushover analyses performed for the three types of mesh discretization.

Finally, a further parametric analysis has been performed on the CDP model parameters to assess their influence on the lateral capacity of the masonry wall. Specifically,

the analysis has regarded the following parameters: the dilatancy angle (ψ), the eccentricity (ξ), the parameter that defines the yield surface in the deviatoric plane (K_C) and the ratio of the initial biaxial compressive yield stress to initial uniaxial compressive yield stress (f_{b0}/f_{c0}).

The results are shown in Figs 3.48-3.51. The most sensitive parameter for the model is the dilatancy angle ψ (Fig. 3.48). In fact, for small values (10 and 15) it manifests poor convergence, while, on the other hand, assuming higher and higher values of ψ (20 and 30) the simulation is successfully carried out; nonetheless the peak resistance tends to increase and the post-peak branch can also be modified. The analyses run for the eccentricity parameter ξ (Fig. 3.49) do not show any significant change for the considered range of values. The curves derived from the K_C parametrization (Fig. 3.50) highlight convergence problems for the minimum value equal to 0.5; for higher values, such problem is avoided and no model sensitivity to this parameter is recognized. Finally, for the f_{b0}/f_{c0} ratio (Fig. 3.51) the simulations show just a slight and negligible deviation of the $f_{b0}/f_{c0}=2$ simulation from the overall behaviour depicted in the other cases.

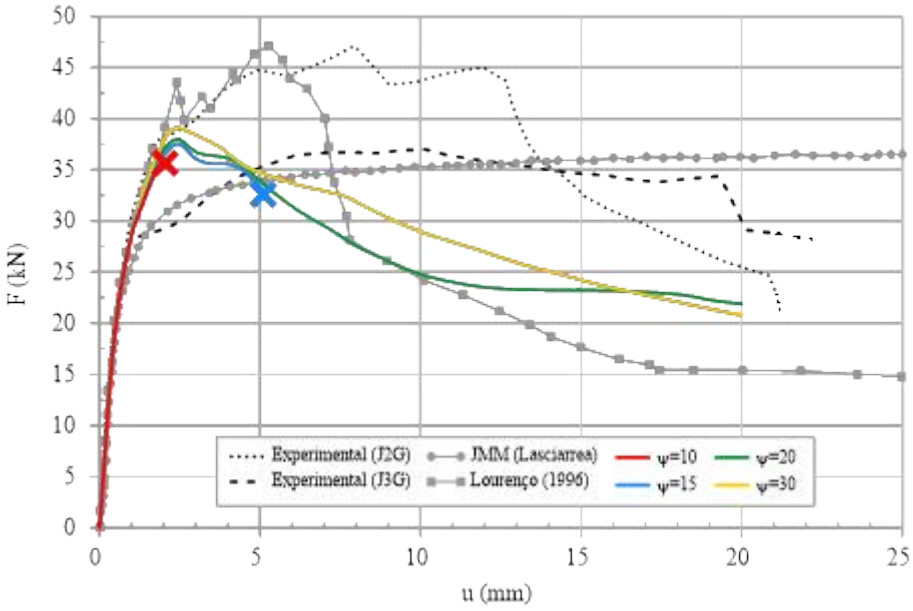

Fig. 3. 48 – Sensitivity analysis on the CDP model parameters: effect of the dilatancy angle ψ .

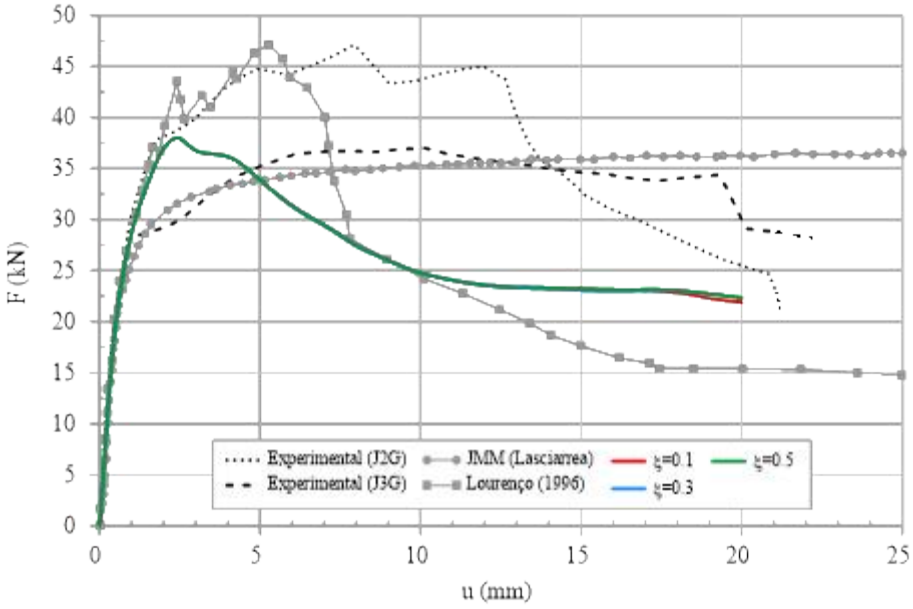

Fig. 3. 49 – Sensitivity analysis on the CDP model parameters: effect of the eccentricity ξ .

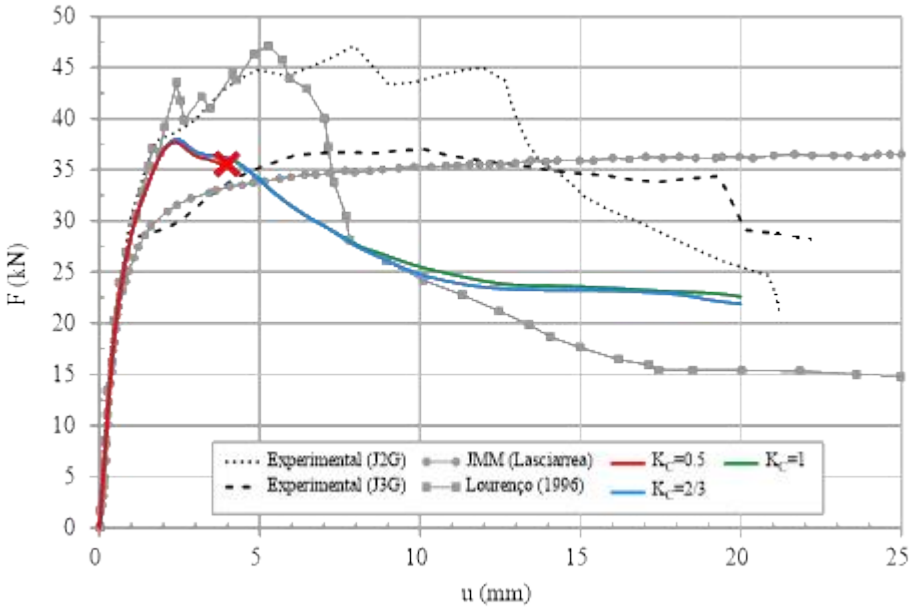

Fig. 3. 50 – Sensitivity analysis on the CDP model parameters: effect of K_C parameter.

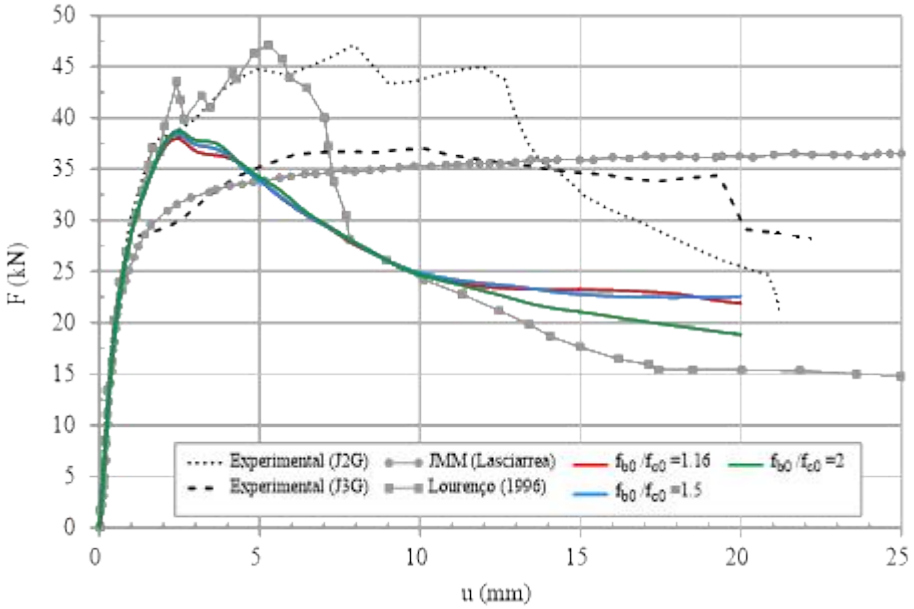

Fig. 3. 51 – Sensitivity analysis on the CDP model parameters: effect of the f_{b0}/f_{c0} ratio

3.2.3.2.2 Cyclic shear tests on masonry walls

Some examples of cyclic shear tests on masonry walls adopting the CDP model are herein briefly recalled with the most significant findings.

In Karimi et al. (2016) a brick masonry wall and an arch were analysed using this constitutive model attaining a good agreement with the experimental outputs in terms of force-displacement curves and damage/crack patterns.

In Zizi et al. (2017) the authors performed a vast parametric analysis (i.e. a total of 108 numerical simulations) in order to properly calibrate the CDP model parameters. Once again, the dilatancy angle was found to be the most sensitive parameter, as well as the compression recovery parameter w_c as already pointed in Section 3.2.3.1. The best comparison with the experimental test obtained by Zizi et al. (2017) is shown in Fig. 3.52, revealing a very good agreement of the numerical outcomes with the experimental data.

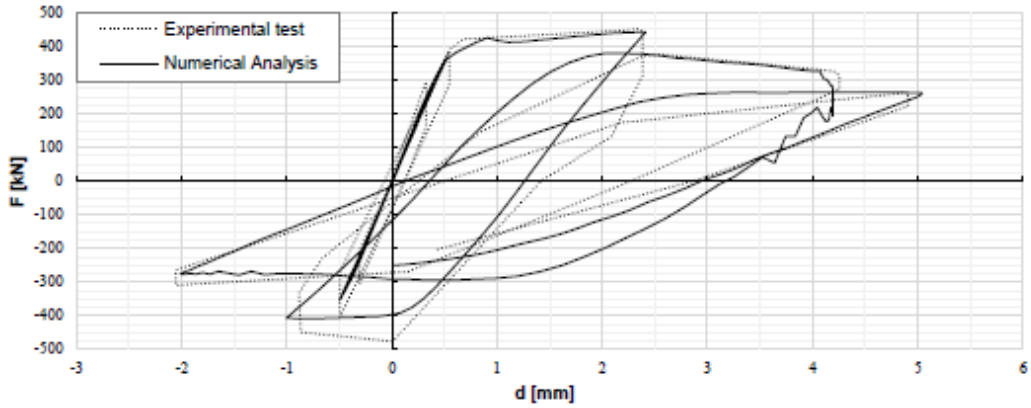

Fig. 3. 52 – Comparison between experimental and numerical results derived adopting the CDP model from Zizi et al. (2017).

Nevertheless, it is also worth pointing out that the model is characterized by some limitations that occasionally can avoid to correctly catch the overall cyclic response of a masonry wall, as reported by Monti Di Sopra (2009). The study mainly focused on the cyclic shear response of clay-brick walls modelled by means of the CDP model. Fig. 3.53 shows the final calibration proposed by the author for the MS1 specimen.

It is clear that, despite the peak resistance is still fairly caught, the numerical results underestimate the experimental data with reference to the residual strength. The author attributes this mismatch to one of the characteristics of the model, i.e. the isotropy formulation. Indeed, masonry damage is strongly dependent on the direction considered and, as already discussed previously, the real weakness of a masonry structure are the horizontal mortar joints and the interface between them and the units, while the vertical joints are usually characterized by a less consistent damage due to the interlocking effect.

In reality, the damage and plasticity formulation adopted in the CDP takes into account an isotropic damage of the material, thus considering it equal in any direction. Hence, a lower residual strength is predicted by the model and, conversely, the energy dissipation is overestimated.

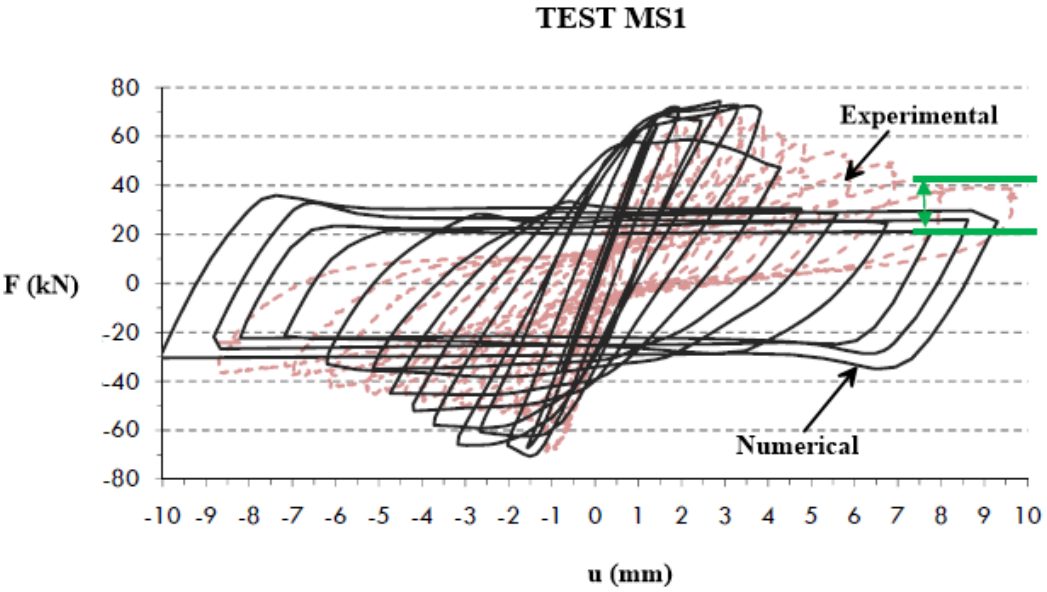

Fig. 3. 53 – Comparison between experimental and numerical results derived adopting the CDP model from Monti Di Sopra (2009) (modified).

CHAPTER 4: SOIL-STRUCTURE INTERATION ANALYSIS OF A REPRESENTATIVE CASE-STUDY

4.1 Introduction

The present Chapter discusses the SSI numerical analyses carried out on a representative case-study, which considers a masonry tower standing on different soil deposits. After the description of the main features characterizing the examined tower, the procedure followed to select the soil profiles is presented. The stratigraphic sequences are classified according to their heterogeneity degree along the depth of the deposit by means of an appropriate parameter.

Two different models have been adopted to characterize the soil dynamic behaviour: a linear visco-elastic (LIN) and an equivalent-linear visco-elastic (EQ-LIN) model. Indeed, the two approaches are functional to investigate two different effects on the dynamic response of the tower: the LIN soil modelling is adopted to analyse the effect given by the stratigraphic heterogeneity, while the effect of the non-linear soil behaviour is examined through the EQ-LIN approach. In the first case (i.e. LIN), the small-strain stiffness and a constant damping ratio are used for each soil layer, thus neglecting the change of the soil dynamic properties with the shear strain level induced by the earthquake. To introduce the non-linear behaviour of the soil into the FE simulations, instead, a simplified procedure has been adopted: starting from the same stiffness profiles implemented in the LIN cases, 1D equivalent-linear visco-elastic analyses have been conducted with EERA (Bardet et al. 2000), accounting for the decrease of shear stiffness and increase of damping with the shear strain. The resulting

profiles with depth of the shear stiffness and damping ratio have been, then, used as input in the EQ-LIN models of the deposit, still adopting a total stress-based visco-elastic model for each soil layer. This allows to account for, in a simplified way, the main effects of the non-linear soil behaviour on the wave propagation process from the bedrock to the surface of the deposit, without using an elasto-plastic constitutive model able to describe these effects. It should be noted that advanced effective stress-based non-linear soil models (e.g. multi-surface kinematic hardening or bounding surface models) are rarely implemented in FE codes, such as Abaqus, as they require the calibration of a big number of parameters and a proper initialization of their state variables, depending on the complex geological stress history of the deposit (Kavvadas & Amorosi 2000; Rouainia & Wood 2000). The advanced approach also requires the solution of the solid-fluid interaction equations under dynamic loading, developed within the framework of the general consolidation theory (Biot 1941). Future developments of the present study will, therefore, consist in the implementation of such advanced soil constitutive laws in Abaqus, to perform non-linear dynamic simulations of a 3D model of the tower with its foundation deposit.

In the following, a preliminary validation of the effectiveness of the dynamic boundary conditions for the seismic ground response analyses (SRA) under free-field conditions is carried out adopting as benchmark the results provided by the code EERA. For this purpose, natural frequencies, amplification functions, spectral acceleration response spectra and Fourier spectra are compared. Then, a complete 3D SSI model consisting in the tower, its foundation and the surrounding soil is considered. The SSI analyses have mainly consisted in modal eigenvalues analyses and linear and non-linear dynamic time-history simulations. Hence, the main outcomes derived from the 3D numerical simulations are discussed, also highlighting the deviations recorded with respect to the tower fixed-base scheme.

4.2 Description of the ideal case study

The structural model of the tower follows the ideal case-study outlined in the work by Casolo et al. (2017), which embodies the main features of many recurring bell towers

located in the seismic areas of Northern Italy. A sketch of the tower, which is supposed to be structurally independent from other buildings, is shown in Fig. 4.1, together with a vertical cross section where the geometrical dimensions are reported. Its configuration is regular both in plan and in elevation, with a square base section of 5.30m x 5.30m, a larger square foundation of 6.80m x 6.80m and a total height of 27m, resulting in a slenderness ratio equal to 5. The masonry walls thickness starts from 1.00m at the basement level and then it reduces to 0.85m.

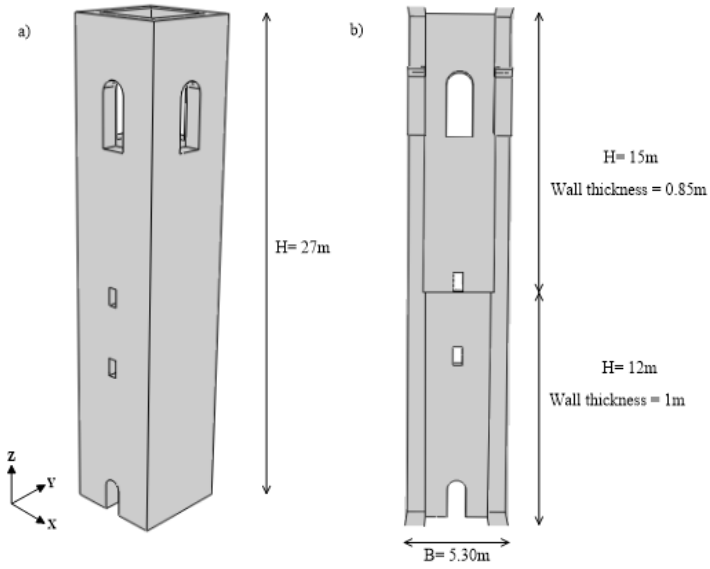

Fig. 4. 1 – a) 3D CAD model of the masonry tower; b) vertical section of the structure.

The soil deposit has been modelled mainly focusing on the stratigraphic heterogeneity aspect. Indeed, the original work by Casolo et al. (2017) considered the tower resting on homogeneous soil deposit. Additionally, a realistic stratigraphic soil sequence is rarely considered in the available scientific literature, with the exception of very few cases (e.g. de Silva et al. 2018a, b; De Angelis et al. 2022).

Thus, the soil deposits are characterized by different stratigraphic sequencies, whose shear wave velocity (V_S) profiles cover the range identified by Falcone et al. (2021)

for typical lithological successions of clay and sand cover soils in Italy. Therefore, the V_S sequences might be considered as representative of real site conditions.

Seven soil deposits, 30m deep, characterised by the same value of the equivalent shear wave velocity ($V_{S,eq}$) equal to 250m/s, are considered (Fig. 4.2a). The $V_{S,eq}$ is defined by:

$$V_{S,eq} = \frac{H}{\sum_{i=1}^{N} \frac{h_i}{V_{S,i}}} \tag{4.1}$$

where N is the number of the layers, h_i is the thickness of the i_{th} layer, $V_{S,i}$ is the shear wave velocity of the i_{th} layer, while H is the deposit depth. Thus, according to the Italian Code NTC2018 (Consiglio dei Ministri, 2018), the soil deposits can be classified as class C, characterised by $180 < V_{S,eq} < 360$m/s.

The soil stratigraphies can be divided into two groups. The first one is composed by multiple soil layers deposits classified by means of the α parameter (Vinale & Simonelli 1983) defined as:

$$\alpha = \frac{V_H}{V_0} \tag{4.2}$$

where V_H and V_0 are, respectively, the shear wave velocity at the bottom and at the surface of the soil deposit; five different values equal to 1 (i.e. homogeneous condition), 2.5, 5, 10 and 15 are taken into account.

The second group is, instead, characterized by a simpler 2 layers geometry, representative of a clay/sand and a sand/clay sequence (respectively the CS and SC profile depicted in Fig. 4.2a) aimed at investigating the effect of a stratigraphic inversion along the soil depth. For the sake of completeness, the CS case would correspond to a heterogeneity degree equal to $\alpha = 2.28$, while the SC case to $\alpha = 0.44$. In Fig. 4.2b the corresponding shear stiffness modulus G_0 profiles are also shown.

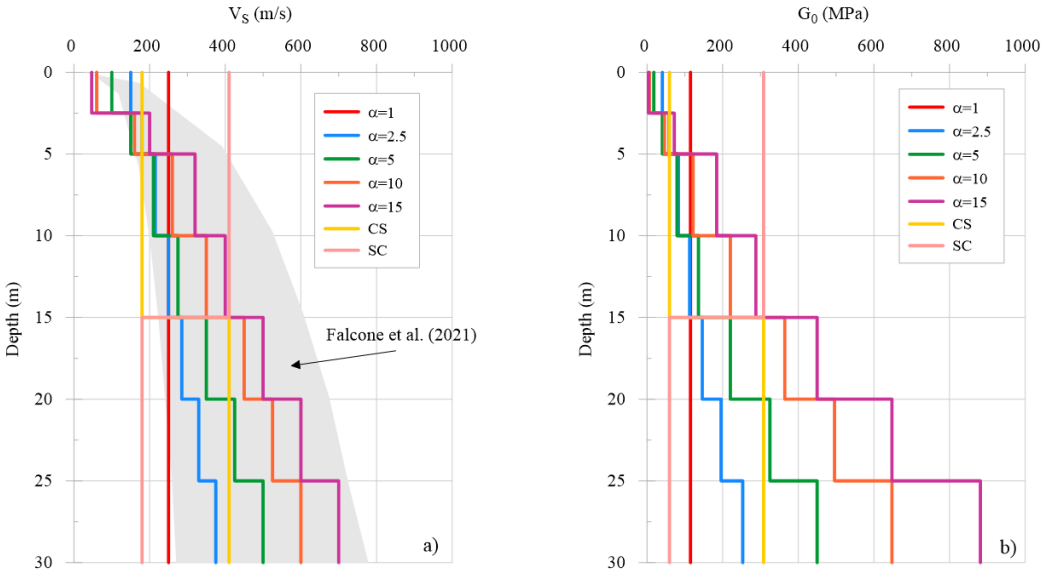

Fig. 4. 2 – Soil profiles selected to describe the stratigraphic heterogeneity: a) V_S and b) G_0 profiles.

Finally, in the equivalent-linear framework, it is necessary to introduce the modulus reduction curve G/G_0 and variation of damping ratio D with shear strain level γ in order to describe the non-linear soil response. Generally, they are set according to the scientific literature or experimental data, if available. In this work, they have been defined according to Vucetic & Dobry (1991) as a function of the plasticity index (PI) of the soil. In particular, the PI=50% curves have been selected as representative of the soil behaviour for all the deposits (Fig. 4.3).

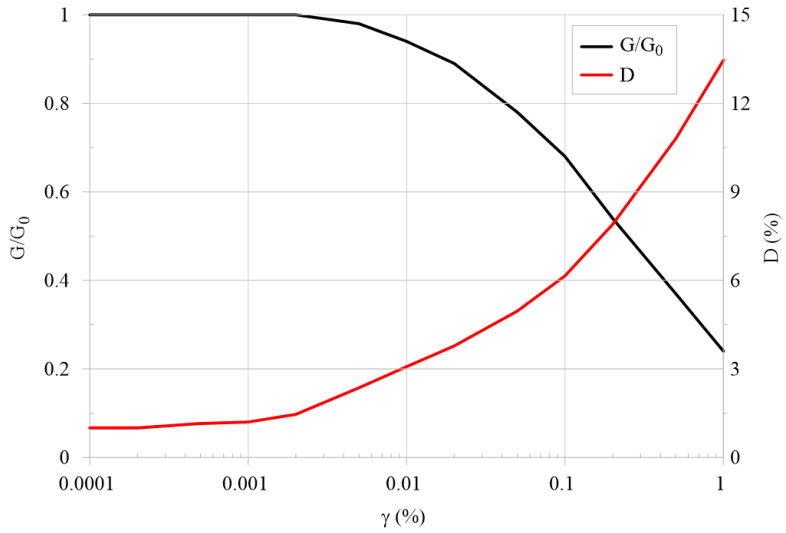

Fig. 4. 3 – Modulus reduction curve G / G_0 and variation of damping ratio D with shear strain level γ defined for a plastic index equal to 50% according to Vucetic & Dobry (1991).

4.3 Preliminary free-field seismic ground response analyses

In order to provide a benchmark for the FE seismic response analyses, a series of linear (LIN) and equivalent-linear (EQ-LIN) visco-elastic analyses have been carried out using the code EERA. EERA is a numerical software able to perform one-dimensional SRA, operating in the frequency domain and relying on the assumption of equivalent-linear visco-elastic soil behaviour. It models the non-linear variation of soil shear modulus and damping with shear strain through a sequence of linear analyses with iterative update of stiffness and damping parameters. For a given soil layer, G and D are assumed to be constant with time during the shaking. Therefore, an iterative procedure is needed to ensure that the properties used in the linear dynamic analyses are consistent with the level of strain induced in each layer by the input motion.

The analysis is performed adopting a total stress approach. This means that excess pore water pressures induced by the earthquake cannot be predicted and the displacements due to consolidation processes cannot be calculated. The model employed to describe the mechanical behaviour of soils is visco-elastic. Therefore, the method cannot predict permanent soil displacements or cumulated strains at the end

of the analysis. Even though the iteration process allows to approximate the non-linear soil behaviour, the approach is still a linear method of analysis. The strain compatible soil properties are constant throughout the duration of the earthquake. The method is, thus, not capable of representing changes in soil stiffness and hysteretic damping during the seismic action. For problems where the strain levels remain low (stiff soil profile and/or relatively weak input motions), the equivalent-linear method can produce reasonable estimates of ground response. For high seismic intensities at bedrock, non-linear time-domain analyses should be preferred as they are likely to provide better results (Kramer 1996; Lanzo & Silvestri 1999).

The modulus reduction curve G/G_0 and variation of damping ratio D adopted in the SRA simulations are those reported in Fig. 4.3. If the simpler linear visco-elastic behaviour (LIN) is assumed, G and D do not vary during the analysis, i.e. the final G profiles coincides with the G_0 ones reported in Fig. 4.2b..

The reference input motion employed in the numerical simulations is represented by the X component of the South Iceland earthquake of the 17 June 2000 recorded on site class A. Its time-history and Fourier spectrum are shown in Fig. 4.4. The seismic signal is characterised by a maximum acceleration of 0.12g, a predominant frequency around 4.20 Hz and a time step equal to 0.005 s. The selected input motion has been directly applied at the bottom of the numerical models, considered as a rigid bedrock. It is worth noting that for the EQ-LIN approach the results are signal-dependent, unlike for the LIN approach.

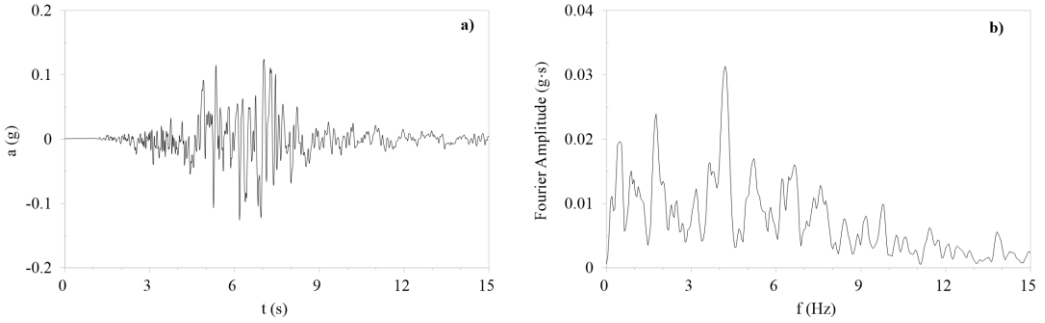

Fig. 4. 4 – South Iceland earthquake of the17 June 2000 recorded on site class A: a) acceleration time-history and b) Fourier spectrum.

The main results of the EERA EQ-LIN analyses are shown in Fig. 4.5a-d, in terms of profiles of maximum shear strain γ_{max}, shear modulus reduction G / G_0, damping ratio D and maximum acceleration a_{max} attained during the input motion. The shear strains reach their highest values where the maximum damping ratio and the minimum shear stiffness are attained, i.e. in the upper part of the deposit with the exception of $\alpha = 1$ and SC profiles. The maximum acceleration (Fig. 4.5d) is expected at the surface in all the analysed cases apart from the SC case, where the peak value is reached at 24m below the surface.

The EERA LIN analyses results are reported in Fig. 4.5e-f in terms of maximum shear strain and acceleration attained during the seismic event. With the purpose to catch the average response of the EQ-LIN analyses (Fig. 4.5c), the LIN simulations have been carried out considering a damping factor D equal to 5% for all the soil layers of cases $\alpha = 10$ and $\alpha = 15$, while an average damping ratio of 4% is assigned to the soils of the remaining stratigraphic profiles.

The shear strains reach their maximum value in the upper part of the deposit with the exception of $\alpha = 1$ and SC profiles; as expected, CS and SC have a mirrored behaviour along the depth (Fig. 4.5e). The maximum acceleration profiles in Fig. 4.5f point out that, starting from a common peak base amplitude equal to 0.12g, the maximum shaking is expected at the surface in all the analysed cases.

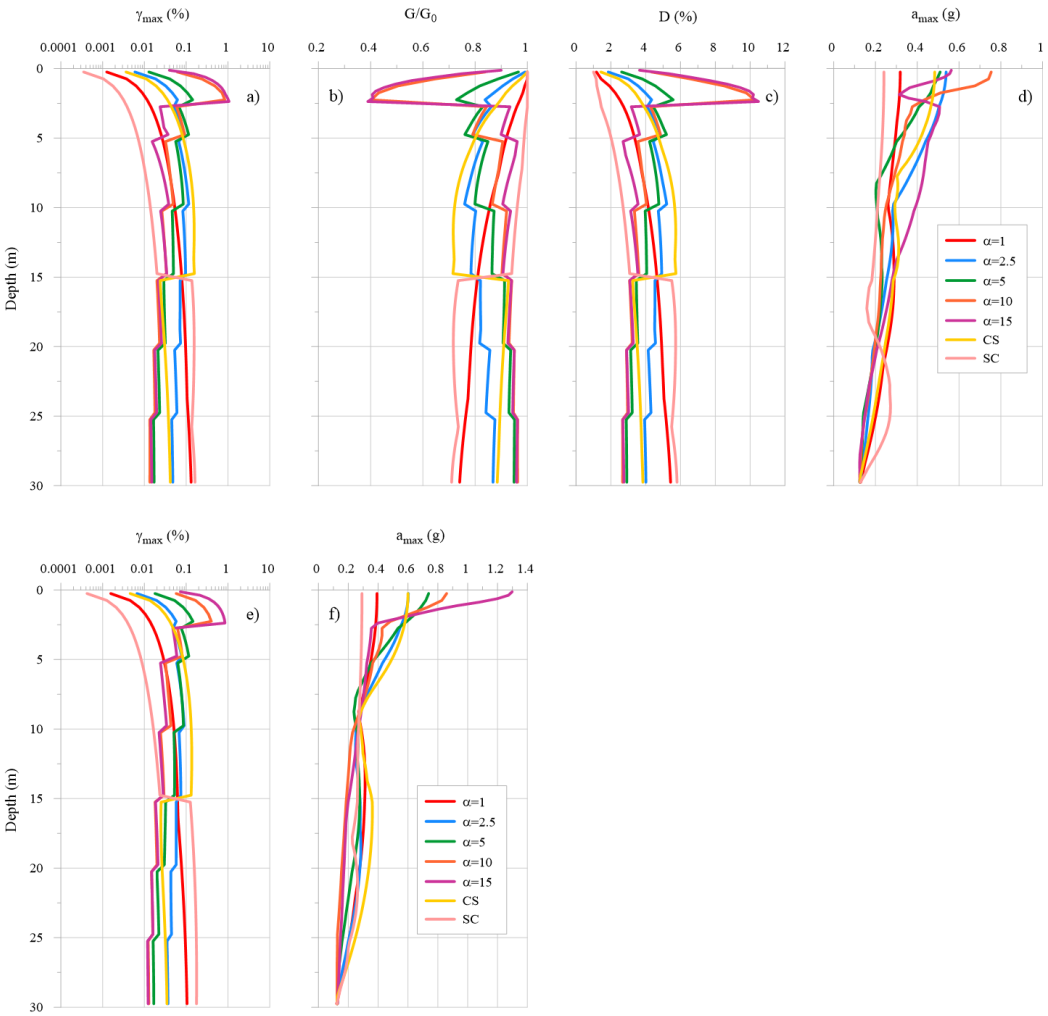

Fig. 4. 5 – a-d) Results of the 1D SRA carried out with EERA for each soil profiles considering the equivalent-linear visco-elastic approach (EQ-LIN): a) maximum shear strains, b) G/G_0, c) damping ratio and d) maximum accelerations along the deposit depth. e-f) Results of the 1D SRA carried out with EERA for each soil profiles considering the linear visco-elastic approach (LIN): e) maximum shear strains and f) maximum accelerations along the deposit depth.

Fig. 4.6 depicts the amplification functions derived from both the LIN and EQ-LIN simulations, while Tab. 4.1 collects the recorded peak ground accelerations values (PGA), magnification factors (MF) (derived as the ratio between a_{max} at the surface and at the bottom of the soil deposit) and the first two resonance frequencies of the

deposits (f_{SOIL}). Consistently with the literature (Vinale & Simonelli 1983, Gazetas 1982), two main phenomena can be recognized: with respect to the homogeneous case, the first natural frequency clearly shifts towards higher values as the parameter α increases (apart for the SC case which, indeed, is the only characterized by a lower heterogeneity parameter α than the homogenous case), while the higher frequencies tend to reduce with increasing heterogeneity. The second frequency is higher than the one characterizing the homogeneous deposit only for CS and α equal to 2.5 and 5, but then reduces considerably for higher values of heterogeneity ratios. Moreover, the heterogeneity implies an evident amplification of all the natural frequencies, except for the SC case. This can be attributed to the lower shear wave velocity adopted for the shallower soil layers as α increases.

On the other hand, the non-linear behaviour introduced in the EQ-LIN simulations implies a reduction of the soil resonance frequencies and an attenuation of the recorded PGA with respect to the LIN analyses (Tab. 4.1), which can be remarkable as testified by the MF values.

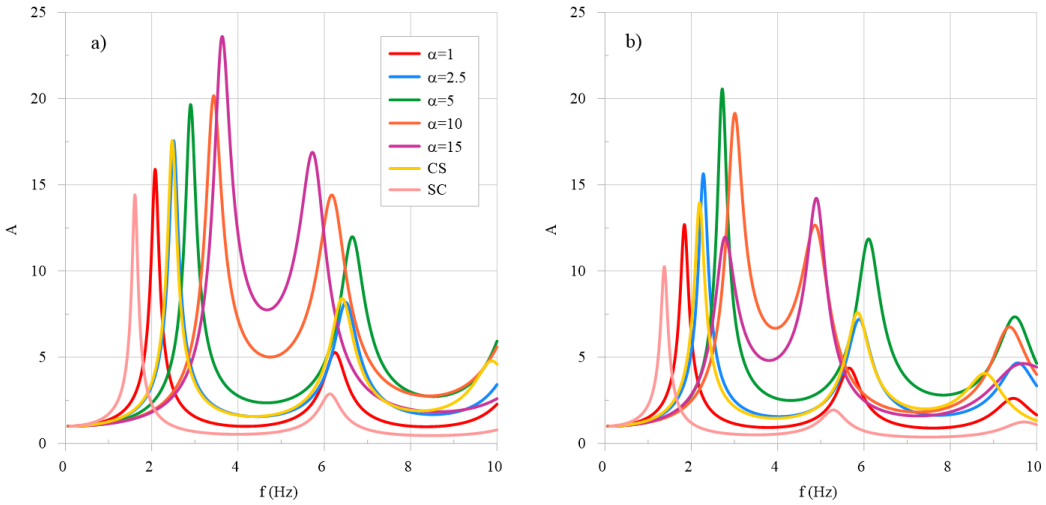

Fig. 4. 6 – EERA amplification functions: a) LIN analyses and b) EQ-LIN analyses.

	LIN				EQ-LIN			
SOIL PROFILE	PGA (g)	MF	f_{SOIL-1} (Hz)	f_{SOIL-2} (Hz)	PGA (g)	MF	f_{SOIL-1} (Hz)	f_{SOIL-2} (Hz)
$\alpha = 1$	0.39	3.11	2.08	6.25	0.31	2.52	1.84	5.66
$\alpha = 2.5$	0.60	4.78	2.51	6.49	0.53	4.26	2.28	5.89
$\alpha = 5$	0.74	5.86	2.90	6.62	0.51	4.03	2.72	6.11
$\alpha = 10$	0.86	6.82	3.44	6.14	0.75	5.98	3.01	4.83
$\alpha = 15$	1.30	10.30	3.64	5.49	0.56	4.47	2.75	4.82
CS	0.60	4.76	2.48	6.40	0.48	3.84	2.19	5.85
SC	0.29	2.31	1.55	6.12	0.24	1.90	1.37	5.29

Tab. 4. 1– Peak ground acceleration (PGA), magnification factor (MF), first and second resonance frequencies derived for each soil deposit from the EERA LIN and EQ-LIN analyses.

The results of the EERA LIN simulations are also proposed in terms of first and second natural periods (T_1 and T_2) of the heterogeneous deposits normalized by the "equivalent" homogeneous ones (T_{eq}) in line with Gazetas (1982). It should be noted that, according to Gazetas (1982), the "equivalent" homogeneous medium has been defined, for each case, as the one having the same shear wave velocity of the heterogeneous profile at the middle of the deposit.

Bearing in mind these remarks, Fig. 4.7 shows the variation of T / T_{eq} as a function of α, excluding the CS and SC cases which have different characteristics from the other profiles (i.e. only two layers versus seven and an inverse trend of V_S with depth for the SC case). It can be stated that T_1 is lower than the first natural period of the equivalent homogeneous deposit until $\alpha = 10$, reaching a minimum for $\alpha = 2.5$; then it becomes bigger for $\alpha = 15$. On the contrary, T_2 is always bigger than T_{eq} and seems to monotonically increase with the heterogeneity ratio.

These trends look consistent with the results provided by Vinale & Simonelli (1983) and Gazetas (1982) based on analytical solutions.

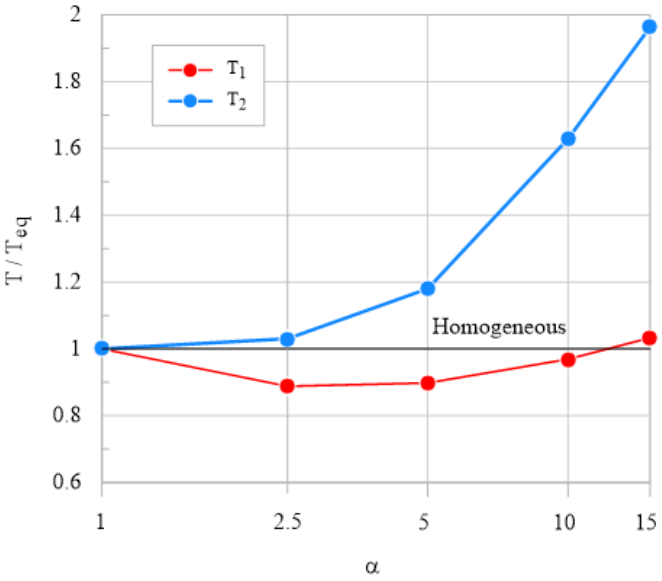

Fig. 4. 7 – First and second soil natural periods (T) normalized for the equivalent homogeneous periods at the middle of the deposit (T_{eq}) plotted as function of α for the EERA LIN analyses.

4.4 Validation of the FE numerical model

When performing dynamic analyses which involve large domains, a crucial point in the reliability of the numerical outputs is represented by the appropriate setting of the dynamic boundary conditions. Indeed, since the numerical model is finite, the mesh boundaries could reflect the energy introduced by the dynamic action in the system back inside the model itself, which is not physically possible and would be a potential source of error in the numerical solution.

The SSI case-study which involves the tower and surrounding soil deposit falls in this set of problems and is even more critical because of the presence of the tower which adds a further complication.

In this context, to verify the effectiveness of the dynamic boundary conditions, also considering that the adopted FE software Abaqus is not extensively used in soil dynamics applications, a series of 2D and 3D SRA analyses have been performed. The results are compared to those obtained with EERA, considered as benchmark.

One of the available solutions to overcome the possible occurrence of multiple reflections along the outer boundaries of the model is to place viscous dampers capable to adsorb the incoming wave energy (Lysmer & Kuhlemeyer. 1969). Abaqus offers a similar option consisting in the so-called “infinite elements”, which are elements defined over semi-infinite domains with suitably chosen decay functions based on Lysmer & Kuhlemeyer (1969).

Another option consists in the use of the so-called “free-field boundary conditions”. This solution requires an independent free-field model as an extension to the main model. In the 2D case, the free-field model comprises two soil columns placed at the edges of the main model, with each column acting as a 1D model. In practice, this extension requires the analysis of free-field motions either prior to, or in parallel with, the analysis of the main model. The procedure is not directly available in Abaqus; however, the subroutine proposed by Nielsen (2006, 2014) can be implemented in the software. The effectiveness of this numerical approach has been demonstrated in Volpini & Douglas (2019) and Volpini et al. (2021).

One more possibility relies on the use of the so-called “tied-nodes” condition, which ensures that the nodes located on the left and right boundaries of the soil domain undergo the same displacements. However, this condition can only be applied if the distribution of nodes along the two vertical boundaries is identical, i.e. the corresponding nodes need to have the same Z-coordinate (Fig. 4.8). Thus, this type of boundary condition is suitable., for example, for one-dimensional seismic ground response analysis or for any geometrically symmetric boundary value problem (Amorosi et al. 2016, 2017; di Lernia et al. 2019). Since the analysed soil-tower interaction problem meets this requirement, “tied-nodes” have been manually implemented through a master-slave relationship boundaries, linking the motion of the control nodes (masters) to the motion of the counterpart nodes (slaves) symmetrically located on the opposite side. At the same time, vertical displacements and rotations are blocked along the Z direction (Fig. 4.8).

The validation of the employed dynamic boundary conditions has been performed with reference to 2D and 3D free-field seismic ground response analyses. The 2D

model (Fig. 4.8a) is a soil column 2m large and 30m deep; the 3D model (Fig. 4.8b) has a square section of 50m x 50m while its depth is equal to 30m. Moreover, the coarseness of the FE mesh of the soil domain has been refined to obtain a distance between two consecutive nodes smaller than approximately one-eighth of the wavelength associated with the maximum frequency content of the input motion (Kuhlemeyer & Lysmer 1973; Bathe 1996), set equal to 15Hz. In addition, since each soil profile is characterized by rather different V_S values, the mesh refinements of the soil domains have been optimized case by case in order verify this requirement (Tab. 4.2).

SOIL PROFILE CASE	2D		3D	
	NUMBER OF ELEMENTS	NUMBER OF NODES	NUMBER OF ELEMENTS	NUMBER OF NODES
$\alpha = 1$	40	63	47245	9251
$\alpha = 2.5$	34	54	74128	13864
$\alpha = 5$	58	90	75634	14305
$\alpha = 10$	34	54	73411	13732
$\alpha = 15$	36	57	72683	13659
CS	60	93	54797	10489
SC	30	48	55563	10615

Tab. 4. 2 – Mesh refinements adopted for each soil profile case in the 2D and 3D models.

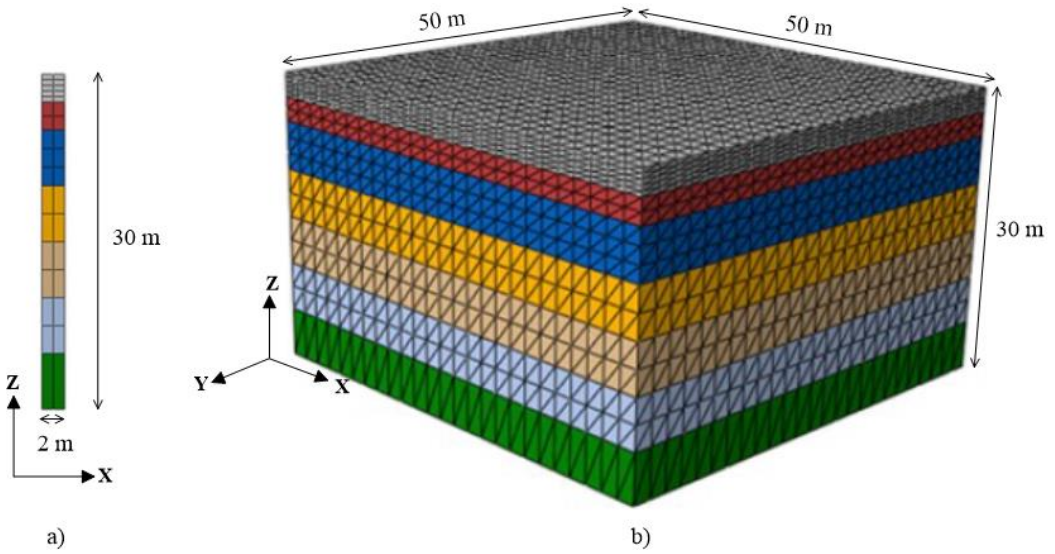

Fig. 4. 8 – a) 2D and b) 3D Abaqus FE models of the heterogeneous soil deposits (α =10 case).

The soil behaviour has been described by a linear elastic model. The dissipative capacity of the soil has been introduced through the frequency-dependent Rayleigh viscous damping formulation (Clough & Penzien 1993), in which the damping matrix $[\mathrm{C}]$ is a linear combination of the mass $[\mathrm{M}]$ and stiffness $[\mathrm{K}]$ matrices of the system:

$$[\mathrm{C}] = \alpha_{\mathrm{R}}[\mathrm{M}] + \beta_{\mathrm{R}}[\mathrm{K}] \tag{4.3}$$

The Rayleigh coefficients α_{R} and β_{R} have been derived as a function of the target damping ratio D according to Eq. 4.4:

$$\begin{Bmatrix} \alpha_{\mathrm{R}} \\ \beta_{\mathrm{R}} \end{Bmatrix} = \frac{2\mathrm{D}}{\omega_{\mathrm{m}} + \omega_{\mathrm{n}}} \begin{Bmatrix} \omega_{\mathrm{m}}\omega_{\mathrm{n}} \\ 1 \end{Bmatrix} \tag{4.4}$$

The angular frequencies ω_{m} and ω_{n} are related to the frequencies f_{m} and f_{n}, defining the interval over which the viscous damping is equal to or lower than the target damping ratio D. The selection of the two frequencies requires a suitable. calibration strategy, as proposed, for example, by Hashash et al. (2002) and Amorosi et al. (2010). In this work, the two Rayleigh frequencies have been set equal to the first and second natural frequencies of the soil deposit. Indeed, modal eigenvalue analyses in-

dicated that the dynamic behaviour of the tower is particularly influenced by the second natural mode of the soil deposit, which confirms the results presented by Casolo et al. (2017).

When the LIN approach is adopted, the shear stiffness profiles implemented in the FE models are those corresponding to the initial shear stiffness G_0 and reported in Fig. 4.2b; on the other hand, the damping ratio D has been kept constant with the depth adopting a value equal to 4% in each analysis, apart for $\alpha = 10$ and $\alpha = 15$ where it has been increased to 5%, as already pointed out in Section 4.3 for the EERA simulations.

Conversely, when the soil non-linearity is also accounted for and, hence, the EQ-LIN approach is considered, each soil layer is characterised by the degraded shear modulus and the relative damping ratio evaluated at the end of the equivalent-linear visco-elastic analyses performed through EERA. Thus, the G and D profiles adopted in the FE model are in this case reported in Fig. 4.9.

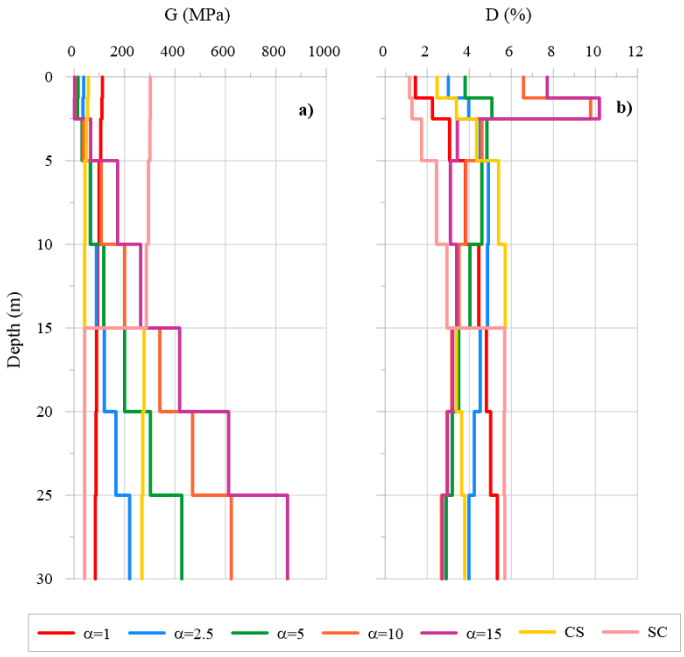

Fig. 4. 9 – Shear modulus G (a) and damping D ratio (b) profiles adopted for the EQ-LIN calibration in the FE simulations.

The comparison with EERA for the $\alpha = 1$ case is reported in Fig. 4.10, depicting for each analysis the acceleration time-history, the Fourier spectrum and the acceleration response spectrum of the signal recorded at the surface of the deposit; in addition, the amplification function of the deposit is shown. The latter, for the 2D and 3D analyses, has been computed as the ratio between the Fourier spectrum of the acceleration at surface and the one used as input at the bottom of the deposit. The results highlight a very good agreement between both the 2D and 3D models and the outcomes provided by EERA since no relevant discrepancies have been detected among all the different numerical simulations.

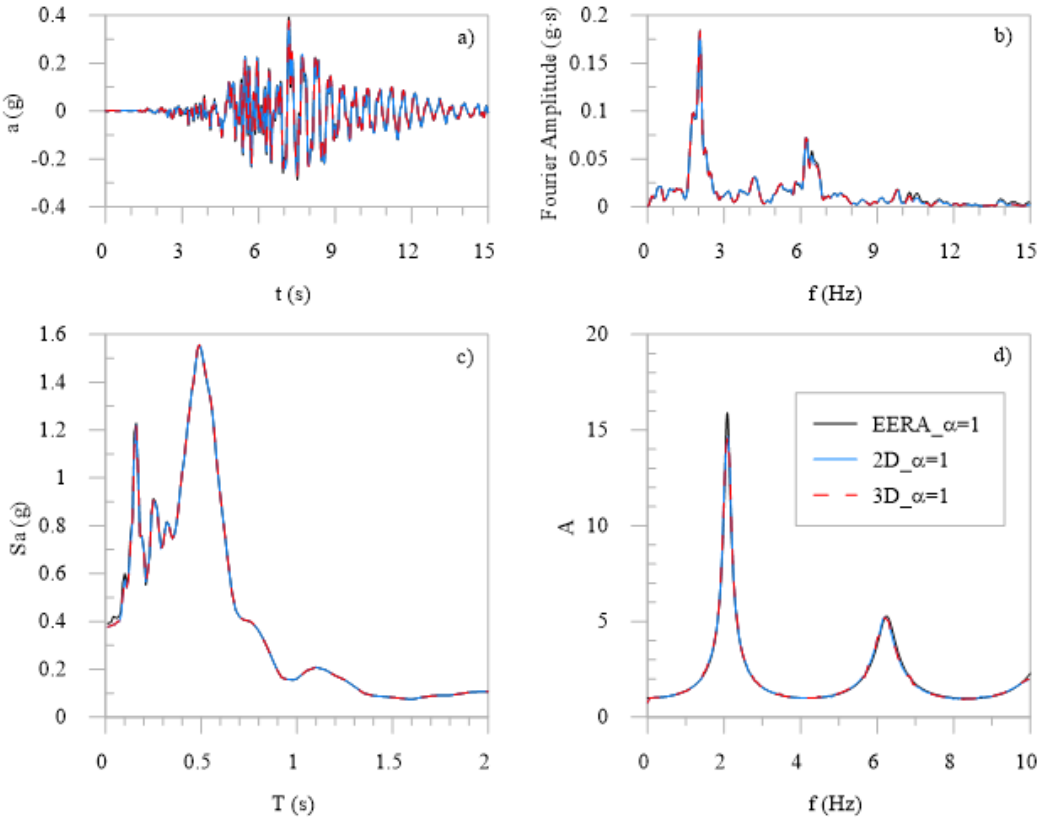

Fig. 4. 10 – Comparison between the outputs derived at the soil surface for the $\alpha = 1$ case from the EERA simulation and the 2D and 3D analyses performed in Abaqus: a) acceleration time-histories; b) Fourier spectra; c) acceleration response spectra; d) amplification functions.

This also applies to the other soil profiles $\alpha = 2.5$, 5, 10 and to the CS and SC cases whose results, for the sake of brevity, are not shown herein.

A slightly different situation occurs for the $\alpha = 15$ case reported in Fig. 4.11. Although the response obtained with the 2D FE model is still practically the same of EERA, the 3D model manifests, on average, a slightly underdamped response. Further investigations have been made increasing the dimension of the 3D model and adopting a finer mesh discretization, but no improvements have been observed. Even if a clear justification has not been found, it is thought that the 3D model mismatch is not linked to any problem with the boundary conditions settings. It could be related to some 3D effects that arise in the simulation as the heterogeneity degree of the deposit increases; probably these effects are not caught by the 2D and 1D (EERA) modelling.

Anyway, the amplification function (Fig. 4.11d) demonstrates that the model is still capable to catch the natural frequencies of the deposit and the amplification peaks expected by EERA, proving the effectiveness of the strategy adopted for the dynamic boundary conditions.

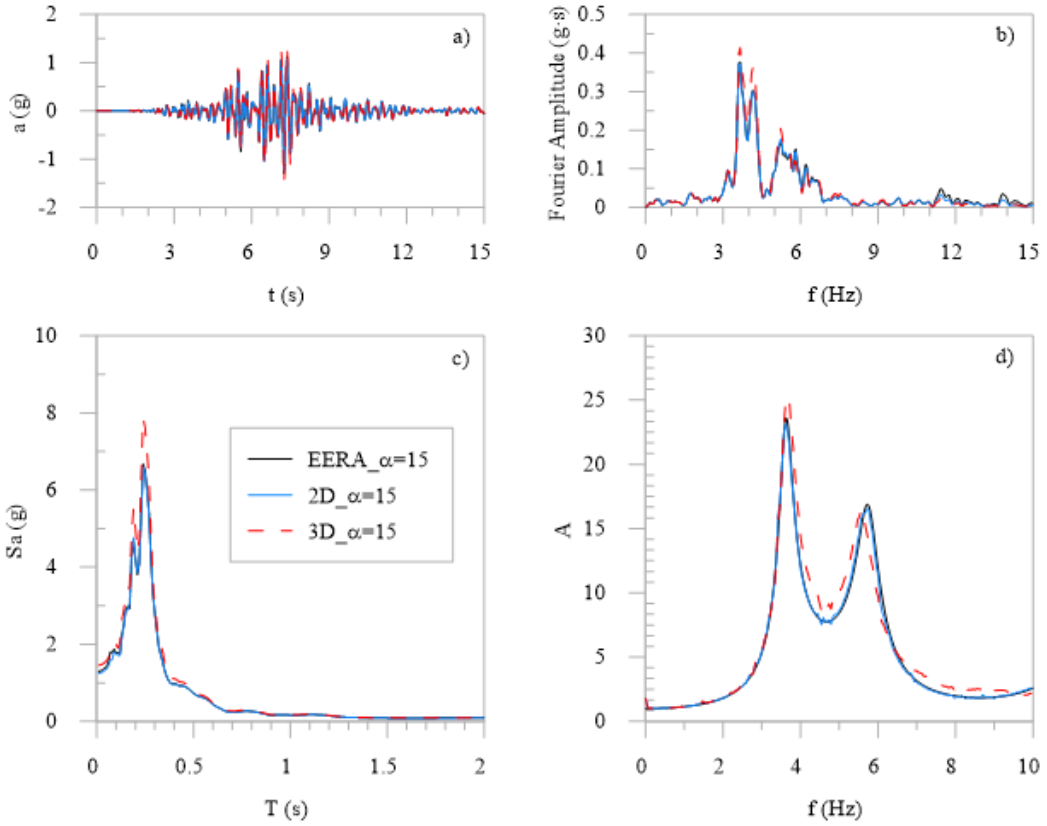

Fig. 4. 11– Comparison between the outputs derived at the soil surface for the α =15 case from the EERA simulation and the 2D and 3D analyses performed in Abaqus: a) acceleration time-histories; b) Fourier spectra; c) acceleration response spectra; d) amplification functions.

4.5. Dynamic soil-structure interaction analysis of the tower

4.5.1 Soil-tower interaction model

The numerical simulations carried out in this study have conducted implementing a complete 3D model constituted by the tower, its foundation and the subsoil which have been assembled in the FE software Abaqus (Fig. 4.12a).

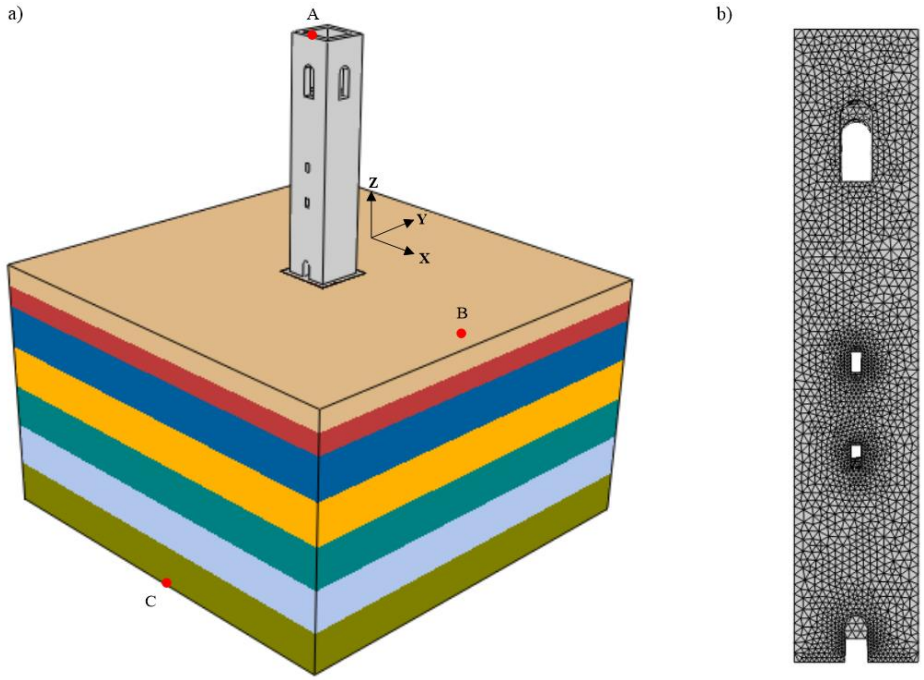

Fig. 4. 12– a) SSI model with the indications of some control points located at the top of the tower (point A), at the soil surface (point B) and at the bedrock of the deposit (point C); b) Mesh discretization of the tower.

The whole FE model is discretized using 4-node linear tetrahedral elements (C3D4). In particular, the tower mesh discretization is shown in Fig. 4.12b; the mesh has been refined around the openings and close to the base, in order to achieve an adequate numerical accuracy, resulting in 97690 elements and 21547 nodes. On the other

hand, the soil deposit dimensions and mesh discretization are the same adopted for the SRA analysis performed in free-field condition (Section 4.4).
The interface between the foundation and the deposit has been realized with a master-slave relationship: a penalty-type interaction law has been defined for the tangential behaviour, while a hard-contact type law has been imposed in the normal direction to prevent the interpenetration between the contact surfaces. The "tied-nodes" boundary condition has been assumed on the outer sides of the soil domain.
The soil behaviour has been described by the linear visco-elastic model with Rayleigh damping, as described in Section 4.4.
The SSI analyses consisted in modal frequency analyses, performed with the Lanczos method, and linear and non-linear time-history dynamic analyses carried out using the unconditionally stable implicit Hilber-Hughes-Taylor time integration scheme, i.e. an extension of the Newmark β-method which ensures the stability of the algorithm without introducing any additional numerical damping.
Finally, in Fig. 4.12a are also depicted some control points used to conduct the dynamic identification of the compliant-base tower by means of linear elastic dynamic analyses.

4.5.2 Dynamic identification of the tower interacting with the soil

The identification of the dynamic properties characterizing the system composed by the tower and the soil deposit has been performed following two complementary strategies. In addition to the typical modal eigenvalues frequency analysis usually adopted in structural engineering to derive the natural frequencies and the modal shapes of the structure, a dynamic analysis of the whole SSI model has been carried out assuming a linear elastic relationship for both the tower and the soil. Indeed, from this latter numerical approach it is also possible to evaluate the resonance frequencies of the structure and of the soil deposit. Moreover, this analysis has acted as a further check to ensure that the dimensions of the soil domain with its boundary conditions are appropriate and do not cause any wave reflection on the outer boundaries. This has been checked comparing the signal computed at point B in Fig. 4.12a from

the SSI model with the acceleration previously obtained in free-field conditions neglecting the presence of the tower.
In the following, the linear-elastic dynamic analysis results are first discussed and then the modal frequency analysis is presented.

4.5.2.1 Linear-elastic dynamic time-history analyses of the system

The first objective of these analyses is to check the adequacy of the dynamic boundary conditions and soil domain size of the SSI model to verify the reliability of the numerical approach. To this purpose, a series of linear visco-elastic dynamic SSI analyses have been performed assuming for both the soil and the tower the linear visco-elastic behaviour. In particular, the G and D profiles of Sections 4.2-4.3 (i.e. LIN approach) have been implemented for the cases of $\alpha = 1$ and $\alpha = 15$, representing the minimum and the maximum soil heterogeneity degree, while the following elastic properties of the structure have been set: $\rho = 1900 \text{Kg/m}^3$, $E = 3500 \text{MPa}$ and $\upsilon = 0.1$, as reported in Casolo et al. (2017).
A series of control points has been selected both on the tower and on the soil (Fig. 4.12a): point A on the top of the tower, point B at the soil surface far enough from the structure to be representative of the free-field response and point C at the bedrock of the deposit.
The amplification functions derived as the ratio of the Fourier spectra recorded respectively at point B and C of the SSI model are reported in Fig. 4.13 (FE_SSI). The SSI amplification functions identifying the resonance frequencies of the soil deposit are also compared with the corresponding ones obtained through both EERA and the previously discussed 3D FE free-field simulations (FE_Free-Field). A fairly good agreement of the SSI model solution against the benchmarks can be recognised, especially for the $\alpha = 1$ case; the comparison is quite satisfactory also for $\alpha = 15$. It might be concluded that the numerical approach can be applied also for the SSI simulations.

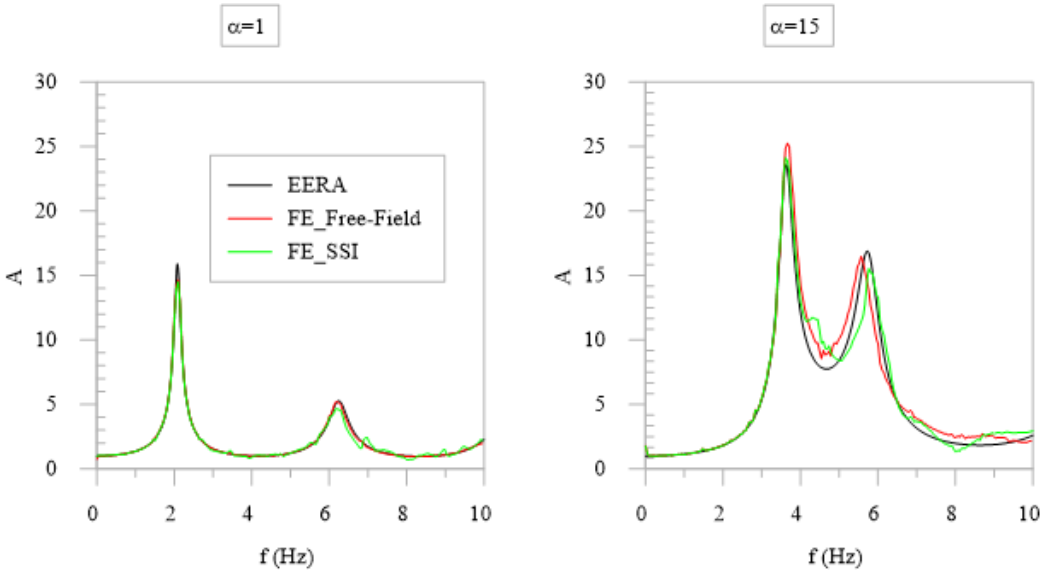

Fig. 4. 13 – Comparison of the amplification functions derived from EERA, the Abaqus FE free-field model and the SSI one for $\alpha = 1$ and $\alpha = 15$.

To identify the resonance frequencies of the tower resting on a deformable base, for each heterogeneous soil profile the amplification functions have been determined as the ratio between the Fourier spectrum at point A and point B. The amplification curves are depicted in Fig. 4.14 for the first 2 natural modes of the structure as a function of normalized frequencies. Specifically, the frequencies are normalized to those relative to the fixed-base condition. Indeed, in addition to the 3D models of the tower resting on a deformable support, a further analysis has been performed considering the structure standing on a very rigid homogeneous subsoil (assuming $V_S = 8000$m/s) to simulate the fixed-base condition.

The amplification functions illustrated in Fig. 4.14 give evidence to some of the effects induced by dynamic soil-structure interaction. Indeed, looking at the first and second mode of the tower, the primary effect of soil compliance is to reduce the dynamic stiffness and increase the damping ratio of the soil-tower system, leading to lower natural frequencies and lower magnitudes of the motion with respect to the fixed-base condition. This effect is more pronounced for higher soil heterogeneity degrees, while

it becomes less significant for less heterogenous soils. For instance, the SC case, which would result in $\alpha = 0.44$, is characterized by the less pronounced frequency reduction and damping increase. Finally, much smaller values of the amplification factors are obtained when the second natural mode is inspected.

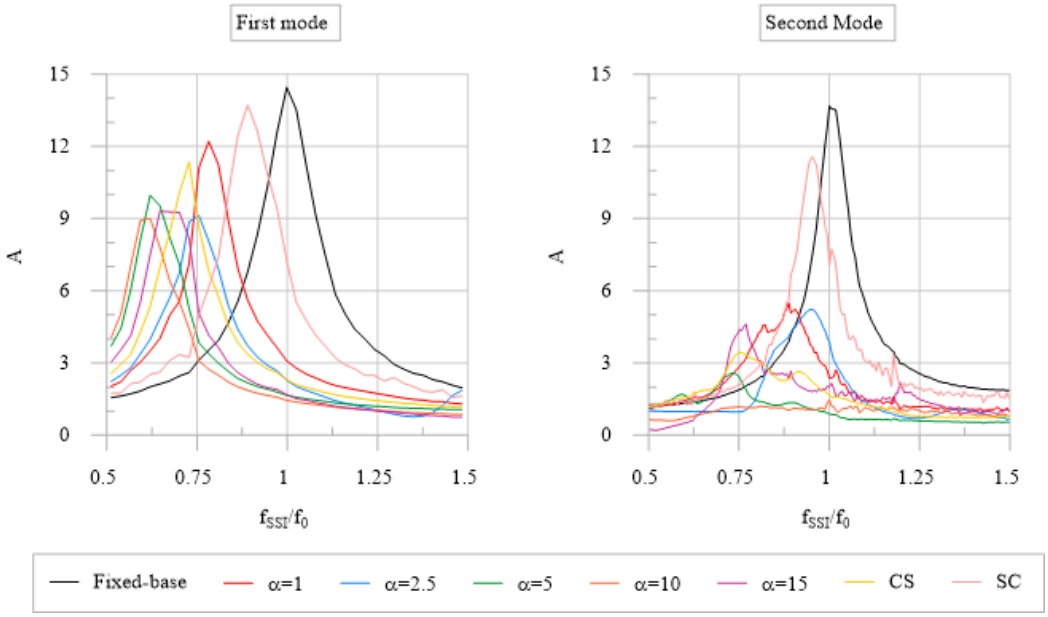

Fig. 4. 14 – Amplification functions of the tower motion normalized by the first and second frequency of the fixed-base tower (f_0) for different heterogeneity ratio α .

The effects of the soil-structure interaction may be significant, with a change in the natural periods of the soil-tower system strongly dependent on the soil profile characteristics. Further confirmations and insights are provided by the eigenvalues analysis presented in the following section.

4.5.2.2 Modal eigenvalues analysis of the system

The modal eigenvalues analyses have been performed to assess the influence of soil deformability on the modal properties of the tower, comparing the natural frequencies and modal shapes of the system with the reference fixed-base condition. The results

obtained considering the fixed-base scenario are summarised in Tab. 4.3. It is evident that, due to the symmetrical geometry characterising the structure, the flexural modes are specular in the X and Y directions (Fig. 4.12a), while the torsional mode contribution is very low (about 0.20% of excited mass). Bearing in mind these considerations, for the sake of convenience, only the modal features related to the X direction will be analysed in the following.

Mode	Frequency (Hz)	Mode type	Excited mass m_x (%)	Excited mass m_y (%)	Excited mass m_z (%)
1	1.92	1st flexural	0	59.4	0
2	1.94	1st flexural	59.6	0	0
3	7.69	1st torsional	0.2	0	0
4	8.71	2nd flexural	21	0	0
5	8.75	2nd flexural	0	20.9	0

Tab. 4. 3 – Modal analyses results for the fixed-base tower.

The frequencies outputs related to the SSI models are listed in Tab. 4.4 for both LIN and EQ-LIN soil behaviour, adopting for the deposit the corresponding G and D profiles as discussed in Section 4.4. Some interesting points can be highlighted:

- in general, the resulting frequencies of the structure on the deformable base, f_{SSI-1}, are quite variable depending on the stratigraphic heterogeneity; this reflects the frequency variability obtained from the EERA analyses discussed in Section 4.3 and confirms the soil compliance relevance;
- independently from the soil modelling approach adopted, a clear reduction in the natural frequencies of the tower standing on deformable soils with respect to the fixed-base condition is recognizable for both the first and second mode of vibration, in agreement with the evidence shown by the linear-elastic dynamic analysis;
- the SC case presents the less significant reduction of the tower natural frequencies, probably because it is characterized by the highest value of V_S in the upper part of the deposit (410 m/s) which makes it the “most close” to a

rigid soil condition; indeed, for a slender tower, de Silva et al. (2014a) found that for $V_S \approx 600$m/s the tower could be considered standing on a rigid deposit;

- as expected, the non-linear soil effects introduced with the EQ-LIN approach produce a further reduction in the structural natural frequencies;
- for both LIN and EQ-LIN approaches, the ratios of the SSI tower frequencies, f_{SSI}, to the corresponding soil ones, f_{SOIL}, respectively denoted as ξ_1 ($= f_{SSI-1}/f_{SOIL-1}$) and ξ_2 ($= f_{SSI-2}/f_{SOIL-2}$), show how, with the exception of the SC case, f_{SSI-1} is lower and quite distant from f_{SOIL-1}, while f_{SSI-2} can be both higher or smaller, but in any case much closer to f_{SOIL-2}; as a consequence, it seems that f_{SOIL-2} might affect the dynamic response of the tower as well as yield to resonance phenomena of the tower in interaction with the soil.

	LIN				EQ-LIN			
SOIL PROFILE	f_{SSI-1} (Hz)	f_{SSI-2} (Hz)	ξ_1	ξ_2	f_{SSI-1} (Hz)	f_{SSI-2} (Hz)	ξ_1	ξ_2
$\alpha = 1$	1.43	7.41	0.68	1.19	1.27	6.75	0.69	1.19
$\alpha = 2.5$	1.30	7.67	0.52	1.20	1.04	6.54	0.46	1.11
$\alpha = 5$	1.15	6.28	0.40	0.95	0.90	5.57	0.33	0.91
$\alpha = 10$	1.12	6.22	0.33	1.01	0.94	5.55	0.31	1.15
$\alpha = 15$	1.22	6.52	0.34	1.19	1.12	6.02	0.40	1.25
CS	1.32	7.57	0.53	0.97	1.02	6.73	0.46	1.15
SC	1.61	7.82	1.04	1.28	1.55	6.93	1.13	1.24

Tab. 4. 4 – First and second natural frequency of the tower resting on deformable soil and normalized values over the corresponding soil resonance frequencies ($\xi_1 = f_{SSI-1}/f_{SOIL-1}$ and $\xi_2 = f_{SSI-2}/f_{SOIL-2}$).

Fig. 4.15 shows the same results plotted in terms of periods of the tower resting on the deformable soil (T_{SSI}) normalized by the fixed-base period (T_0) of the tower, as a

function of the heterogeneity parameter α (it is recalled that the CS and the SC cases correspond to α =0.44 and α =2.28, respectively). The first natural period increases much more than the second one for each considered heterogeneity ratio, no matter the soil behaviour is LIN or EQ-LIN. The chart also confirms the expected phenomenon of the elongation of the periods due to the soil stiffness reduction introduced in the EQ-LIN approach with respect to the LIN one. Moreover, the trends of the curves look quite similar. The T_{SSI-1} curves show a progressive increase of the values until the case of α =10 for LIN and α =5 for EQ-LIN soil; the period start to decrease afterward. The T_{SSI-2} curves are, instead, characterized by a first flatted trend until α =2.5 and then by show a sharp increase in the elongation for α =5; T_{SSI-2} it seems to reduce again for α =15.

Anyway, the effects of the soil-structure interaction may be really significant leading to double the fixed-base tower periods (see T_{SSI-1} for α =5 in the EQ-LIN case), with a change in the natural periods of the soil-tower system strongly dependent on the soil profile characteristics. Hence, these effects should be taken into account to obtain an accurate evaluation of the dynamic response of the system.

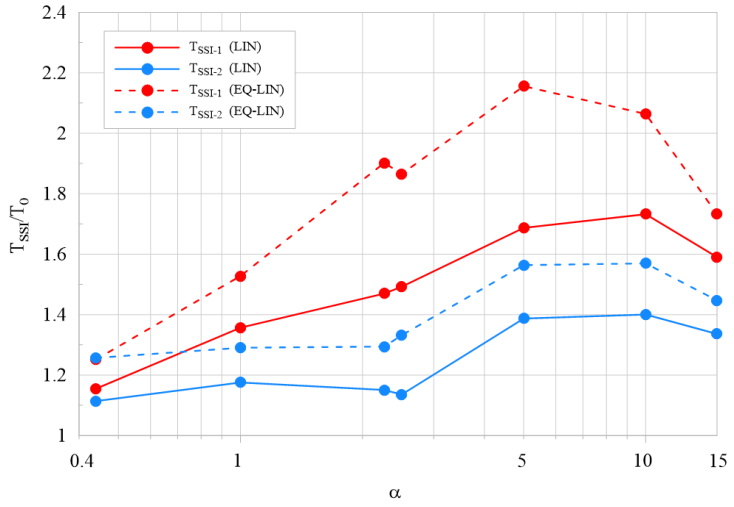

Fig. 4. 15 – First and second natural period of the SSI tower (T_{SSI}) normalized for the corresponding values in fixed-base condition (T_0) plotted as a function of the heterogeneity parameter α .

Finally, for the sake completeness, the one-to-one comparison between resonance frequencies derived from the dynamic time-history analyses and the modal analyses are reported in Fig. 4.16 for the LIN approach. For both the first and second mode the results show a good agreement between the two numerical strategies, confirming the reliability of the numerical approach followed to build up the SSI model.

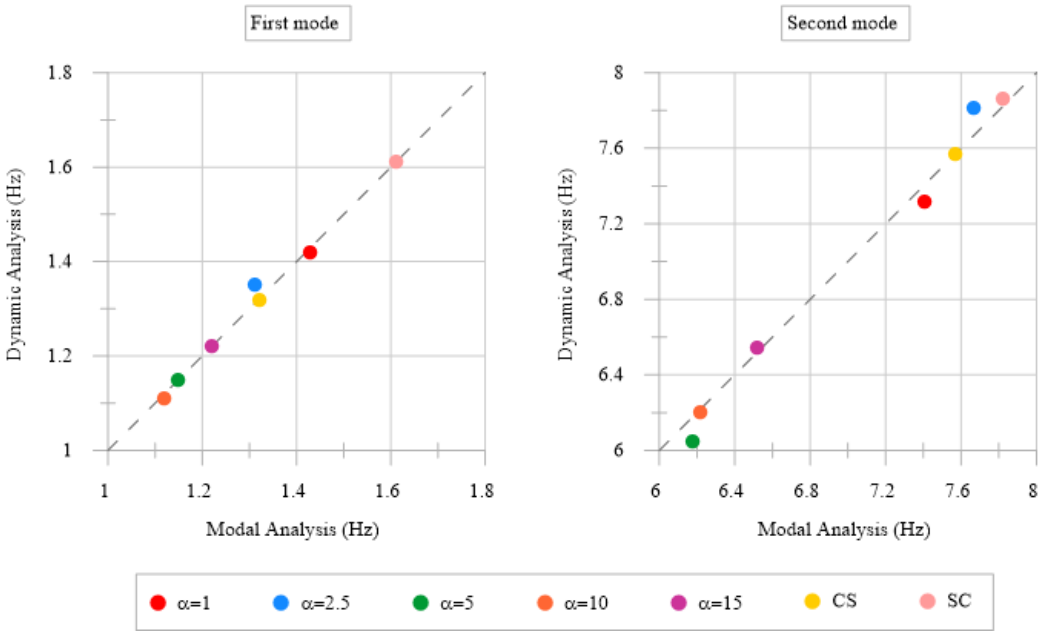

Fig. 4. 16 – Comparison between the f_{SSI} frequency outputs derived from the modal eigenvalues analysis and the linear-elastic dynamic analysis for the LIN soil case.

Another important outcome extracted from the eigenvalues analyses is represented by the modal shapes exhibited by the structure. The first and second modal shapes are illustrated in Fig. 4.17 for both LIN and EQ-LIN soil behaviour. To present a more effective comparison with the fixed-base scheme, the translational displacements recorded at the base of the compliant models are removed and the resulting displacements are then normalized with respect to the corresponding displacements attained at top of the structure of each model (point A in Fig. 4.12a).

It can be noted that the first modal shape does not seem to be heavily altered by SSI: all the structural deformed shapes superimpose each other and are rather close to the fixed-base case (black line in Fig. 4.17) for both LIN and EQ-LIN soil behaviour. Conversely, the second modal shape displays a more evident dependence on the soil compliance, consistently with the scientific literature (Casolo et al. 2017, de Silva et al. 2015a). Even if a clear trend cannot be identified, it seems that as the soil heterogeneity degree increases, the modal shapes variability reduces.

Moreover, it can be observed that the most remarkable changes related to non-linearity effects are restrained to $\alpha = 1$ and SC cases. This might be explained referring to the EQ-LIN shear modulus reduction profiles reported in Fig. 4.5b; in fact, these profiles present the most significant shear stiffness degradation (close to 25-30%) localized in the bottom part of the soil deposit. It follows that these profiles are also characterized by the most significant reduction of the V_H values. Hence $\alpha = 1$ and SC also present the most altered heterogeneity ratios ($\alpha = \frac{V_H}{V_0}$) after that the EERA EQ-LIN analyses are performed, which might justify the modification with respect to the LIN analyses. On the other hand, the remaining profiles present lower stiffness reductions and, as a result, the second modal shape does not change a lot when the EQ-LIN soil behaviour is adopted.

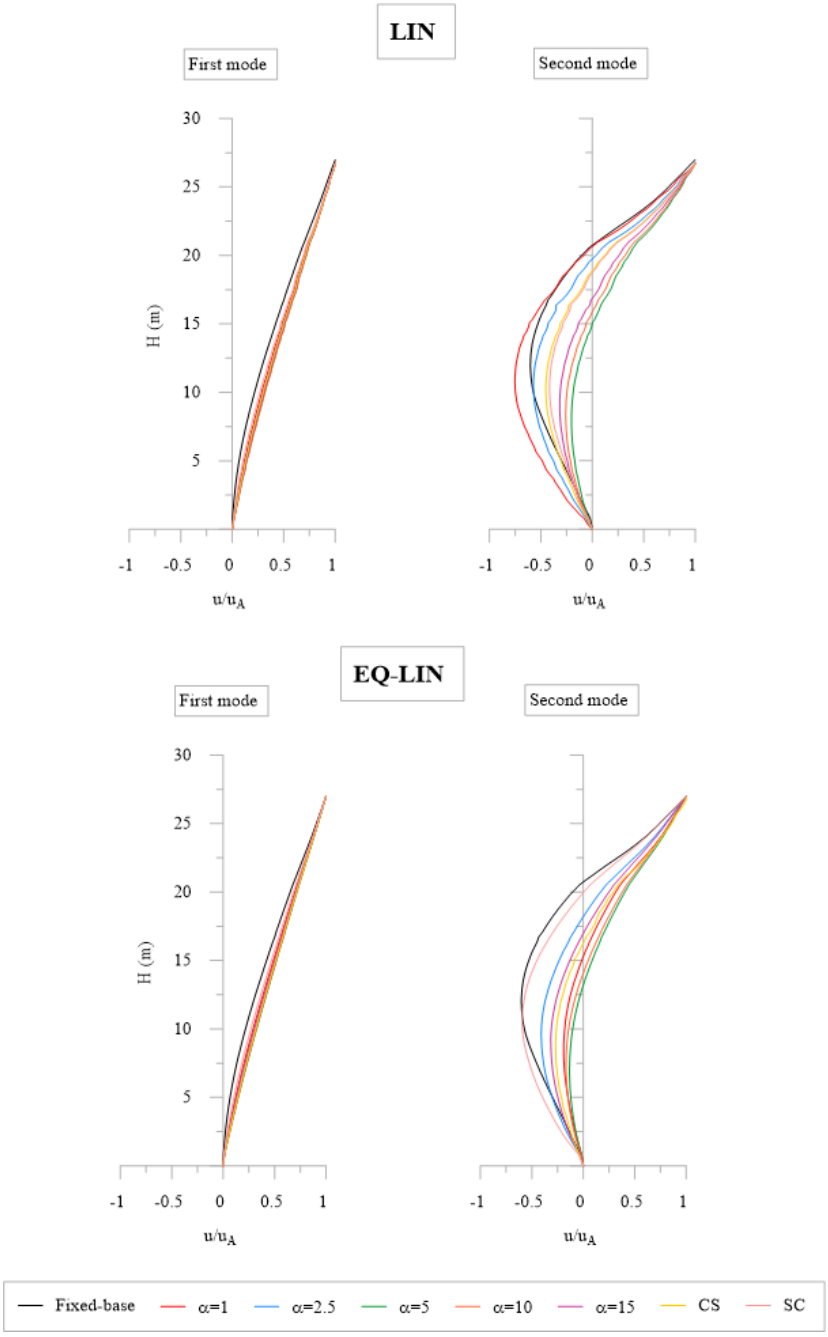

Fig. 4. 17 – First and second modal shapes in the X direction depurated from the translational displacement at the base of the structure and normalized for the maximum horizontal top displacement (u_A): LIN and EQ-LIN analyses.

4.5.3 Investigation of the nonlinear response of the tower

After the extensive investigation carried out on the soil behaviour adopted to characterize the foundation deposit, the reliability of the dynamic boundary conditions adopted for the soil domain and the dynamic identification of both soil deposit and structure on compliant-base in the elastic field, this Section presents the results derived from non-linear dynamic time-history analyses of the soil-tower system.

4.5.3.1 Cyclic shear response of the adopted dataset for the masonry mechanical behaviour

The dynamic SSI simulations have been performed adopting the CDP plastic-damage model to describe the masonry behaviour of the tower. The main features of the constitutive model have been already introduced in Section 3.2.2, while the material properties and the tensile and compressive laws adopted in this study are consistent with those proposed by Casolo et al. (2017) and are reported in Tab. 4.5 and Fig. 4.18. In addition, the damage relationships follow a linear law both in tension and compression, starting from $d = 0$ until $d = 0.95$, which is attained at the strain value corresponding to the residual resistance (Fig. 4.18).

ρ	E_0	ν	ψ	f_{b0} / f_{c0}	ε	K_C	w_c	w_t
(Kg/m^3)	(MPa)	(-)	(°)	(-)	(-)	(-)	(-)	(-)
1900	3500	0.1	20	1.16	0.1	2/3	1	0

Tab. 4. 5 – Model parameters adopted for the masonry.

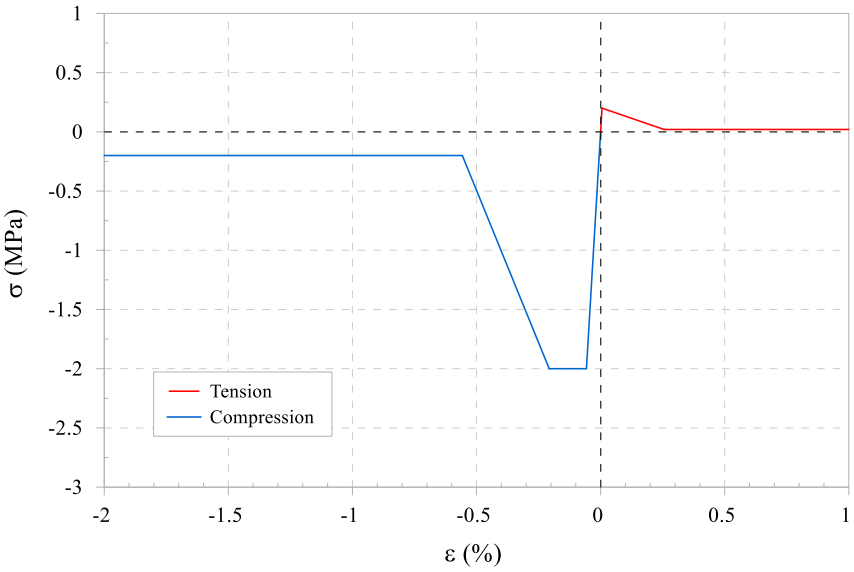

Fig. 4. 18 – Stress-strain relationships adopted for the masonry.

Herein the response of the CDP model under shear loading using this dataset is discussed following the approach presented in Section 3.2.3.1. A set of numerical cyclic shear simulations has been performed on a cube element of 1m length, discretized with one 3D 4-node tetrahedral element mesh (C3D4). A sketch of the FE model is displayed in Fig. 4.19.

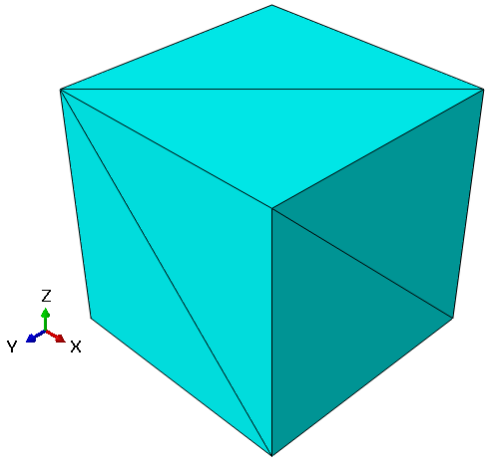

Fig. 4. 19 – Cube specimen discretized with a single C3D4 mesh element.

The cube is perfectly fixed at the base, while on the upper surface the shear condition is applied through a prescribed displacement preventing any other movement. The tests are performed following a displacement control procedure using the two load paths illustrated in Fig. 4.20: a harmonic displacement time-history with constant amplitude equal to 1mm and a displacement time-history with variable amplitude. Both the load paths are characterized by 12 cycles. In particular the variable one can by divided into 4 different phases composed by 3 cycles of constant amplitude: the first one reaches 0.1mm (between 0s and 6s), the second one 0.5mm (6s-12s), the third 1mm (12s-18s), i.e. equal to the constant amplitude of the first displacement time-history, and the fourth 2mm (18s-24s).

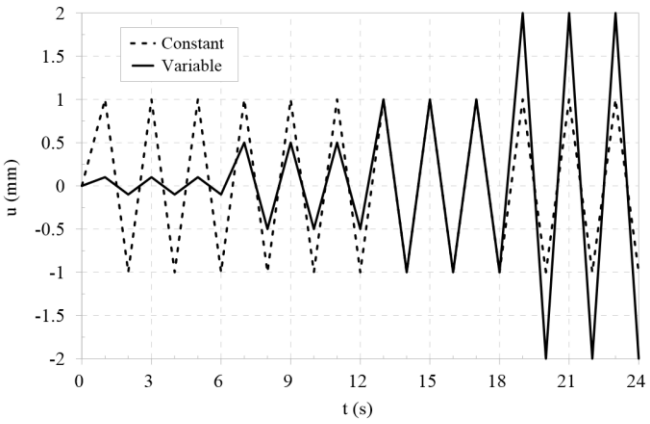

Fig. 4. 20 – Displacement time-histories applied during the cyclic shear tests on the cube specimen.

The first two cyclic shear tests have been carried out considering a plastic and a plastic-damage behaviour, in order to assess their relative contribution on the shear performance of the constitutive model. The numerical tests have been carried out using the constant displacement time-history only and the obtained results are shown in Fig. 4.21 in terms of $\tau - \gamma$ curves.

The plastic model (green line) exhibits an evident dissipative capacity in the first 6 cycles characterized by well-defined closed loops (Fig. 4.21a); in addition, higher and higher shear resistances are also gradually mobilized. On the other hand, during cycles 7-12 (Fig. 4.21b) a “steady-state” condition is also attained with much smaller

associated $\tau - \gamma$ loops and, hence, almost no energy dissipation. It also appears that the secant shear stiffness of the model does not change for the whole duration of the test, achieving a value of 1585MPa equal to the initial shear stiffness modulus G_0.

When the plastic-damage behaviour is considered (red line), an overall lower plastic dissipation is recorded if compared to the pure plastic model during the cycles 1-6 (Fig. 4.21a); indeed, in this case the energy is no more dissipated only for plasticity, but also for the material deterioration due to the introduction of the damage formulation. This implies that the shear strength reduces according to the progressive stiffness degradation. Furthermore, a "steady-state" condition if finally attained during the cycles 7-12 (Fig. 4.21b), which are characterised by a secant shear stiffness modulus G equal to 817MPa, 51% lower than the initial shear stiffness modulus G_0.

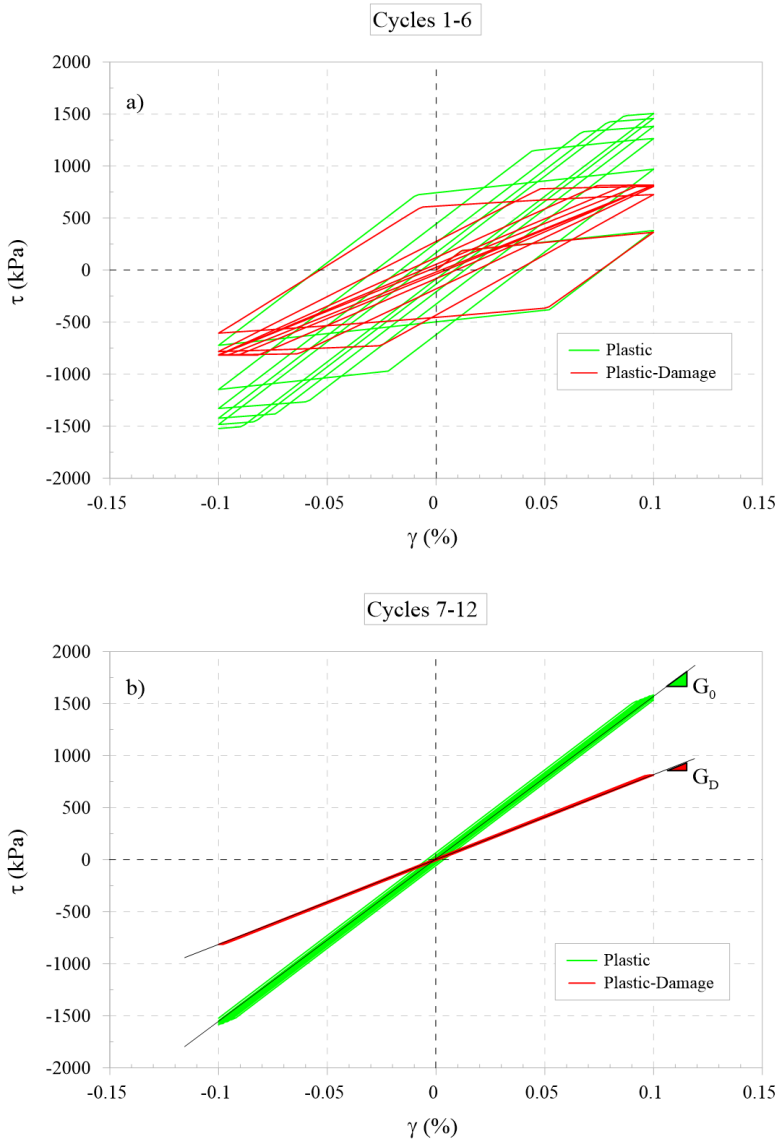

Fig. 4. 21 – Shear stress-strain curves obtained for the plastic and plastic-damage behaviour considering the constant load-path type.

The second set of simulations has been aimed at evaluating the effect of the loading type on the shear response of the model, using the constant and variable path (named CT analysis and VT analysis in the following) reported in Fig. 4.20; in these simulations, only the plastic-damage behaviour is considered.

The $\tau - \gamma$ results are depicted in Fig. 4.22. The overall response is shown in Fig. 4.22a for the entire duration of the tests (i.e. 12 cycles), while Fig. 4.22b reports the stress-strain curves exhibited during the first 9 cycles of the VT analysis with amplitudes less or equal to the CT one (i.e. 1mm). In the cycles range 1-6 of the VT test (thin blue curve) the non-linear capacity of the material has already been mobilized (showing energy dissipation and stiffness degradation of the material), despite the imposed amplitudes are lower than 1mm. When the subsequent phase of cycles 7-9 of 1mm amplitude is considered (thick blue curve), the plastic-damage effects increase. Comparing this latter phase of the VT simulation with the CT one during the cycles 1-3, it can be stated that the smother path used in the VT analysis to attain displacements of 1mm has initially produced a stiffer response of the material, even though the effect gradually reduces over the subsequent cycles. Therefore, this suggests that there is a dependency of the model response on the load history path. Finally, when the more demanding target displacement of 2mm is prescribed in the VT simulation, a more remarkable strength and stiffness degradation of the material is observed (Fig. 4.22a).

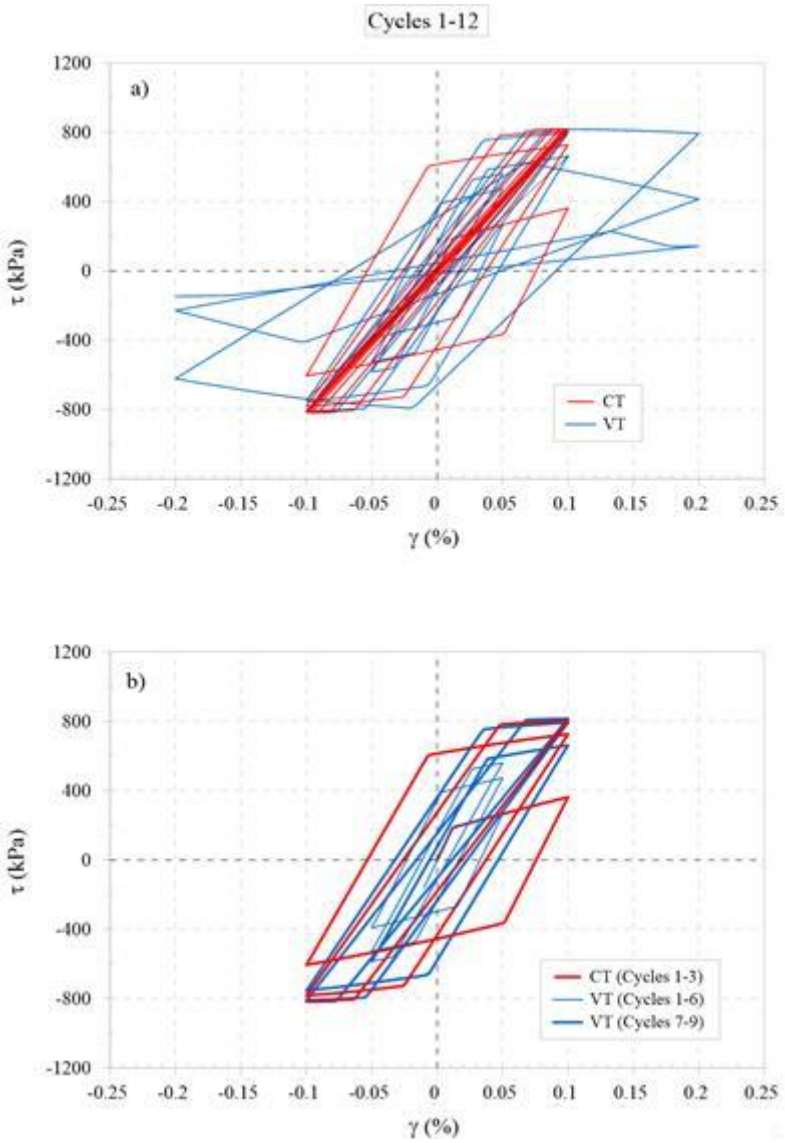

Fig. 4. 22 – Shear stress-strain curves obtained for the plastic-damage behaviour using the constant and variable displacement time-histories.

One last numerical analysis has been performed to assess the effect of the simultaneous application of a displacement time-history along the X and Y directions of the cube specimen, which should be representative of a bidirectional seismic input motions condition applied to a structure. In this case, only the plastic-damage behaviour

and the variable load-history type have been considered. The results are shown in Fig. 4.23. The application of both displacement components (yellow line) determines a remarkable reduction of the material stiffness and of the peak and residual resistances with respect to the single component case (blue line).

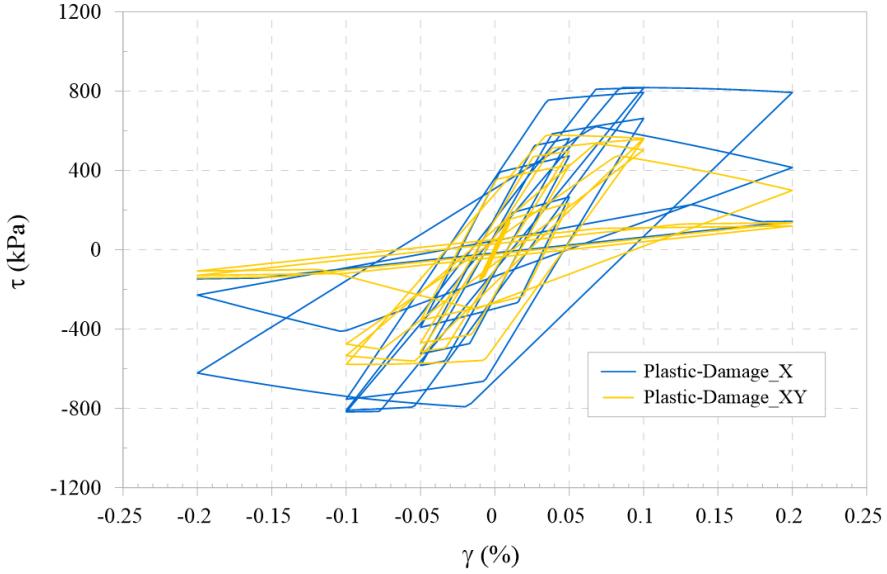

Fig. 4. 23 – Shear stress-strain curves obtained for the plastic-damage behaviour using the variable displacement time-history applied along the X direction or simultaneously along the X and Y directions.

4.5.3.2 Non-linear dynamic time-history analyses

The non-linear dynamic time-history analyses of the 3D soil-tower system are herein discussed. One of the main purposes of the study is to assess the influence of the soil compliance on the seismic response of the masonry tower. To this aim, the adopted strategy has consisted in performing the numerical simulations following two approaches:

- a coupled approach which involves the whole SSI model;
- a decoupled approach, in which the tower is modelled by means of a fixed-base scheme subjected to the input motion derived from the fully coupled SSI simulation at the foundation level.

Thus, in both coupled and decoupled approach (form now on identified as SSI and FIX, respectively), the structure is actually subjected to the same signal at the base and all the deviations in the tower structural response observed between the two classes of simulations can be related to the soil compliance.

To evaluate the effects of the soil heterogeneity on the non-linear response of the tower, the dynamic SSI simulations have been performed assuming the linear visco-elastic profiles for the soil deposit (LIN), while, to investigate the influence of the soil non-linearity, the SSI analyses have been carried out adopting the equivalent-linear visco-elastic approach for the soil deposit (EQ-LIN). Both set of simulations have been performed applying at the bottom of the model the South Iceland input motion (Fig. 4.4).

The results of the non-linear analyses are illustrated in terms of tensile damage, acceleration response spectra recorded at different control points of the model, bending and rocking displacements (defined as in Fig. 4.24). Indeed, the total horizontal displacement (u_{tot}) of the tower-foundation system is composed by three parts: the translational displacement (u_u) and the rocking displacement (u_δ) (computed throughout the rotation of the foundation δ), which constitute the foundation movement induced by the earthquake, and the bending displacement (u_θ) of the structure.

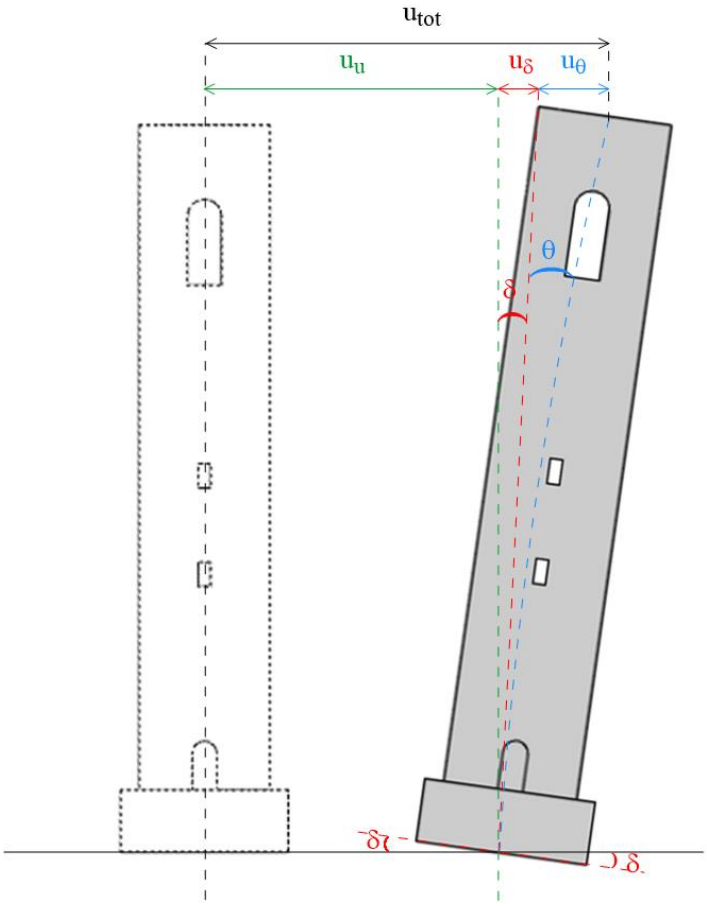

Fig. 4. 24 – Sketch of the translational (u_u), rocking (u_δ)and bending (u_θ) displacements affecting the tower during the seismic action.

4.5.3.2.1. Results of the analyses with the linear visco-elastic soil approach

First of all, the tensile damage distributions at the end of the seismic event are depicted in Fig. 4.25.

More specifically, for the homogeneous soil case ($\alpha = 1$) the SSI simulation appears to produce a more hazardous scenario with respect to the FIX one. Indeed, the FIX scheme presents a damage localization close to the basement level of the tower; conversely the SSI one provides a more severe concentration right above the main entrance, characterized by inclined cracks, and in correspondence of the minor open-

ings in the middle of the structure. In both models the upper part of the tower is not much affected (Fig. 4.25a).

In the $\alpha = 2.5$ case, both schemes are characterized by an evident damage localization in the belfry area, while only in the FIX simulation the first half of the tower results affected by the seismic action (Fig. 4.25a).

In the $\alpha = 5$ case, the SSI analysis predicts a damage pattern concentrated at the bell cell, while in the FIX analysis it is localized only right above the door (Fig. 4.25a).

In the $\alpha = 10$ case, the SSI analysis provides just very mild damage at the basement level and in correspondence of the upper openings, while the FIX one shows a much more hazardous scenario with diagonal cracks in the first half of the tower and more limited material degradation at the belfry (Fig. 4.25b).

For $\alpha = 15$, a rather comparable scenario predicted by the two modelling strategies, characterized by a severe damage especially at the bell cell level, can be observed (Fig. 4.25b).

In the CS case, the SSI analysis shows that the belfry is once again very affected by the earthquake, while a smaller damage distribution is observed at the basement level and close to the minor openings. Conversely, the FIX analysis manifests severe damage patterns both in the upper and lower part of the structure (Fig. 4.25c).

Finally, the SC case presents, at least qualitatively, a similar damage scenario for both the fully-coupled and the decoupled modelling approach, showing shear diagonal cracks which develop in the first half and at the basement level of the structure (Fig. 4.25c).

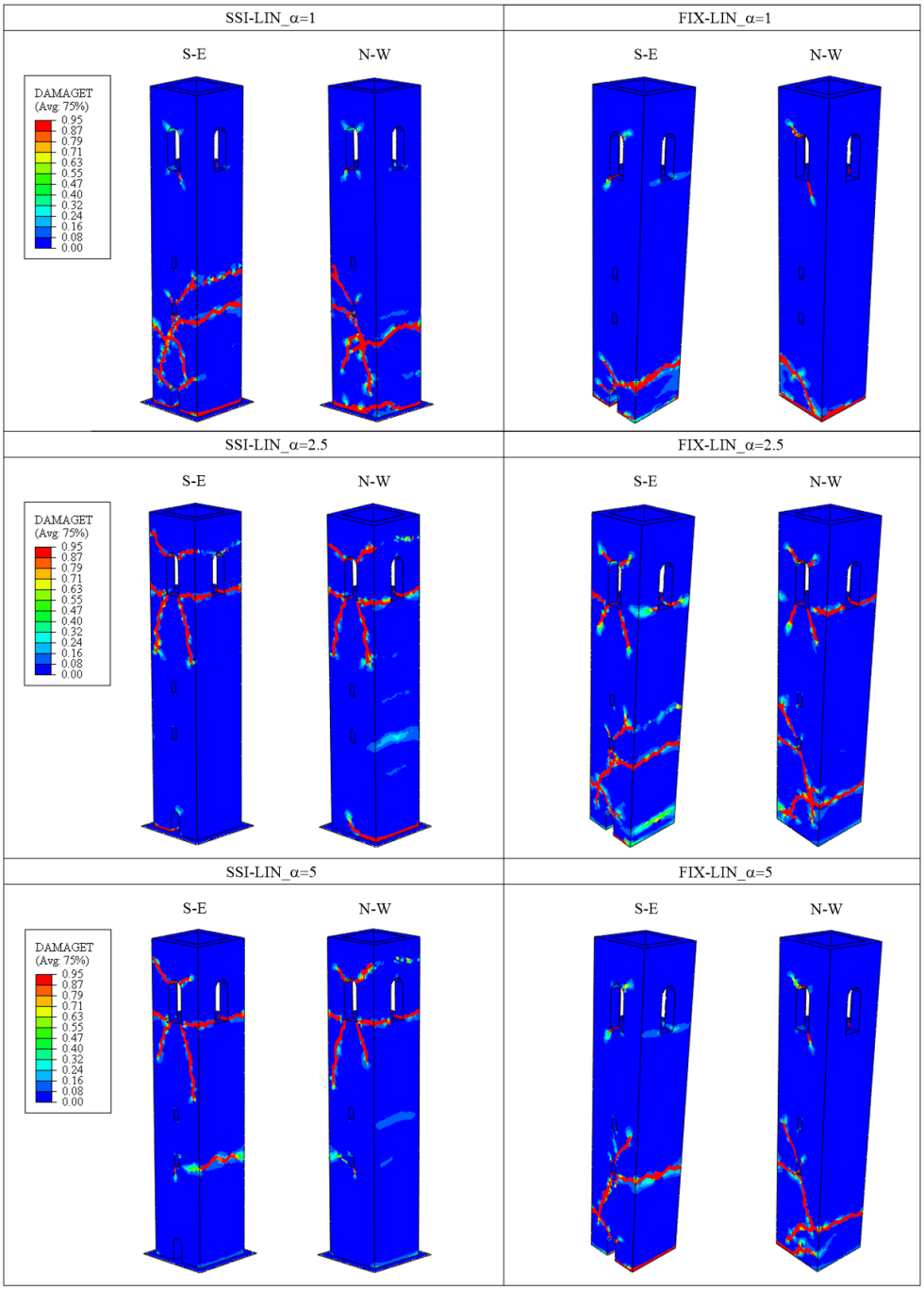

Fig. 4. 25a – Tensile damage contours plots at the end of the seismic input motion for the LIN analyses, considering the SSI and FIX models (α =1; 2.5; 5)

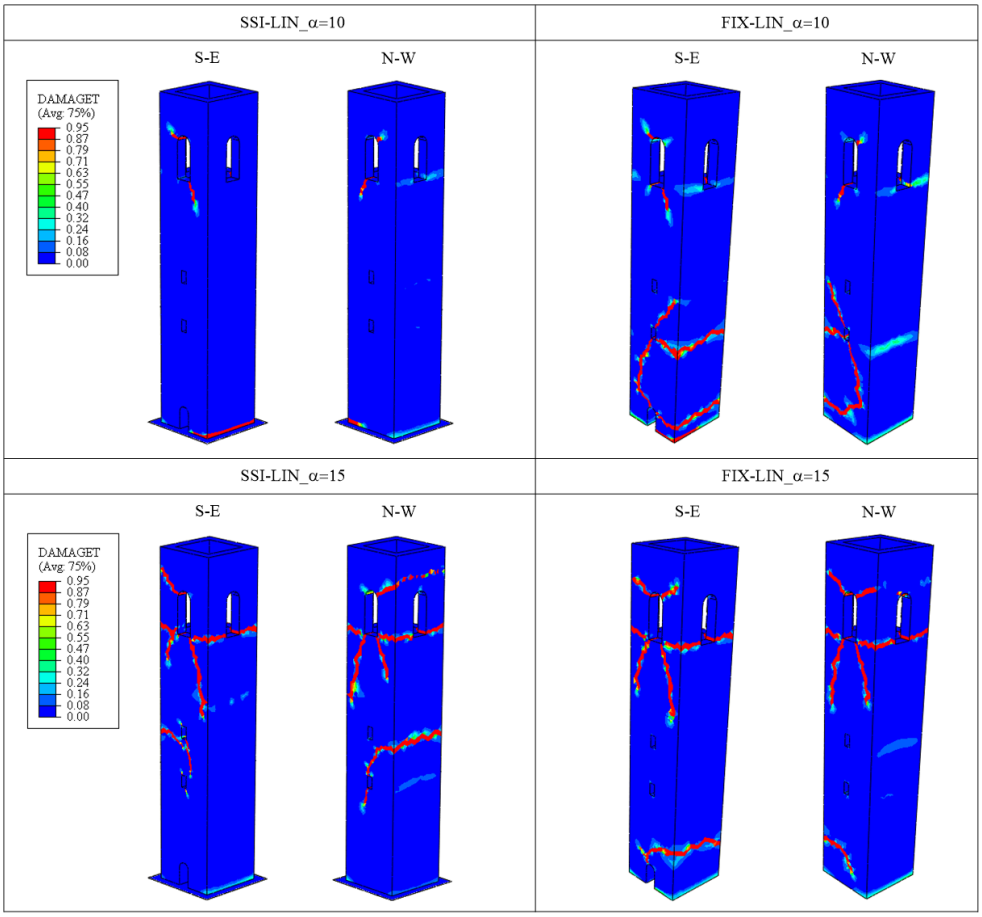

Fig. 4.25b – Tensile damage contours plots at the end of the seismic input motion for the LIN analyses, considering the SSI and FIX models (α =10; 15).

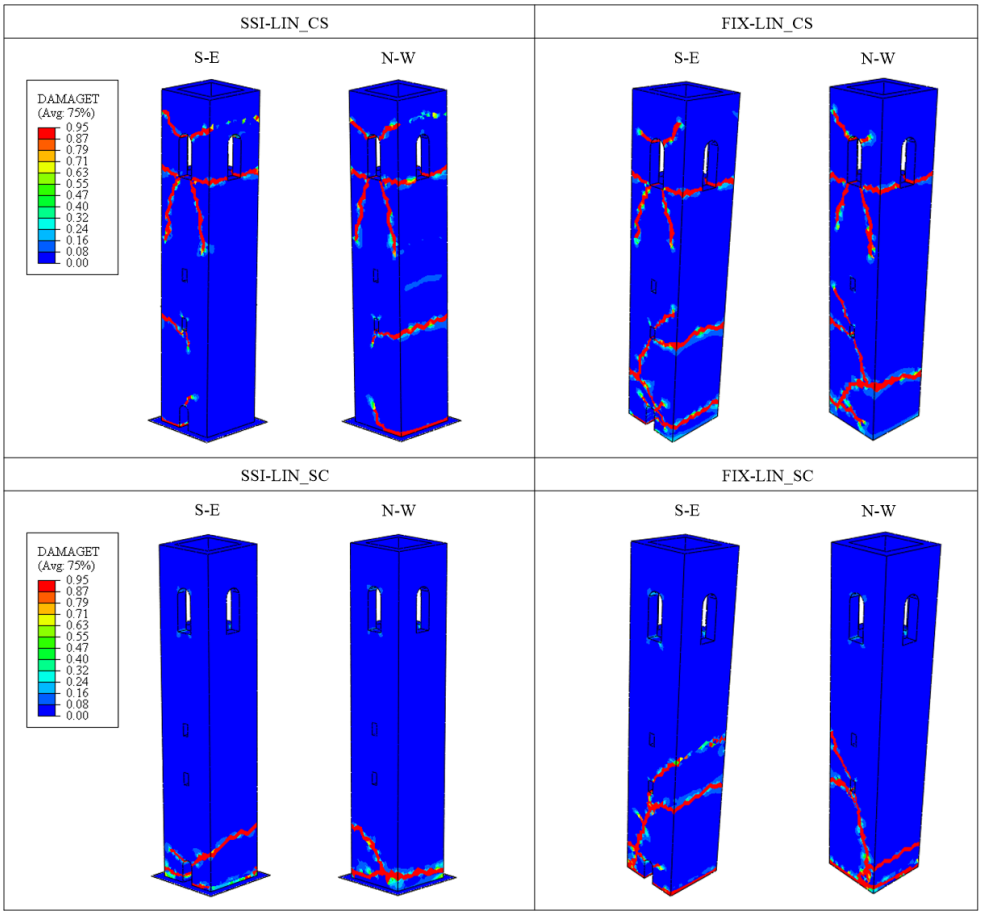

Fig. 4.25c – Tensile damage contours plots at the end of the seismic input motion for the LIN analyses, considering the SSI and FIX models (CS; SC).

The different damage distributions induced by the earthquake might be explained through the analysis of the acceleration response spectra reported in Fig. 4.26, showing the signals recorded at the foundation level (thick red line), representing the seismic actions in common between the coupled and uncoupled approaches, and at top of the tower both for the SSI and the FIX cases. In addition, the corresponding first two natural periods of the structure considered on deformable (discontinuous red lines) and fixed (discontinuous black lines) base are also reported. The phenomenon of period elongation due to inertial interaction produces a reduction of the seismic demand to the structure for the 1st period of oscillation (with the exception of the SSI-LIN_SC case); conversely for the 2nd period of oscillation the inertial interaction provides the increase of the spectral accelerations values.

Moreover, the spectra recorded at the top of the tower highlight that the seismic signal propagation along the structure might be very different considering or not the soil compliance. Indeed, the spectral acceleration are usually amplified in correspondence of the natural periods of the structure. As a consequence, the more the period elongation phenomenon is relevant, the more the SSI and FIX spectral shapes differ and different damage scenarios are likely to occur.

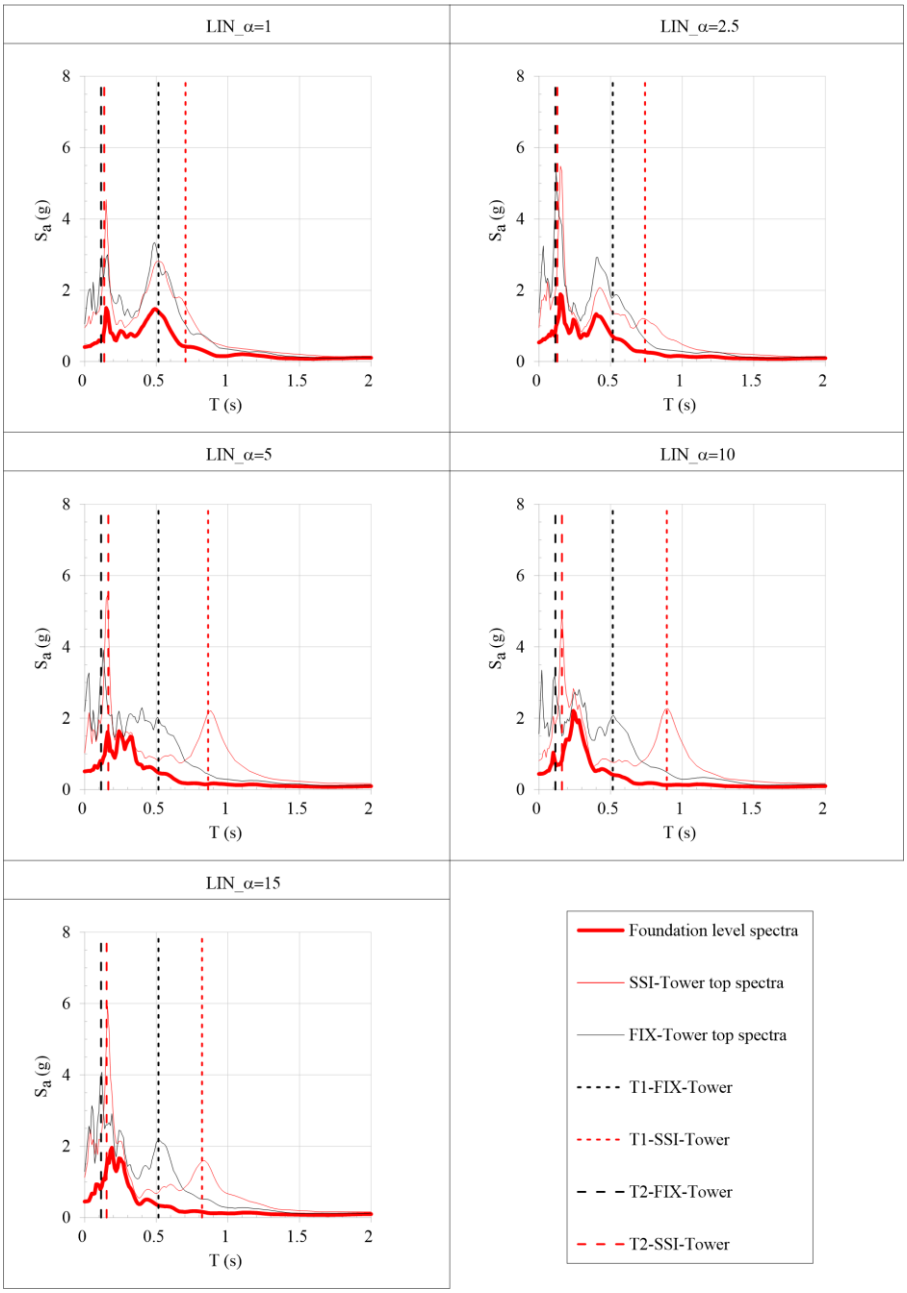

Fig. 4. 26a– Acceleration response spectra recorded at the foundation level (thick red lines) and at the top of the SSI-Tower (thin red lines) and FIX-Tower (thin black lines) for the LIN analyses (α =1; 2.5; 5; 10; 15).

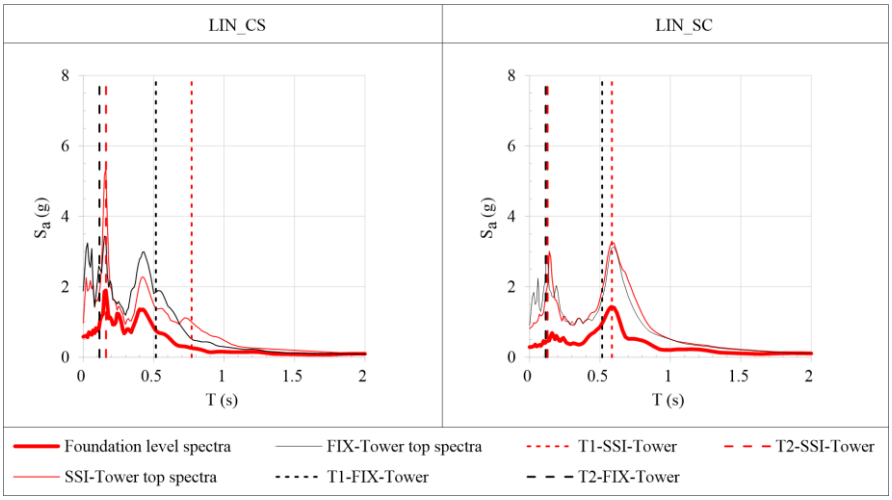

Fig. 4.26b – Acceleration response spectra recorded at the foundation level (thick red lines) and at the top of the SSI-Tower (thin red lines) and FIX-Tower (thin black lines) for the EQ-LIN analyses (CS; SC).

Fig. 4.27 shows the bending displacement u_θ time-histories at the top control point of each analysed scenario. The records show remarkable changes in both magnitude and sign, despite the same seismic signal has been inputted at the base of the SSI and FIX models. Significant residual displacement values are recognized especially for the $\alpha = 1$ and SC cases, which represent the most demanding scenarios independently from the modelling approach adopted. Different trends between the two approaches are, instead, observed when comparing the other cases involving higher degree of soil heterogeneity, which, however, are characterized by limited bending displacements.

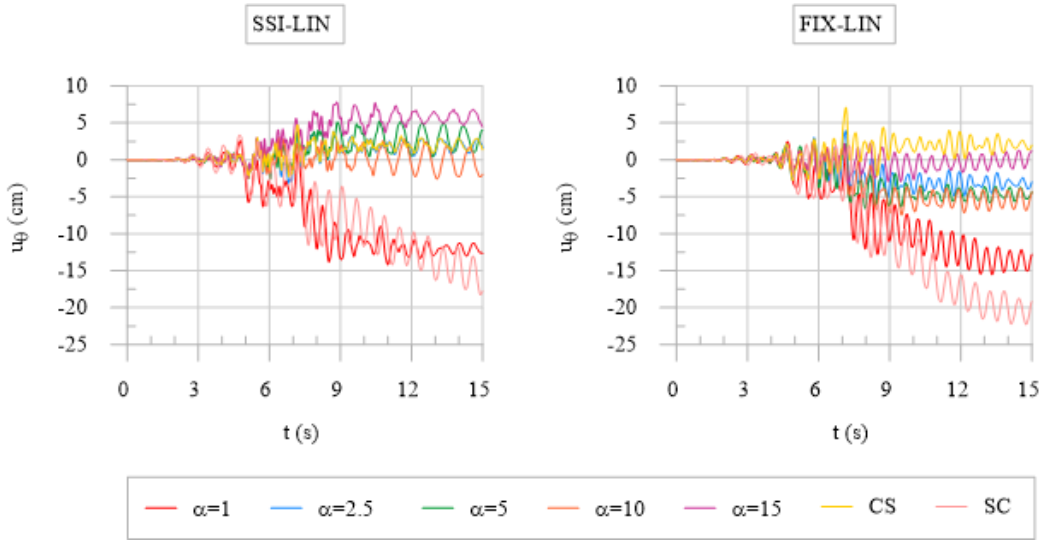

Fig. 4. 27 – Bending displacements (u_θ) time-histories recorded at the top of the tower for each SSI and FIX model during the LIN set of analyses.

4.5.3.2.2 Results of the analyses with the equivalent-linear visco-elastic soil approach

The tensile damage distributions for the EQ-LIN set of analyses at the end of the seismic event are shown in Fig. 4.28.

The α =1 case is characterized by a rather similar damage scenario for both the SSI and FIX analyses, with clear inclined cracks developing in the first half of the tower and negligible material degradation in the upper part of the structure (Fig. 4.28a). On the other hand, the α =2.5 presents different patterns depending on the modelling approach adopted. Indeed, the SSI analysis predicts negligible damage along whole structure, while the FIX analysis provides evident damage concentration right above the main entrance and at the belfry of the tower (Fig. 4.28a).

The α =5 case shows once again low damage levels affecting the structure if the fully coupled approach is considered; conversely, a more demanding damage distribution at the basement level of the tower characterizes the uncoupled analysis (Fig. 4.28a).

The $\alpha = 10$ shows, instead, a rather comparable damage pattern no matter what kind of models is considered. In fact, the belfry area results very affected by the seismic action in both SSI and FIX model; also the middle part of the structure presents relevant cracks at minor openings, especially in the SSI case. Conversely, in the FIX case a slight material degradation at the base of the structure can be also recognized (Fig. 4.28b).

The $\alpha = 15$ case provides once again high damage levels at the bell cell of the two modelling approaches; on the other hand, the SSI analysis is characterized by more severe damage distribution at the middle of the tower with respect to the FIX case (Fig. 4.28b).

The CS case predicts only mild damage at the base of the SSI tower, while more severe cracks distributions are observed in the FIX tower above the main entrance and at bell cell (Fig. 4.28c). Finally, the SC case provides rather comparable damage scenarios in both the analyses, predicting damage localization only at the base of the structure (Fig. 4.28c).

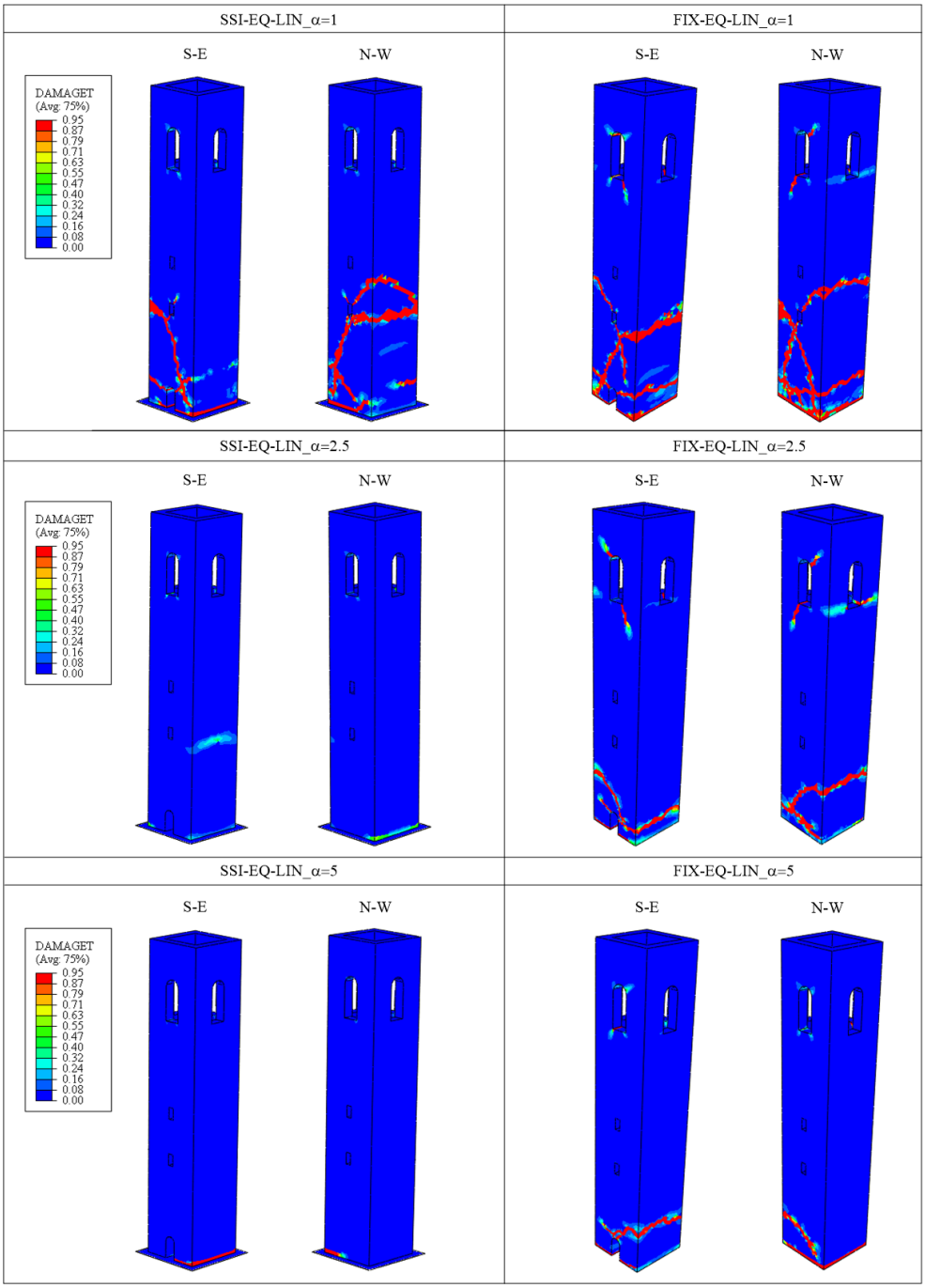

Fig. 4. 28a – Tensile damage contours plots at the end of the seismic input motion for the EQ-LIN analyses, considering the SSI and FIX models (α =1; 2.5; 5)

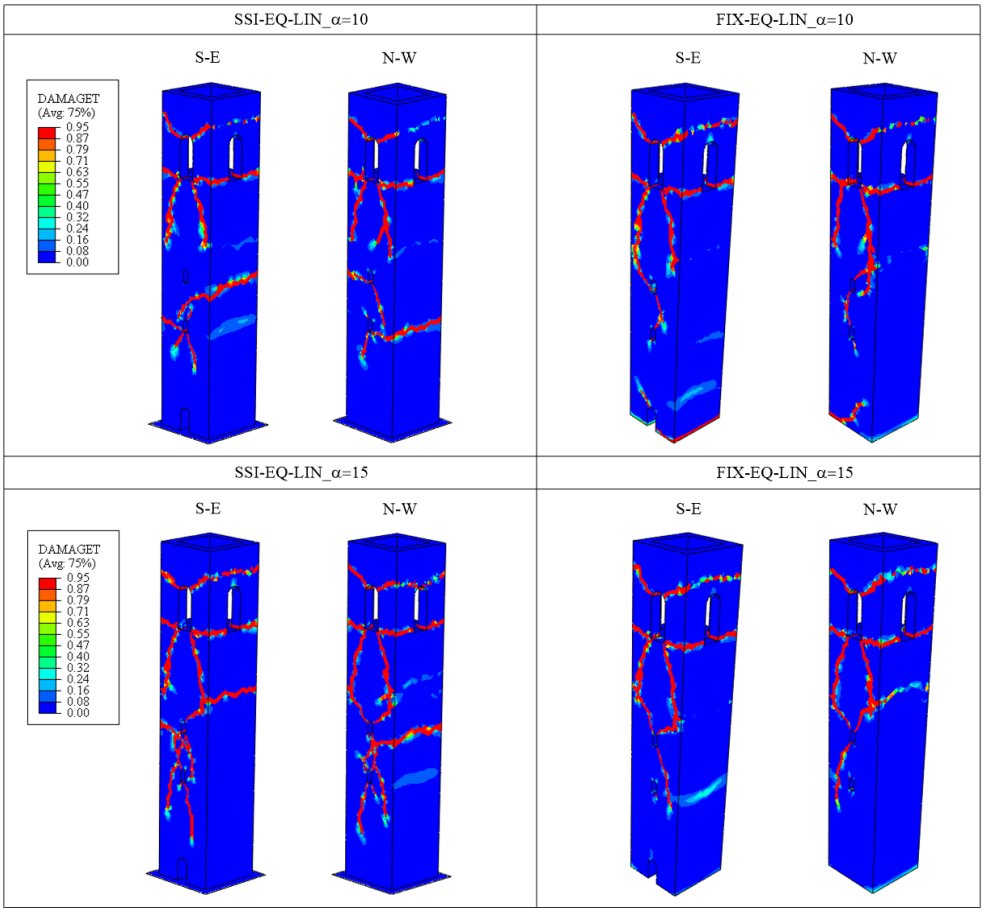

Fig. 4.28b – Tensile damage contours plots at the end of the seismic input motion for the EQ-LIN analyses, considering the SSI and FIX models (α =10; 15).

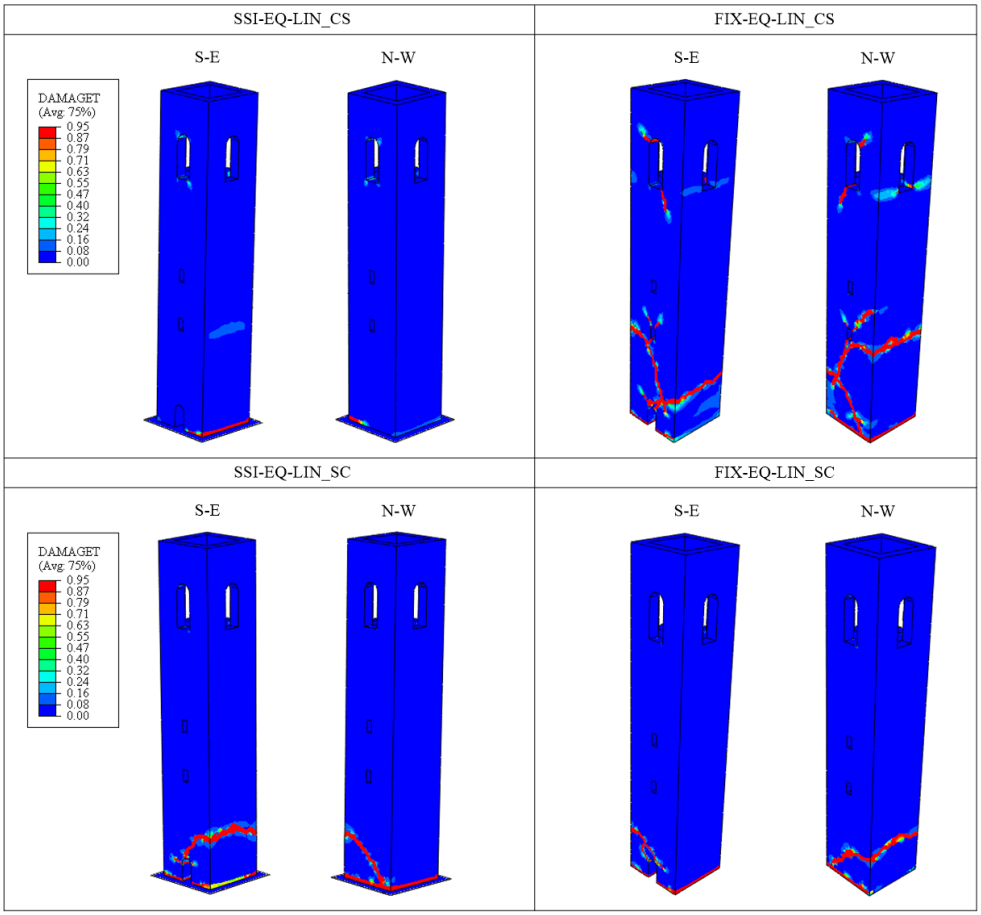

Fig. 4.28c – Tensile damage contours plots at the end of the seismic input motion for the EQ-LIN analyses, considering the SSI and FIX models (CS; SC).

In Fig. 4.29 the acceleration response spectra at the top of both the tower models and at the foundation level are reported. As already previously observed for the LIN set of analyses, the period elongation phenomenon generally produces a reduction of the spectral acceleration demand for the 1st period, while it tends to increase for the 2nd period. The signal propagation along the structure can be very different depending on the base-scheme adopted, as highlighted by the spectra obtained at the top of the structure, which are amplified in correspondence of the natural periods of the SSI and the FIX models.

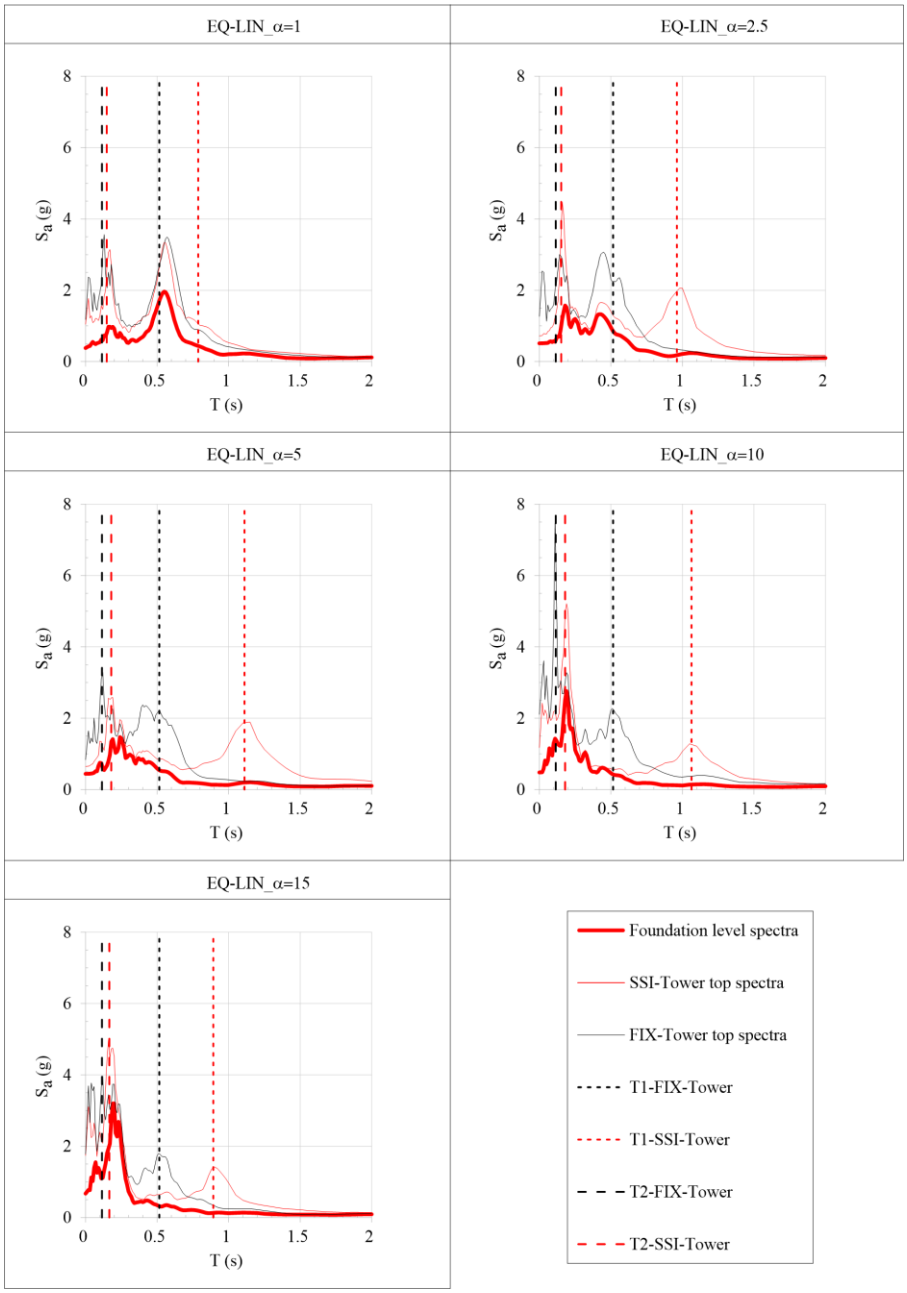

Fig. 4. 29a – Acceleration response spectra recorded at the foundation level (thick red lines) and at the top of the SSI-Tower (thin red lines) and FIX-Tower (thin black lines) for the EQ-LIN analyses (α =1; 2.5; 5; 10; 15).

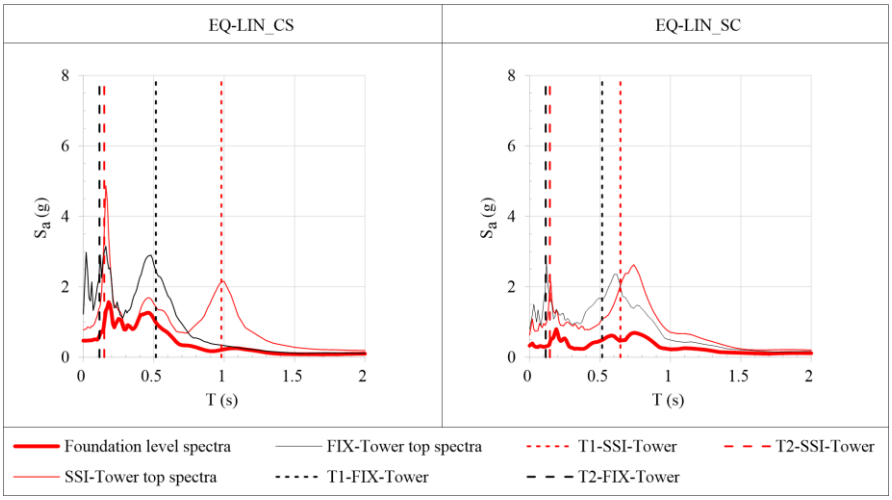

Fig. 4. 29b – Acceleration response spectra recorded at the foundation level (thick red lines) and at the top of the SSI-Tower (thin red lines) and FIX-Tower (thin black lines) for the EQ-LIN analyses (CS; SC).

Finally, Fig. 4.30 collects the bending displacements u_θ time-histories recorded at the control point located at the top of the SSI and FIX tower. The records show remarkable changes between the two approaches, both in magnitude and sign. In particular, different trends are observed for the SC case and for the $\alpha = 1$ case, which are characterized by the accumulation of high displacements, suggesting the possible collapse of the structure, if the SSI approach is considered. In the remaining cases, more demanding, or at least comparable, residual displacements are expected for the FIX set of analyses.

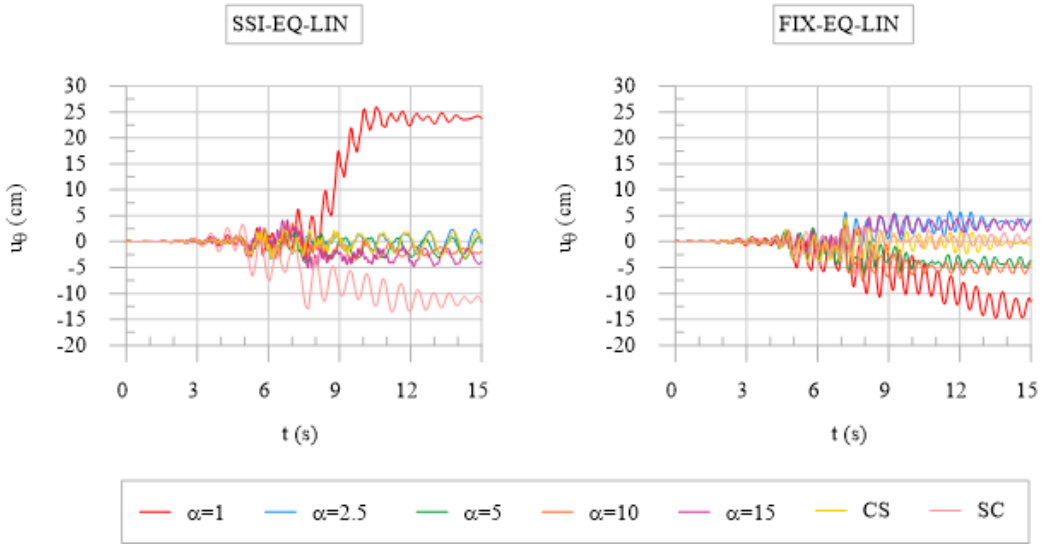

Fig. 4. 30 – Bending displacements (u_θ) time-histories recorded at the top of the tower for each SSI and FIX model during the EQ-LIN set of analyses.

4.5.3.2.3 Comparison between the results

The results of the non-linear dynamic time-history analyses have been presented for both the LIN and the EQ-LIN calibration of the soil dynamic behaviour.

As a general finding, it can be stated that the soil compliance can potentially affect the damage distribution along the height of the tower, since it can be very different between the SSI and the FIX models. Significant different patterns are, for example, recorded for $\alpha = 5$ and $\alpha = 10$ in the LIN set of analyses and for $\alpha = 2.5$, $\alpha = 5$ and CS for the EQ-LIN one; in particular, this latter group always show a more limited damage intensity level when the fully coupled approach is considered. Similar trends, instead, can be identified between the two set of simulations, as for the $\alpha = 15$ and SC cases in the LIN set and $\alpha = 1$, $\alpha = 10$ and SC cases for the EQ-LIN one. In addition, for both the LIN and EQ-LIN sets, as the heterogeneity ratio increases the damage distribution looks to affect more often the bell cell, which is known as one of the most seismic sensitive structural parts of ancient masonry towers (Ferrante et al. 2019; Poiani et al. 2018).

Anyway, the obtained damage patterns are quite variable from case to case and it is rather difficult to establish “a-priori” if the soil compliance can produce a significant change of the damage patterns.

The analysis of the acceleration response spectra has highlighted that the period elongation phenomenon due to the soil compliance determines a change in the seismic demand, which usually results in lower spectral accelerations for the 1st natural period; conversely, for the 2nd one an increase is more likely to occur with respect to the fixed-base condition. Obviously, this trend become more significant when the EQ-LIN soil behaviour is considered, due to the introduction of the non-linear soil effects.

The analysis of the bending displacement time-histories recorded at the control point located at the top of the tower models has also underlined significant differences between the SSI and the FIX models, providing displacement demands which can be higher for the SSI approach as well as for the FIX one.

Further insights about the role of the soil behaviour influence on the dynamic response of the structure can be derived from Fig. 4.31, where the comparison between the bending and the rocking displacements obtained at the top control point of the SSI tower for the two soil deposits calibrations is shown. As can be noted, the soil behaviour can significantly influence the magnitude and sign of the accumulated bending displacements, in particular for $\alpha = 1$, $\alpha = 5$ and $\alpha = 15$; conversely, a rather similar trend is observed for the SC case. Moreover, the introduction of the soil non-linearity through the EQ-LIN approach generally produces higher rocking displacements in each analysed case. This aspect is especially evident in the $\alpha = 2.5$, $\alpha = 5$ and CS cases, representing the scenarios in which the tower is less affected by damages at the end of the seismic event. Furthermore, rocking displacements of the order of the bending ones are also recognized for the LIN_$\alpha = 10$ analysis, which has shown limited damages. This suggests that the occurrence of consistent rocking motion could mitigate the damage distribution affecting the structure.

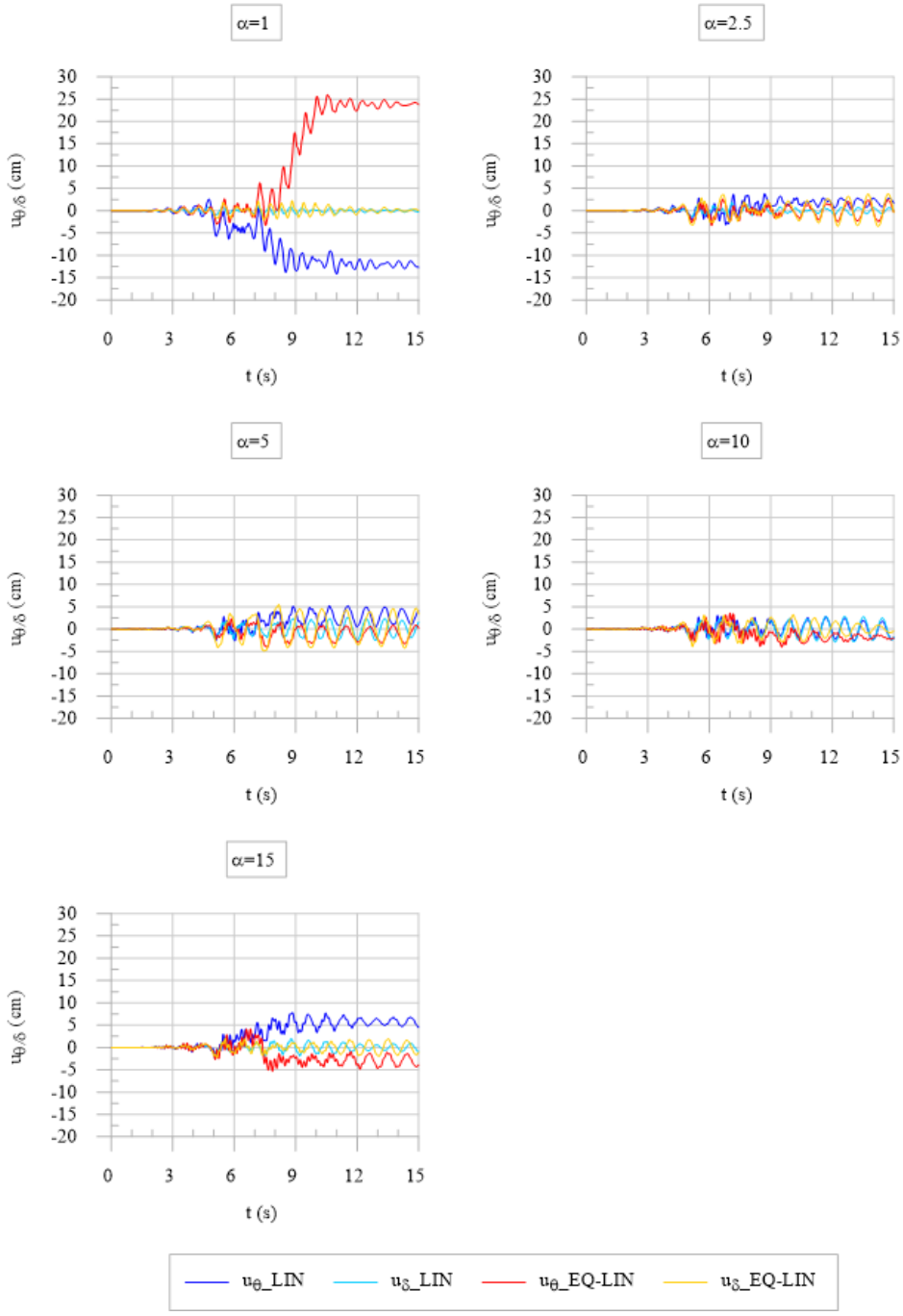

Fig. 4. 31a – Bending (u_θ) and rocking (u_δ) displacements time-histories recorded at top of the tower for each SSI-LIN and SSI-EQ-LIN models (α =1; 2.5; 5; 10; 15).

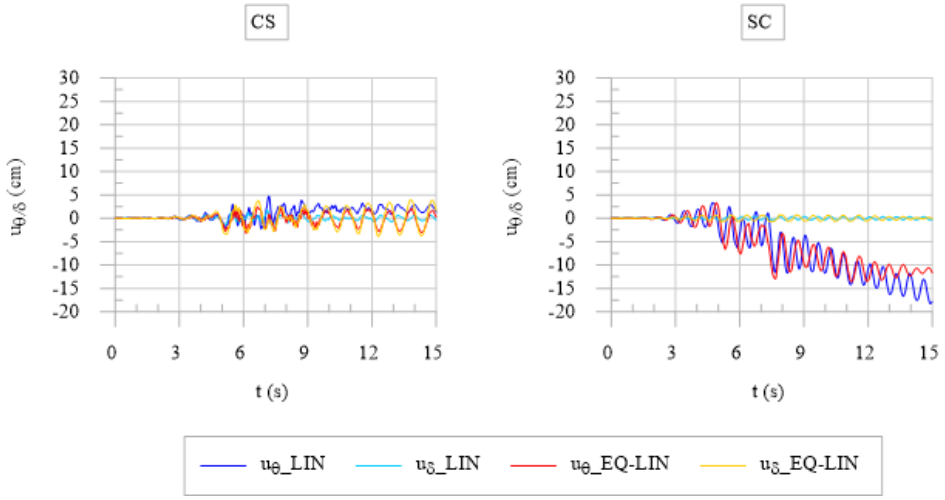

Fig. 4.31b – Bending (u_θ) and rocking (u_δ) displacements time-histories recorded at top of the tower for each SSI-LIN and SSI-EQ-LIN models (CS; SC).

Finally, in Fig. 4.32 the maximum bending displacements profiles recorded in 5 control points located along the height of the tower are plotted. Once again it is possible to note that significant differences might occur considering or not the soil compliance. The SSI models not always result in more demanding displacements profiles with respect to the FIX ones. The plots also highlight the possible relation between the observed damage and the differential displacement along the tower. For instance, all the analyses carried out with $\alpha = 15$ show a sharp gradient in the bending displacements around 20m high, which might indicate a partial collapse of the belfry in agreement with the tensile damage maps. On the other hand, the monotonic increase of the bending displacements observed during the SC analyses indicate the possible formation of a failure mechanism localised close to the basement level of the tower, while for the SSI-EQ-LIN_$\alpha = 1$ case the collapse occurs higher along the structure height.

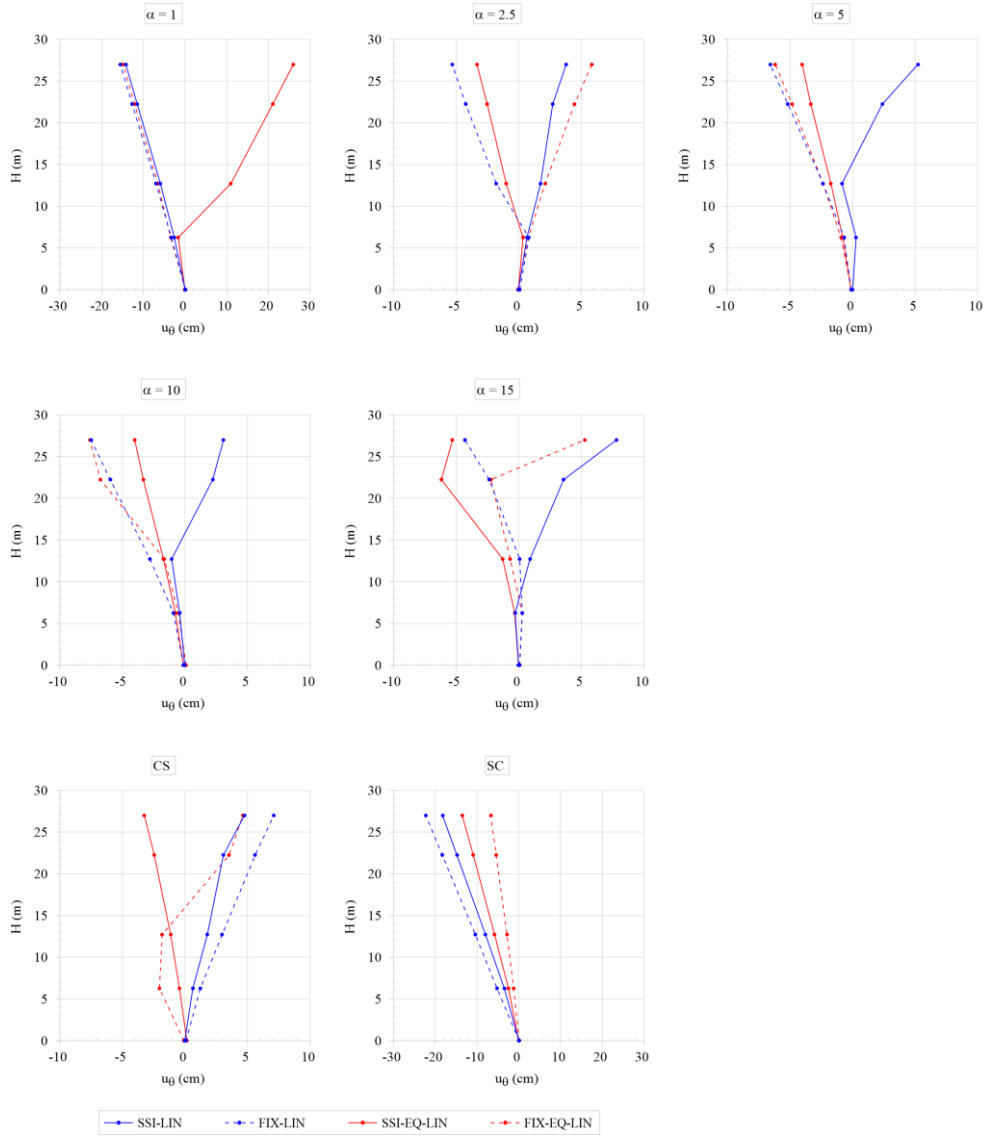

Fig. 4. 32 – Maximum bending displacements (u_θ) profiles along the tower height for each SSI and FIX model during the LIN and EQ-LIN set of analyses.

CHAPTER 5: INFLUENCE OF THE STRUCTURAL SLENDERNESS RATIO ON THE DYNAMIC SOIL-STRUCTURE INTERACTION OF MASONRY TOWERS

5.1 Description of the additional case-studies

The present Chapter deals with the effect of one of the most important geometrical features controlling the dynamic response of a structure, i.e. its slenderness ratio given by the height of the structure over its base length (H/B). This aspect is investigated in relation to the SSI phenomena, in order to recognize when the soil compliance effect produces a more evident deviation with respect to the fixed-base condition.

According to de Silva et al. (2015a), masonry towers can be collected into three categories based on their structural slenderness: squat ($H/B<3$), slender ($3<H/B<6$) and very slender ($H/B>6$). The numerical simulations, described in Chapter 4, have been performed with reference to a slender tower, as it was characterised by a H/B ratio equal to 5. In the following, those simulations are referred to as "slender tower". Thus, two additional masonry structures are considered in the simulations, i.e. a squat and a very slender tower. Fig. 5.1 reports the geometrical features chosen to characterize the structures. The squat tower, 13m high, is characterised by $H/B=2.5$, while the very slender tower, 53m high, presents a slenderness ratio equal to 10. For both models, the base length has been kept equal to that of the slender tower, i.e. 5.3m, as well as the openings dimensions. The material properties adopted for the masonry behaviour in the following analyses have not been varied with respect to those previously considered for the slender tower. The soil profiles used in the SSI

models and the LIN and EQ-LIN calibrations adopted for the soil dynamic behaviour are the same already presented in Chapter 4, together with the seismic input motion applied at the bottom of the FE models.

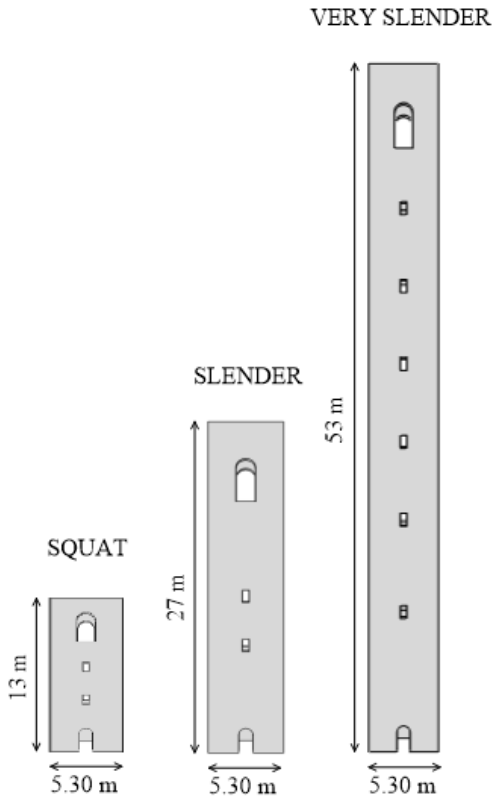

Fig. 5. 1– Vertical section of the 3D CAD models and geometrical features of the squat, slender and very slender masonry towers.

5.2 Dynamic identification of the towers

The dynamic identification of the squat and very slender towers has consisted in performing modal eigenvalues analyses, starting from the fixed-base condition whose results are collected in Tabs. 5.1-5.2.

Mode	Frequency (Hz)	Mode type	Excited mass m_x (%)	Excited mass m_y (%)	Excited mass m_z (%)
1	7.21	1st flexural	61.70	0	0
2	7.22	1st flexural	0	60.19	0
3	15.82	1st torsional	0.06	0	0
4	22.93	2nd flexural	20.56	0	0
5	23.76	2nd flexural	0	20.94	0

Tab. 5. 1– Modal analysis results for the fixed-base squat tower.

Mode	Frequency (Hz)	Mode type	Excited mass m_x (%)	Excited mass m_y (%)	Excited mass m_z (%)
1	0.51	1st flexural	0	60.24	0
2	0.52	1st flexural	60.19	0	0
3	2.89	2nd flexural	0	19.97	0
4	2.90	2nd flexural	20.16	0	0
5	3.94	1st torsional	0.01		0

Tab. 5. 2 – Modal analysis results for the fixed-base very slender tower.

As already observed for the slender tower case (section 4.5.2.2), it is evident that, due to the symmetrical geometry characterising the structures, the flexural modes are specular in both X and Y directions, while the torsional mode contribution is very low.
The different slenderness ratio shifts the squat tower natural frequencies to higher values in comparison to the slender case and, vice versa, moves to lower values those of the very slender tower.
Tabs. 5.3 and 5.4 show the natural frequencies of the SSI models derived for both the squat and very slender cases considering the LIN and EQ-LIN soil modelling. Moreover, the values computed for ξ_1 and ξ_2 are also reported; in particular, the ξ_1 values of the squat tower suggest that possible resonance phenomena between the tower and the soil deposit are more likely to occur for α =5, 10 and 15 both for the LIN and EQ-LIN soil behaviour. On the contrary, resonance should not be expected for the very slender tower for any analysed scenario. Only f_{SSI-1} is reported for the squat tower, since a clear and reliable identification of the second frequency f_{SSI-2} has not been

possible from the modal analyses outputs. Moreover, the amplification functions derived from additional linear dynamic analyses also showed an unclear identification of the peaks, and hence of the resonance frequencies, for frequencies higher than 12-15 Hz as, after this threshold, the frequency content of the input signal is very low, as depicted in Fig. 4.4.

	LIN		EQ-LIN	
SOIL PROFILE	f_{SSI-1} (Hz)	ξ_1	f_{SSI-1} (Hz)	ξ_1
α =1	4.36	2.10	3.42	1.86
α =2.5	3.59	1.43	2.70	1.18
α =5	3.22	1.11	2.15	0.79
α =10	3	0.87	2.49	0.83
α =15	3.36	0.92	2.90	1.06
CS	3.44	1.38	2.70	1.23
SC	5.99	3.74	4.64	3.39

Tab. 5. 3 – First natural frequency of the squat tower resting on deformable soil and normalized values over the corresponding soil resonance frequency ($\xi_1 = f_{SSI-1}/f_{SOIL-1}$).

	LIN				EQ-LIN			
SOIL PROFILE	f_{SSI-1} (Hz)	f_{SSI-2} (Hz)	ξ_1	ξ_2	f_{SSI-1} (Hz)	f_{SSI-2} (Hz)	ξ_1	ξ_2
α =1	0.45	2.55	0.22	0.41	0.41	2.36	0.22	0.42
α =2.5	0.41	2.33	0.16	0.36	0.35	2.13	0.15	0.36
α =5	0.37	2.25	0.13	0.34	0.32	2.10	0.12	0.34
α =10	0.36	2.22	0.10	0.36	0.32	2.12	0.11	0.44
α =15	0.39	2.30	0.11	0.40	0.37	2.25	0.13	0.46
CS	0.41	2.32	0.16	0.36	0.35	2.09	0.16	0.36
SC	0.48	2.67	0.30	0.44	0.46	2.56	0.34	0.48

Tab. 5. 4 – First and second natural frequency of the very slender tower resting on deformable soil and normalized values over the corresponding soil resonance frequencies ($\xi_1 = f_{SSI-1}/f_{SOIL-1}$ and $\xi_2 = f_{SSI-2}/f_{SOIL-2}$).

Fig. 5.2 and Fig. 5.3 illustrate the results in terms of natural period normalized to the corresponding fixed-base values as a function of the heterogeneity parameter α.

The soil stratigraphy remarkably influences the dynamic features of the squat tower, as highlighted by the curves of the normalized period elongation T_{SSI} / T_0 exhibiting values ranging between 1.2 and 3.4 (Fig. 5.2). In particular, under the linear assumption, the ratio T_{SSI} / T_0 increases up to 2.4 for increasing heterogeneity parameter and then decreases to 2.2 for $\alpha = 15$. The increase in T_{SSI} / T_0 is even higher when soil nonlinearity is accounted for (i.e. EQ-LIN approach). In this case, the T_{SSI} / T_0 increases up to 3.4 for $\alpha = 5$ and, then, decreases to 2.4 for heterogeneity parameters greater than 5.

The very slender tower (Fig. 5.3) shows, instead, a more limited period elongation (also with respect to the slender case illustrated in Fig. 4.15), but surely not negligible and still quite evident. Indeed, the T_{SSI-1} / T_0 ratio exhibits values ranging between 1.10-1.45 and 1.13-1.63 if the LIN and EQ-LIN soil approaches are respectively considered. Even more limited values are recorded for the T_{SSI-2} / T_0 ratio, ranging between 1.10-1.3 for the LIN analyses and 1.13-1.40 for the EQ-LIN ones.

It is worth to highlight that similar trends have also been recognized for the slender tower (Fig. 4.15). Hence, this confirms that the effects of the soil-structure interaction may be significant in all the three typologies of tower (i.e. squat, slender and very slender), with a change in the natural periods of the soil-tower system strongly dependent on the soil profile characteristics.

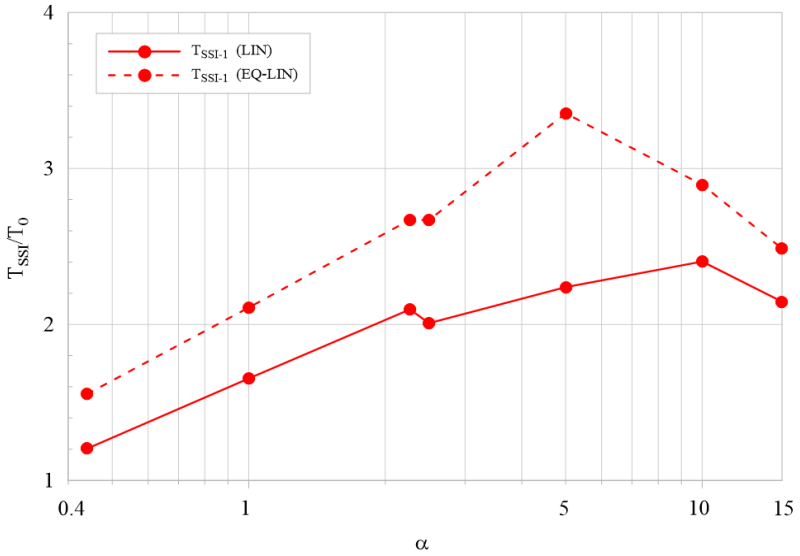

Fig. 5. 2 – First natural period of the SSI squat tower (T_{SSI}) normalized for the corresponding value in fixed-base condition (T_0) plotted as a function of the heterogeneity parameter α .

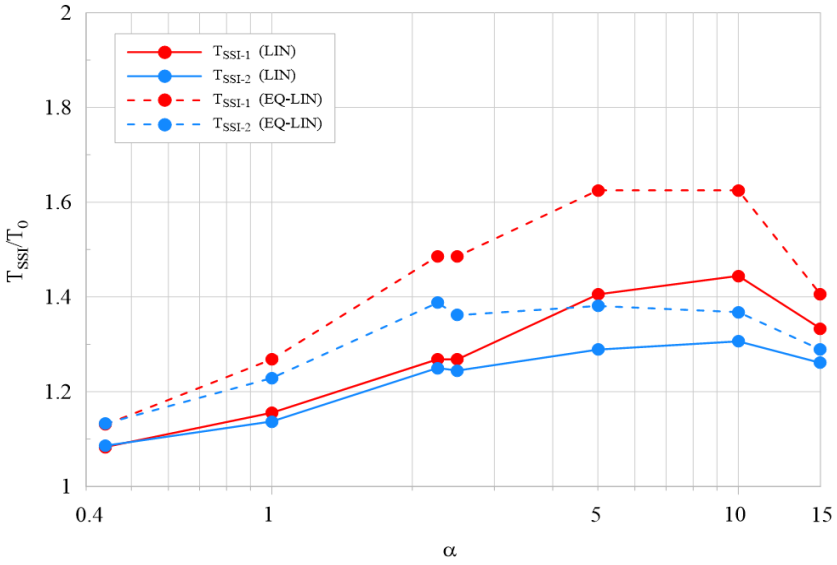

Fig. 5. 3 – First and second natural period of the SSI very slender tower (T_{SSI}) normalized for the corresponding values in fixed-base condition (T_0) plotted as a function of the heterogeneity parameter α .

The corresponding modal shapes have also been extracted and are reported in Figs. 5.4-5.5, for the squat and very slender tower, respectively. Aiming to present a more effective comparison with the fixed-base scheme, the results are reported removing the translational displacement recorded at the base of the SSI models and, then, a normalization is adopted considering the displacement value attained at top of the structure. The outcomes are in agreement with those previously observed for the slender tower. Indeed, the 1st mode of the two towers looks not to be much influenced by the soil compliance, not considerably changing from the fixed-base scheme. Conversely, the second mode of the very slender tower still shows a relevant dependency on the characteristics of the soil deposit, but not on the soil modelling (LIN and EQ-LIN). The modal shapes manifest greater modification when higher values of α are considered, even if they do not change much. On the other hand, the $\alpha = 1$ and the SC cases are characterized by very close 2nd modal shapes to the fixed-base scheme, especially in the LIN analyses.

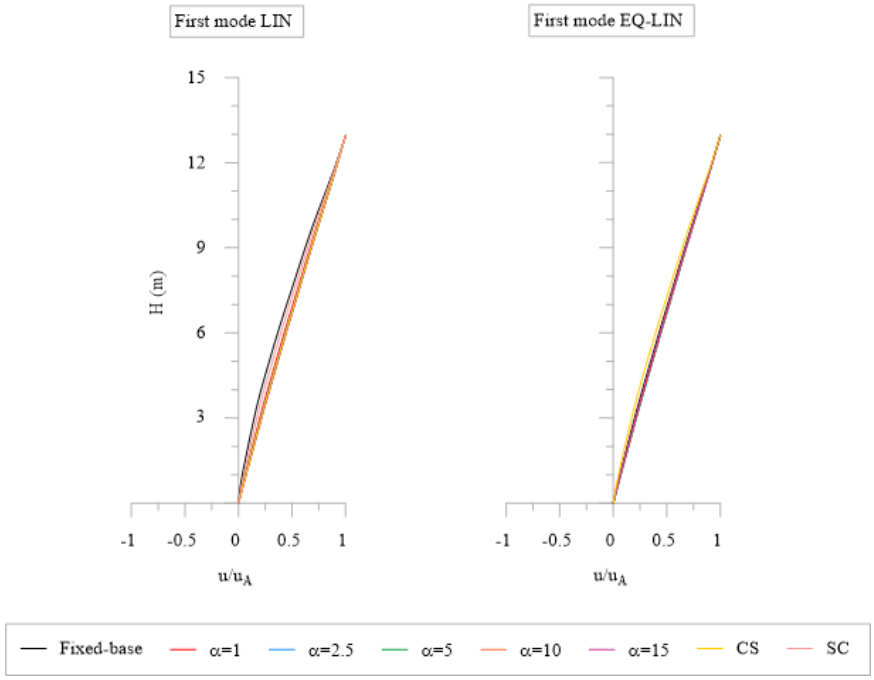

Fig. 5. 4 – First modal shape of the squat tower in the X direction depurated from the translational displacement at the base of the structure and normalized for the maximum horizontal top displacement (u_A): LIN and EQ-LIN analyses.

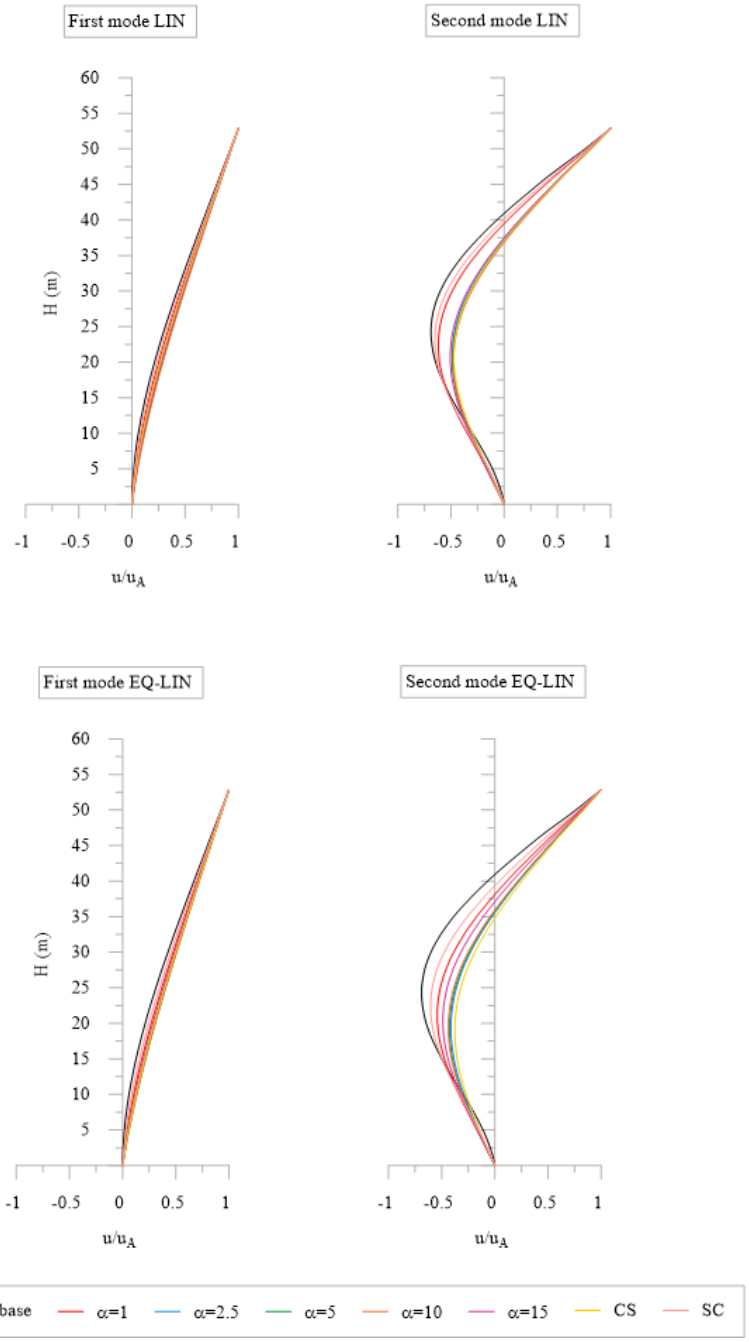

Fig. 5. 5 – First and second modal shape of the very slender tower in the X direction depurated from the translational displacement at the base of the structure and normalized for the maximum horizontal top displacement (u_A): LIN and EQ-LIN analyses.

The FE-based results in terms of f_{SSI} / f_0 have been compared to those obtained by the well-known analytical solution proposed by Veletsos & Nair (1975) for a SDOF. The results from the LIN approach have been compared with an equivalent SDOF oscillator characterized by a height (h_G) equal to the distance from the base to the centroid of mass of the structure (Veletsos & Nair 1975) and a concentrated mass equal to the whole mass of the tower. The foundation embedment effect has been estimated using the foundation impedance functions proposed by Gazetas (1991).

However, the Veletsos & Nair solution was originally conceived for a homogenous deposit and cannot be directly applied to the cases of this study in which a layered soil is considered. Therefore, an equivalent soil-structure stiffness parameter σ_{eq} has been defined as:

$$\sigma_{eq} = \frac{V_{S-eq}}{f_0 h_G} \tag{5.1}$$

where V_{S-eq} is the equivalent shear wave velocity computed in the soil volume expected to be excited by the foundation motion.

Gazetas (1983) and Stewart et al. (2003) suggested that the soil affected by the foundation swaying and rocking extends to a depth less than half the foundation width, which is almost coincident with the depth of the upper soil layer for the analysed case studies. Nevertheless, there is no general consensus on the soil volume mobilised during earthquake excitation because of the huge variability in the structural response. For this reason, there are cases in which it is also considered equal to twice the width of the structure (Piro et al. 2020). Bearing in mind this aspect, in this work a soil volume extension equal to 1.5B has been chosen, because of the high variability in the soil layers sequences which are placed in the upper part of the deposit close to the foundation level.

The V_{S-eq} has been evaluated for each soil profile case through a weighted average of the soil areas which surround the foundation (Fig. 5.6):

$$V_{S-eq} = \frac{V_{S-1}A_1 + V_{S-2}A_2 + V_{S-3}A_3 + V_{S-4}A_4}{\sum_{i=1}^{n} A_i} \tag{5.2}$$

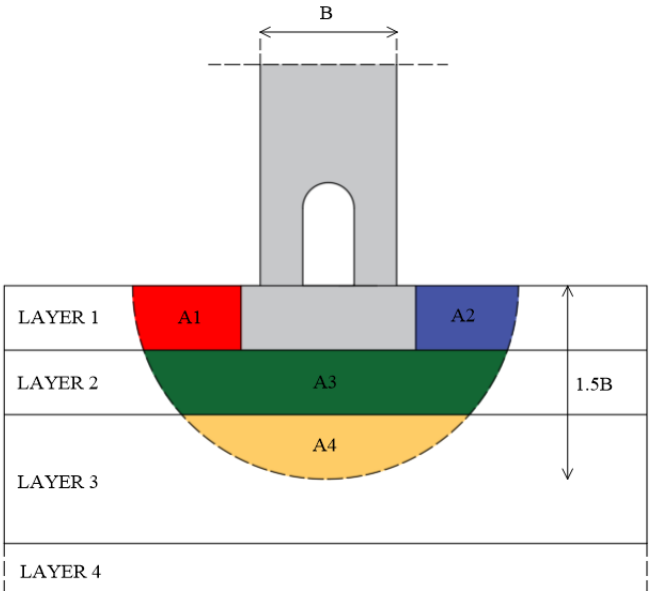

Fig. 5. 6 – Soil volume affected by the earthquake motion and identification of the areas of the soil layers used to compute V_{S-eq}.

The comparison between the analytical solution and the numerical FE-based outcomes for all the three towers is reported in Fig. 5.7 in terms of f_{SSI} / f_0 variation with σ_{eq} for different slenderness ratios. As expected, keeping σ_{eq} constant, the SSI effects become more relevant as the slenderness ratio increases. In addition, for very high values of σ_{eq} the soil compliance effect loses relevance and the structure could be described with a cantilever scheme. The two highest σ_{eq} ratios for the very slender tower correspond to the $\alpha = 1$ and the SC soil profiles (18.83 and 30.88, respectively) and, as consequence, are those closer to a fixed-base condition. This justifies the fact that also their second modal shape does not result to be much influenced from the soil compliance, because their relative soil-structure stiffness is already very

high. Additionally, it might be observed that the general trend of the analytical curves is captured by the numerical results, despite some quantitative discrepancies can be noticed. The analytical solution systematically underestimates the SSI effects expected by the FE analyses. This is due to several reasons:

a) it was already pointed out that the theory was conceived for a simpler homogenous soil case and not for a layered deposit;
b) the analytical solution is anyway based on a SDOF system that cannot fully reproduce the behaviour of a 3D complex structure like a masonry tower;
c) the presence of openings can also play a role in reducing the stiffness of the structure and deviate the behaviour of the tower from that of the SDOF system.

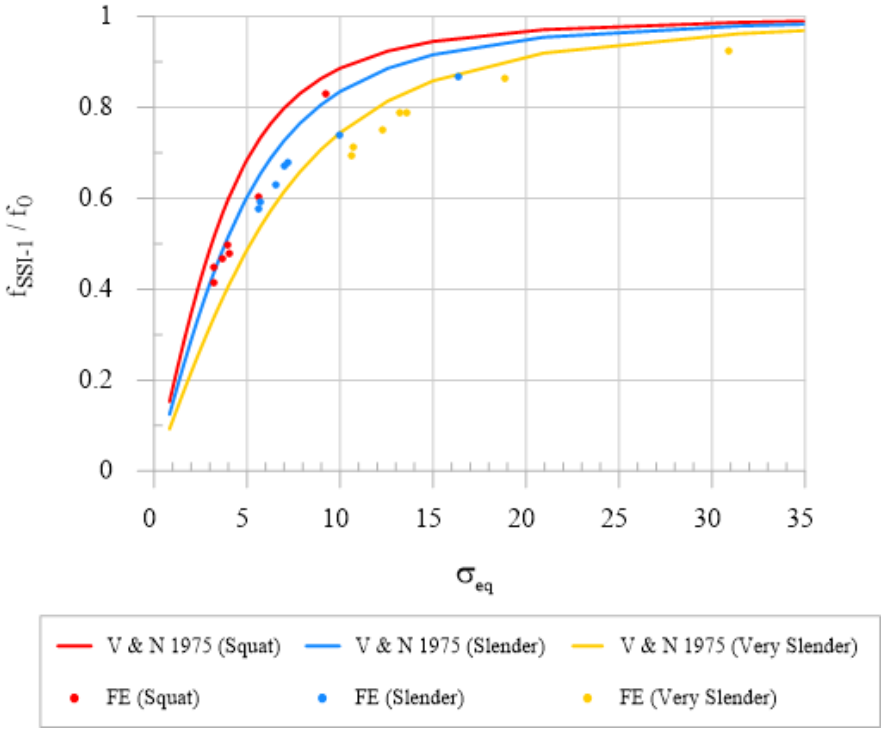

Fig. 5. 7 – Comparison of the FE results (1st natural frequency) versus the analytical solution proposed by Veletsos & Nair (1975) for SDOF systems.

5.3 Investigation of the non-linear response of the squat and very slender tower

In this section the main outcomes provided by the non-linear dynamic analyses performed on the squat and very slender tower are presented. The results provided by the fully coupled model (SSI) are compared with the decoupled model consisting in a fixed-base tower (FIX) which is subjected to the input motion derived from SSI simulation at the foundation level.

The effect of solely heterogeneity and the couple of soil heterogeneity and nonlinearity are also highlighted.

5.3.1 Non-linear dynamic response of the squat tower

5.3.1.1 Results of the squat tower analyses with the linear visco-elastic soil approach

The comparison of the damage contours plots of the SSI squat tower versus the FIX models is reported in Fig. 5.8 for the LIN set of analyses. The results shows that there is a small variability in the damage scenario provided by the different simulations. Indeed, the damage distribution is always localized at the basement level of the structure, while the rest of the structure seems to be not affected by the seismic excitation.

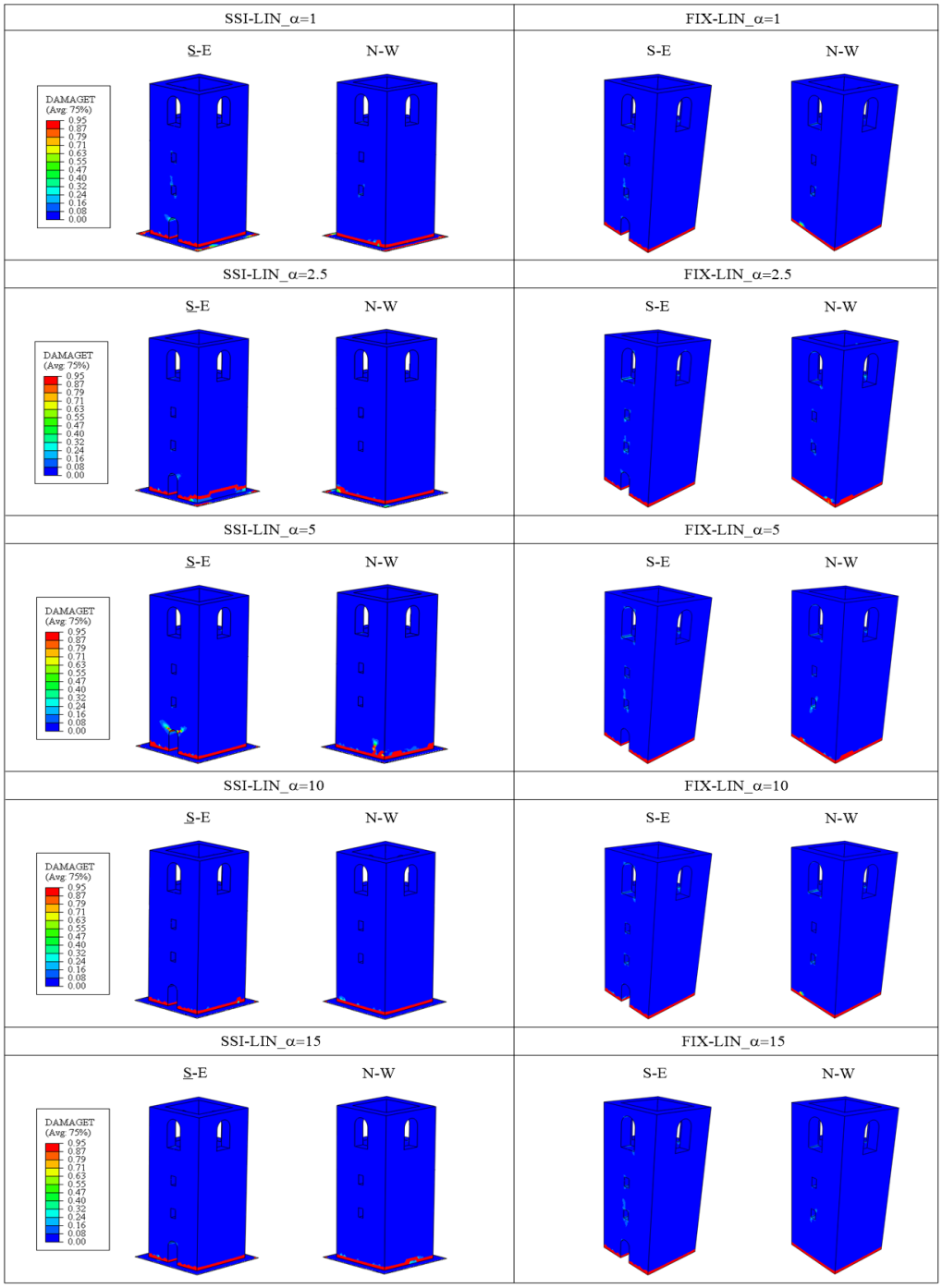

Fig. 5. 8a – Squat tower tensile damage plots at the end of the seismic input motion: LIN analyses for the coupled SSI and corresponding FIX models (α =1; 2.5; 5;10: 15).

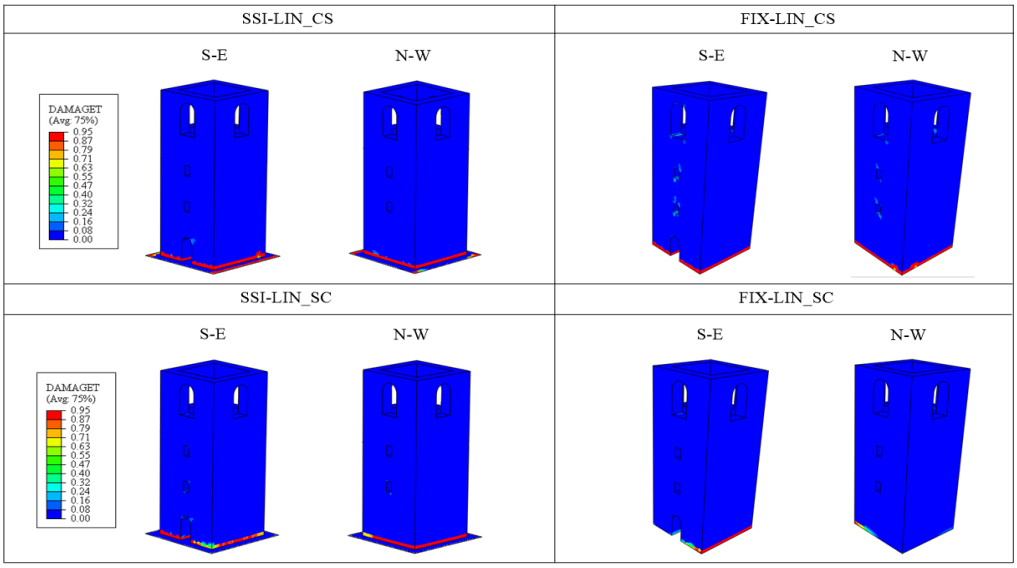

Fig. 5. 8b – Squat tower tensile damage plots at the end of the seismic input motion: LIN analyses for the coupled SSI and corresponding FIX models (CS; SC).

The acceleration response spectra, shown in Fig. 5.9, can help to explain the response observed in terms of tensile damage parameter. In fact, looking at the spectra recorded at the tower foundation level (red thick line), it seems that, despite the elongation phenomenon due to the SSI, the structure is generally subjected to similar spectral accelerations in both SSI and FIX models. Nevertheless, it is also evident that the soil compliance still produces a different dynamic response of the structure with respect to the fixed-base scheme. Inspecting the acceleration spectra recorded at the top of the models (thin red and black lines for the SSI and FIX towers, respectively), it is clear that the spectral shape results much amplified in correspondence of each natural period.

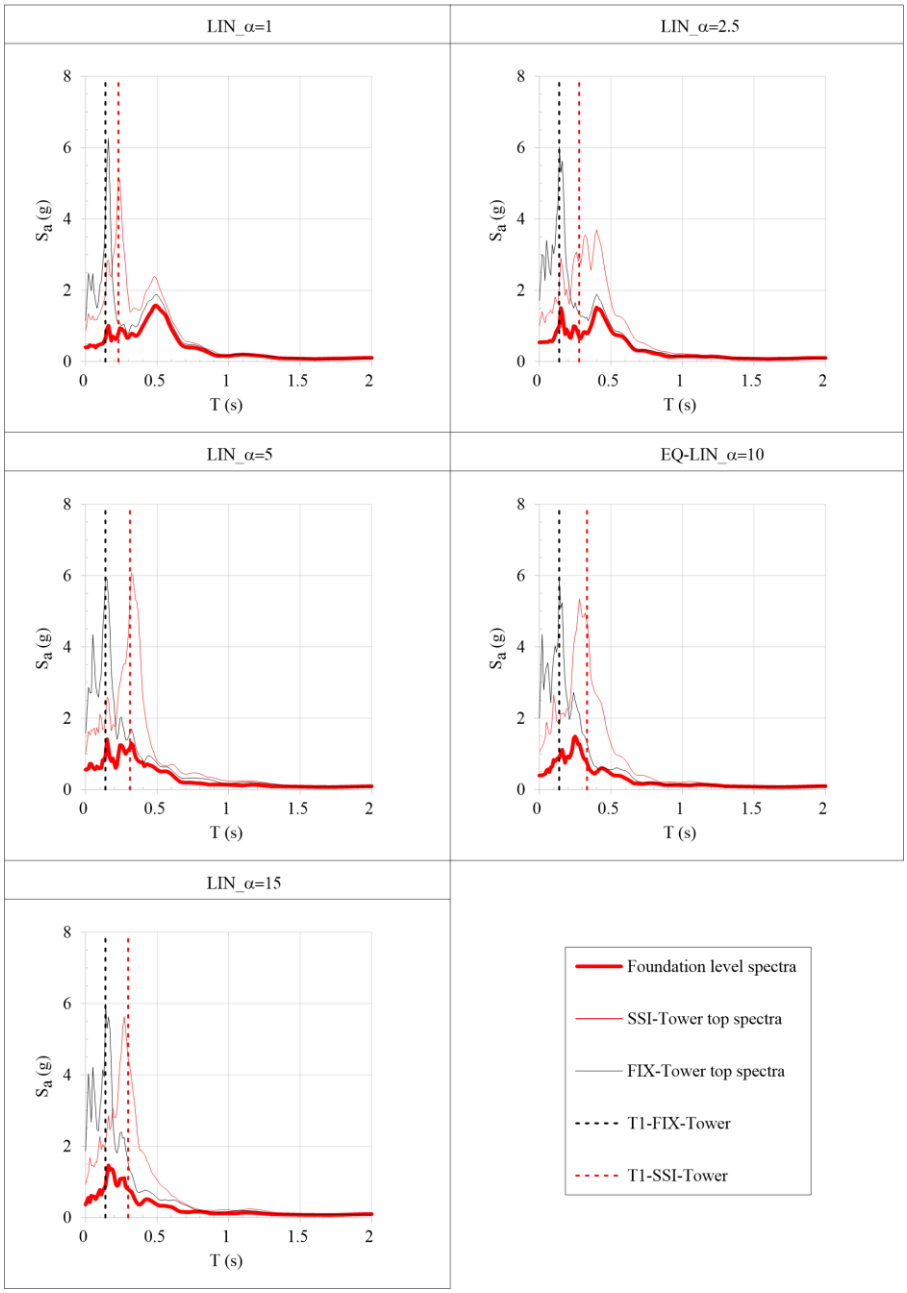

Fig. 5. 9a – Acceleration response spectra of the squat tower recorded at the foundation level (thick red lines) and at the top of the SSI-Tower (thin red lines) and FIX-Tower (thin black lines) for the LIN set of analyses (α =1; 2.5; 5; 10; 15).

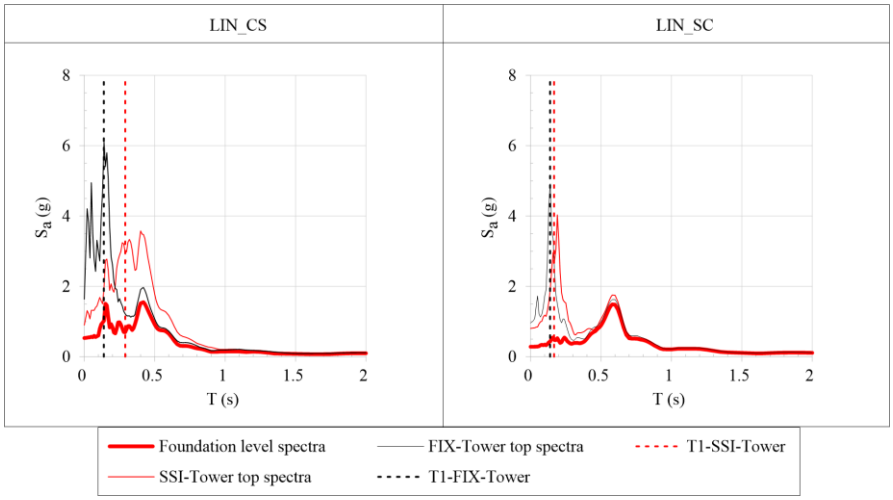

Fig. 5. 9 – Acceleration response spectra of the squat tower recorded at the foundation level (thick red lines) and at the top of the SSI-Tower (thin red lines) and FIX-Tower (thin black lines) for the LIN set of analyses (CS; SC).

Fig. 5.10 shows the bending displacement u_θ time-histories at the top control point of each analysed scenario. The records show remarkable changes in both magnitude and sign, despite the same seismic signal has been inputted at the base of each corresponding SSI and FIX model. Higher displacements are expected in all the analyses which account for the coupled approach, except for the $\alpha = 2.5$ case. The SSI simulations provide accumulation of bending displacement up to 5 cm; conversely the FIX ones do not exceed 2 cm.

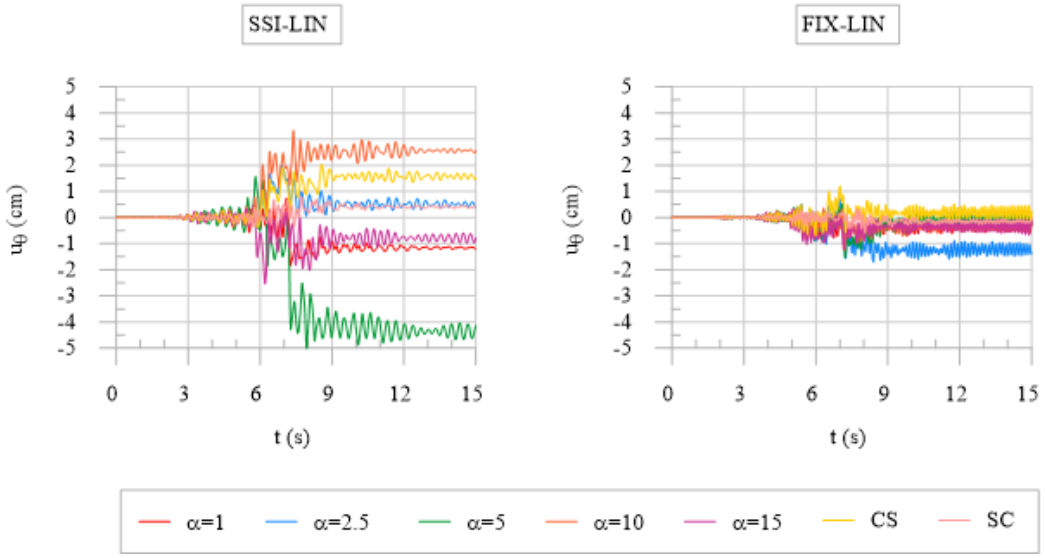

Fig. 5. 10 – Squat tower bending displacements (u_θ) time-histories recorded at the top control point of the structure for each SSI and FIX model for the LIN set of analyses.

5.3.1.2 Results of the squat tower analyses with the equivalent-linear visco-elastic soil approach

The comparison of the damage contours of the SSI squat tower versus the FIX models is reported in Fig. 5.11 for the EQ-LIN set of analyses. As already observed for the LIN set, the outcomes show a small variability in the damage scenario, always localized at the basement level of the structure, in the different simulations. The only cases where the material degradation is manifested also at the belfry level of the tower are the α =10 and α =15 analyses carried out with the fixed-base scheme.

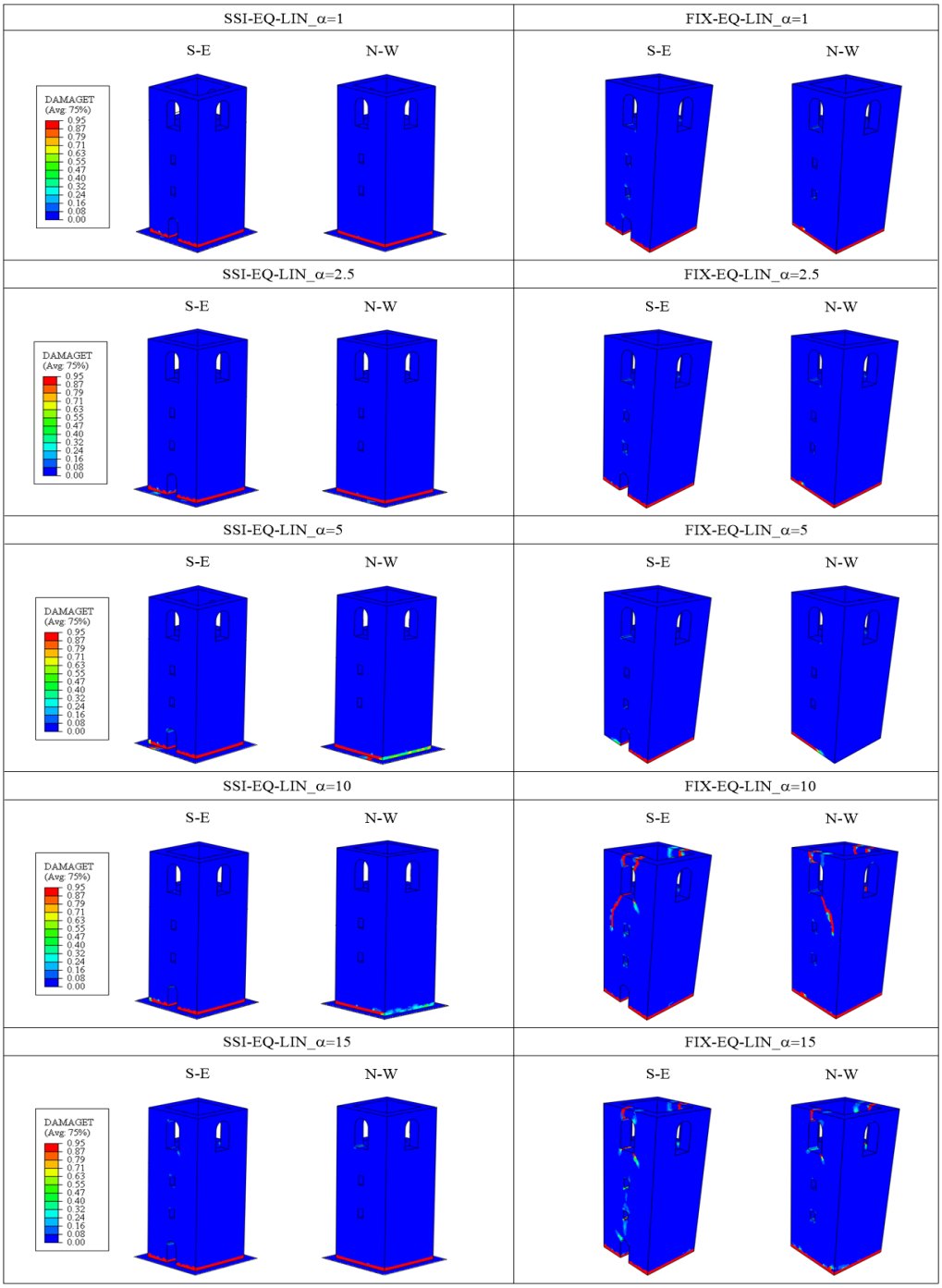

Fig. 5. 11a – Squat tower tensile damage plots at the end of the seismic input motion: EQ-LIN analyses for the coupled SSI and corresponding FIX models (α =1; 2.5; 5;10; 15).

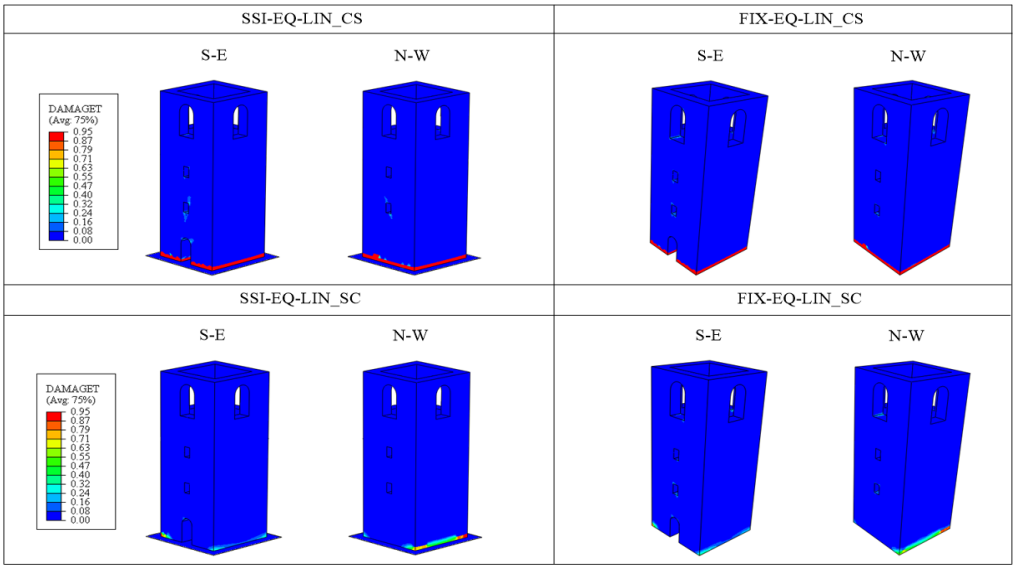

Fig. 5. 11b – Squat tower tensile damage plots at the end of the seismic input motion: EQ-LIN analyses for the coupled SSI and corresponding FIX models (CS; SC).

In Fig. 5.12 the acceleration response spectra derived at different control points of the towers are reported. Looking at the spectra recorded at the tower foundation level (red thick line), the relevant elongation effect given by the soil compliance, which tends to provide lower spectral acceleration values for the SSI towers with respect to the FIX ones, can be observed. This is particularly evident for the $\alpha = 10$ and $\alpha = 15$ analyses, where much higher spectral accelerations are associated to the 1st period of the structure in fixed-base condition.

Finally, as already seen for the LIN analyses, the acceleration spectra recorded at the top of the models (thin red and black lines for the SSI and FIX towers, respectively) highlight that the spectral peaks occur in correspondence of the 1st natural period of each tower model.

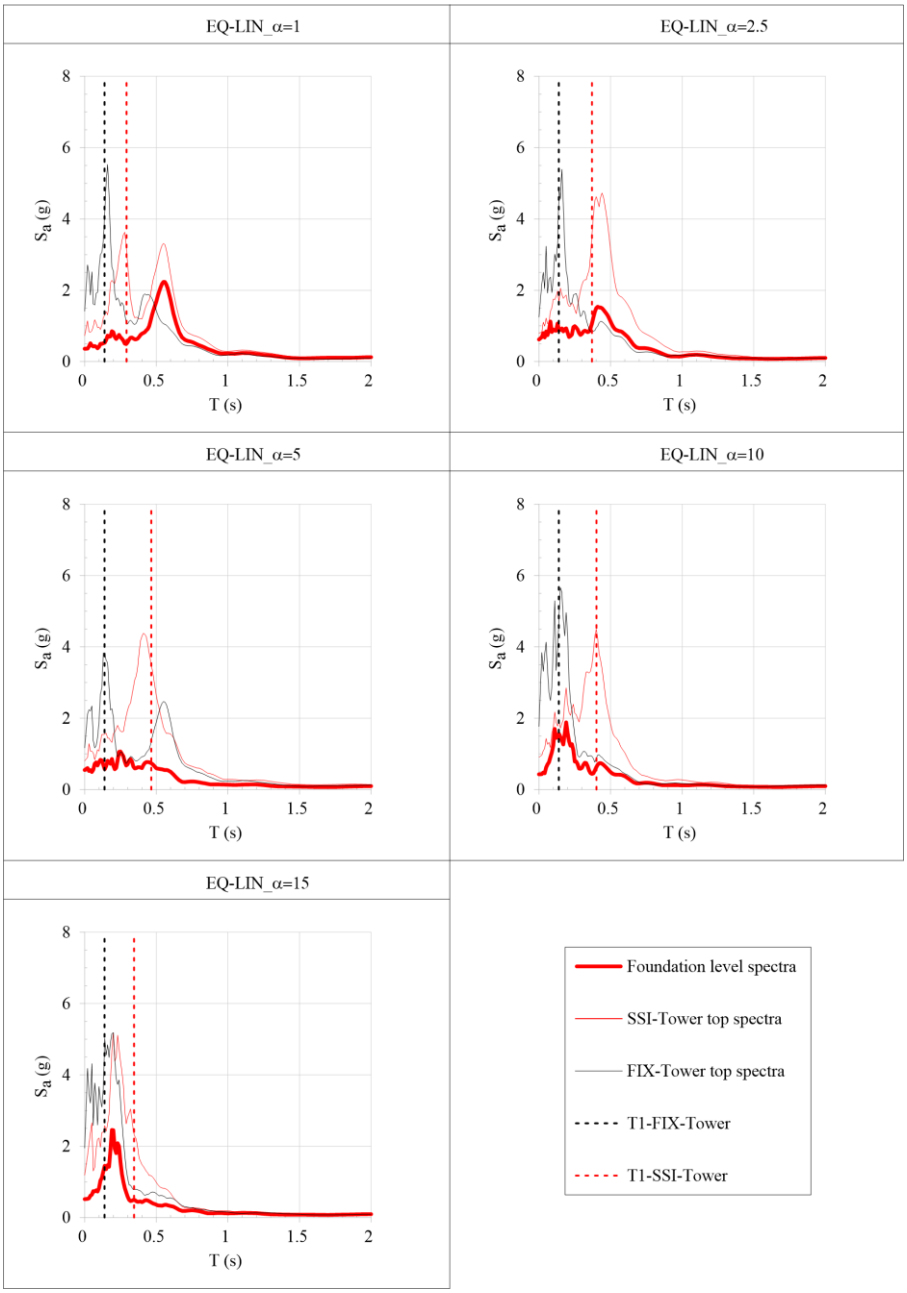

Fig. 5. 12a – Acceleration response spectra of the squat tower recorded at the foundation level (thick red lines) and at the top of the SSI-Tower (thin red lines) and FIX-Tower (thin black lines) for the EQ-LIN set of analyses (α =1; 2.5; 5; 10; 15).

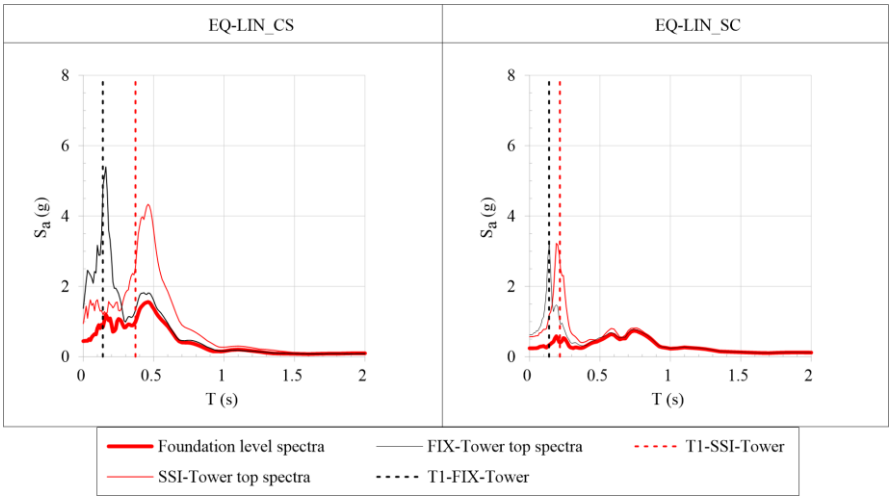

Fig. 5. 12b – Acceleration response spectra of the squat tower recorded at the foundation level (thick red lines) and at the top of the SSI-Tower (thin red lines) and FIX-Tower (thin black lines) for the EQ-LIN set of analyses (CS; SC).

Fig. 5.13 shows the bending displacement u_θ time-histories at the top control point of each analysed case. As already observed for the LIN set of analyses, the records show significant differences between the SSI and FIX approach. In fact, higher displacements are provided in all the analyses which account for the coupled approach, except for the α =15 case. The SSI simulations are characterized by greater residual displacements, up to 5cm for α =5; conversely the FIX ones are all smaller than 2cm.

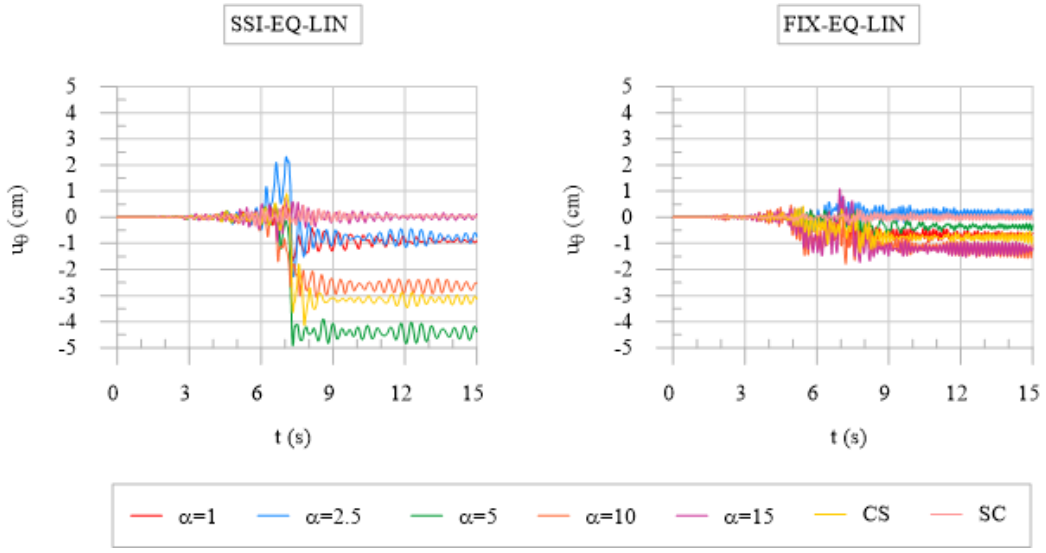

Fig. 5. 13 – Squat tower bending displacements (u_θ) time-histories recorded at the top control point of the structure during each SSI and FIX model for the EQ-LIN set of analyses.

5.3.1.3 Comparison of the results for the squat tower

The damage contour plots show a rather flat response in all the analysed scenarios, no matter if soil compliance is considered or not. Indeed, the damage concentration has been always recognized at the basement level of the structure and only in very few cases the bell cell results affected by the seismic event, i.e. for the FIX-EQ-LIN_α =10 and the FIX-EQ-LIN_α =15 simulations.

The analysis of the acceleration response spectra highlights that the period elongation due to the soil compliance usually results in lower spectral accelerations in correspondence of the 1st natural period of the tower. Obviously, this trend becomes more significant when the EQ-LIN soil behaviour is considered, due to the introduction of the non-linear soil effects.

The analysis of the bending displacement time-histories recorded at the top of the tower models also show that the coupled approach generally produces higher displacement demand in comparison to the fixed-base scheme.

Further insights concerning the soil modelling influence on the dynamic response of the structure can be drawn from Fig. 5.14, where the comparison between the bend-

ing and the rocking displacements at the top control point of the SSI tower for the LIN and EQ-LIN set of analyses is shown. Rather different responses can be observed in terms of bending displacement time-histories for the $\alpha = 2.5$, $\alpha = 10$ and CS cases; conversely, a similar trend is observed for $\alpha = 1$ and $\alpha = 5$. Moreover, the introduction of the soil non-linearity through the EQ-LIN approach generally induces higher spikes in the rocking displacements records, for each analysed stratigraphy.

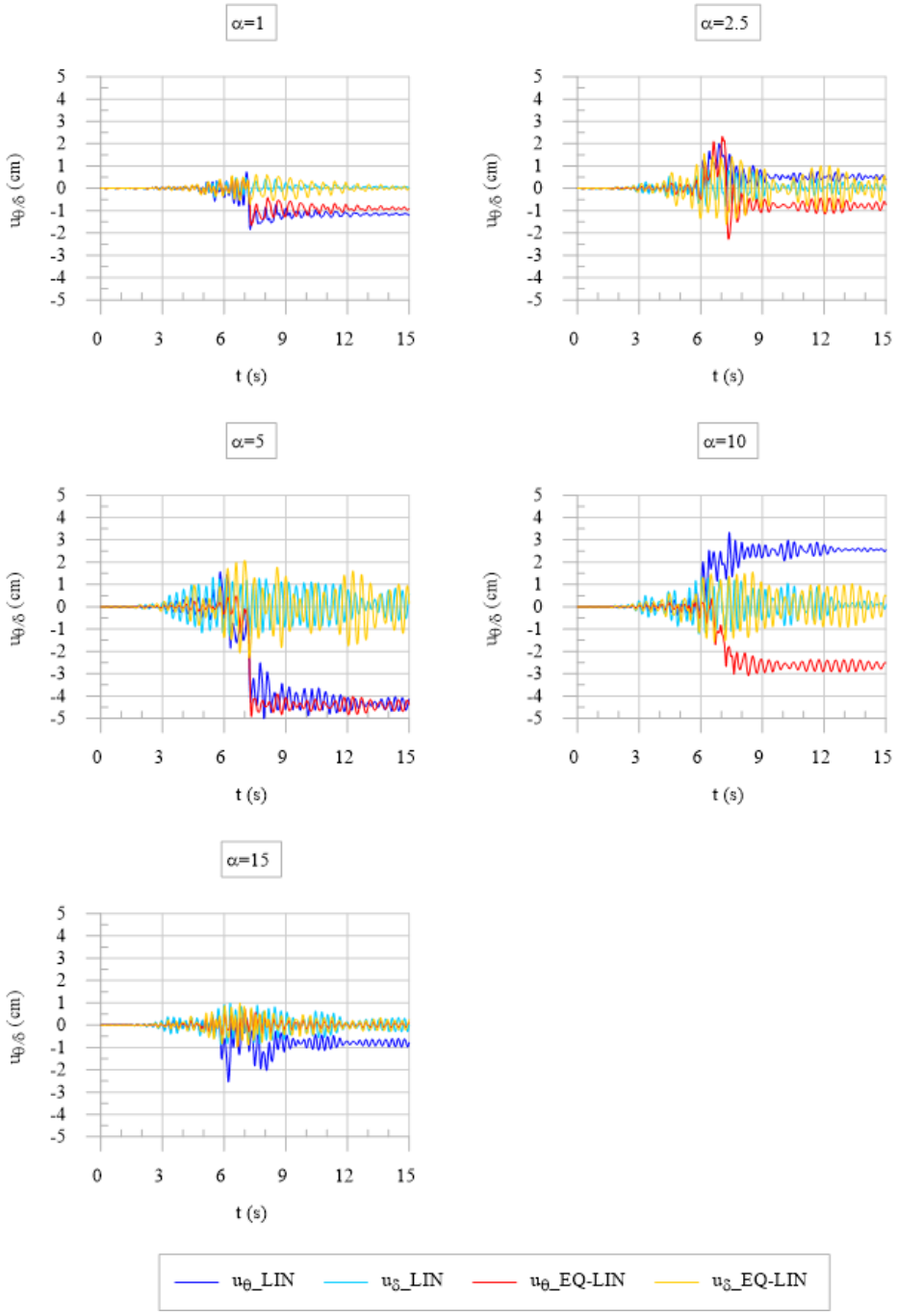

Fig. 5. 14a – Squat tower bending (u_θ) and rocking (u_δ) displacements time-histories recorded at top of the tower during each SSI-LIN and SSI-EQ-LIN models (α =1; 2.5; 5; 10; 15).

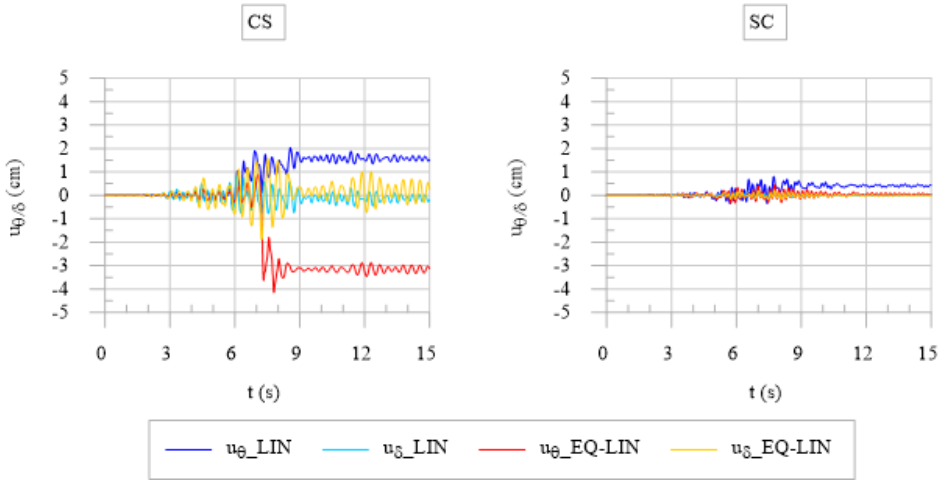

Fig. 5. 14b – Squat tower bending (u_θ) and rocking (u_δ) displacements time-histories recorded at top of the tower during each SSI-LIN and SSI-EQ-LIN models (CS; SC).

Finally, the maximum bending displacements profiles recorded at 5 control points located along the height of the tower in each analysed scenario are shown in Fig. 5.15. The SSI models result in more demanding displacements profiles with respect to the FIX ones, except for very few cases (i.e. $\alpha = 1$ for the EQ-LIN set and SC for the LIN one). The plots also highlight regular trends along the tower height, without any relevant differential displacement. This applies for both the SSI and FIX scheme, suggesting that the structure has not suffered any relevant damage during the seismic motion.

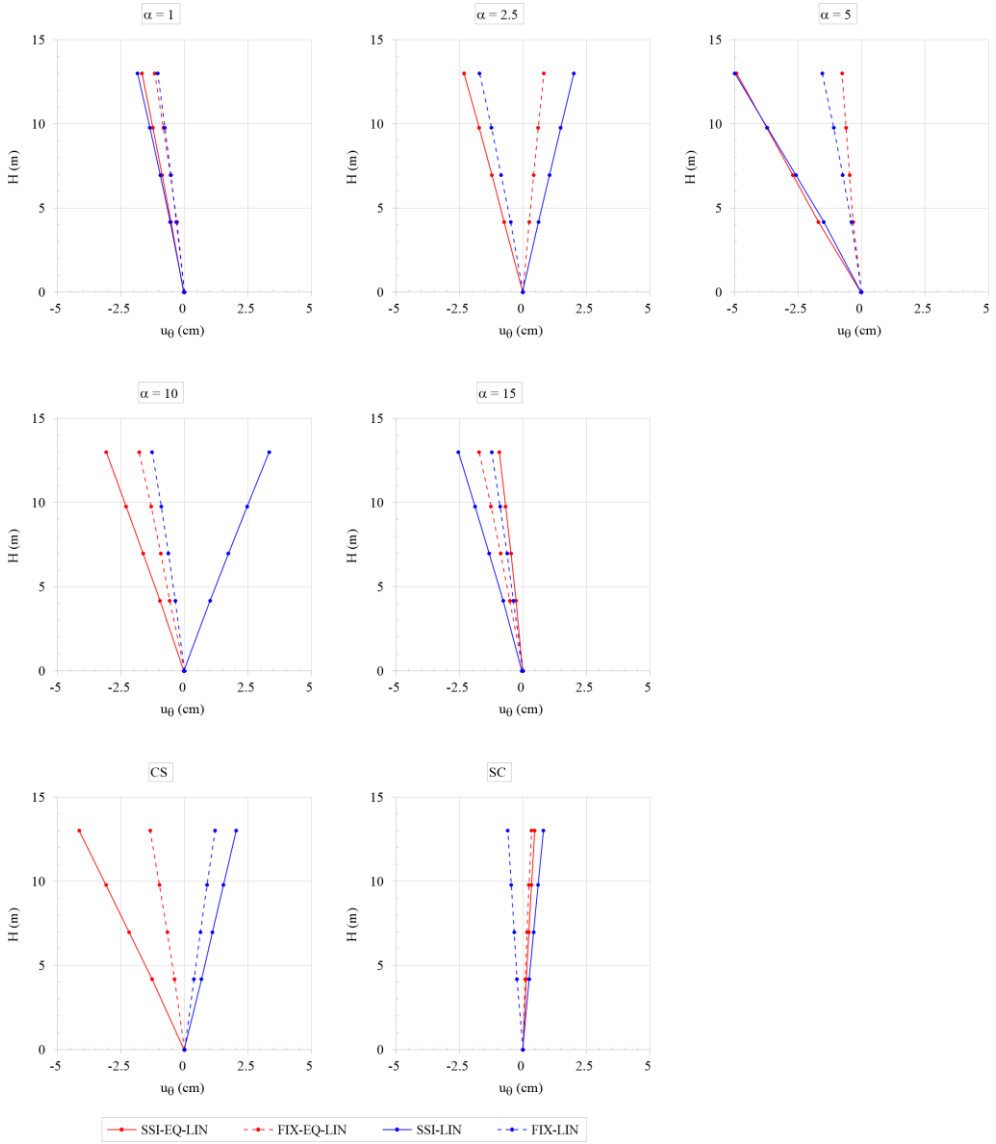

Fig. 5. 15 – Squat tower maximum bending displacements (u_θ) profiles along the tower height for each SSI and FIX model during both the LIN and EQ-LIN analyses.

5.3.2.1 Results of the very slender tower analyses with the linear visco-elastic soil approach

The numerical results obtained for the non-linear dynamic analyses of the very slender tower are illustrated, in terms of damage contour plots, for each SSI and FIX simulations in Fig. 5.16 considering the LIN assumption. Some analyses have not reached the end of the seismic input for convergence issues. Hence, the time at which the analysis stopped is also reported in each damage map.

Differently from the squat tower case, the very slender tower exhibits more variability in the damage pattern distribution, showing different responses depending on the soil conditions and the tower base-scheme adopted.

In the $\alpha = 1$ case, both the SSI and the FIX models stopped before the end of the seismic input motion, at around 9.2s. In the SSI model, the damage is rather diffuse along all the tower height, also involving the belfry level. However, it is the basement area that suffers the worst situation with a more intense damage concentration right above the main entrance; several vertical cracks are also present in the first half of the tower, reminding a vertical splitting collapse mode of the structure. On the contrary, the corresponding FIX model shows a remarkable localization of the deformation at the basement level with diagonal cracks and a smaller damage distribution involving the middle part of the tower (Fig. 5.16a).

In the $\alpha = 2.5$ case, a clear vertical damage path located in the middle of the SSI tower, from which secondaries horizontal cracks develop in correspondence of the minor openings of the structure, can be recognised, while the belfry is limitedly damaged. The FIX simulation provides a similar scenario with more intense damage localized at the bottom and at the top of the structure (Fig. 5.16a).

The results for $\alpha = 5$ and $\alpha = 10$ (Fig. 5.16b) show a very different situation depending on the tower base condition. Indeed, both the SSI models result in quite mild damage distribution localized at the middle of the structure. On the contrary, the FIX models are more affected by the seismic action and show a clear vertical damage concentration for $\alpha = 5$ and a cylindrical hinge right above the main entrance for $\alpha = 10$; moreover both these latter models present cracks at the belfry level.

The $\alpha = 15$ case is, instead, characterized by some cracks at the belfry level of the two models with a similar pattern (Fig. 5.16c).
The CS case presents an analogue situation to that described for $\alpha = 2.5$.
Finally, the SC case outlines a probable shear diagonal collapse, occurring close to the bottom of the tower, no matter if the soil compliance is considered or not (Fig. 5.16d).

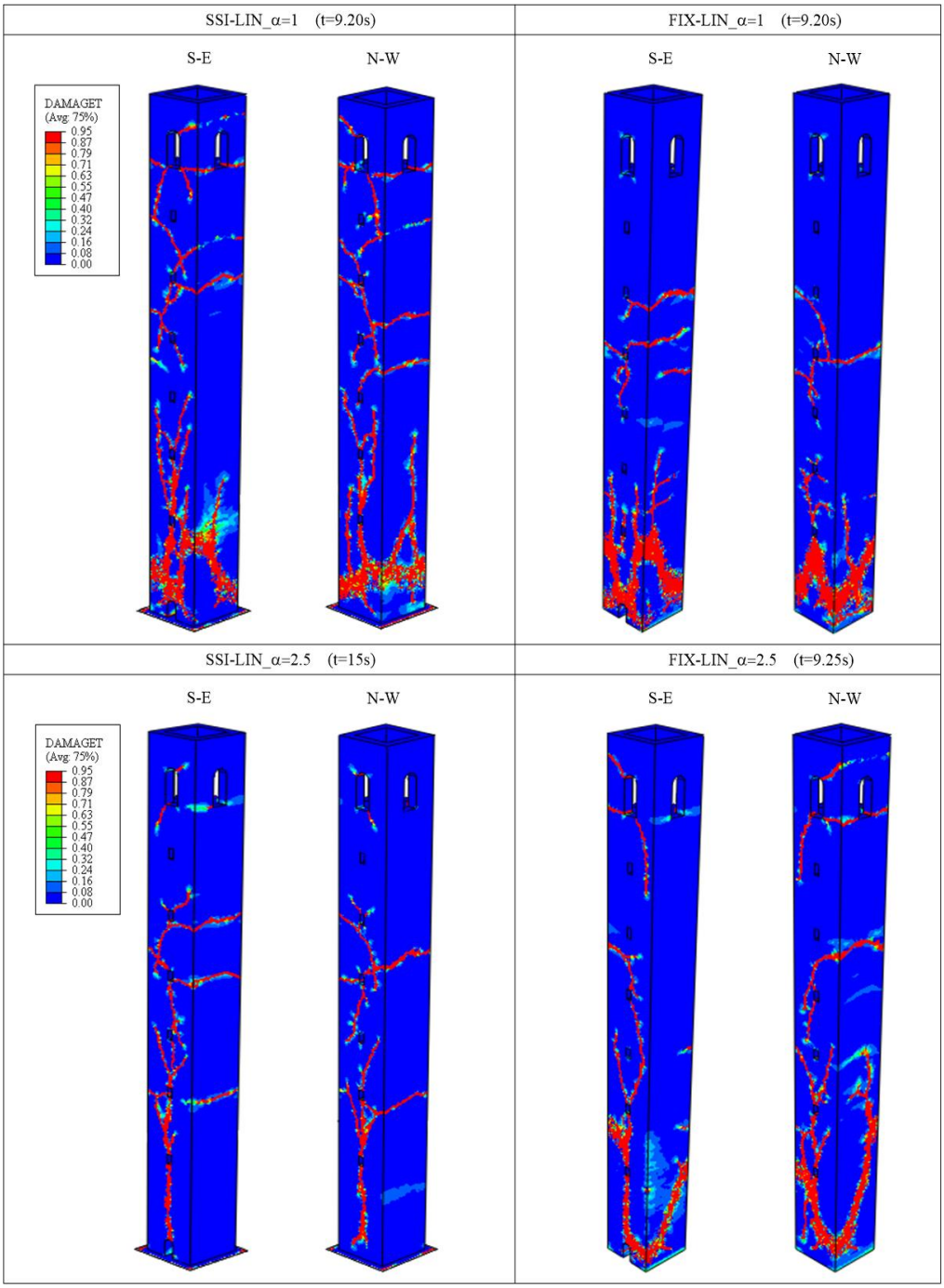

Fig. 5. 16a – Very slender tower tensile damage plots: LIN analyses for the coupled SSI and corresponding FIX models (α =1; 2.5).

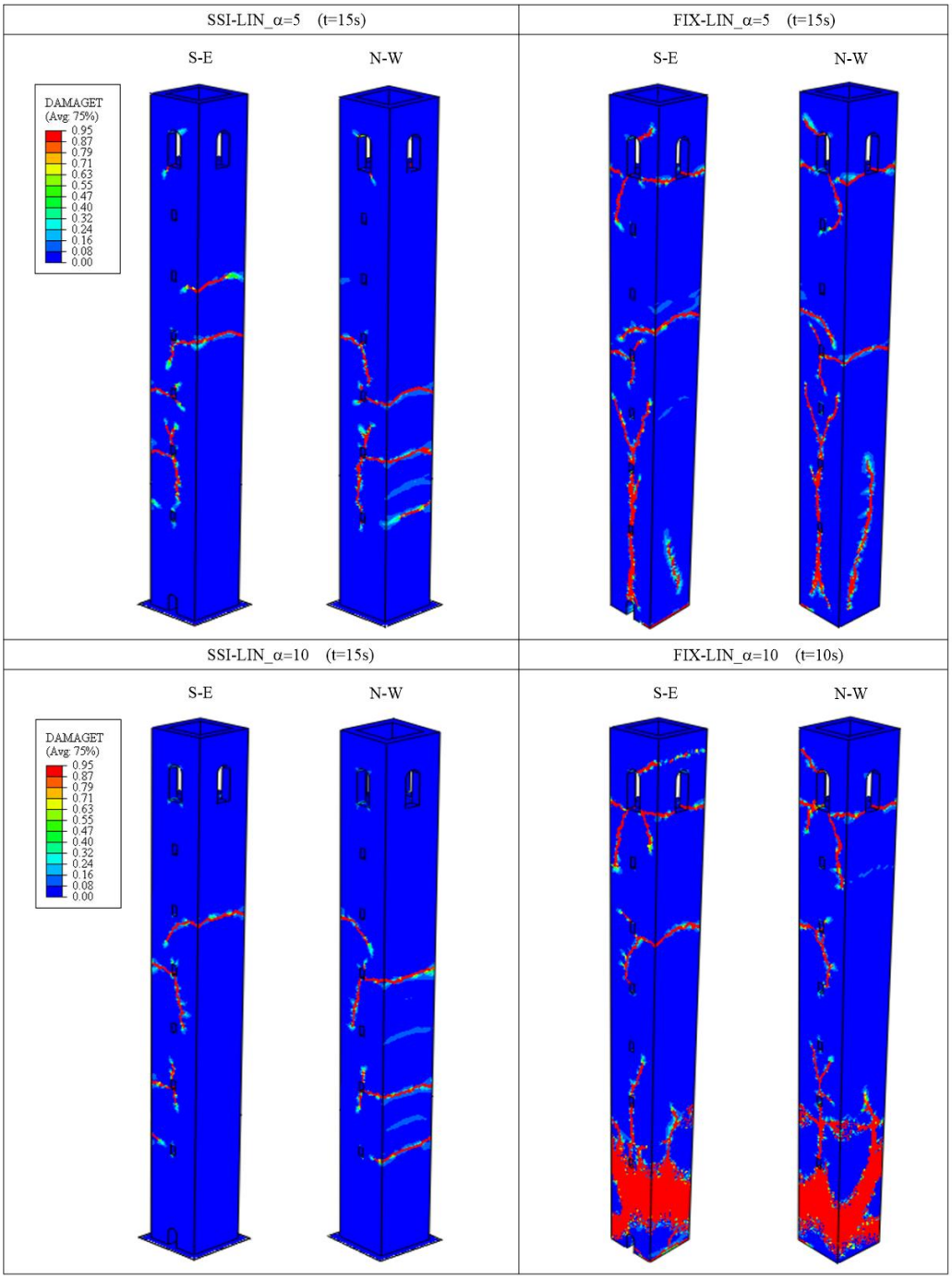

Fig. 5. 16b – Very slender tower tensile damage plots: LIN analyses for the coupled SSI and corresponding FIX models (α =5; 10).

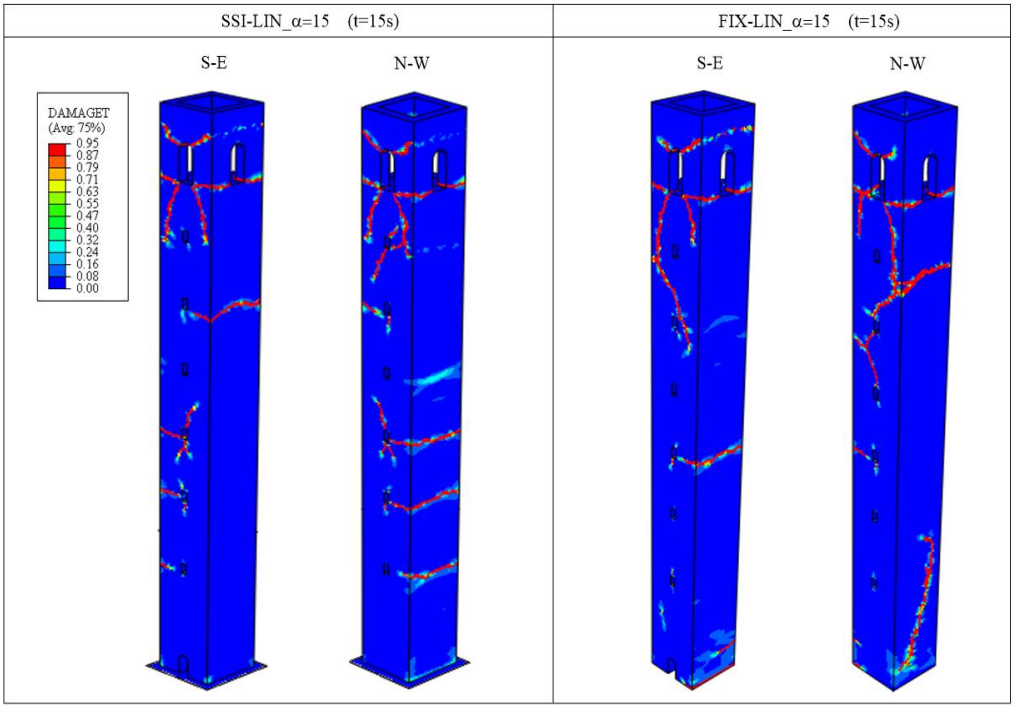

Fig. 5.16c – Very slender tower tensile damage plots: LIN analyses for the coupled SSI and corresponding FIX models (α =15).

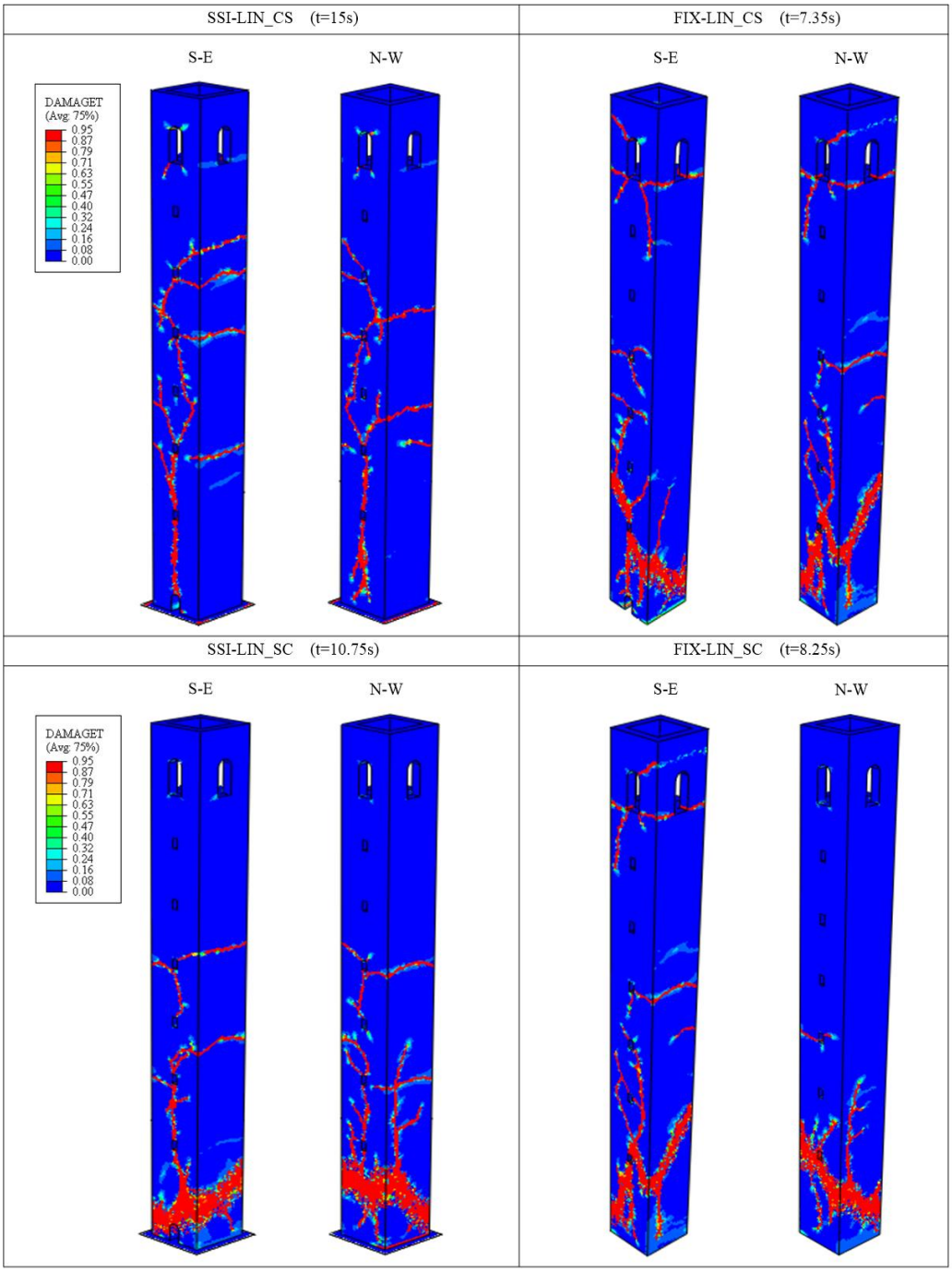

Fig. 5. 16d – Very slender tower tensile damage plots: LIN analyses for the coupled SSI and corresponding FIX models (CS; SC).

The acceleration response spectra recorded at the tower foundation level are reported in Fig. 5.17, together with the 1st and 2nd natural periods of the structure in fixed-base condition and interacting with the soil. The plots highlight the elongation effect due to the soil compliance. The 1st period elongation does not produce any relevant reduction in the seismic demand, since even in the fixed-base condition the period of the structure falls into the descending branch of the foundation spectra (red thick line). For the 2nd period the elongation phenomenon results much more limited and, consequently, the seismic demand does not change much when the soil compliance is considered; nevertheless, actually a slight increase is observed in this case.

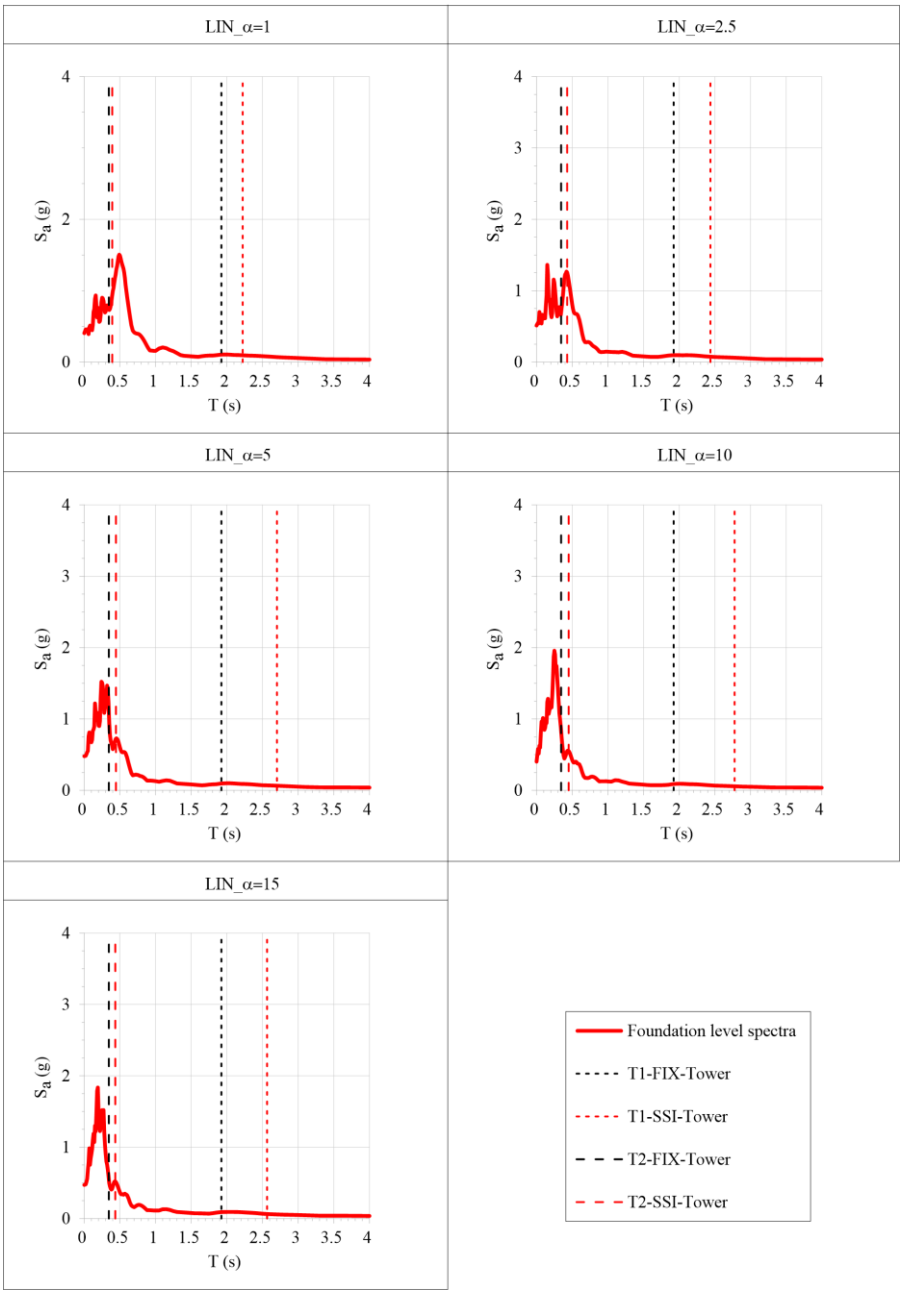

Fig. 5. 17a – Acceleration response spectra of the very slender tower recorded at the foundation level (thick red lines) and at the top of the SSI-Tower (thin red lines) and FIX-Tower (thin black lines) for the LIN set of analyses (α =1; 2.5; 5; 10; 15).

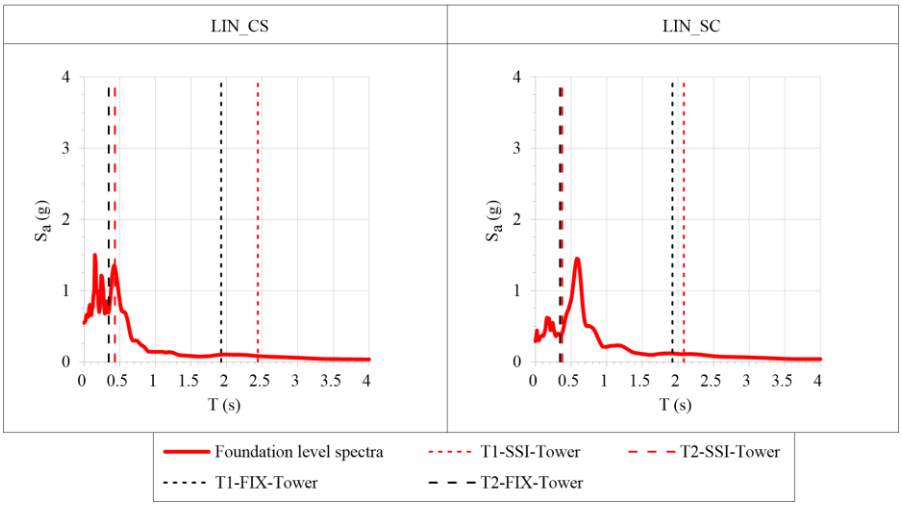

Fig. 5. 17b – Acceleration response spectra of the very slender tower recorded at the foundation level (thick red lines) and at the top of the SSI-Tower (thin red lines) and FIX-Tower (thin black lines) for the LIN set of analyses (CS; SC).

The bending displacement records derived at the top of the tower, considering the SSI and the FIX corresponding models, are plotted in Fig. 5.18. The time-histories report a cross when the analysis stopped because of poor convergence. In this regard, 5 of the 7 analyses performed adopting the fixed-base scheme have not been completed, while just 2 out of 7 stopped when the compliant-base scheme has been adopted. Nevertheless, relevant accumulation of permanent displacements is observed also in all the successfully completed analyses considering soil-structure interaction, of the order of 10-15cm.

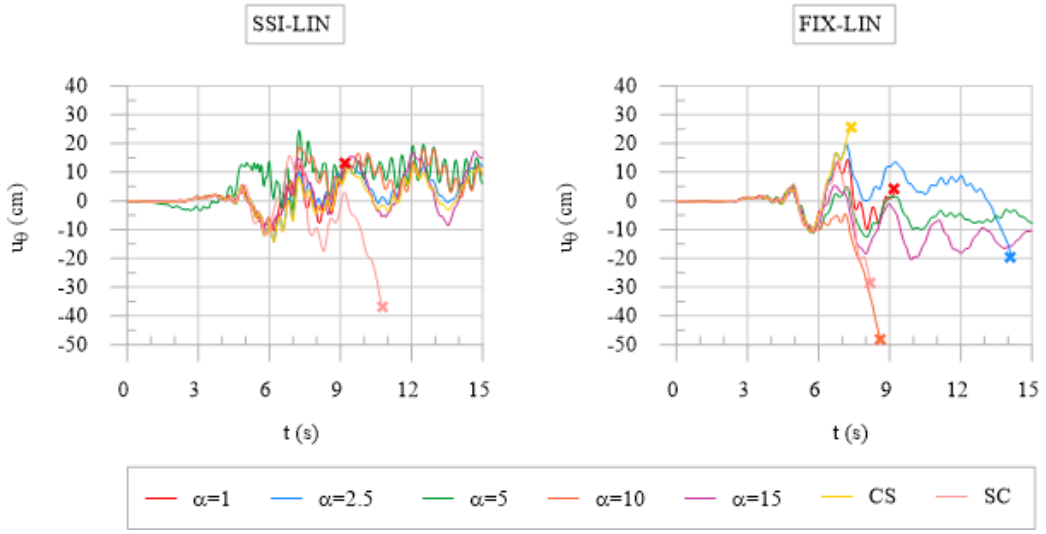

Fig. 5. 18 – Very slender tower bending displacements (u_θ) time-histories recorded at the top control point of the structure during each SSI and FIX model for the LIN set of analyses.

5.3.2.2 Results of the very slender tower analyses with the equivalent-linear visco-elastic soil approach

The damage scenarios obtained for the EQ-LIN soil modelling approach is depicted in Fig. 5.19.

The $\alpha = 1$ case shows a similar damage pattern both for the SSI and FIX models, characterized by a huge damage concentration close to the base level inducing the collapse of the structure (Fig. 5.19a).

The $\alpha = 2.5$ provides a vertical splitting of the tower for the SSI case. In the FIX condition, the vertical damage concentration then evolves in a sort of plastic-damage hinge located right above the main entrance of the structure (Fig. 5.19a).

The $\alpha = 5$ case outlines just some horizontal cracks located at the middle of the tower for the SSI model, while the recurring vertical splitting mechanism is recognizable in the FIX analysis (Fig. 5.19b).

For both the $\alpha = 10$ (Fig. 5.19b) and $\alpha = 15$ (Fig. 5.19c) cases the damage contour plots are very similar, irrespective of the base condition of the tower; indeed the dam-

age distribution is mainly localized at the belfry level and in the second half of the tower.

The CS case (Fig. 5.19d) is characterised by a probable vertical splitting collapse, when the soil compliance is considered, and by a shear diagonal failure mode, when the tower is fixed at the base.

Finally, the SC case manifests a clear diagonal damage concentration right above the main entrance both in the SSI and FIX analyses (Fig. 5.19d).

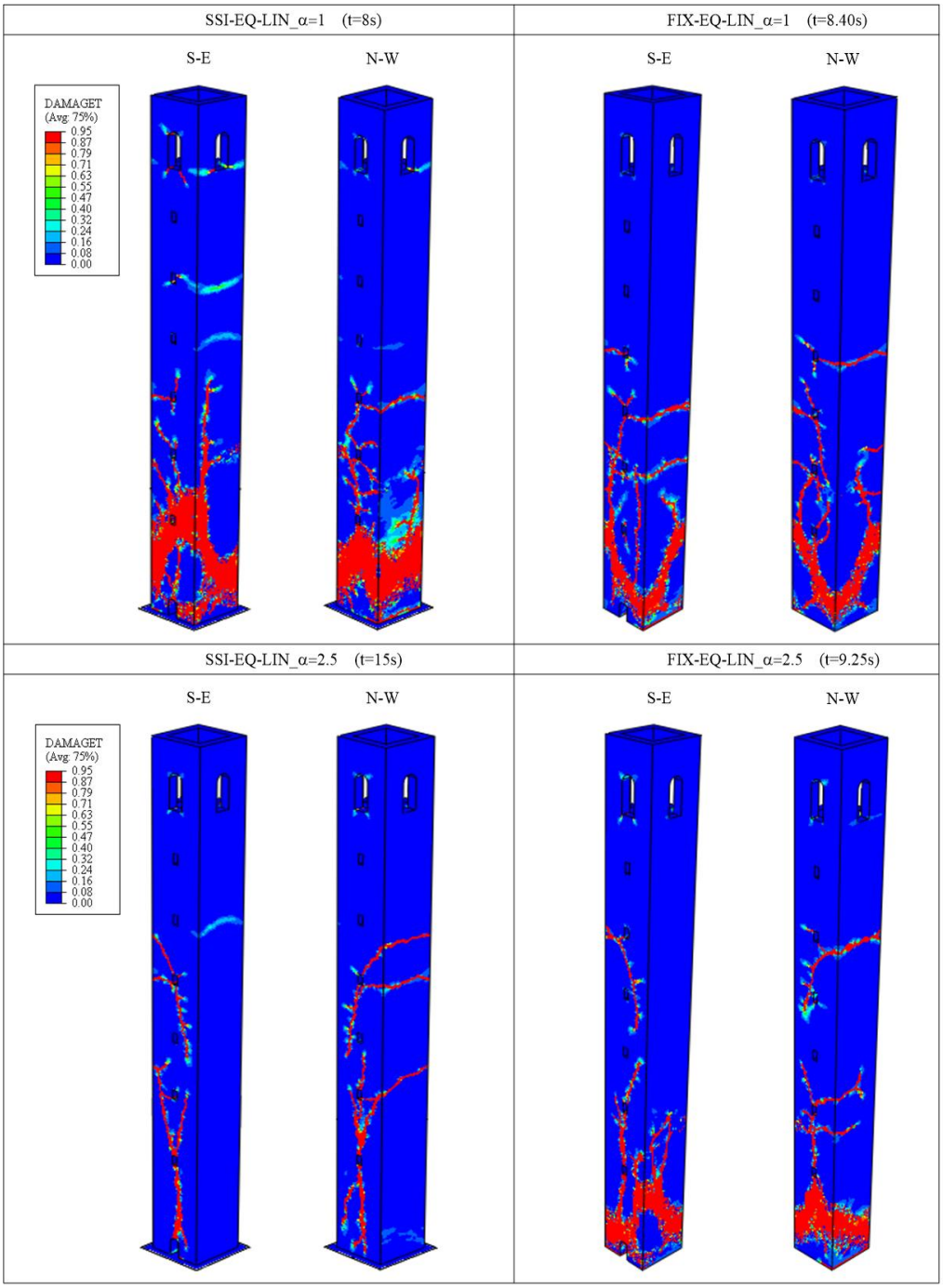

Fig. 5. 19a – Very slender tower tensile damage plots: EQ-LIN analyses for the coupled SSI and corresponding FIX models (α =1; 2.5).

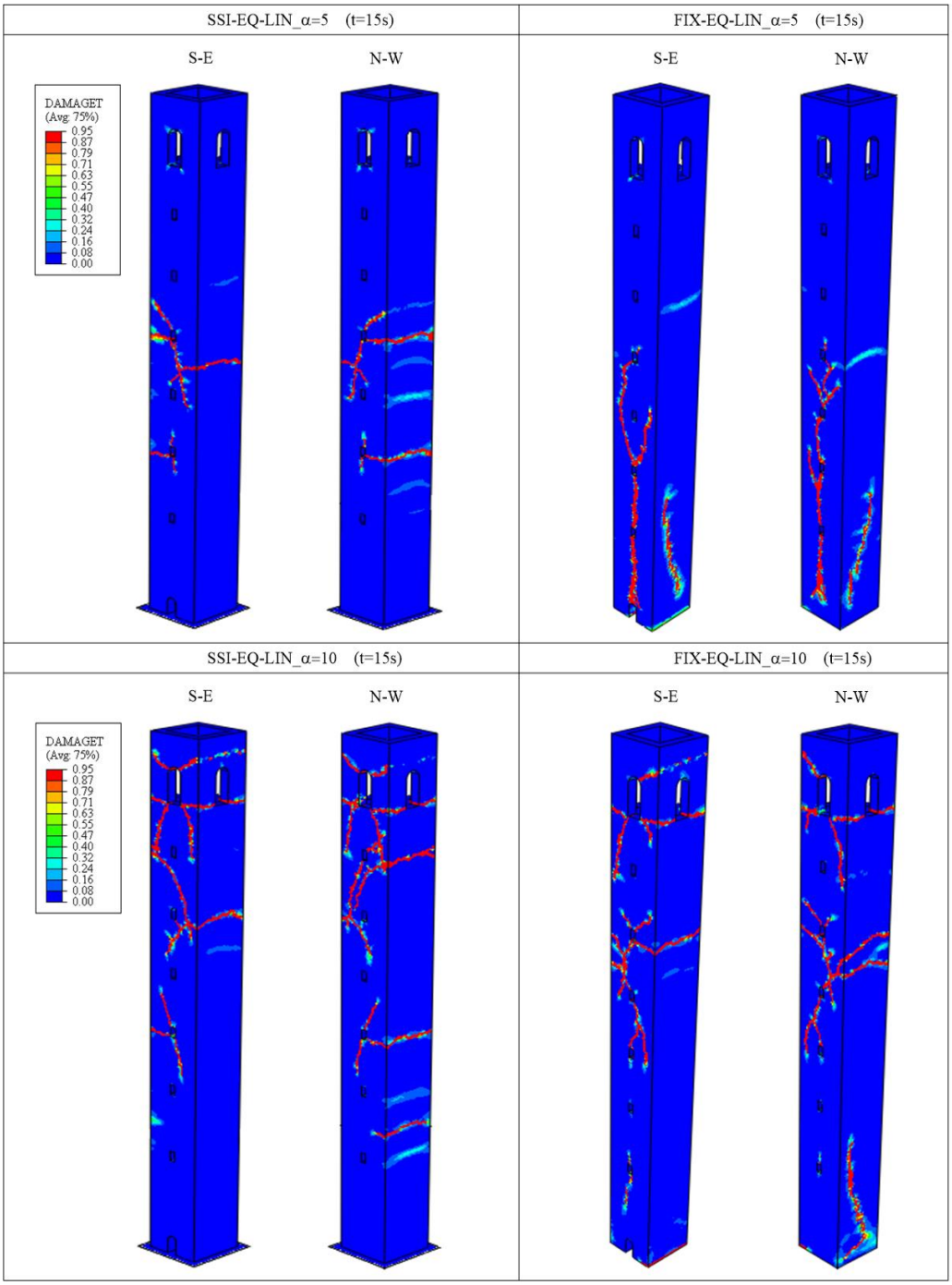

Fig. 5. 19b – Very slender tower tensile damage plots: EQ-LIN analyses for the coupled SSI and corresponding FIX models (α =5; 10).

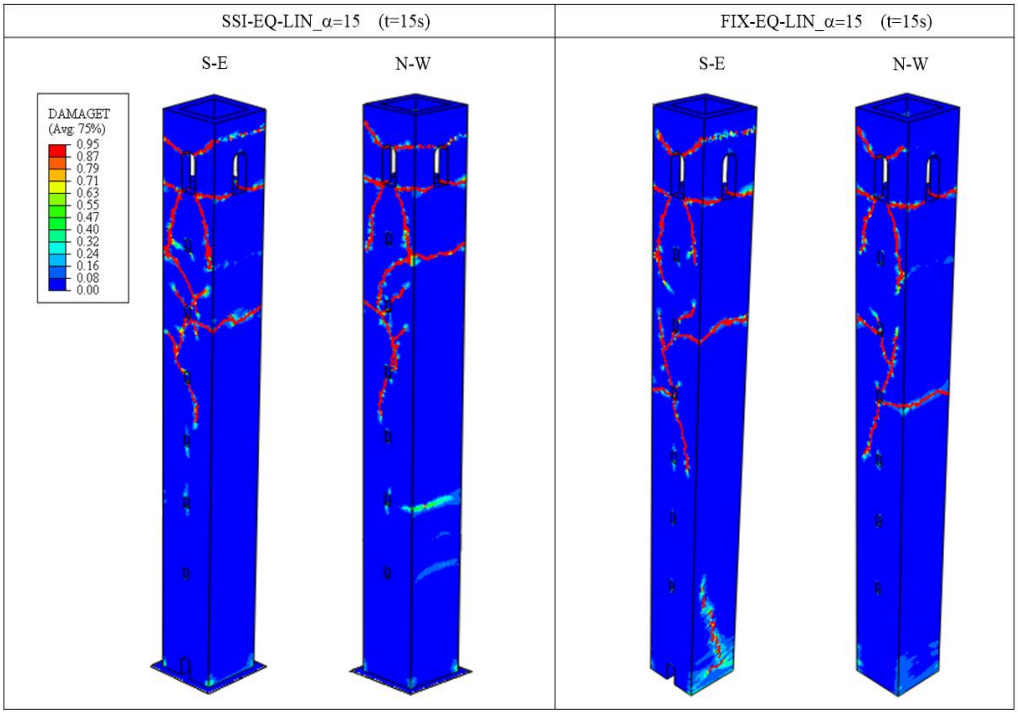

Fig. 5. 19c – Very slender tower tensile damage plots: EQ-LIN analyses for the coupled SSI and corresponding FIX models (α =15).

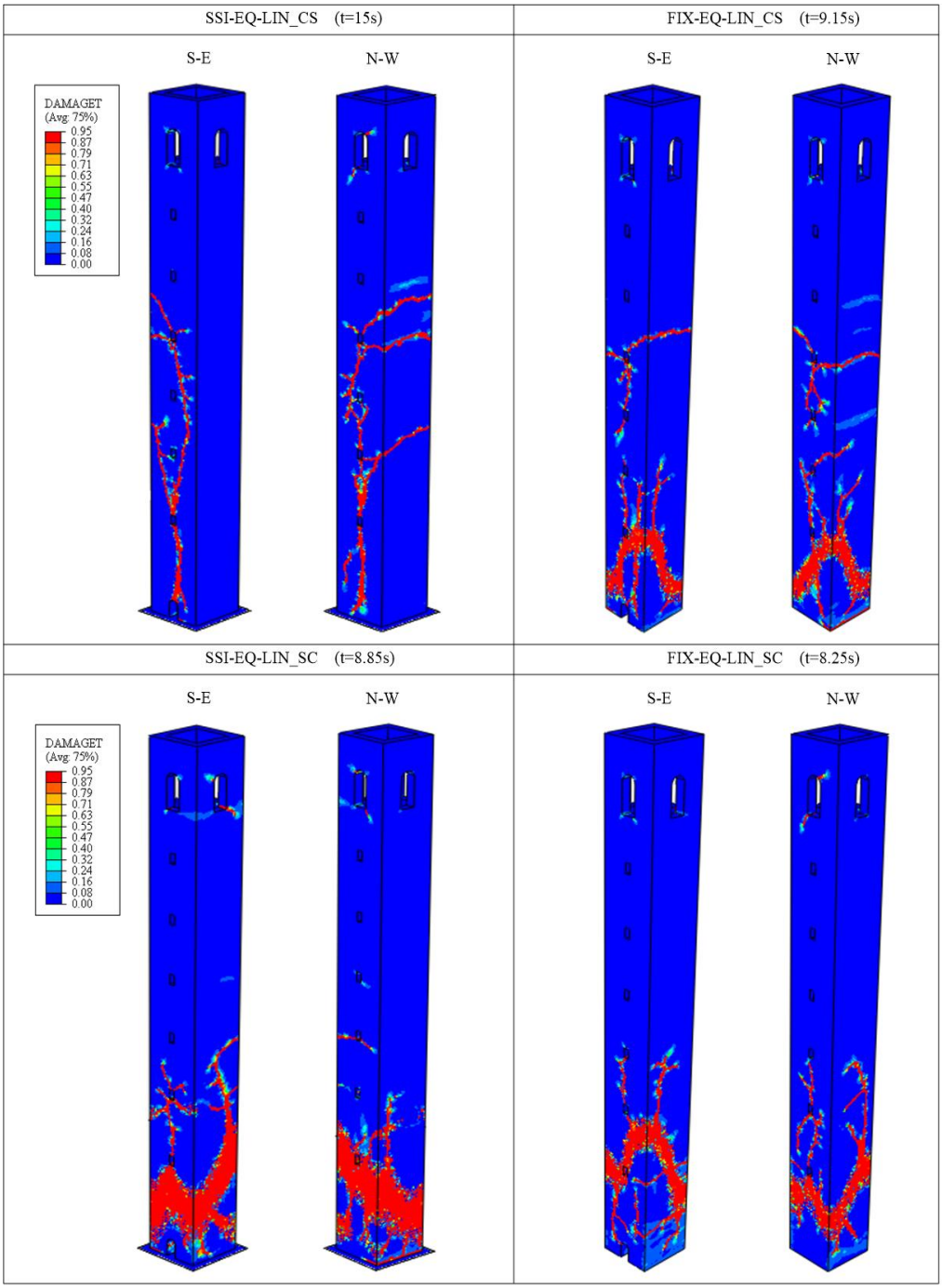

Fig. 5. 19d – Very slender tower tensile damage plots: EQ-LIN analyses for the coupled SSI and corresponding FIX models (CS; SC).

As already done for the LIN set of simulations, the acceleration response spectra recorded at different control points of the tower are reported in Fig. 5.20. The 1st and 2nd natural periods depicted on the charts highlight the elongation effect due to the soil-structure interaction phenomena. The 1st period elongation does not produce any relevant reduction in the seismic demand, since even in the fixed-base condition the period of the structure falls into the descending branch of the foundation spectra (red thick line). On the contrary, the elongation of the 2nd period generally results in higher spectral accelerations.

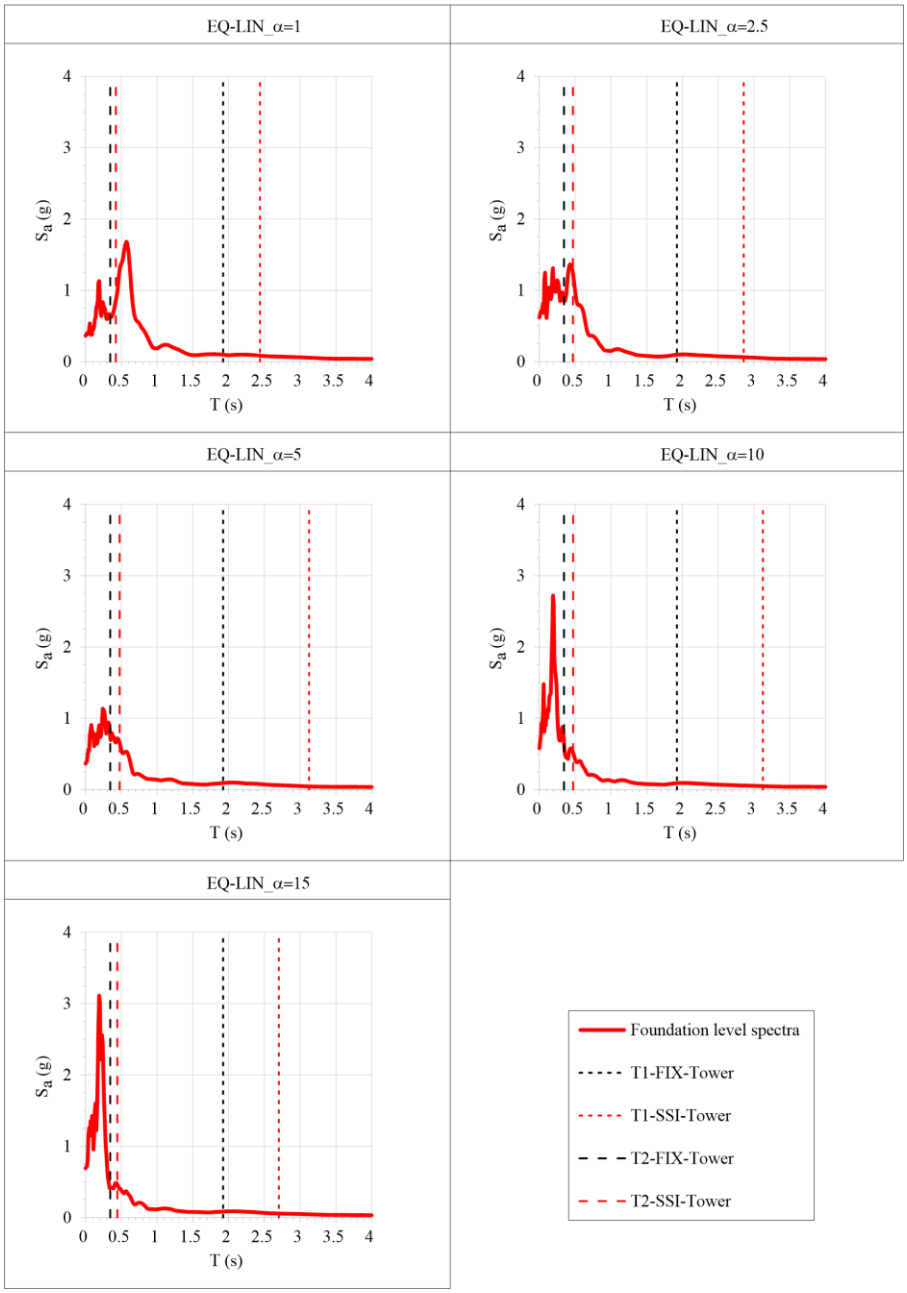

Fig. 5. 20a – Acceleration response spectra of the very slender tower recorded at the foundation level (thick red lines) and at the top of the SSI-Tower (thin red lines) and FIX-Tower (thin black lines) for the EQ-LIN set of analyses (α =1; 2.5; 5; 10; 15).

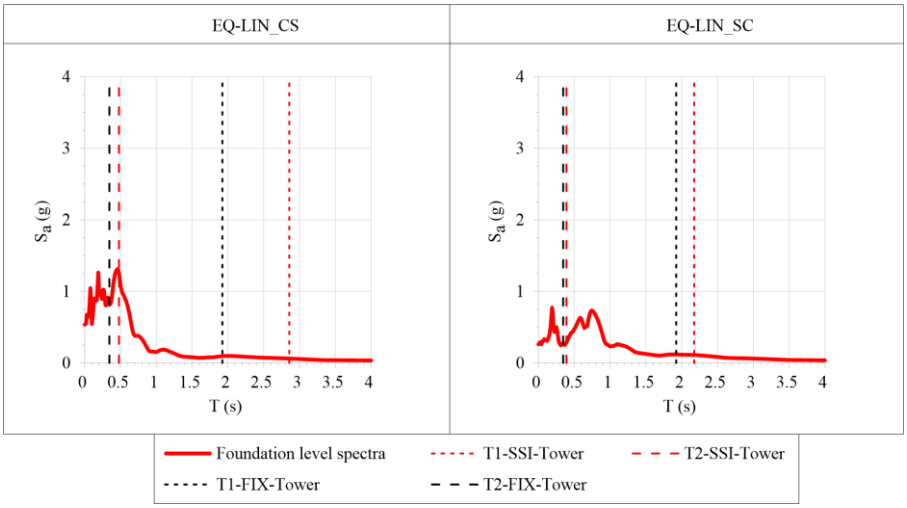

Fig. 5. 20b – Acceleration response spectra of the very slender tower recorded at the foundation level (thick red lines) and at the top of the SSI-Tower (thin red lines) and FIX-Tower (thin black lines) for the EQ-LIN set of analyses (CS; SC).

Fig. 5.21 collects the bending displacement time-histories obtained at the top of the SSI and FIX tower. The records also report a cross when the analysis stopped because of poor convergence. In the specific, it can be noted that 4 of the 7 analyses performed adopting the fixed-base scheme have not been completed, while just 2 on 7 when the SSI model was considered. An important accumulation of displacement is observed in all the successfully completed SSI analyses, which reach the 30cm for the $\alpha = 2.5$ and CS cases. More limited values are, instead, obtained from the successfully completed FIX simulations in comparison with the corresponding SSI cases.

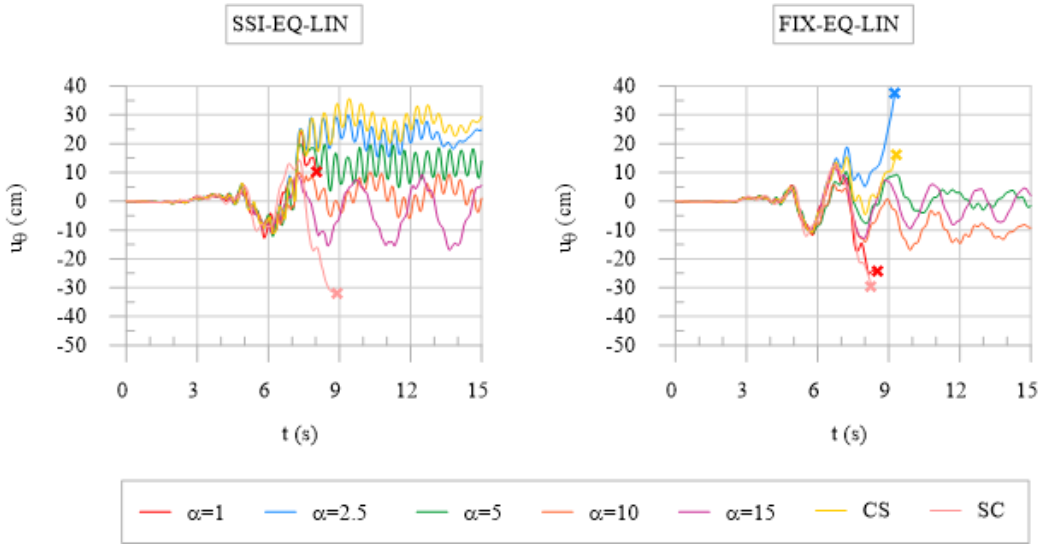

Fig. 5. 21 – Very slender tower bending displacements (u_θ) time-histories recorded at the top control point of the structure during each SSI and FIX model for the EQ-LIN set of analyses.

5.3.2.3 Comparison of the results for the very slender tower

As a general finding, it is observed that the soil compliance can potentially affect the damage distribution along the height of the very slender tower, since it can be very different between the SSI and the FIX models. Particularly different patterns are, for example, recorded for α =5 and α =10 in the LIN set of analyses and for α =2.5, α =5 and CS cases in the EQ-LIN one. However, it is also possible to identify similar trends, like the ones recorded for the α =15 case in the LIN set and α =1, α =10, α =15 and SC cases in the EQ-LIN set. The obtained damage patterns of the SSI analyses look to be more variable with respect to the FIX analyses when the LIN soil approach has been considered. In addition, as already observed for the slender tower analyses, as the heterogeneity ratio increases the damage pattern looks to affect more often the upper part of the structure for both the LIN and EQ-LIN sets.

The analysis of the acceleration response spectra highlights that the period elongation due to the soil compliance produces a change in the seismic demand, which usually results in lower spectral accelerations for the 1st natural period; conversely, for the 2nd one an increase is more likely to occur with respect to the fixed-base condition. Obvi-

ously, this trend become more significant when the EQ-LIN soil approach is adopted, due to the introduction of the non-linear soil effects.

The analysis of the bending displacement time-histories recorded at the top of the tower models also show significant differences between the SSI and the FIX models, providing displacement demands which are greater when the coupled models are used, especially for the EQ-LIN set of analyses.

Further insights about the role of the soil modelling approach adopted on the dynamic response of the structure can be derived from Fig. 5.22 comparing the bending and the rocking displacements at the top control point of the SSI tower for the two soil calibrations used in the study. The choice of the calibration adopted to model the soil dynamic behaviour can influence the magnitude and sign of the accumulated bending displacements. This is particularly evident for the $\alpha = 2.5$ and the CS profiles where important residual displacements are provided by the EQ-LIN simulations at the end of the seismic event. Moreover, the introduction of the soil non-linearity through the EQ-LIN approach generally generates higher rocking displacements in each analysed scenario with respect to the LIN approach, even though the overall trends are still quite comparable.

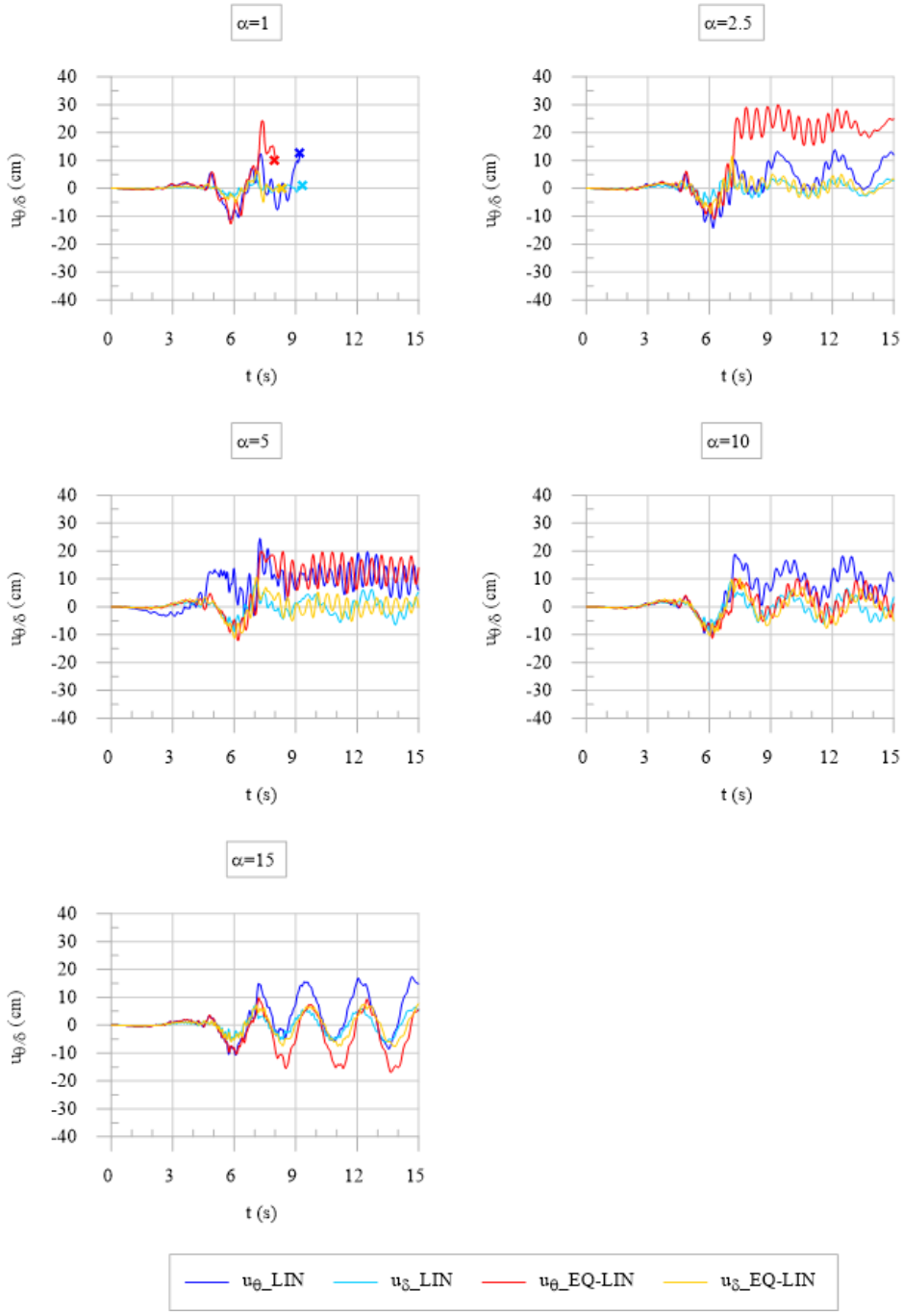

Fig. 5. 22a – Very slender tower bending (u_θ) and rocking (u_δ) displacements time-histories recorded at top of the tower during each SSI-LIN and SSI-EQ-LIN models (α =1; 2.5; 5; 10; 15).

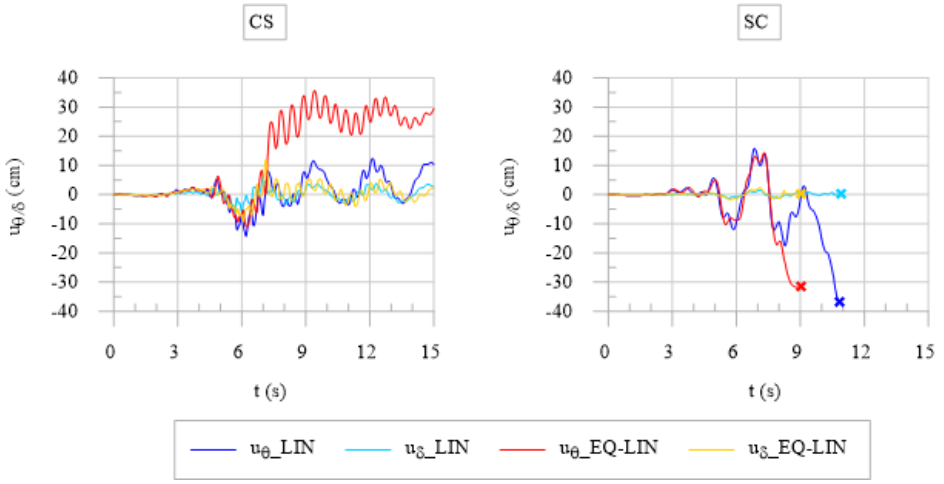

Fig. 5. 22b – Very slender tower bending (u_θ) and rocking (u_δ) displacements time-histories recorded at top of the tower during each SSI-LIN and SSI-EQ-LIN models (CS; SC).

Finally, the maximum bending displacements recorded at 10 different control points along the tower height are reported in Fig. 5.23. The profiles confirm the localization of high level of deformations where damage occurred. For example, the displacements peaks identified between 5 and 10m of height in the $\alpha = 1$ set as in the FIX-EQ-LIN_$\alpha = 2.5$, FIX-LIN_$\alpha = 10$ or in the SSI-EQ-LIN_SC, suggest the activation of a failure mode of the tower. Moreover, the cases where the belfry and the upper part of the structure exhibit severe damage able to cause a partial collapse mode are evident: for instance the FIX-LIN_$\alpha = 2.5$ case, the SSI and FIX models of the EQ-LIN set for the $\alpha = 10$ and $\alpha = 15$ stratigraphies, or the SSI-LIN_CS analysis.

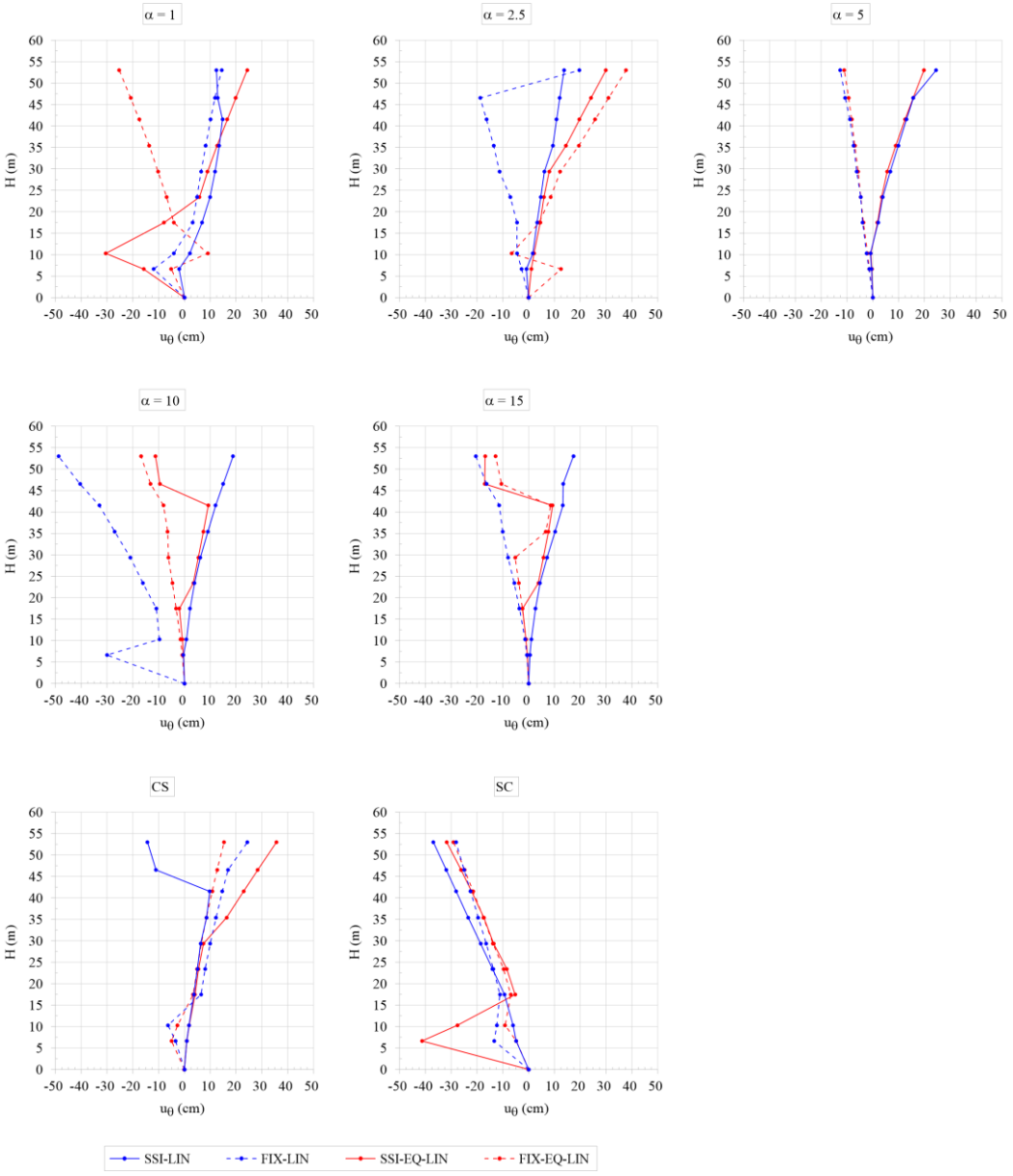

Fig. 5. 23 – Very slender tower maximum bending displacements (u_θ) profiles along the tower height for each SSI and FIX model during both the LIN and EQ-LIN analyses.

CHAPTER 6: FINAL REMARKS AND FUTURE PERSPECTIVES

6.1 Summary of the results of the study

The present thesis has dealt with the numerical investigation of the dynamic soil-structure interaction phenomena of masonry towers of different slenderness ratios resting on heterogeneous soil deposits. The research framework has mainly covered three aspects of the problem:

1. The role of the soil deposit conditions studied throughout the investigation of the soil stratigraphic heterogeneity influence. The soil stratigraphies have been classified by means of the α parameter (Vinale & Simonelli 1983), defined as the ratio between the shear wave velocity at the bottom and at the surface of the soil deposit, respectively. Five different degree of heterogeneity, equal to 1 (i.e. homogeneous condition), 2.5, 5, 10 and 15, have been taken into account, while two additional cases representative of a simpler clay/sand (CS) and sand/clay (SC) sequence ($\alpha = 2.28$ and $\alpha = 0.44$, respectively) have also been considered.
2. The influence of the heterogeneity and non-linearity of the soil inspected adopting two different approaches: a linear visco-elastic (LIN) and an equivalent-linear visco-elastic model (EQ-LIN).
3. The role played by the structural slenderness ratio H/B (height over the base length), considering three different values equal to 2.5, 5 and 10 (i.e. a squat, a slender and a very slender tower, respectively).

The whole study has been performed exploiting the finite element code Abaqus, a commercial software used in various civil engineering problems, among which structural and geotechnical applications. The constitutive model adopted to simulate the masonry behaviour has been the Concrete Damaged Plasticity model, a plastic-damage model originally conceived for concrete, but frequently used in masonry modelling.

The work initially has concerned the elastic response of the SSI system, with the purpose of identifying the dynamic properties of the tower resting on deformable soil deposits and quantifying the deviations from the fixed-base condition due to the SSI effects.

The results of the modal eigenvalues analyses performed for the three towers and for the whole set of soil profiles are reported in Fig. 6.1. They are plotted in terms of period of the tower resting on the deformable soil (T_{SSI}) normalized by the corresponding one in the fixed-base condition (T_0), as a function of the heterogeneity parameter α.

The findings can be summarized as follows:

1. the soil compliance produces the elongation of the natural periods which is strongly dependent on the soil profiles characteristics. The trends of the curves suggest that the elongation can be really significant for each analysed scenarios, but is generally more important for medium/medium-high heterogenous soils (α =5, 10); for higher α ratio (α =15) the phenomenon tends to stabilize or starts to reduce;
2. the period elongation is more remarkable for the first natural period rather than the second one;
3. the non-linear soil response introduced by the EQ-LIN approach enhances the period elongation;
4. for the analysed cases, the period elongation decreases as H/B increases; this is due to the relative soil-structure stiffness ratio that increases as H/B rises, leading the tower closer to the fixed-base scheme.

The numerical outputs derived from the modal eigenvalues analyses have been also compared with the analytical solution proposed by Veletsos & Nair (1975) for single

degree of freedom systems. Despite a similar trend between the two approaches has been recognized, the comparison shows that the analytical solution systematically underestimated the SSI effects as predicted by the FE analyses.

As far as the modal shapes, the results of the modal analyses show that:

1. the 1st mode of vibration seems not to be influenced by the soil compliance and, hence, it does not change much from the fixed-base scheme;
2. the 2nd mode of vibration shows instead a relevant dependency on the characteristics of the deposit; in fact, the modal shapes manifest greater modification when higher values of α are considered.

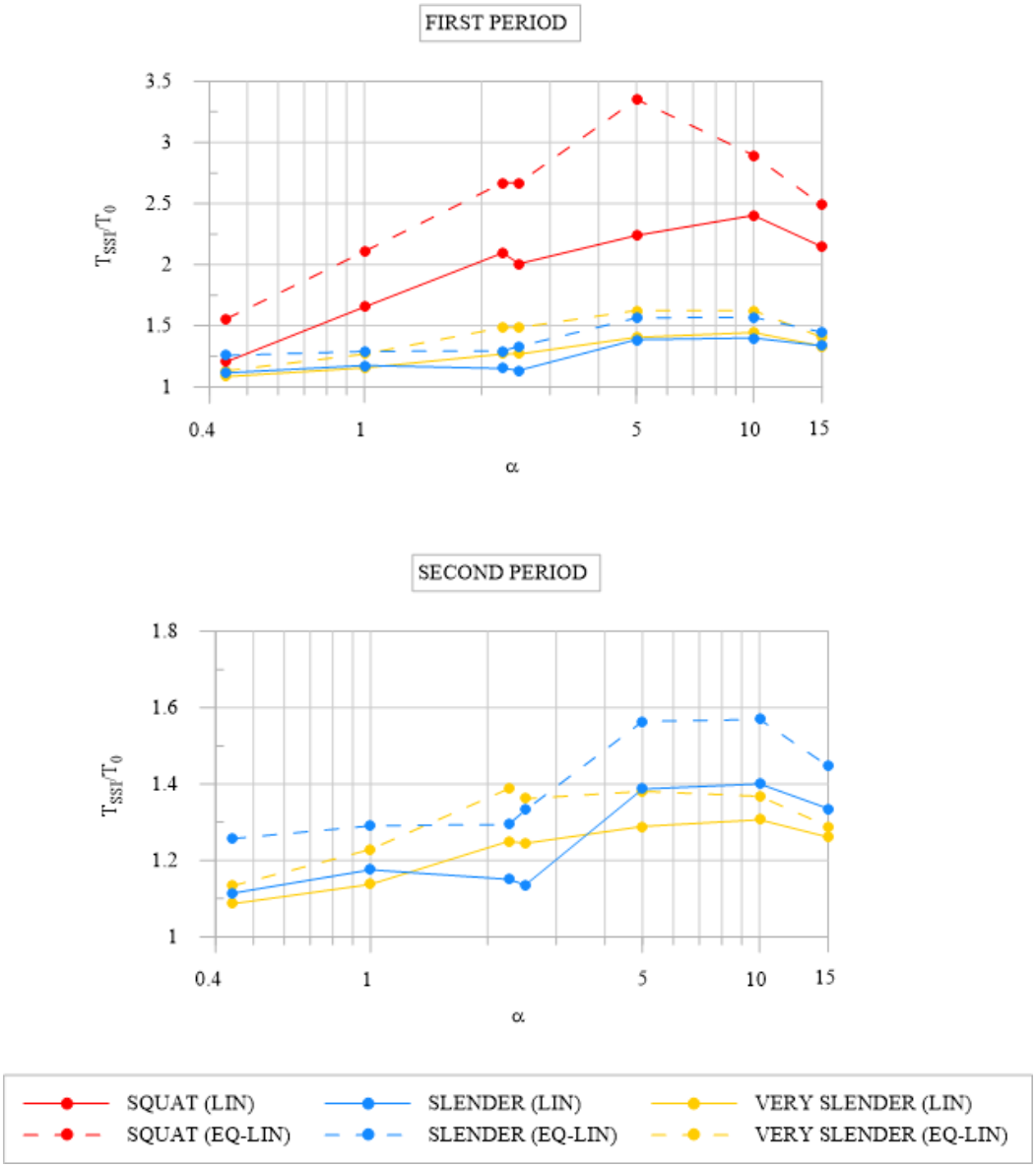

Fig. 6. 1– Natural periods of the SSI tower (T_{SSI}) normalized for the corresponding values in fixed-base condition (T_0) plotted as a function of the heterogeneity parameter α : squat, slender and very slender tower.

Once the dynamic identification of the SSI system has been performed, the seismic response of the towers using non-linear time-history analyses has been assessed. One of the main purposes of the present study has been to investigate the influence of the soil compliance on the seismic response of masonry towers with respect to the fixed-base condition. Thus, the adopted strategy has consisted in two different approaches:

1. a coupled approach which involves the whole soil-tower interaction model;
2. a decoupled approach in which the tower is modelled by means of a fixed-base scheme subjected to the input motion derived from the coupled simulation at the foundation level.

Thus, in both coupled and decoupled approach, the structure has been subjected to the same signal and all the deviations in the tower structural response can be related to the soil compliance influence.

The analysis of the acceleration response spectra recorded at the foundation level of the tower has revealed that the period elongation phenomenon causes a modification in the seismic demand of the structure with respect to the fixed-base condition. Even though a general trend is not inferable, lower spectral accelerations are expected for T_{SSI-1} while higher values are provided for T_{SSI-2} with respect to the fixed-base scheme. Moreover, the response spectra derived at the top control point of the models suggest a different response of the structures between the SSI and the FIX models for each considered tower, with more amplified spectral accelerations in correspondence of the natural periods which characterize each analysed scenario.

The analysis of the non-linear response of the masonry towers, modelled through the CDP constitutive model, has allowed to evaluate the possible failure modes affecting the structure. From the interpretation of the tensile damage distributions, a total of 6 recurring damage scenarios have been identified, as reported in Fig. 6.2:

1. damage mainly located at the basement level which could evolve in a cylindrical hinge;
2. diagonal failure in the first half of the tower close to its main entrance;

3. vertical splitting of the structure characterized by a vertical crack running in the middle of the tower;
4. a mixed mode composed by diagonal failure and vertical splitting;
5. inclined cracks close to the minor openings along the height of the tower;
6. damage mainly localized at the belfry level which can also cause its collapse.

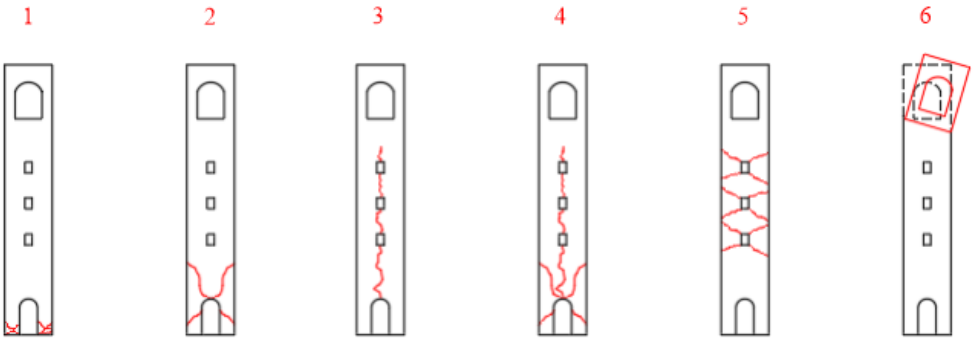

Fig. 6. 2– Sketch of the main recurring damage modes recognized from the analysed masonry towers models: 1) Basement level damage; 2) Diagonal failure; 3) Vertical splitting; 4) Mixed diagonal failure and vertical splitting; 5) Inclined cracking at the minor openings; 6) Belfry collapse.

The main recurring damage modes recognized in each modelled tower are summarised in Tab. 6.1. Apart from the squat tower, characterised by the mode 1 as the dominant pattern for all the modelling approaches, the slender and very slender tower manifest a rather variable response. Indeed, for both the latter typologies of towers, the damage mode can be very different considering the SSI or the FIX approach. The slender tower is often characterized by mode 1 and mode 2 if the soil compliance is considered, especially for the LIN soil set of analyses. For the very slender tower recurring damage patterns consist in mode 5 and 6 for both coupled and fixed-base models; nonetheless, mode 3 and 4 are likely to occur, especially with the fixed-base scheme. Moreover, high degrees of soil heterogeneity are likely to cause damage localization in the upper part of the structure and hence close to the belfry level (mechanism 6) in the case of the slender and very slender tower.

The approach adopted to model the soil behaviour potentially plays a role on the possible damage distribution, but it does not look as relevant as the soil compliance con-

dition at least in the analysed scenarios. A general trend has not been detected and it is not possible to state “a priori” in which case the soil compliance surely alters the damage pattern in comparison to the fixed-base scheme.

	SOIL PROFILE	LIN		EQ-LIN	
		SSI	FIX	SSI	FIX
SQUAT TOWER	$\alpha = 1$	1	1	1	1
	$\alpha = 2.5$	1	1	1	1
	$\alpha = 5$	1	1	1	1
	$\alpha = 10$	1	1	1	1+6
	$\alpha = 15$	1	1	1	1+6
	CS	1	1	1	1
	SC	1	1	/	/
SLENDER TOWER	$\alpha = 1$	1/2+5	1/2	1/2+5	1/2+5
	$\alpha = 2.5$	1+6	2+6	/	2+6
	$\alpha = 5$	6	1/2	1	1/2
	$\alpha = 10$	/	1/2+5	5+6	1+6
	$\alpha = 15$	5+6	2+6	3+5+6	5+6
	CS	1+5+6	1/2+5+6	1	1/2+5+6
	SC	1/2	1/2+5	1/2	1/2
VERY SLENDER TOWER	$\alpha = 1$	4+5+6	4+5	2+5	2+5
	$\alpha = 2.5$	3+5	4	3+5	4+5
	$\alpha = 5$	5	3+6	5	3
	$\alpha = 10$	5	4+6	5+6	5+6
	$\alpha = 15$	5+6	6	5+6	5+6
	CS	3+5	4+6	3+5	4+5
	SC	4+5	3+6	2	2

Tab. 6. 1 – Summary of the main recurring damage modes recognized from the analysed towers models according to the sketch reported in Fig. 6.2.

Finally, the average of the maximum bending and rocking displacements recorded at the top of each SSI masonry tower are reported in Tab. 6.2. The values are also normalized for the height of the structure (and expressed in percentage) in order to make

a more effective comparison among the three considered structural slenderness ratios. The numerical results suggest that:

1. the bending and rocking displacements become more relevant as the slenderness ratio increases;
2. the bending displacement demand is lower for the SSI slender and very slender towers in comparison to the FIX scheme for the LIN set of analyses; on the contrary, greater displacements are expected for the SSI squat tower with respect to the FIX model;
3. the bending displacement demand is higher for all the SSI towers if compared to the corresponding FIX scheme in the EQ-LIN set of analysis;
4. the bending displacement demand tends to increase when the soil nonlinearity is accounted for (SSI-LIN vs SSI-EQ-LIN approach); conversely, an opposite trend is suggested by the FIX approach;
5. the rocking displacement demand is expected to be higher when the soil nonlinearity is considered (SSI-EQ-LIN), i.e. when the soil is more deformable due to the higher strain level induced by the earthquake.

	BENDING DISPLACEMENTS (%)				ROCKING DISPLACEMENTS (%)	
	LIN		EQ-LIN			
	SSI	FIX	SSI	FIX	SSI-LIN	SSI-EQ-LIN
SQUAT TOWER	0.193	0.095	0.193	0.088	0.067	0.102
SLENDER TOWER	0.302	0.363	0.314	0.270	0.067	0.119
VERY SLENDER TOWE	0.372	0.454	0.457	0.399	0.119	0.165

Tab. 6. 2 – Average of the maximum bending and rocking displacements recorded at the top of each masonry tower model and normalized by height of the structures. Values are expressed in percentage.

6.2 Conclusions and future perspectives

A numerical investigation on the dynamic soil-structure interaction phenomena involving masonry towers has been presented in the thesis. The whole problem is characterized by a high degree of complexity due to the great multidisciplinary of the topic involving seismic, structural and geotechnical engineering. In the specific case, the study has mainly focused on some specific key points which can influence the dynamic response of a tower resting on soft soils: the soil stratigraphic conditions, the soil non-linearity and the tower structural slenderness.

The obtained results suggest that all these aspects surely can play a relevant role on the seismic performance of ancient masonry towers. Indeed, the modal properties, the seismic demand and the possible collapse modes affecting the structure can be significantly modified if the soil compliance is considered in the analysis. In particular, the period elongation is significantly dependent on the stratigraphy which characterizes the subsoil foundation. Moreover, the soil compliance mainly influences the higher vibrational modes rather than the first one. The displacement seismic demand increases when the soil non-linear response is considered, both for the bending and the rocking displacement.

With regards to the possible collapse mode, the upper part of the structure including the bell cell results more sensitive to damage if significant heterogenous subsoil conditions are considered. In addition, the damage pattern distribution of the tower can be significantly affected by the soil compliance. Thus, it is highly recommended to take into account the soil compliance in the dynamic soil-structure interaction simulation of masonry towers, in order to catch all these aspects and perform more accurate structural assessments.

Further efforts should be spent to generalize these findings. Although a total of 84 non-linear time-history analyses have been carried out in this work, the analysed sample is still too small and needs to be enlarged considering, for example, different subsoil conditions, tower geometries and masonry mechanical properties, or investigating the influence of the selected seismic input motion.

In addition, a future aspect that could be improved is represented by the adoption of a more complex and accurate modelling strategy of the masonry material which, in the present study, has consisted of an equivalent homogeneous medium.

Finally, more advanced soil constitutive models capable of simulating the non-linear response of the soils need to be adopted. The equivalent-linear visco-elastic approach used in this thesis work is a useful model to simulate the soil dynamic behaviour, but it is characterized by some limitations. Indeed, although the non-linear behaviour is approximated through iterations, the approach remains a linear method of analysis and does not allow to consider the variation of stiffness and damping during the earthquake loading. The approach is more suitable when weak seismic motions are considered in the simulations. Moreover, the equivalent-linear visco-elastic approach is a total stress approach, which neglects the build-up of excess pore water pressures during the seismic action.

Therefore, further studies should be carried out accounting for a more reliable description of the dynamic behaviour of the soil foundation deposit, through the use of effective stress-based elasto-plastic soil constitutive laws and the solution of the solid-fluid interaction equations under dynamic loading, assessing the influence of these advanced soil models on the dynamic response of the structure in elevation.

REFERENCES

Abaqus (2014). *Abaqus documentation version 6.14.* Dassault Systèmes, Providence, RI.

Acito, M., Bocciarelli, M., Chesi, C., & Milani, G. (2014). *Collapse of the clock tower in Finale Emilia after the May 2012 Emilia Romagna earthquake sequence: Numerical insight.* Engineering Structures, 72, 70-91.

Alfarah, B., López-Almansa, F., & Oller, S. (2017). *New methodology for calculating damage variables evolution in Plastic Damage Model for RC structures.* Engineering Structures, 132, 70-86.

Amorosi, A., Boldini, D., & Elia, G. (2010). *Parametric study on seismic ground response by finite element modelling.* Computers and Geotechnics, 37(4), 515-528.

Amorosi, A., Boldini, D., & Di Lernia, A. (2016). *Seismic ground response at Lotung: Hysteretic elasto-plastic-based 3D analyses.* Soil Dynamics and Earthquake Engineering, 85, 44-61.

Amorosi, A., Boldini, D., & Di Lernia, A. (2017). *Dynamic soil-structure interaction: a three-dimensional numerical approach and its application to the Lotung case study.* Computers and Geotechnics, 90, 34-54.

Annecchiarico, M., Portioli, F., & Landolfo, R. (2010). *Micro and macro finite element modeling of brick masonry panels subject to lateral loadings.* In Proc., COST C26 Action Final Conf (pp. 315-320).

Bardet, J. P., Ichii, K., & Lin, C. H. (2000). *EERA: a computer program for equivalent-linear earthquake site response analyses of layered soil deposits.* University of Southern California, Department of Civil Engineering.

Bartoli, G., Betti, M., Spinelli, P., & Tordini, B. (2006). *An "innovative" procedure for assessing the seismic capacity of historical tall buildings: the "Torre Grossa" masonry tower.* In Proc V Int Conf Struct Anal Hist Constr SAHC (pp. 929-937).

Bartoli, G., Betti, M., & Giordano, S. (2013). *In situ static and dynamic investigations on the "Torre Grossa" masonry tower.* Engineering Structures, 52, 718-733.

Bartoli, G., Betti, M., & Vignoli, A. (2016*). A numerical study on seismic risk assessment of historic masonry towers: a case study in San Gimignano.* Bulletin of Earthquake Engineering, 14(6), 1475-1518.

Bartoli, G., Betti, M., & Monchetti, S. (2017). *Seismic risk assessment of historic masonry towers: comparison of four case studies.* Journal of Performance of Constructed Facilities, 31(5), 04017039.

Bartoli, G., Betti, M., Galano, L., & Zini, G. (2019). *Numerical insights on the seismic risk of confined masonry towers.* Engineering Structures, 180, 713-727.

Bathe, K. J. (1996). *Finite element procedures in engineering analysis, (2nd ed.)* Upper Saddle River, NJ: Prentice Hall.

Bayraktar, A., Hökelekli, E., Halifeoğlu, F. M., Mosallam, A., & Karadeniz, H. (2018). *Vertical strong ground motion effects on seismic damage propagations of historical masonry rectangular minarets.* Engineering Failure Analysis, 91, 115-128.

Binda, L., Mirabella, G., Tiraboschi, C. e Abbaneo S. (1994). *Measuring masonry material properties.* US-Italian Workshop on Guidelines for Seismic Evaluation and Rehabilitation of Unreinforced Masonry Buildings, Techn. Rep. NCEER-94-0021, NCEER-SUNY Buffalo.

Biot, M. A. (1941). *General theory of three-dimensional consolidation.* Journal of applied physics, 12(2), 155-164.

Breccolotti, M., & Materazzi, A. L. (2016). *The role of the vertical acceleration component in the seismic response of masonry chimneys.* Materials and Structures, 49(1), 29-44.

Burland J.B., Viggiani C. (1994). *Osservazioni sul comportamento della Torre di Pisa.* Rivista Italiana di Geotecnica, vol. XXVIII, n. 3, pp. 179-200.

Casciati, S., & Borja, R. I. (2004). *Dynamic FE analysis of South Memnon Colossus including 3D soil–foundation–structure interaction.* Computers and Structures, 82(20-21), 1719-1736.

Casolo, S. (1998). *A three-dimensional model for vulnerability analysis of slender medieval masonry towers.* Journal of Earthquake Engineering, 2(04), 487-512.

Casolo, S. (2001). *Significant ground motion parameters for evaluation of the seismic performance of slender masonry towers.* Journal of earthquake engineering, 5(02), 187-204.

Casolo, S., Milani, G., Uva, G., & Alessandri, C. (2013a). *Comparative seismic vulnerability analysis on ten masonry towers in the coastal Po Valley in Italy.* Engineering Structures, 49, 465-490.

Casolo, S., & Uva, G. (2013b). *Non-linear dynamic analysis of masonry towers under natural accelerograms accounting for soil-structure interaction.* In: 4th ECCOMAS, Thematic Conference on Computational Methods in Structural Dynamics and Earthquake Engineering. Crete, Greece, 2013, pp. 4488–4506.

Casolo, S., Diana, V., & Uva, G. (2017). Influence of soil deformability on the seismic response of a masonry tower. Bulletin of Earthquake Engineering, 15(5), 1991-2014.

Castellazzi, G., D'Altri, A. M., de Miranda, S., Chiozzi, A., & Tralli, A. (2018). *Numerical insights on the seismic behaviour of a non-isolated historical masonry tower.* Bulletin of Earthquake Engineering, 16(2), 933-961.

Ceroni, F., Pecce, M., Voto, S., & Manfredi, G. (2009). *Historical, architectural, and structural assessment of the bell tower of Santa Maria del Carmine*. International Journal of Architectural Heritage, 3(3), 169-194.

Clementi, F., Milani, G., Ferrante, A., Valente, M., & Lenci, S. (2020). *Crumbling of Amatrice clock tower during 2016 Central Italy seismic sequence: Advanced numerical insights.* Frattura Ed Integrità Strutturale 14(51), 313–335.

Clough, R. W., & Penzien, J. (1993). *Dynamics of Structures.* McGraw-Hill.

Consiglio dei Ministri. (2018). *DM 17 gennaio 2018 in materia di "aggiornamento delle norme tecniche per le costruzioni".* Gazzetta ufficiale n.42 del 20 febbraio 2018.

Cosentini, R. Foti, S. Lancellotta, R. Sabia, D. 2015. *Dynamic behaviour of shallow founded historic towers: validation of simplified approaches for seismic analyses.* Int J Geotech Eng:13–29.

D'Ambrisi, A., Mariani, V., & Mezzi, M. (2012). *Seismic assessment of a historical masonry tower with nonlinear static and dynamic analyses tuned on ambient vibration tests.* Engineering Structures, 36, 210-219.

Day SM. (1978). *Seismic response of embedded foundations.* In Proceedings of the ASCE Convention, Chicago, IL, 16–20 October 1978; Preprint no. 3450.

De Angelis, A., Ambrosino, A., Sica, S., & Lourenco, P. B. (2022). *Soil contribution on the structural identification of a historical masonry bell-tower: Simplified vs advanced numerical models*. In Geotechnical Engineering for the Preservation of Monuments and Historic Sites III (pp. 904-916). CRC Press.

de Felice, G., Amorosi, A., & Malena, M. (2010). *Elasto-plastic analysis of block structures through a homogenization method.* International journal for numerical and analytical methods in geomechanics, 34(3), 221-247.

de Silva, F., Di Laora, R., Sica, S., & Silvestri, F. (2014a). *Influenza delle caratteristiche di terreno e struttura sull'interazione in campo dinamico.* In IARG 2014 Chieti.

de Silva, F., Ceroni, F., Sica, S., Pecce, M. R., & Silvestri, F. (2014b). *L'interazione terreno-struttura sotto azione sismica: il caso di studio del Campanile del Carmine a Napoli.* Atti del XXV Convegno Nazionale di Geotecnica "La geotecnica nella difesa del territorio e delle infrastrutture dalle calamità naturali, 2, 109-116.

de Silva, F., Ceroni, F., Sica, S., Pecce, M. R., & Silvestri, F. (2015a*). Effects of soil-foundation-structure interaction on the seismic behaviour of monumental towers: the case study of the Carmine Bell Tower in Naples.* Rivista Italiana di Geotecnica, 49(3), 7-27.

de Silva, F., Ceroni, F., Sica, S., Pecce, M. R., & Silvestri, F. (2015b). *Influenza del sottosuolo sul comportamento dinamico del Campanile del Carmine a Napoli.* In IARG 2015 Cagliari.

de Silva, F., Pitilakis, D., Ceroni, F., Sica, S., & Silvestri, F. (2018a). *Experimental and numerical dynamic identification of a historic masonry bell tower accounting for different types of interaction.* Soil Dynamics and Earthquake Engineering, 109, 235-250.

de Silva, F., Ceroni, F., Sica, S., & Silvestri, F. (2018b). *Non-linear analysis of the Carmine bell tower under seismic actions accounting for soil–foundation–structure interaction.* Bulletin of Earthquake Engineering, 16(7), 2775-2808.

de Silva, F. (2020). *Influence of soil-structure interaction on the site-specific seismic demand to masonry towers.* Soil Dynamics and Earthquake Engineering, 131, 106023.

de Silva, F., & Silvestri, F. (2022). *A large-scale evaluation of the seismic demand for historic towers laying on soft soil.* In Geotechnical Engineering for the Preservation of Monuments and Historic Sites III (pp. 871-882). CRC Press.

di Lernia, A. (2014). *Interazione dinamica terreno-struttura mediante approcci non lineari tridimensionali agli elementi finiti.* PhD Thesis.

di Lernia, A., Amorosi, A., & Boldini, D. (2019). A multi-directional numerical approach for the seismic ground response and dynamic soil-structure interaction analyses. In Earthquake Geotechnical Engineering for Protection and Development of Environment and Constructions (pp. 2145-2152). CRC Press.

Di Nino, S., & Luongo, A. (2019). *A simple homogenized orthotropic model for in-plane analysis of regular masonry walls.* International Journal of Solids and Structures, 167, 156-169.

Doğangün, A., Livaoğlu, R., & Acar, R. (2007). *A study on seismic behaviour of minarets considering soil-structure interaction.* In International earthquake symposium, Kocaeli (pp. 393-404).

D'Oria A. F., Elia G., di Lernia A., Uva G. (2022). *Influence of soil deposit heterogeneity on the dynamic behaviour of masonry towers*, In Geotechnical Engineering for the Preservation of Monuments and Historic Sites III (pp. 780-791). CRC Press.

DPCM 2011. *Direttiva del Presidente del Consiglio dei Ministri per la valutazione e riduzione del rischio sismico del patrimonio culturale con riferimento alle NTC2008*. G. U. n. 47 del 26.02.2011 [in Italian].

Elsabee, F., Morray, J. P., & Roesset, J. M. (1977). *Dynamic behaviour of embedded foundations.* Massachusetts Institute of Technology, Department of Civil Engineering, Constructed Facilities Division.

Falcone, G., Acunzo, G., Mendicelli, A., Mori, F., Naso, G., Peronace, E., ... & Moscatelli, M. (2021). *Seismic amplification maps of Italy based on site-specific microzo-nation dataset and one-dimensional numerical approach.* Engineering Geology, 289, 106170.

Ferrante, A., Clementi, F., & Milani, G. (2019*). Dynamic behaviour of an inclined existing masonry tower in Italy.* Frontiers in Built Environment, 5, 33.

Fioravante, V., Giretti, D., Abate, G., Aversa, S., Boldini, D., Capilleri, P. P., ... & Vannucchi, G. (2013). *Earthquake geotechnical engineering aspects: the 2012 Emilia-Romagna earthquake (Italy).* In Proceedings of the Seventh Int. Conf. on Case Histories in Geotechnical Engineering. Invited Lecture No. EQ-5. Wheeling, Il (Chicago, Il Area)–April (pp. 1-34).

Fiorentino, G., Lavorato, D., Quaranta, G., Pagliaroli, A., Carlucci, G., Nuti, C., ... & Bartelletti, R. (2017). *Numerical and experimental analysis of the leaning Tower of Pisa under earthquake.* Procedia engineering, 199, 3350-3355.

Gazetas, G. (1982). *Vibrational characteristics of soil deposits with variable wave velocity.* International Journal for Numerical and Analytical Methods in Geomechan-ics, 6(1), 1-20.

Gazetas, G. (1983). *Analysis of machine foundation vibrations: state of the art.* International Journal of soil dynamics and earthquake engineering, 2(1), 2-42.

Gazetas, G. (1991). *Formulas and charts for impedances of surface and embedded foundations.* Journal of Geotechnical Engineering, 117(9), 1363-1381.

Gazetas, G., & Mylonakis, G. (1998). *Seismic soil-structure interaction: new evidence and emerging issues.* Geotechnical special publication, (75 II), 1119-1174.

Gesualdo, A., & Nunziante, L. (2005). *Omogeneizzazione di murature storiche.* In Proceedings XVII National Congress AIMETA.

Grazzini, A., Chiabrando, F., Foti, S., Lingua, A. M., & Spanò, A. (2018). *Damage assessment and seismic vulnerability analysis of S. Agostino church in Amatrice.* In 16th European Conference on Earthquake Engineering, Thessaloniki, Greece, June (pp. 18-21).

Hashash, Y. M., & Park, D. (2002). *Viscous damping formulation and high frequency motion propagation in non-linear site response analysis.* Soil Dynamics and Earthquake Engineering, 22(7), 611-624.

Heyman, J. (1992). *Leaning towers.* In Masonry Construction (pp. 153-159). Springer, Dordrecht.

Jennings, P. C., & Bielak, J. (1973). *Dynamics of building-soil interaction.* Bulletin of the seismological society of America, 63(1), 9-48.

Kachanov, L. (1958). *Rupture time under creep conditions.* Izv. Akad. Nauk SSSR, 8, 26-31.

Karimi, A. H., Karimi, M. S., Kheyroddin, A., & Shahkarami, A. A. (2016). *Experimental and numerical study on seismic behavior of an infilled masonry wall compared to an arched masonry wall.* In Structures (Vol. 8, pp. 144-153). Elsevier.

Kavvadas, M., & Amorosi, A. (2000). *A constitutive model for structured soils.* Géotechnique, 50(3), 263-273.

Kuhlemeyer, R. L., & Lysmer, J. 1973. *Finite element method accuracy for wave propagation problems.* Journal of the Soil Mechanics and Foundations Division, 99(5), 421-427.

Kim, S., & Stewart, J. P. (2003). *Kinematic soil-structure interaction from strong motion recordings.* Journal of Geotechnical and Geoenvironmental Engineering, 129(4), 323-335.

Kramer S.L. (1996) *Geotechnical earthquake engineering* (Prentice-Hall international series in civil engineering and engineering mechanics). Pearson Education

Lacanna, G., Ripepe, M., Coli, M., Genco, R., & Marchetti, E. (2019). *Full structural dynamic response from ambient vibration of Giotto's bell tower in Firenze (Italy), using modal analysis and seismic interferometry.* NDT & E International, 102, 9-15.

Lancellotta R. (2013). *La torre della Ghirlandina: una storia di interazione struttura-terreno.* Rivista Italiana di Geotecnica, 47, n. 2, pp. 7-34.

Lanzo, G., & Silvestri, F. (1999). *Risposta sismica locale: teoria ed esperienze.* Hevelius.

Lasciarrea, W. G., Amorosi, A., Boldini, D., de Felice, G., & Malena, M. (2019). *Jointed Masonry Model: A constitutive law for 3D soil-structure interaction analysis.* Engineering Structures, 201, 109803.

Lee, J., & Fenves, G. L. (1998). *Plastic-damage model for cyclic loading of concrete structures.* Journal of engineering mechanics, 124(8), 892-900.

Lourenço, P. B., Rots, J. G., & Blaauwendraad, J. (1995). *Two approaches for the analysis of masonry structures: micro and macro-modeling.* HERON, 40 (4), 1995.

Lourenço, P. B. (1996). *Computational strategies for masonry structures.* PhD thesis Delft University Press.

Lourenço, P. B., Milani, G., Tralli, A., & Zucchini, A. (2007). *Analysis of masonry structures: review of and recent trends in homogenization techniques.* Canadian Journal of Civil Engineering, 34(11), 1443-1457.

Lubliner, J., Oliver, J., Oller, S., & Oñate, E. (1989). *A plastic-damage model for concrete.* International Journal of solids and structures, 25(3), 299-326.

Lysmer, J., & Kuhlemeyer, R. L. (1969). *Finite dynamic model for infinite media.* Journal of the engineering mechanics division, 95(4), 859-877.

Madiai, C., Renzi, S., & Vannucchi, G. (2017). *Geotechnical aspects in seismic soil–structure interaction of San Gimignano towers: probabilistic approach.* Journal of Performance of Constructed Facilities, 31(5), 04017059.

Maravas, A., Mylonakis, G., & Karabalis, D. L. (2014). *Simplified discrete systems for dynamic analysis of structures on footings and piles.* Soil Dynamics and Earthquake Engineering, 61, 29-39.

Milani, G. (2019). *Fast vulnerability evaluation of masonry towers by means of an interactive and adaptive 3D kinematic limit analysis with preassigned failure mechanisms.* International Journal of Architectural Heritage, 13(7), 941-962.

Minghini, F., Milani, G., & Tralli, A. (2014). *Seismic risk assessment of a 50 m high masonry chimney using advanced analysis techniques.* Engineering Structures, 69, 255-270.

Monti Di Sopra, E. (2009). *Modelli di danno e plasticità per l'analisi di elementi strut-turali in muratura.* PhD Thesis

Mortezaei, A., & Motaghi, A. (2016). *Seismic assessment of the world's tallest pure-brick tower including soil-structure interaction.* Journal of Performance of Constructed Facilities, 30(5), 04016020.

Mylonakis, G., & Gazetas, G. (2000). *Seismic soil-structure interaction: beneficial or detrimental?.* Journal of earthquake engineering, 4(3), 277-301.

Mylonakis, G., Nikolaou, S., Gazetas, G. (2006). *Footings under seismic loading: Analysis and design issues with emphasis on bridge foundations.* Soil Dynamics and Earthquake Engineering, 26(9), pp. 824–853.

Nielsen, A. H. (2014). *Towards a complete framework for seismic analysis in Abaqus.* Proceedings of the institution of civil engineers-engineering and computational mechanics, 167(1), 3-12.

Nielsen, A. H. (2006, May). *Absorbing boundary conditions for seismic analysis in ABAQUS.* In ABAQUS users' conference (pp. 359-376).

Olivito, R. S. (2003). *Statica e stabilità delle costruzioni murarie.* Pitagora

Pande, G. N., Liang, J. X., & Middleton, J. (1989). *Equivalent elastic moduli for brick masonry.* Computers and Geotechnics, 8(3), 243-265.

Pieraccini, M., Dei, D., Betti, M., Bartoli, G., Tucci, G., & Guardini, N. (2014). *Dynamic identification of historic masonry towers through an expeditious and no-contact approach: Application to the "Torre del Mangia" in Siena (Italy).* Journal of Cultural Heritage, 15(3), 275-282.

Piro, A., de Silva, F., Parisi, F., Scotto di Santolo, A., & Silvestri, F. (2020). *Effects of soil-foundation-structure interaction on fundamental frequency and radiation damping ratio of historical masonry building sub-structures.* Bulletin of Earthquake Engineering, 18(4), 1187-1212.

Poiani, M., Gazzani, V., Clementi, F., Milani, G., Valente, M., & Lenci, S. (2018*). Iconic crumbling of the clock tower in Amatrice after 2016 central Italy seismic sequence: advanced numerical insight.* Procedia Structural Integrity, 11, 314-321.

Rainieri, C., & Fabbrocino, G. (2012*). Estimating the elastic period of masonry towers.* In Topics in Modal Analysis I, Volume 5 (pp. 243-248). Springer, New York, NY.

Raijmakers, T. M. J., Vermeltfoort, Ath. (1992) *Deformation controlled tests in masonry shear walls.* Report B-92-1156, TNO-Bouw, Delft.

Rouainia, M., & Muir Wood, D. (2000). *A kinematic hardening constitutive model for natural clays with loss of structure.* Géotechnique, 50(2), 153-164.

Sarhosis, V., Milani, G., Formisano, A., & Fabbrocino, F. (2018). *Evaluation of different approaches for the estimation of the seismic vulnerability of masonry towers.* Bulletin of Earthquake Engineering, 16(3), 1511-1545.

Sica, S., Ceroni, F., & Pecce, M. R. (2013). *Soil structure interaction on the dynamic behaviour of two historic masonry structures.* In 2nd International Symposium on Geotechnical Engineering for the Preservation of Monuments and Historic Sites; Napoli; Italy (pp. 657-667). CRC Press/Balkema.

Shehu, R. (2021). *Implementation of pushover analysis for seismic assessment of masonry towers: Issues and practical recommendations.* Buildings, 11(2), 71.

Stewart, J. P., Kim, S., Bielak, J., Dobry, R., & Power, M. S. (2003). *Revisions to soil-structure interaction procedures in NEHRP design provisions.* Earthquake Spectra, 19(3), 677-696.

Szczecina, M., & Winnicki, A. (2015). *Calibration of the CDP model parameters in Abaqus.* In The 2015 World Congress on Advances in Structural Engineering and Mechanics (ASEM15).

Szczecina, M., & Winnicki, A. (2017). *Relaxation time in CDP model used for analyses of RC structures.* Procedia engineering, 193, 369-376.

Taliercio, A. (2014). *Closed-form expressions for the macroscopic in-plane elastic and creep coefficients of brick masonry.* International Journal of Solids and Structures, 51(17), 2949-2963.

Tiberti, S., Acito, M., & Milani, G. (2016). *Comprehensive FE numerical insight into Finale Emilia Castle behavior under 2012 Emilia Romagna seismic sequence:*

Damage causes and seismic vulnerability mitigation hypothesis. Engineering Structures, 117, 397-421.

Torabi, H., & Rayhani, M. T. (2014). *Three-dimensional finite element modeling of seismic soil–structure interaction in soft soil.* Computers and Geotechnics, 60, 9-19.

Valente, M., & Milani, G. (2016). *Seismic assessment of historical masonry towers by means of simplified approaches and standard FEM.* Construction and Building Materials, 108, 74-104.

Valente, M., & Milani, G. (2018). *Effects of geometrical features on the seismic response of historical masonry towers.* Journal of Earthquake Engineering, 22(sup1), 2-34.

Van der Pluijm, R. (1992). *Material properties of masonry and its components under tension and shear.* In Proceedings 6th Canadian Masonry Symposium, 15-17 June 1992, Saskatoon, Canada (pp. 675-686). University of Saskatchewan.

Van der Pluijm, R. (1993). *Shear behaviour of bed joints*. In 6th North American Masonry Conference, 6-9 June 1993, Philadelphia, Pennsylvania, USA (pp. 125-136). Technomic Publ. Co.

Veletsos, A.S., Verbic, B. (1973). *Vibration of viscoelastic foundations.* Earthquake Engineering and Structural Dynamics, 2(1), pp. 87–102.

Veletsos, A.S., Meek, J.W. (1974). *Dynamic behaviour of building-foundation systems.* Earthquake Engineering and Structural Dynamics, 3(2), pp. 121–138.

Veletsos, A.S., Nair, V.D. (1975). *Seismic interaction of structures on hysteretic foundations.* Journal of the structural division, ASCE, 101(1), pp. 109–129.

Veletsos, A. S., & Prasad, A. M. (1988). *Seismic interaction of structures and soils: stochastic approach.* National Center for Earthquake Engineering Research.

Vinale, F., & Simonelli, A. L. (1983). *L'eterogeneità dei terreni nei fenomeni di amplificazione locale.* Atti XV Conv. Naz. Geot., Spoleto, 4-6.

Volpini, C., & Douglas, J. (2019). *An accessible approach for the site response analysis of quasi-horizontal layered deposits.* Bulletin of Earthquake Engineering, 17, 1163-1183.

Volpini, C., Douglas, J., & Nielsen, A. H. (2021). *Guidance on conducting 2D linear viscoelastic site response analysis using a finite element code.* Journal of Earthquake Engineering, 25(6), 1153-1170.

Vucetic, M., & Dobry, R. (1991). *Effect of soil plasticity on cyclic response.* Journal of geotechnical engineering, 117(1), 89-107.

Wolf, J.P. (1985). *Dynamic soil-structure interaction.* Englewood Cliffs, NJ: Prentice Hall.

Zizi, M., Campitiello, F., & De Matteis, G. (2017). *Non-Linear FE Model for cyclic response of brick-cement mortar masonry shear-walls.* In XV International Forum Le Vie dei Mercanti. Jun (pp. 15-17).

SHORT CURRICULUM

Aldo Fabio D'Oria, M.Sc. Eng.
Ph.D. Candidate in "Risk and Environmental, Territorial and Building Development"
DICATECh – Politecnico di Bari

Born in Corato (Italy) on January 9th, 1994. The author obtained a Bachelor's Degree in Civil and Environmental Engineering in 2016 from the Politecnico di Bari, developing a thesis in Geotechnics entitled "Influence of the chemical composition of the pore fluid on the earth pressure". In April 2019, from the same university, he obtained a Master's Degree in Civil Engineering (curriculum Geotechnics) with full marks, defending a thesis in Soil Dynamics entitled "Assessment of the dynamic performance of an anchored diaphragm wall". After the graduation, the author won a Internship with the Erasmus+ Program at the Newcastle University (UK), where he spent 3 months as visiting student. On November 2019, he started the PhD course in "Risk, Environmental, Territorial and Building Development" (XXXV cycle). During the three years of the doctorate program, the author deepened his knowledge concerning the dynamic soil-structure interaction phenomena, particularly focusing on masonry structures. During his Ph.D., he was author or co-author of some journal and conference papers and he supported the didactic activities for the "Foundations" course (Master's Degree in Civil Engineering, chair: Prof. C. Vitone).

LIST OF THE PUBLICATIONS

1. Elia, G., Rouainia, M., di Lernia, A., & D'Oria, A. F. (2021). Assessment of damping predicted by kinematic hardening soil models during strong motions. Géotechnique Letters, 11(1), 48-55.

2. D'Oria, A. F., Elia, G., di Lernia, A., & Uva, G. (2022). Influence of soil deposit heterogeneity on the dynamic behaviour of masonry towers. In Geotechnical Engineering for the Preservation of Monuments and Historic Sites III (pp. 780-791). CRC Press.

3. D'Oria, A. F., Elia, G., di Lernia, A., & Uva, G. (2022). Influenza dell'eterogeneità stratigrafica sulla risposta dinamica di torri in muratura. In IARG 2022 Caserta.